Computational investigation and design of coordination compounds for hydrogen storage

Hummelshøj, Jens Strabo

Publication date:
2009

Document Version
Early version, also known as pre-print

Computational investigation and design of coordination compounds for hydrogen storage

Jens Strabo Hummelshøj

Submitted in candidacy
for the degree of Doctor of Philosophy

February 2009

Center for Atomic-scale Materials Design, Department of Physics
Materials Research Division, Risø National Laboratory for Sustainable Energy
The Technical University of Denmark

Abstract

Two classes of high capacity hydrogen storage materials, the metal tetrahydroborates and the metal ammines, were investigated at the atomic scale using density functional theory simulations. It was shown that simple model structures could be used to asses the stabilities of complex systems. Trends in stabilities were reproduced for known systems and the correlations were used to predict the stabilities of unknown systems. Of these, 20 tetrahydroborate systems formed stable mixtures with promising stabilities. A few mixed metal ammine systems showed promising decomposition energies but their stabilities are questionable and should be investigated further. The ab-/desorption cycles of magnesium and calcium ammines were analyzed and the faster kinetics of the magnesium ammines could be explained by a layered structure of magnesium chloride. It was found that doping calcium chloride with iodine could force it into a layered structure which is expected to improve the kinetics. Iodine doping could also be used for improving ion conduction in lithium tetrahydroborate, which is useful for batteries. Only the high temperature phase of lithium tetrahydroborate show a high ion conduction, and it was shown that doping lithium tetrahydroborate with iodine stabilizes the high temperature phase, in agreement with experiment. Finally, examples on how systematic structural studies of metal halides and hydrides can aid the design of new materials were given.

Resume

To typer højkapacitets brintlagringsmaterialer, metal borohydrider og metal amminer blev undersøgt vha. DFT beregninger. Det blev vist at simple strukturer kunne bruges til at beregne stabiliteter af systemer med komplekse strukturer. Eksperimentelle trends for stabiliteter blev reproduceret og stabiliteten af ukendte systemer blev beregnet. Af disse var 20 borohydrid systemer stabile og havde interessante dekomponeringsenergier. Et par nye metal ammin systemer viste lovende dekomponeringsenergier men deres stabiliteter var tvivlsomme. Den hurtigere kinetik i magnesium amminer blev foklaret ved den lagdelte struktur af magnesium klorid, og i følge beregningerne vil en delvis udskiftning af klor med iod i calcium klorid kunne tvinge systemet i den lagdelte struktur og dermed forbedre kinetikken. Iod kan ligeledes bruge til at stabilisere højtemperatur fasen i lithium borohydrid, der har en høj ionledningsevne anvendelig i batterier. Endelig blev det vist hvordan systematiske strukturelle studier af metal halider og hydrider kan benyttes til at designe nye materialer.

Preface

This thesis is submitted in candidacy for the Ph. D. degree from the Technical University of Denmark (DTU). It is based on the work carried out at the Center for Atomic-scale Materials Design (CAMD), Department of Physics and at the Materials Research Division, Risø National Laboratory for Sustainable Energy from February 2006 to Februrary 2009 under the supervision of Professor Jens K. Nørskov, DTU and Tejs Vegge, DTU. Financial support was provided by NESSHY, Danish Center for Scientific Computing (DCSC), and the Lundbeck Foundation.

First of all, I would like to thank Tejs Vegge for his great help, supervision, patience and friendship. Thanks to Jens K. Nørskov, Helle W. Wellejus, Marianne Ærsøe and Inge Toldsted for taking so good care of me. I thank David Landis, Johannes Voss, Adem Tekin and the chemist guys for great team work, and the CAMD and Risø groups for interesting meetings and the friendly social environment.

A number of persons have been helpful and have inspired me through all this, those are: Poul G. Moses, Jan Rossmeisl, Frank A. Pedersen, Zbigniew Łodziana, Souheil Saadi, Jesper Kleis, Thomas Bligaard and Kristian S. Thygesen. I thank Heine A. Hansen for Col de la Forclaz.

Infinite thanks to my family – and to Ginnie Maya Amor Filstrup for not leaving me during the last year, where my face was a shining apple...

Lyngby, February 28, 2009
Jens Strabo Hummelshøj

Contents

List of Tables

List of Figures

1 Introduction

1.1 Oil gone

The era where our primary source of energy is fossil fuels is ending. Some projections even predict a peak in the world production in 2010 for oil[7, 8], in 2020 for natural gas[9] and in 2150 for coal[7]. The coal peak could come much sooner[10, 11]. Since especially the oil peak has a large effect on oil prices and policy, these numbers are being debated all the time. But even if the predictions are wrong, the resources *are* being depleted, the question is not if – but when. At the same time the world energy demand rises, following the increasing populations and standards of living in third world countries. Solving this apparent paradox is the most important challenge the world faces today – and tomorrow. But maybe it is all for the better? Our possible effect on the climate during the fossil fuel era is frightening, and perhaps, a much larger problem would exist if we had sufficient of oil and gas for the next thousand years...

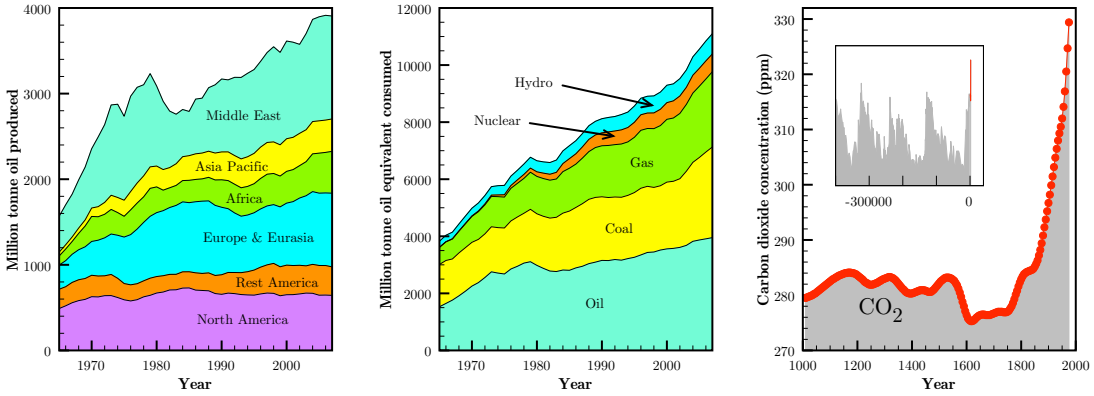

Figure 1.1: World oil production and consumption and the CO_2 concentration as measured from ice-cores. (Data from http://www.bp.com and http://cdiac.ornl.gov/trends/co2/)

There is no obvious alternative to fossil fuels. Fossil fuels are in essence chemically stored solar energy that have undergone a million year compression process in the earths crust. They are fuels because, when extracted, we can use them where and when we need it, which is practical for our stationary uses and necessary for out mobile uses.

Of the alternative energy sources only the fissionable materials can be considered fuels in that sense, but technology will probably never move in favor for nuclear power for widespread transportable uses, nor is it likely that it will supply all our stationary uses in the near future. The largest nuclear power plants build today deliver around 1GW electricity (see http://world-nuclear.org/info/reactors.html), so it would take in the order of 10.000 plants to replace the order of 10TW delivered by fossil fuels today; or one new plant per day the next thirty years. Even if nuclear power reaches this level, it can only be used to build a bridge to a long term solution in the future, since the resources of uranium or other fission materials will not last forever. This long

term solution might be nuclear power, but based on fusion instead of fission. No one knows when the technological barriers for using fusion as our energy source can be overcome, and we will need other alternatives in the meantime.

Except ground heat, the remaining alternatives involve conversion of solar energy into some into something useful like electricity or fuels. The solar energy can be more or less directly harvested: directly by solar cells, indirectly through wind, water, wave or even by producing biofuels. Most likely, we will need a combination of many of the alternatives (including nuclear power) to produce enough energy.

Most of the renewable energy sources produce electricity, which can be connected to the power grid and supply energy for our stationary uses. But the efficiency is lowered because the electricity is not produced when and where we need it. Moreover, it cannot be used directly cars, ships and aircrafts. For the renewable energies to be a viable solution, we need a way to store the energy, for our transportation uses and for load balancing our stationary uses.

There is only one sensible choice when choosing how to store energy, and that is to store it chemically. This is how nature does it, and that is what the fossil fuels we have become so dependent on, also tell us. Apart from nuclear power, chemically stored energy is by far the most compact way to store energy. As a comparison of how much energy that can be stored in chemical bonds compared to mechanical energy, we consider an example. The energy stored in 1L gasoline is the same as in 35.000L of water pumped to a height of 100m!

In summary, as the fossil fuels era is ending we need to produce our own fuels. But which fuel should one produce? Hydrogen has been proposed as a potential future energy carrier as we shall see.

1.2 Hydrogen economy

The principle of a hydrogen economy is to use hydrogen as an energy carrier instead of the fossil fuels used today. Where a fossil fuel is both an energy source and carrier at the same time, hydrogen is only an energy carrier and we need to produce it ourselves. When produced, it need to be stored so we can use it when and where we need it, for instance in a car.

Hydrogen is proposed since it has some favorable properties. It is very abundant, it is light, has a high energy content and it is an effective fuel for fuels cells that convert the chemical energy directly into electricity. In some ways, it resembles the fossil fuels that are also chemically stored energy originating from solar energy, the difference is that we produce it and at a much shorter timescale. And then, it is clean. The only byproduct when consuming hydrogen is water.

Using hydrogen as an energy carrier is also very challenging. It is hard to produce, the small and light hydrogen molecules are very volatile and hard to store in a compact way, and the fuel cells for retrieving the energy are not optimal yet, the best today are based on expensive metals like platinum.

In conclusion, the challenges in a hydrogen economy are related to the hydrogen production, hydrogen storage and fuel cells and major advances are needed in all three areas before a hydrogen economy can be realized. But there are also many possibilities to search. For instance, hydrogen can be produced by the use of electric power in electrolysis, chemically from other fuels, or directly from the sunlight in photocatalysis.

This work concerns the challenge of storing hydrogen. While it is possible to store hydrogen physically as a liquid at low temperatures or as a gas in high pressure tanks, it is generally accepted that in the long term, we need to find an efficient way to store it chemically. Most research being done on hydrogen storage, as the work presented here, is aimed at finding materials that store hydrogen chemically. (The use of the word chemically here also includes physisorption.)

1.3 Hydrogen storage

1.3.1 Demands for hydrogen storage materials

The main problem one attempts to solve by storing hydrogen chemically in a material, is related to the low volumetric density of pure hydrogen. At ambient temperatures and pressures hydrogen

is a gas and therefore a lot can be gained, if a material can contain the hydrogen as a solid or even a liquid. A critical demand for hydrogen storage materials is that they improve the volumetric density significantly.

One of the favorable features of hydrogen is its high gravimetric energy density and while the volumetric density perhaps increases, the gravimetric density certainly decreases when hydrogen is mixed with other elements. On the system level, however, the gravimetric density of pure hydrogen is lowered by the mass of the high pressure tank or cooling system. Since for most transportable uses the total mass of the system is critical for energy efficiency the final gravimetric density of a storage material needs to be sufficiently high. The gravimetric and volumetric densities of some selected materials, including a metal ammine, a metal tetrahydroborate, and a front edge lithium ion nanowire battery[12], are compared in Table 1.1.

Energy carrier	MJ/L	MJ/kg
Gasoline	33.4	47.6
Liquid hydrogen	10.0	141
Hydrogen at 200 bar	2.4	141
$LiBH_4$	14.3	21.7
$Mg(NH_3)_6Cl_2$	14.3	11.4
Liquid Ammonia	17.9	25.2
Advanced battery	1.2	0.7
Lithium ion nanowire battery		2.54

Table 1.1: Comparison of energy densities of selected energy carriers.

Of what we could call the basic demands, a third is related to the abundance of the involved elements, and consequently the price. A world-wide hydrogen economy will demand huge amount of the storage material, and a realistic candidate material needs to consist of elements with a high abundance. Luckily, the elements with a high abundance in the earths crust are also the ones that are light, so there is no build-in controversy with the gravimetric density.

Except for special uses like military or space technology, it is a demand that a storage material can be recycled in an efficient way. Preferably, the host material can be charged and uncharged with hydrogen in a reversible process. In close relation to the reversibility, we find the demand of fast kinetics. The hydrogen needs to be delivered sufficiently fast when powering the fuel cell, and depending on the way the material is reloaded (see Section 1.3.3) the kinetics for hydrogen uptake might also need to be fast. Along with the energy efficiency of a material, the reversibility and kinetics are probably the most intensively studied parameters, when investigating materials for hydrogen storage, since the three basic demands or parameters are often known beforehand.

The energy efficiency of a hydrogen storage material is connected to the principle behind the chemical storage. If the hydrogen is stored thermodynamically then heat is released when hydrogen is absorbed in the material and energy (in general heat) needs to be provided to get it out. By energy efficiency, one often means onboard energy efficiency, and the energy that is used to get the hydrogen out is considered a loss. (We discuss this point later in Section 1.3.3.) For a high energy efficiency the energy needed to release the hydrogen has to be minimized.

Often the parameter used is the temperature at which the hydrogen release sets in. The fuel cell is operating at a certain temperature and a release temperature below this, gives a high energy efficiency of the total system. But the temperature should of course not be too low, since one wants to keep the hydrogen in the material when it is not needed. In principle, the hydrogen could be kinetically kept in the material, which would mean that no energy is lost getting it out. Simply raising the temperature (not loosing heat to the material) or adding a catalyst would be sufficient.

Besides the mentioned, there are also demands concerning security. The storage material should not be explosive, and preferably not poisonous.

1.3.2 DoE targets

To quantify the demands for hydrogen storage materials the American Department of Energy (DoE) has set up milestones to be reached[13]. The numbers, for instance 5.5 system wt.% reversible

storage below 100°C by the year 2015, were based on a scenario where hydrogen powered cars should be able to compete with the existing gasoline and diesel powered cars. This "market pull instead of technology push" principle is normally the right way of thinking. However, markets change and with the increasing oil prices and the environmental focus today, this market is at the doorstep of major changes.

Today cars are build to go faster and faster without compromising security in the event of a car-crash, which consequently make them heavier and heavier. This basically very uneconomic principle is a luxury which perhaps in the future will belong to the past. A hydrogen powered car with a maximum speed of 100km/h, would need a much lighter construction leaving more weight and space available for the storage material if a long range is the goal, or lower energy cost during acceleration if efficiency is the goal. But the way we transport ourselves might also change fundamentally. The coming generations might prefer high-speed trains for travels longer than the near vicinity, and for the near vicinity a cheap, energy efficient car with a maximum speed of 60km/h, which would drastically lower the demands for the electric cars.

It is good to have realistic goals to strive for, but the reality we need to measure against is in the future. We do not have the solution yet and it might take us fifty years to get there. At that time 5 wt.% might be sufficient, and it is the energy efficiency, the reversibility and other practical macroscopic factors that determine the success of a hydrogen storage material. Who needs a material with 20 wt.% anyways, if it is poisonous, explosive in contact with water, mostly made of palladium and only works as a powder.

1.3.3 Hydrogen storage in practice

Before we move our focus to the atomic scale, we consider how chemical storage of hydrogen might function in practice. The part when the storage material is in place and functioning, in a car for instance, is probably easy to imagine. The excess heat from the fuel cell is used to release hydrogen as it is needed. We can imagine that the heat exchange and the kinetics of the material are good enough to supply hydrogen for accelerations and so on, or there might be a buffer tank of hydrogen in gas phase for accelerations or for starting the engine. What we want to focus on here is how the hydrogen is reloaded, and the infrastructure of production and storage material.

The first scenario is the analogue to the gasoline infrastructure we have today. Pure hydrogen, either liquified or kept at high pressure, are delivered to hydrogen stations where the consumer can refill their car with pure hydrogen. This is how it works in the hydrogen stations that exist today and the hydrogen are kept in high-pressure tanks in the car. If instead of filling a tank, the hydrogen is absorbed in the storage material already present in the car, a problem arises. If the storage principle is thermodynamic, it means that the same energy needed to release the hydrogen for the usage, is now released as heat when the hydrogen is refilled.

The heat released when the usual measure of 10 kg hydrogen (enough to go 400km) is absorbed in a material with a close to optimal release temperature of 350K is now calculated. We assume that the entropy of the hydrogen in the storage material is zero, and the desorption enthalpy of hydrogen is therefore the entropy of hydrogen in the gas phase at 350K which is $\Delta U \approx 350\,\mathrm{K} \cdot 130\,\mathrm{J/mol\,H_2 \cdot K} \approx 45\,\mathrm{kJ/mol\,H_2} \approx 225\,\mathrm{MJ/(10\,kg\,H_2)}$. This energy will be released as heat when hydrogen is absorbed. In comparison, the energy it takes to melt our light-weight hydrogen car made of 500 kg pure aluminum is 200 MJ, so the car will melt down during the few minutes we are willing to wait while refilling it, unless some very high performance heat exchange system is present in the car.

While it might be possible to get rid of this heat and perhaps even use some percentage of it for something useful, one could imagine that it would be easier and certainly safer to use the heat released if the refilling took place centrally, in a power plant for instance. The 225 MJ correspond roughly to the energy stored in 6,5 L gasoline so they are really worth saving. In fact, if the heat was used for e.g. district heating, then the energy used to release hydrogen in our cars, which we before called a loss, is not actually a loss. In principle, the heat for our houses are simply payed when we drive our cars.

In a central refilling scenario it is the storage materials itself that needs to be filled in the car. Since the storage material only is a carrier for the hydrogen the host material without the hydrogen has to be removed before refilling. If the storage material is a solid and kept in a container, this

can happen like exchanging a battery.

Since this is very far from what we are used to, many have objections to such a scenario arguing that this would require a completely new infrastructure, where every gas station need to be rebuild, and that the consumer would never accept replacing a battery, they want to step out of their car and refill it like they are used to, and there might even be some legal issues concerning the safety of the containers and so on. They are partly right; a new infrastructure would be required, but the chances that we can reuse the original gasoline infrastructure in its current form in a hydrogen economy are very small anyways. From the consumers point of view, no one really likes stepping out of the car to refill it, and replacement of an energy container could actually happen without leaving the car.

We can imagine a consumer driving in to a station and the container is automatically replaced from the bottom of the car. Naturally, the car would need a small container for reserve (or two full size containers, but this would reduce the storage capacity by a factor of two) to use all the hydrogen stored in the main storage container.

Exactly, this scenario is part of the plan in a recently announced electric car project to be implemented in Denmark (and other countries) the coming years. The project is a corporation between the californian company Project Better Place and the danish energy company Dong Energy, and in essence it will allow the danes to reach the whole country in their battery powered cars by placing 150 battery replacement stations spread around the country (see Figure 1.2).

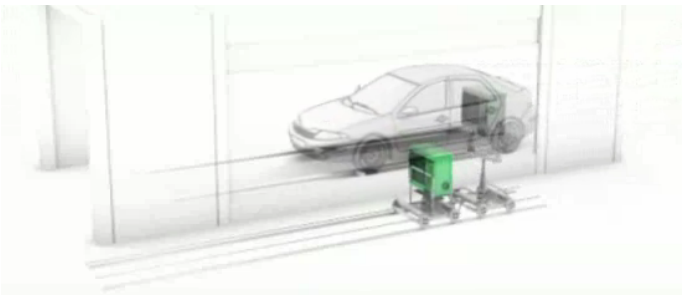

Figure 1.2: A battery exchange station. (From http://www.betterplace.com.)

It is not unlikely that many similar projects will be launched before the perfect hydrogen storage material is found, and that the transition to hydrogen powered cars will actually be a transition from the battery powered cars. The widespread use of battery powered cars could pave the way for hydrogen powered cars in the future. At least the engine is the same. The reason why one would choose the hydrogen powered car in this case is in the energy densities. (see Table 1.1).

A class of materials that could open the door for the conventional gasoline infrastructure is the so-called slurry, for instance the magnesium hydride slurry[14], which is liquified material that can be pumped through the existing tubing systems. At this point their densities a however quite low.

But perhaps what really determines which infrastructure a future hydrogen economy will use is how the hydrogen is produced. As an example, we imagine that in the future electrolysis has become by far the most effective way to produce hydrogen, and that the electrolysis systems are cheap and easy to function. Moreover, the perfect storage material also exists which is kept in the battery form mentioned before, and which reversible absorb and desorb hydrogen while producing or using heat. In this scenario, each power plant, household or battery exchange station could have their own hydrogen production and refilling facilities, and the electric grid would be the main part of the infrastructure. Electricity, is delivered to the households when the wind blows and this can be used as electricity in the house, or to produce hydrogen that is filled to the storage material whenever heat is needed. The hydrogen can be used in the cars or as electricity in the house when the wind is not blowing... and so on. In the case that photocatalysis becomes a major contributor to the hydrogen production the picture might be different, but part of it might be the same though.

We leave the macroscopic scale and move to the atomic scale where the work described in this thesis had its focus.

1.4 This work

Two classes of high capacity hydrogen storage materials, the metal tetrahydroborates and the metal ammines, were investigated at the atomic scale using density functional theory simulations. The aim was to get insight into thermodynamics and kinetics of known system, and to use this insight to model unknown systems in the search of materials with improved properties. This required representative models of the systems at the atomic scale, and due to the structural complexity in some of the materials studied and in many cases lack of experimental support in the literature, the work performed was to a large part a structural study.

While many contributions to the free energy determines the preferred phase of these classes of systems at working conditions, the focus of this study was to a large extend limited to comparing the electronic energies as calculated at zero kelvin. The underlying assumption, we hoped could validate this approach, was that the ignored contributions to the free energy could be expected to show small variations within the same class of materials, and that the chemistry captured by the ground-state electronic structure calculations might therefore be able to predict relative energies (or trends) for the real systems at working conditions. This crude simplification allowed us to search many different materials, and provide results that were not definite nor very precise, but which could serve as suggestions for further investigation either experimental or computational.

A secondary goal was to get insight into the different energy contributions that determines the stability and kinetics of the systems studied. The hope was that these different contributions could be separated and that it would be possible to identify certain descriptors that determine the properties of a system. Such descriptors could aid the design of improved materials for hydrogen storage, either through a simple correlation like the one between the stability of a metal tetrahydroborate and the electronegativity of the metal, or by collecting detailed structural correlations into a database and use this to design new structures.

The outline of the remaining chapters is as follows:

Method This chapter briefly introduce the storage systems, their quality parameters and some considerations on computational design. At the atomic scale the two classes of materials have some similarities which are captured by the field of coordination chemistry, and some concepts of coordination compounds are introduced. The model behind all the results is explained and the parts of the free energy not included in the model are mentioned.

Halides The first results are presented in this chapter. Although the metal halides are not hydrogen storage materials, they are included here to provide some structural insight and to evaluate the methods ability to predict structures and stabilities. This class of materials were chosen since a lot of experimental data on both structures and stabilities are available, and since they are a natural starting point for both the metal tetrahydroborates where the anion is simply substituted, and for the metal ammines where the halides systems are expanded and ammonia is introduced.

Tetrahydroborates The metal tetrahydroborates are introduced. Besides making the system a hydrogen storage material, the substitution of a halide ion with the tetrahydroborate ion adds a lot of structural complexity. Different structures of alkali and alkaline earth tetrahydroborates are compared. For magnesium tetrahydroborate a full free energy comparison between different experimental and theoretical structures was performed in an included paper. A screening study of mixed metal tetrahydroborates is presented in another included paper, and the insight it provided is used to build a few new structures of known and unknown tetrahydroborates.

Ammines The metal ammines are introduced. The structures of magnesium and calcium ammines are presented. The magnesium ammine structures are used to calculate binding energies of ammonia in the different phases of ammines of Mg, Ca, Mn, Fe, Co, Ni, and a relation to experimental desorption enthalpies is established. This relation is used to estimate desorption enthalpies of mixed metal ammines where either the metals or anions are mixed. Some considerations on hydrogen positions, dynamics and desorption mechanism are included for the magnesium system as a representative of this class of materials. A way to

improve the kinetics in calcium ammine is proposed, and an idea of using chemical energy via ligand substitution to desorb ammonia from the magnesium ammine is presented.

Summary and outlook As the title says.

All energies are per formula unit unless otherwise noted.

List of included papers

Paper I

Indirect, reversible high-density hydrogen storage in compact metal ammine salts.
R. Z. Sørensen, J. S. Hummelshøj, A. Klerke, J. B. Reves, T. Vegge, J. K. Nørskov, and C. H. Christensen
J. Am. Chem. Soc. 130(27), 8660–8. (2008).

Paper II

Structural stability and decomposition of $Mg(BH_4)_2$ isomorphs – an *ab initio* free energy study
J. Voss, J. S. Hummelshøj, Z. Łodziana, and T. Vegge
J. Phys. Condens. Matter 21, 012203–10 (2009).

Paper III

DFT based screening of novel alkali-transition metal borohydrides – a computational materials design project
J. S. Hummelshøj, D. D. Landis et al.
Submitted to J. Chem. Phys.

Paper IV

Experimental and computational studies on structural transitions in the $LiBH_4$-LiI pseudobinary system
H. Oguchi, M. Matsuo, J.S. Hummelshøj, T. Vegge, J.K. Nørskov, T. Sato, Y. Miura, H. Takamura, H. Maekawa, and S. Orimo
Accepted by Appl. Phys. Lett.

Paper V

Ammonia dynamics in magnesium ammine salts from DFT
A. Tekin, J. S. Hummelshøj, Jens K. Nørskov, and T. Vegge
To be submitted.

List of papers not included

Paper VI

Generation of Nanopores during Desorption of NH_3 from $Mg(NH_3)_6Cl_2$
J. S. Hummelshøj, R. Z. Sørensen, M. Yu Kustova, T. Johannessen, J. K. Nørskov, and C. H. Christensen
J. Am. Chem. Soc. 128(1), 16–17. (2006).

Bookchapter

Indirect hydrogen storage in metal ammines
T. Vegge, R. Z. Sørensen, A. Klerke, J. S. Hummelshøj, T. Johannessen, J. K. Nørskov, and C. H. Christensen
Solid State Hydrogen Storage: Materials and Chemistry,
ed. G. Walker, Woodhead Publishing, Cambridge, UK (2008).

2 Method

2.1 Materials design

2.1.1 Materials and quality parameters

The hydrogen storage materials we investigate here are the metal tetrahydroborates $M(BH_4)_x$ and the metal ammines $M(NH_3)_xA_2$. The storage principle is thermodynamic, the user supplies heat and the hydrogen is released. In such systems there is a compromise between safety and energy efficiency and a main quality parameter is the temperature at which the hydrogen is released, and optima exist that depend on whether safety or efficiency has the priority. Another quality parameter is kinetics which preferably should be as fast as possible. In this study only the kinetics of the metal ammines have been investigated. Besides that, these materials have the universal quality parameters of high densities, low price, reversibility, etc. Any attempts at functional materials design, including this work, aim at finding the optimal combination of these parameters.

2.1.2 Design principles

When searching for improved functional materials either experimentally or computationally, one can choose between or combine two fundamentally different approaches: one can empirically screen different materials, or apply detailed knowledge and do advanced design of one material at a time. We will present some examples of both.

2.1.3 Computational design

Computational materials investigation and design adds the important difference, that one is dealing with a model, and the results provided by the model can only serve as suggestions for chemists to try synthesizing. A material designed in a computer has no practical value on its own, one need to verify the link to reality. But the computational approach do also have some advantages. One can get atomic scale insight into real systems on the computer that is impossible to get in experiments. On the more theoretical end, one can do calculations of systems that would never occur in real life. In such impossible experiments, one use the missing link to reality as an opportunity instead of a limitation, and get insight which can turn out to be helpful in the search of real materials. The details of the model is explained in the next section.

The computational approach also adds the choice of precision, or in which detail the model correspond to reality. Doing very realistic modeling is actually extremely hard and expensive in terms of computer power, and approximations are always needed. The choice is where to be situated on the scale between high precision and, let us say, high throughput. This is in many cases the choice between theory and technology. From a practical point of view we do not care about precision as long as it answers our questions. In some cases we need very high precision to get the answers, but in other cases we can link the results to reality by saying for instance, this material has a stability between that of $Li(BH_4)$ and $Al(BH_4)_3$, and this might be sufficient, even though the absolute numbers are far off, and even if we know, that we are making crude approximations. There might also be situations where it can pay off do to very expensive calculations on a candidate material, because the experimental verification is even more expensive.

This work places itself at the low precision end of the scale. The focus has been to investigate many different materials, their structures and relative stabilities as calculated from electronic ground-state energies. Where it was possible, the link to reality was verified by comparing to experimental results. Collaborating/supplemental work of J. Voss aimed at higher precision by including more contributions to the free energy.

2.2 Modeling

2.2.1 Fractal clever-laziness

The title refers to the way approximations are made at the different levels of the modeling. As mentioned approximations are needed, and the general principle is to focus on getting the major part right and approximate the rest. At the first level, we know that there are many contributions to the free energy that determine the stability of a material, (as will be sketched in the next section,) but we focus on the electronic energy since this is expected to be dominant. The electronic energy is itself calculated by getting the major part right and approximate the rest, as explained later. But even then, we try to be clever-lazy again, and look for descriptors that determine the stability or whatever macroscopic property of a material we are interested, so that we do not even have to model the full system but only some segment of it. I have chosen the word "clever-lazy" because it is clever to be lazy, since computer time is money, but also because you need to be lazy in a clever way to get the right results.

2.2.2 Contributions to the free energy

Typically one wants to know when hydrogen release sets in for a given hydrogen storage material, or put another way, when the preferred state of the system is separation of host material and hydrogen in gas phase. The preferred state of a system at a given temperature is determined by minimizing Gibbs energy. Gibbs energy or the free energy contains the internal energy, the mechanical work on the surroundings and the entropy

$$G = U + pdV - TS.$$

For the systems treated here the internal energy is mainly the ground state electronic energy plus a contribution from integrating the heat capacity from 0K.

The mechanical term is small compared to the electronic energy and one needs to go to very high pressures to see an effect. The volumetric density of hydrogen in these material are in the order of $1\,\mathrm{g/cm^3}$ or correspondingly an order of $1\,\mathrm{mol\,H_2/cm^3}$. If we were able to compress the system to half its volume, that would be an order of $\mathrm{cm^3}$ per mol H_2, and the pressure would have to be 10.000 bar to get $1\,\mathrm{kJ/mol}$, which is the order of the hydrogen binding energy and the electronic energy differences between polymorphs. For some systems very high pressure *can* induce a phase transition between two polymorphs that are very close in energy.

Disregarding the minor terms, it is often fair to say that hydrogen release happens when the entropy gained by having hydrogen in gas form becomes equal to the binding energy of hydrogen in the material. If the system is not too, complicated the binding energy can be obtained by the method we describe later, and the main challenge is typically to get the entropy of the storage material.

The entropy contains contributions from vibrational modes of the atoms, and the collective vibrations or phonons. When modeling the system, these contributions can be calculated using for instance a harmonic approximation, but for this you need atomic structures that are very well relaxed, which can be difficult to obtain. Moreover, the phonon contribution varies over a temperature range, and one has to calculate phonon dispersion, which is very time consuming, and in practice it can only be performed on a few selected systems as done for $Mg(BH_4)_2$ in [15]. This level of theory has therefore been abandoned in the initial screening of materials presented in this thesis. By the same argument zero point corrections are not included in the calculations, simply because we want to do a fast screening of many materials. For the metal ammines, the effect of including of zero point energies has been investigated and the relative energies were not affected.

But there can be other contributions to the entropy that perhaps are impossible to calculate. For the tetrahydroborate systems we will see that there are many different structures for a given system that are close in energy. If the potential energy landscape get sufficiently rough as a consequence of the many polymorphs close in energy, then configurational entropy might be significant. The disorder caused by the system having many structures to choose from could actually stabilize it further. This contribution is probably impossible to quantify, and at a certain point you just have to give up and focus on getting the major part right.

Getting the major part right is what we hope to do when calculating the ground state electronic energy, but before we leave ambient conditions and move to 0K and stay there for the rest of the thesis, a few considerations on how we calculate the original quality parameters or the materials are in place.

2.2.3 Modeling quality parameters

A main parameter is the stability of the material or consequently the binding energy of hydrogen. This will simply be calculated by comparing the electronic energies of relevant systems. But sometimes there is the choice of which structures to use.

If the experiments tells us that a high temperature and a low temperature phase exists, which one should we choose when trying to estimate the binding energy? In the ground state calculations we might find that the low temperature structure actually has the lowest energy, and we know that the high temperature phase is stabilized by the entropy at elevated temperatures, but we have given up the calculation of this part completely; we are only willing to calculate the ground state electronic energy. Which should we choose?

In another situation, only a high temperature phase is reported from experiments, and the calculations predicts another structure to be the most stable while the high temperature phase has a hopelessly high energy; which should we choose?

In the last example a low temperature experimental structure is reported, but the calculations predict another to have an even lower energy, so either the experiments or the calculations are wrong, and again we need to make a choice. In that case we need to remember that while the calculations may very well be wrong, (we are for instance not including the van der Waals interaction, or zero point energy correction) the true ground state might not be observed in the experiment due to kinetics and metastability. To detect it experimentally one needs to wait forever for a phase transition to occur.

To answer all these questions we need to remember that in this pseudo-modeling, the structure does not need to be realistic only representative. We use a simple scheme to capture energy differences between different compositions and the important thing is to be consequent. This will in most cases mean to follow the calculations and pick the most stable structures, even if we know they are unrealistic. It is of no use to calculate the different compositions in a structure we know that is only kept stable by the entropy that we are neglecting, if this gives us an energy too high compared with other structures we use. We need to play after the rules at 0K, and in our mind add the entropy and the realistic structures post-hoc.

But this does not need to be as bad as it sounds. In the calculations we have the unique possibility to throw away the complications of entropy and see what structures the systems would prefer if it was not for the entropy. This can be utilized when designing mixed structures where the entropic situation might be totally different.

In many cases the experimental structures will work just fine, and when calculating the kinetics we *are* dependent on realistic structures. In that case we are asking what is the barrier for diffusion in this particular structure. These are calculated by finding the diffusion path which has the lowest barrier, and returning that barrier.

2.3 Electronic structure calculations

2.3.1 Many-body wavefunction

The atomic systems we model consist of nuclei and electrons, and the first step before calculating the electronic structure is to apply the Born-Oppenheimer approximation[16] to decouple the nuclei

and the electrons. When this is done, we can treat the nuclei as a fixed external potential and minimize the energy of the electronic system in this potential. The reasoning for this simplification is that the light electrons respond instantly to the movements of the nuclei. One can attempt to reintroduce the coupling at a later point by considering electron–phonon interaction; this has not been done in this study.

Within the Born-Oppenheimer approximation the electrons are described by the Hamiltonian acting on a many-body wavefunction that contains all about the electronic state[17]. The Hamiltonian can be split into the kinetic energy, electron–electron interaction, and the interaction with the external potential

$$H = T + V_{ee} + V_{ext}.$$

2.3.2 Density functional theory

In density functional theory (DFT) the many-body wavefunction is replaced by the ground state electron density. One simply utilize the fact the electrons satisfy the Schrödinger equation, and therefore it is sufficient to know their preferred density at 0K to know everything about the system.

As an intuitive argument for this, consider an isolated system of atomic nuclei in two dimensions as shown in Figure 2.1a. Given this nucleic configuration at 0K, we add some electrons and ask where do the electrons go? According to quantum mechanics the answer is a probability density, showing the probability of observing an electron in a given point of space. Let us assume that this so-called ground state electron density turns out to be the one shown in Figure 2.1b, and for the moment not consider degenerate states. If someone told us that the given nucleir configuration always will produce this electron density at 0K, then we would probably believe him. It seems logical that only this density minimizes the energy (when disregarding degeneracy).

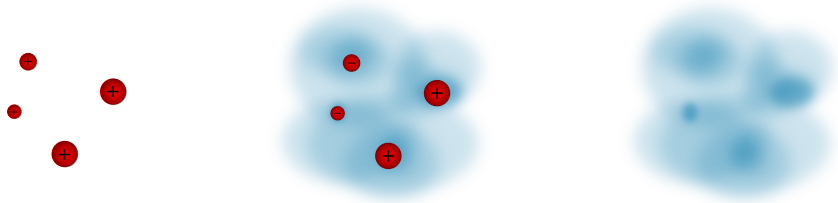

a) Nuclei b) Nuclei and electron density c) Electron density alone

Figure 2.1: Two dimensional system of four atoms.

We now turn the picture around and consider the same electron density without the nuclei (Figure 2.1c). In this case we ask, where can we place some nuclei to minimize the energy? Classically, the problem is the same as before, the only difference is that now we need to place point charges in a continuum of opposite charge, where before it was the other way around. Intuitively, it perhaps even seems more easy to go this way. Consequently, if someone told us that the electron density will always lead to the nucleic positions from before, then it would be perhaps be even more convincing.

If degenerate states exists, then different electron densities can be used as starting point to get the same nucleic positions, which should not pose a problem from this point of view. But can degenerate nucleic positions, so to speak, exist for a given ground state electron density? The Hohenberg-Kohn theorem states that the answer is no. This means that from a ground state density, we can in principle deduce the nuclei positions and then we have all the information of our system.

According to the Hohenberg-Kohn theorem[18] there exists a functional that maps the ground state electron density n_0 to the ground state energy E_0:

$$E_0 = E[n_0].$$

Even though the functional E is unknown, this theorem has great practical importance, since ultimately it allows us to do electronic structure calculations without using many body wave

functions. If we knew the functional E and how to modify it for different external potentials, we could search for electron densities that minimizes the energy for a given external potential (for instance, the one setup by the nucleic configuration in Figure 2.1a), and these would then be the true ground state electron densities (or density for the non-degenerate case). Or we could go the other way, modifying the external potential part of the functional E until it minimized the energy of a given electron density. The latter shows, that from a ground state density, we can in principle deduce the external potential and from that calculate all observables on the system, as well as all excited states. Again, all information about a system is included in the ground state electron density.

2.3.3 Kohn Sham scheme

In all results presented later, the scheme proposed by Kohn and Sham[19] has been used to calculate the ground state electron density and the corresponding energy. The scheme ends up being an approximation of density functional theory, and as already mentioned, the approximation is made by getting the major part right and approximate the rest. We shall briefly go through the scheme here.

The first step is to split the unknown funtional E into the kinetic energy of a fictitious non-interacting system with the same density, and a potential energy that contains all the interaction (from now on we omit the zeros)

$$E[n] = T_s[n] + V_s[n].$$

The kinetic energy for the non-interacting system is found by

$$T_s[n] = -\frac{\hbar^2}{2m}\sum_i^N \int \phi_i^*(\mathbf{r})\nabla^2\phi_i(\mathbf{r})\mathrm{d}\mathbf{r},$$

where the ϕ_i are solutions to the single particle Schrödinger equation

$$\hat{H}_s\phi_i = \left(\hat{T}_s + \frac{\delta V_s[n]}{\delta n}\right)\phi_i = \epsilon_i\phi_i, \tag{2.1}$$

and the interating potential energy $V_s[n]$ is used to get the real density n of the interacting system. Since the interacting potential is a density functional, the single particle orbitals are found in a potential, which depends on the density they produce. This means that the equations have to be solved iteralively. Luckily, this does not pose a big problem and self-consistence is often obtained after a dozen iterations. The interacting potential energy can be written as

$$V_s[n] = (V_{ext}[n] + V_{\mathrm{el-el}}[n])_{\mathrm{classical}} + E_{\mathrm{xc}}[n],$$

where the unknown parts due to exchange and correlation is included in the exchange-correlation functional $E_{xc}[n]$. The interaction with the external potential is

$$V_{ext}[n] = \int n(\mathbf{r})v_{ext}(\mathbf{r})\mathrm{d}\mathbf{r},$$

and the electron–electron interaction which is called the Hartree energy U_H is simply

$$V_{\mathrm{el-el}}[n] = U_H[n] = \frac{1}{2}\int\int \frac{n(\mathbf{r})n(\mathbf{r}')}{|\mathbf{r}-\mathbf{r}'|}\mathrm{d}\mathbf{r}\mathrm{d}\mathbf{r}' = \frac{1}{2}\int n(\mathbf{r})v_H(\mathbf{r})\mathrm{d}\mathbf{r}.$$

where the Hartree potential is

$$v_H(\mathbf{r}) = \int \frac{n(\mathbf{r}')}{|\mathbf{r}-\mathbf{r}'|}\mathrm{d}\mathbf{r}'.$$

Collecting the terms we finally get

$$\frac{\delta V_s[n]}{\delta n} = v_{ext}(\mathbf{r}) + v_H(\mathbf{r}) + \frac{\delta E_{\mathrm{xc}}}{\delta n}, \tag{2.2}$$

which this completes the Kohn-Sham equations Equation 2.1-Equation 2.2.

To summarize, using DFT and the Kohn-Sham theory we have extracted what we know how to calculate and put the rest in a functional $E_{\mathrm{xc}}[n]$. A part of the kinetic energy is calculated in a auxiliary system of single particle states, and a part of the electrostatic interactions are treated classically. The rest $E_{\mathrm{xc}}[n]$ is called the exchange correlation functional, and it contains corrections due to the Pauli principle[20] and quantum fluctuations[21]. In calculations we approximate E_{xc} and herein lies the major approximation of DFT.

2.3.4 Implementation - Dacapo

The self-consistent DFT calculations were performed using the GGA-RPBE[**?**] approximation for exchange and correlation, under the Atomic Simulation Environment[22]. Ultrasoft pseudopotentials[23] was used to describe the ionic cores and the one-electron valence states were expanded in a basis of plane waves with an energy cutoff of 350eV and a density cutoff of 700eV. The electron density was determined self-consistently by iterative diagonalization of the Kohn-Sham hamiltonian, Pulay mixing[24] of the resulting electronic density and Fermi occupation[25] of the Kohn-Sham states (kT =0.1eV). All total energy calculations were extrapolated to zero electronic temperature[26]. If nothing else is mentioned the Brioullin zone was sampled using approximately 15 k-points per $\mathrm{\AA}^{-1}$ in each direction. Calculations on molecules were performed by a Γ-point calculation.

2.4 Systems

2.4.1 Coordination compounds

A coordination compound is a material that contains coordination complexes. A coordination complex is a central atom, often a metal, surrounded by ligands that are said to be coordinated to the metal. The coordination number denotes the number of ligands surrounding the metal. Examples of the ligands can be simple anions like Cl^- or polarized species like ammonia. In the case of complex ligands, the denticity denotes by how many atoms it connects to the metal, and mono-, bi- and tridentate means 1,2 and 3 atoms.

In the Lewis model, the bond between the metal and the ligands is a coordinative covalent bond, where both electrons of the shared electron pair is coming from one part, the Lewis base. The electron pair acceptor is called the Lewis acid. An example of a coordination complex is the BH_4^{-1} ion, in which the Lewis acid is the neutral BH_3 molecule and the Lewis base is the H^- ion.

In reality, there is no clear limit between ionic and covalent bonds. Every ionic bond has some degree of covalency in it. Depending on the context it can be helpful to keep the clear distinction or let it go. In this context, we do not draw a clear limit between ionic and covalent, but instead we adopt a less strict meaning of the word coordination compound and focus on the similarities between the different class of materials treated here. For the metal halide systems the halide atoms are the ligands, for the metal tetrahydroborates the BH_4^{-1} groups are the ligands, and for the metal ammines the ligands are both the halide ions and the NH_3 molecules.

In general, one observes certain arrangements of the ligands being more represented than others. The coordination of the ligands often follows regular geometrical shapes, in which the ligands are places at the vertices of metal centered polyhedra. Some examples of coordination polyhedra are given in Figure 2.2.

There are two very different reasons for the regular shapes observed. One is has to do with electronic structure: the atomic orbitals of the metal make some directions preferred over other. The other with ligand–ligand repulsion: since ligands often have the same charge or polarization they repel each other and the largest separation between the ligands, at a certain distance from the metal, occurs when they are situated at the vertices of regular polyhedra. The two effects can either supplement each other, increasing the stability of the material, or be competing depending on the relative sizes of the metal and the ligands. For instance the atomic orbitals of a metal could favor a octahedral coordination, but the ligands are too large compared to the metal atom so it is forced into a tetrahedral coordination by the ligand repulsion.

But how can the metal choose freely between having four or six ligands, does this not depend on the stoichiometric ratio of metal and ligands in the material? The answer is that the coordination polyhedra can be connected, sharing their corners, edges or faces to yield the right stoichiometric

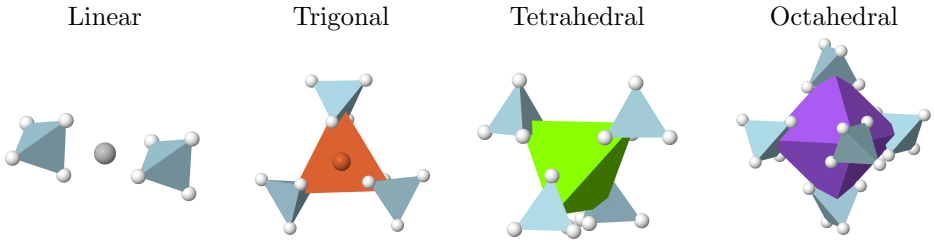

Figure 2.2: Examples of coordination polyhedra made by tetrahydroborate ions surrounding a metal

ratio, and this is what generates the crystal structure which can consist of a single or multiple networks of polyhedra. A network is either three dimensional (bulk), two dimensional (layer) or one dimensional (polymeric or chain); in the latter the material may form a liquid depending on the binding between individual chains. The polyhedra can also be isolated forming a liquid, a so-called molecular solid, or they can be kept in the lattice of something else. An example of the latter is $Mg(NH_3)_6Cl_2$ in which the $Mg(NH_6)^{2+}$ complexes are kept in a cubic lattice of Cl^- ions.

Connecting the polyhedra adds another competitor to the stability, namely the coordination of metals to the ligands. When the coordination polyhedra share their corners, edges or faces, it means that a ligand is coordinated to more than one metal. Seen from the ligands point of view the metals are coordinated to it. So the connection of the original coordination polyhedra needs to favor the preferred coordination of the ligands.

There are many factors that determine final structure of a coordination compound, which in the end will be a compromise. This compromise can further be adjusted by adjusting the metal–ligand distance. To a preferred coordination corresponds a preferred distance. If ligand repulsion makes it impossible to favor both, a compromise may be reached by adjusting the distance. Observations of ionic radii is seen to depend on the combination of cation and anion as well as the coordination of both the cation and the anion [27].

One should distinct between observed coordination and preferred coordination. We know that the observed coordination is a compromise between many factors, and that the true preferred coordination of a metal might not be what we observe; in fact it might never be observed if the metal atom is too small. Instead of saying, this metal prefers this coordination when combined with this anion, and that coordination when combined with that anion, it is more useful to say, this metal always prefers this coordination but when combined with that anion it is forced into that coordination. The reason is that when designing complex materials, you need to know which factors that draw the stability in what direction, and not be fooled by what one usually observes.

How can one determine the preferred coordination of an atom or a molecule? This is actually very difficult and perhaps only possible for a few atoms based on experimental data alone. One often needs to make assumptions and check for consistency, and here theoretical approaches based on atomic orbital and ligand field theory is a great help. This is out of the scope of this thesis. Instead an alternative way of saying something about preferred coordination through the use of computer experiments was sought (see Section 3.3.4). In general, the approach was experimental; The calculations performed, could be considered computer experiments. Systems were measured at 0K in different structures and the energies compared.

The last subject included here is the effect of superstructures. Everything said on coordination compounds until now has been concerned with the local coordination. One could ask if the non-local coordination has an effect on stability. In [15] the effect of superstructures for $Mg(BH_4)_2$ was shown to be small. It is an underlying assumption in this work that the effect of superstructures alone is neglectable. This is not to say that large superstructures are not more stable than small structures, but just that if they are, it is caused by the local structure of the metals and ligands involved.

2.4.2 Periodic representation

The coordination compounds were modeled by the periodic repetition of a unit cell that defined the system. In most of the systems studied, the different phases had very symmetric structures and usually small unit cells containing only one or a few formula units was sufficient to model the crystal structure.

In the calculations, the periodicity is obtained by imposing periodic boundary conditions on the Kohn-Sham eigenfunctions and due to Bloch's theorem the energy can be calculated in the first Brillouin zone alone. To limit the calculation time the Brillouin zone is sampled in a finite set of points which number depend on the size of the zone. The small real space unit cells lead to large Brillouin zones and a high k-point sampling was needed. However, this made the calculations well suited for parallelization and many systems could be calculated fast and efficiently.

2.4.3 Structure optimization

As mentioned the structures were modeled by a unit cell and its periodic repetition. Optimizing a structure in this model meant both optimizing the atomic coordinates internally in the unit cell and optimizing the lattice vectors that repeated the unit cell. Unfortunately, this could not be done at the same time, because the algorithms used did not include cell dynamics, so all optimizations had to iteratively relax the internal coordinates and the lattice vectors.

In most cases, this was not a problem since the energy did not have a critical dependence on the exact dimensions of the lattice vectors; only the local structure of each atom seemed to play a role. To put this differently, stretching or skewing the unit cell slightly did not affect the energy, which helped a lot since if the opposite was the case, it would be impossible to find the energy minimum. Since start guesses were build by creating regular coordination polyhedra and using a database of ionic radii for different coordinations (that increasingly got larger), the relative dimensions of the lattice vectors were therefore close to optimal in the outset. A proportional scaling of the unit cell and the internal relaxation of atomic coordinates was therefore often sufficient to optimize a structure.

The small unit cells had few degrees of freedom, which made them easy to optimize fast. This was important for a study like this, where we wanted to compare many systems in many structures. For the tetrahydroborate systems it was sometimes necessary to use a larger unit cell, either to minimize the repulsion between the hydrogen of different BH_4^{-1} groups or to obtain a preferred coordination of hydrogen around a metal.

In all uses of the word optimized structure, we are of course only talking about local minima on the potential energy surface. The point is, we wanted to compare the energies of a system in different local minima, in the hope that one of them would come close to the real global minimum. Alternative methods, like simulated annealing or relaxing a larger unit cell could have been used to search for an unknown global minimum, but the principle of calculating a system in a finite set of prototype structure and compare their energies was chosen, since it allowed us to sample many different structures fast and to learn from the systematical collection of energy differences to make better prototype structures ad-hoc.

The relaxation of the atomic positions, or equivalently, the internal degrees of freedom used a Quasi Newton algorithm to replace the atoms until all internal forces came below a specified maximum. Typical values of this maximum was in the range 0.05-0.001 eV/Å.

Optimization of the lattice constant was achieved by scaling the unit cell proportionally to 90%, 95%, 100%, 105%, 110% of the original unit cell volume, and a Murhagnan equations of state plot was used to find the optimum. Since the structures were constructed using a database of ionic radii, the optimum was often found in this range of unit cell volumes. In a few cases a second iteration of the optimization procedure was necessary.

2.4.4 A comment on spacegroups

Before we move on, a comment is added on spacegroups. While spacegroups are very useful when we need to reproduce experimental structures in the calculations, one should move the other way with caution. As mentioned, we can often change the lattice vectors a little or even move some of the atomic coordinates with no significant energy difference. But this will in many cases give a

totally different spacegroup even though the structure has only changed a little because we have destroyed a symmetry or created a new. In this work, the spacegroups of the calculated structures were not given much attention, instead the focus was kept on the phenomological characteristics of the structures, and two structures were considered the same if the had the same arrangement of coordination polyhedra, even if these were elongated or in other ways distorted in one of the structures.

3 Halides

The calculations on the metal halides serve multiple purposes: a) to evaluate the methods ability to predict structures and stability trends b) to quantify energy differences, which could be used in future database based materials design. For these purposes the metal halides are a suitable class of materials, since large amounts of experimental data are available on both structures and stabilities. From a structural point of view the metal halides are a natural starting point for the study of the tetrahydroborates in which the anions (F,Cl,Br or I) are simply substituted with BH_4^{-1} ions, and for the study of the metal ammines in which ammonia is absorbed in a metal halide. Most of the metal halides are modeled by very simple unit cells containing only one or two formula units of the material, and as we will see these simple model structures successfully reproduce the experimental trends in structures and stabilities.

3.1 Setup

Metal halides of the form MA_{1-3};M∈{Li,Na,K,Cs,Be,Mg,Ca,Sr,3d-metals,4d-metals,Al};A∈{F,Cl,Br,I} were modeled in a number different crystal structures and compared to experimental results from the literature. The structures chosen probed different coordination of both the metal and the halide atom and most of them corresponded to experimentally detected structures of certain compounds. We restricted the comparison with experiments to include only the structural data available in the ICSD database[28] and the thermodynamic data available in the NIST[29] and CRC HBCP[30] databases.

Each crystal structure was modeled by periodic repetition of a unit cell containing only a few formula units of the material. An initial guess was constructed by populating a template structure with the metal and halide atoms and the structure was relaxed by an initial relaxation of the atomic positions, followed by a proportional scaling of the unit cell and finally a relaxation of the internal degrees of freedom again. Electronic energies were calculated with a kinetic energy cutoff of 350eV, a density cutoff of 700eV and a Brioullin zone sampling of approximately 15 k-points per $Å^{-1}$ in each direction. The calculations of the molecules only included the internal relaxation and were performed by a Γ-point calculation in a 15Å×15Å×15Å unit cell. Calculations for the structural comparison were done non-spinpolarized.

The prototype structures used for all the MA, MA_2 and MA_3 type metal halides are illustrated in Figures 3.1–3.3. A few structures were added to calculate some of the systems in their experimental (or closely related) structures. These are shown in Figure 3.4.

3.2 Results

3.2.1 Structures

Due to the high symmetry in the majority of the structures, both the initial and the final relaxation of the atomic positions did not move the atoms out of their initial positions, and the relaxation of the structure consisted only of the relaxation of the lattice constant. For the MA_2-o$MgBr_2$, MA_2-o$Ca(BH_4)_2$, MA_3-tetra1-2 structures the internal relaxation led to minor changes in some bond-lengths (mostly shortenings); for part of the MA_3-tetra1 structures the angle between the

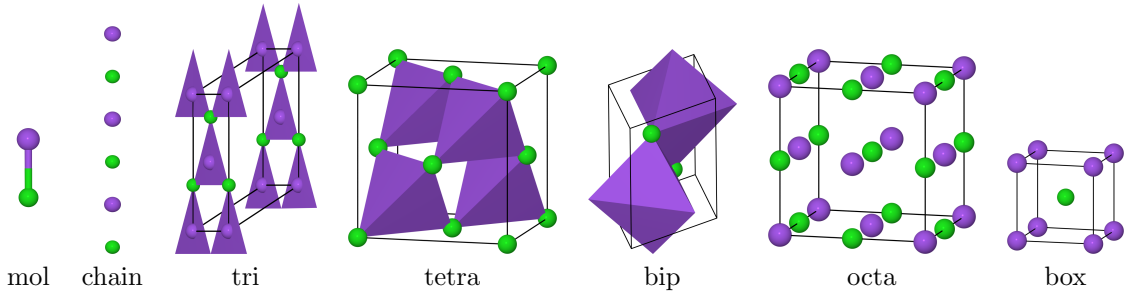

Figure 3.1: Template structures of MA type metal halides.

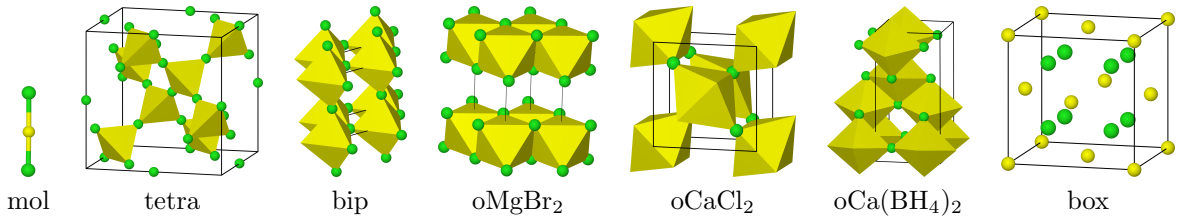

Figure 3.2: Template structures of MA_2 type metal halides.

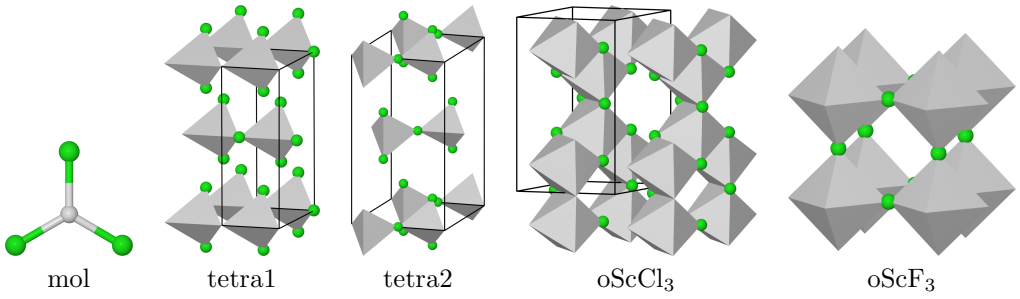

Figure 3.3: Template structures of MA_3 type metal halides.

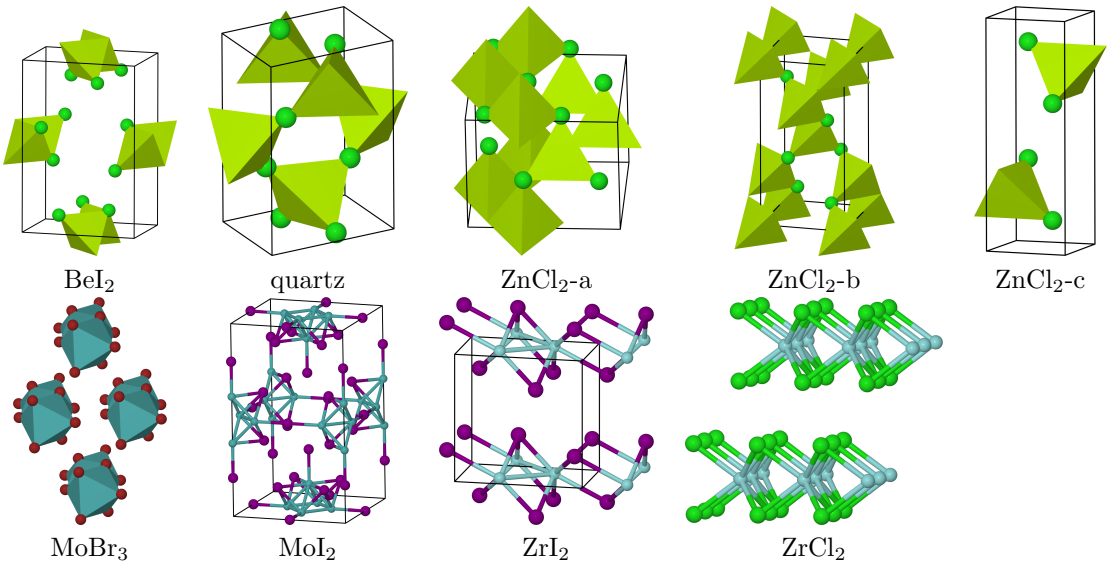

Figure 3.4: Extra experimental structures.

tetrahedra changed. For some of the MA_3-tetra1-2,o$ScCl_3$;M∈{Cu,Ag,Zn,Cd};A∈{Br,I} the structures change significantly, (for instance due to the valency of the cation being pushed over the limit for Zn and Cd,) in some cases forming molecules of the anion, and the energies of these structures are not reliable. But apart from those, it is fair to say that the energies treated next correspond to the systems in the prototype structures.

To evaluate the methods ability to predict structures, the energy relative to the molecular energy has been calculated for each structure and composition and compared to the experimentally reported structure. In Figures 3.5–3.11 it can be seen that in most cases the calculations agree with the experiments on which structure that is the most stable (i.e. where the red circles are below the other points). For some systems like $CaBr_2$ the experimental structure is very close in energy to the most stable in calculations, but there are also some notable deviations.

The first is the under-coordination of lithium that is significant for all the lithium halides systems, and since lithium plays an important role in the tetrahydroborate systems treated later, it is treated separately in Section 3.3.3, that also include the monovalent Cu and Ag systems.

For CsCl, CsBr and CsI the calculations also predict a coordination number that is too low, in this case 6 instead of the experimental 8. However, experiments on vacuum deposition of thin layers of these systems show the NaCl structure in agreement with the calculations[31].

For MA_2;M∈{Ni,Cu};A∈{Cl,Br,I} the wrong octahedral structure is predicted. This was investigated further, and it turned out that this inconsistency was resolved when doing the calculations spin-polarized.

In general, the non-spinpolarized calculations do quite well in predicting structures. Of course, the conclusions can only be based on the structures included here. We return to the structures in the analysis later.

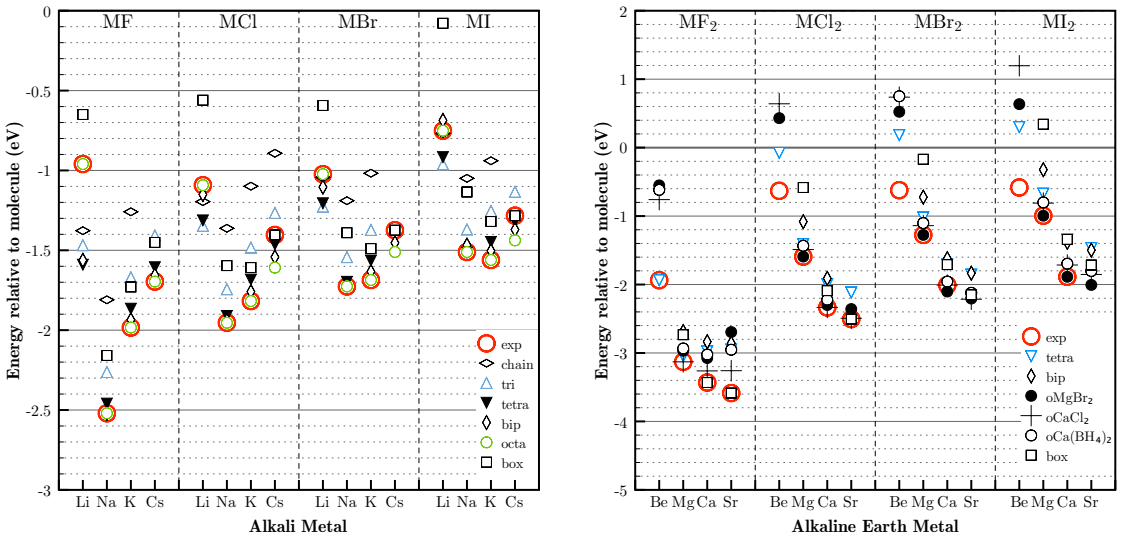

Figure 3.5: Relative energies of alkali and alkaline earth halides.

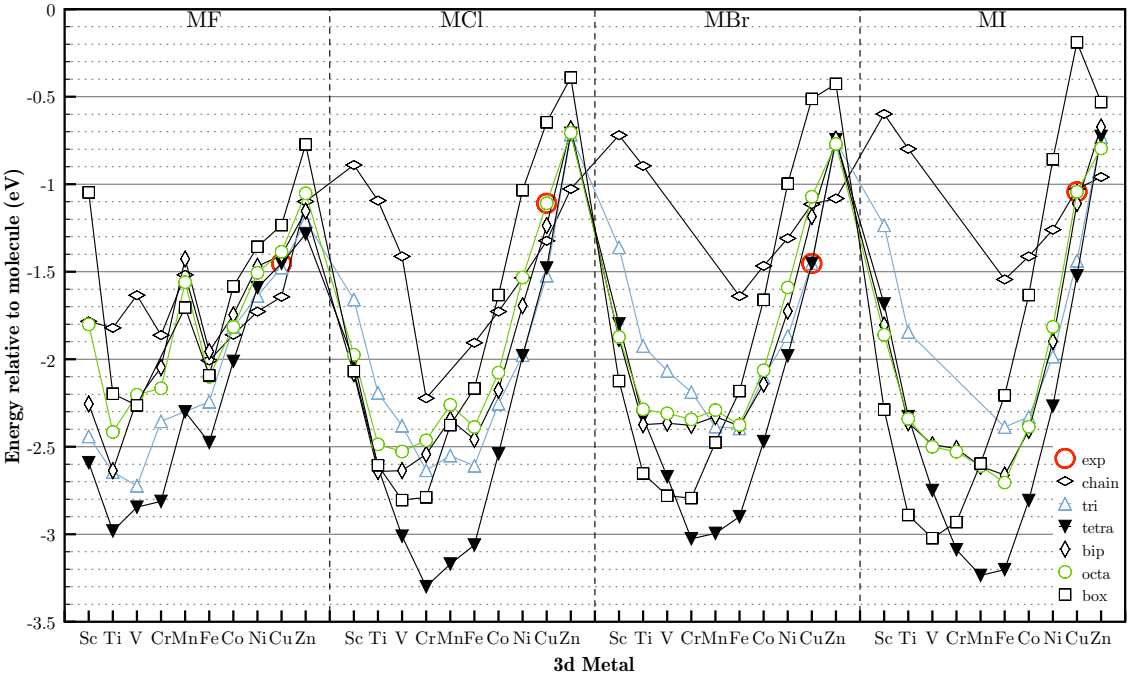

Figure 3.6: Relative energies of MA type 3*d*-metal halides

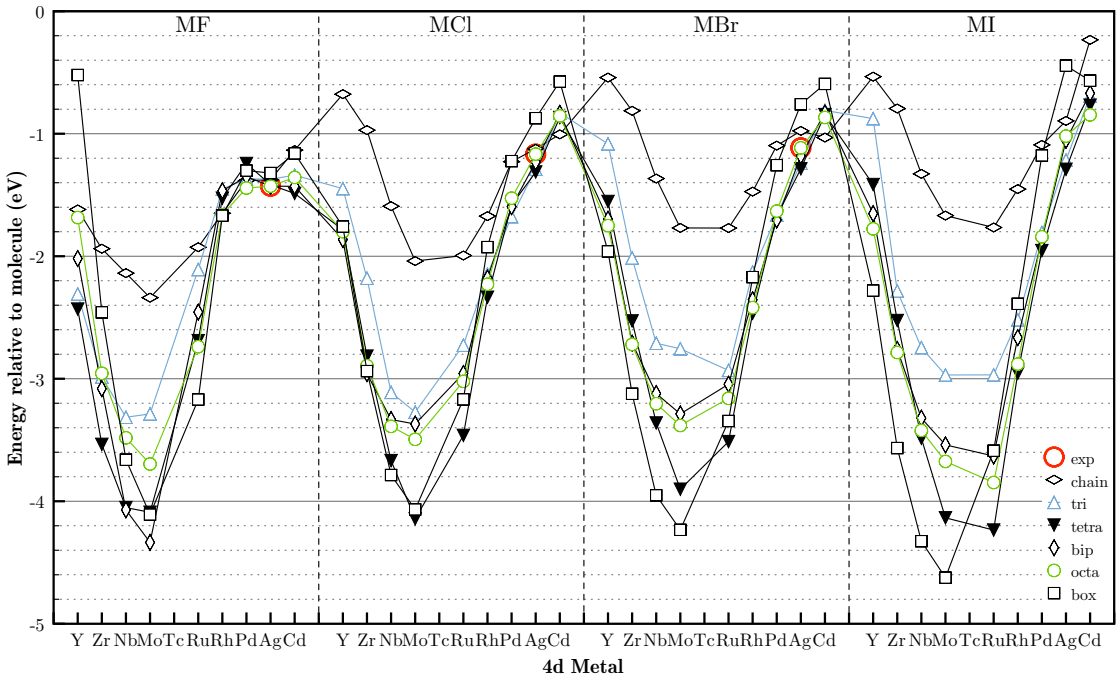

Figure 3.7: Relative energies of MA type 4*d*-metal halides

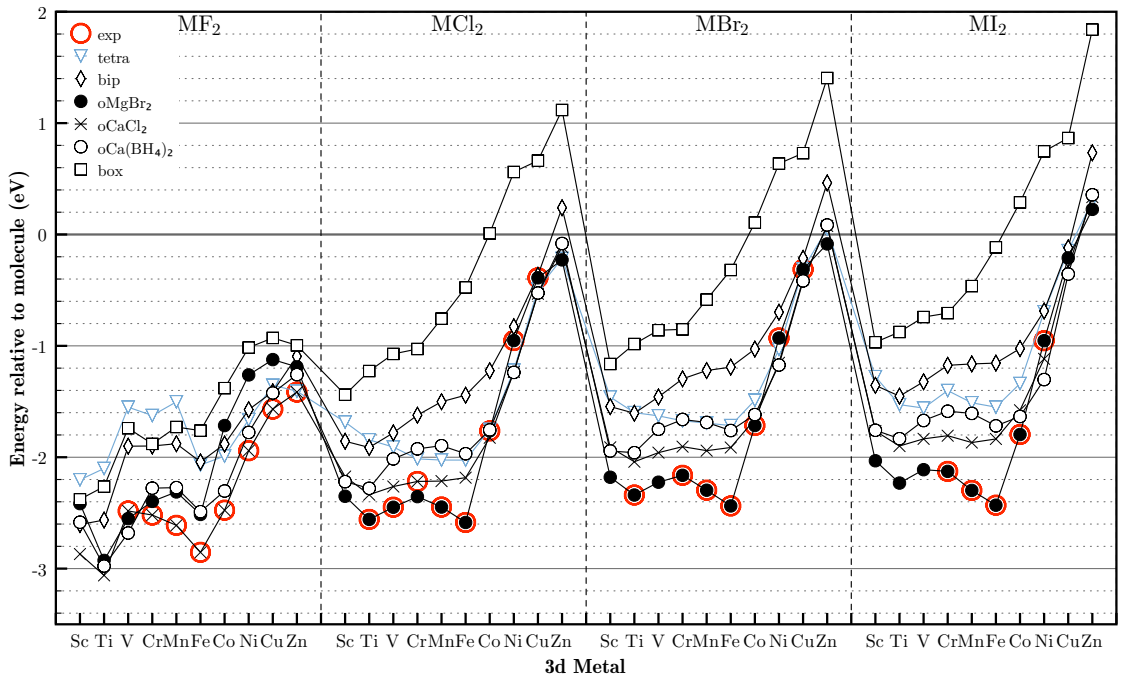

Figure 3.8: Relative energies of MA_2 type 3*d*-metal halides

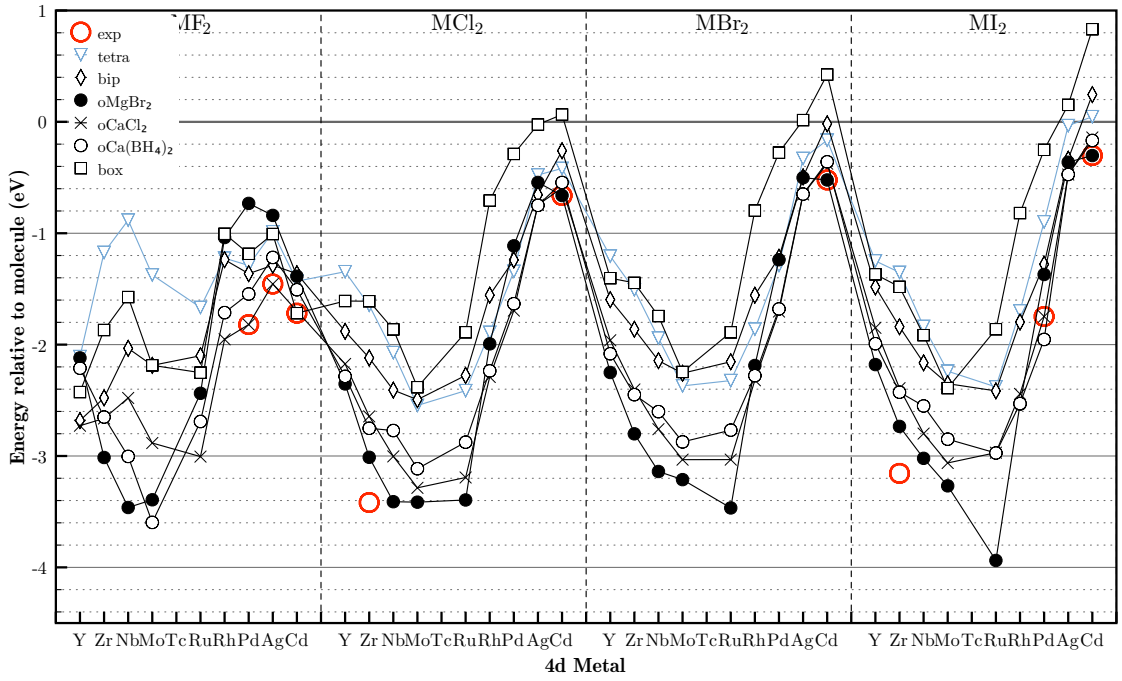

Figure 3.9: Relative energies of MA_2 type 4*d*-metal halides

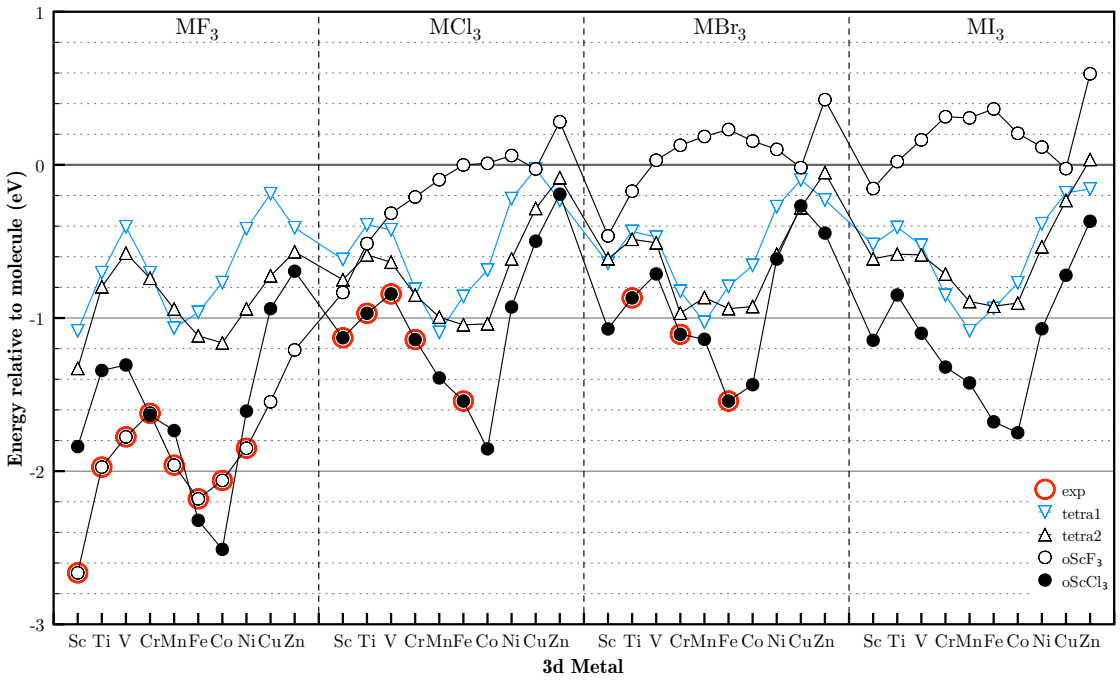

Figure 3.10: Relative energies of MA_3 type 3*d*-metal halides

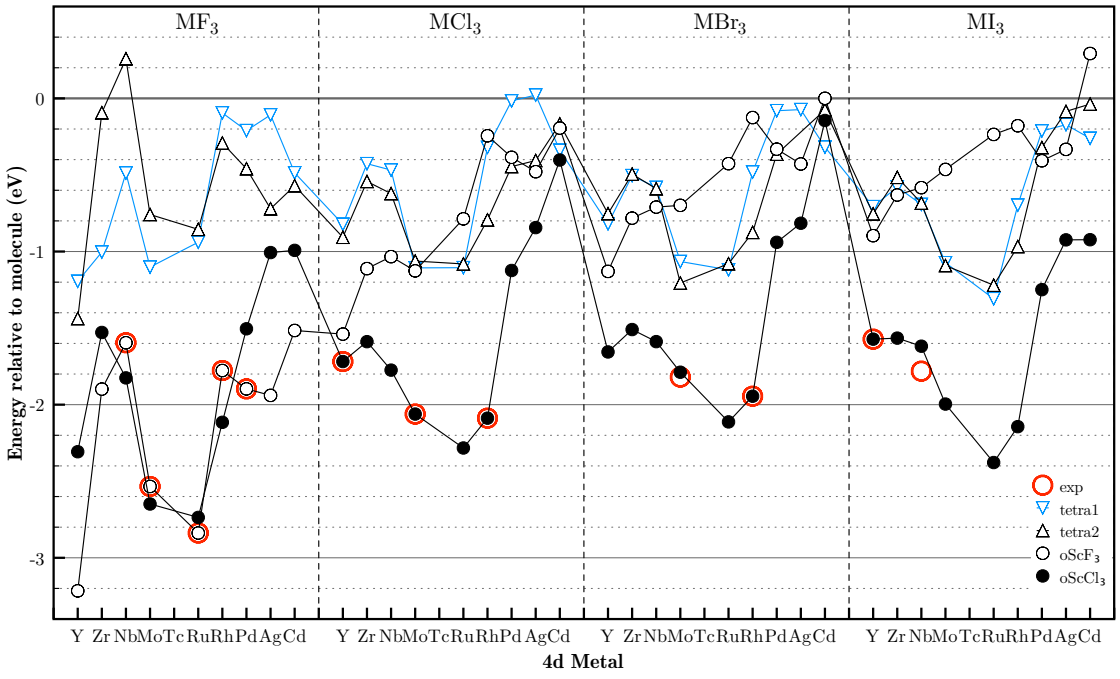

Figure 3.11: Relative energies of MA_3 type 4*d*-metal halides

3.2.2 Binding energies

To get the binding energies, additional calculations were done on all the metals with and without spin, and on the halide atoms as molecules. The metals where setup in their experimental structures and the lattice constant relaxed. We used $8 \times 8 \times 8$ k-points to sample the Brioullin zone for the metals. Binding energies where calculated by comparing the energies of a metal halide system to the energies of its components.

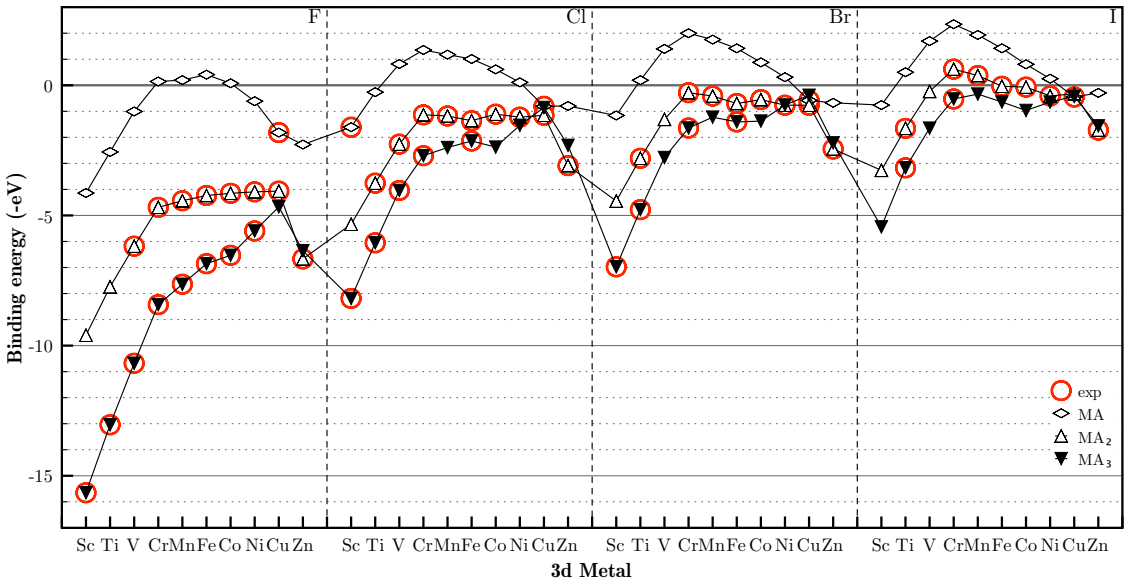

Figure 3.12: Binding energies of the most stable MA, MA_2 and MA_3 type $3d$-metal halides. Red circles indicates that the system is observed experimentally.

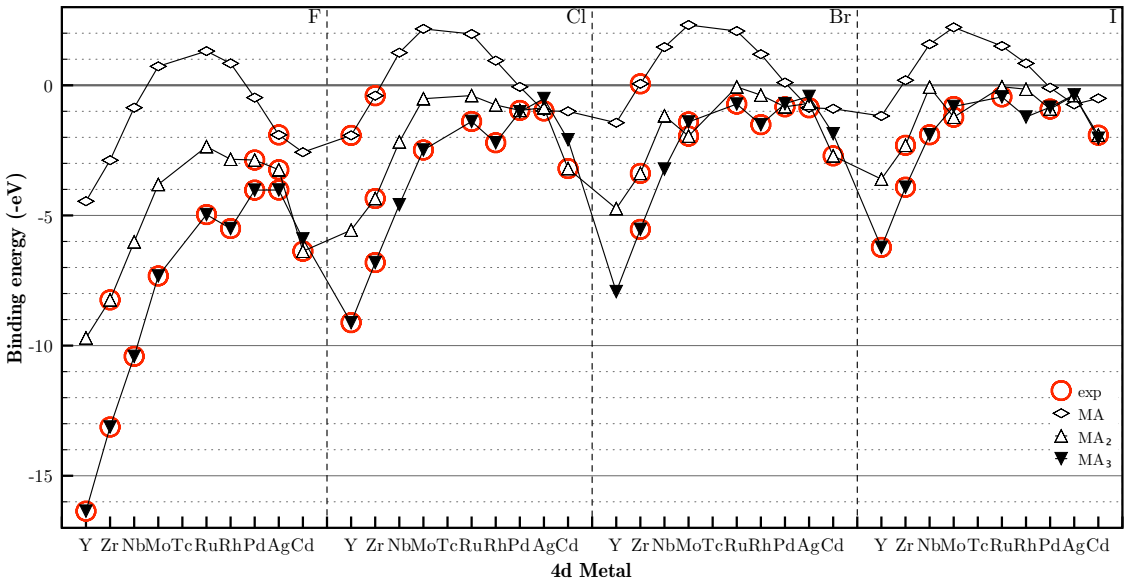

Figure 3.13: Binding energies of the most stable MA, MA_2 and MA_3 type $4d$-metal halides. Red circles indicates that the system is observed experimentally.

In Figures 3.12 and 3.13 the non-spin-polarized binding energies of the transition metal halides are compared qualitatively to experiments. (Note the units: a positive binding energy corresponds to a negative number.) For each oxidation state of the metal, the most stable structure was used for the comparison. A red circle around a point indicate that the system was found in either the database of experimental structures, or the database of experimental standard enthalpies of formation.

Except for CrI_2 and MnI_2 the experimentally observed systems also have a positive binding energy in the calculations; including spin makes the two systems stable. Some systems have a positive binding energy but do not have a red circle. This is either because the experimental data we compare to is limited, or because another phase of the material is always preferred (e.g. Zn and Cd dihalides).

As an attempt to do a quantitative comparison to experiment, the binding energies are compared to experimental values of the standard enthalpy of formation in Figure 3.14. Even though the standard enthalpy of formation also includes contributions from the heat capacity, (a larger heat capacity gives a larger enthalpy of formation,) one often find at least the relative energies to be in agreement for a given class of materials. The reason is that the contribution from the heat capacity is relatively small and does not vary much among a given class of material.

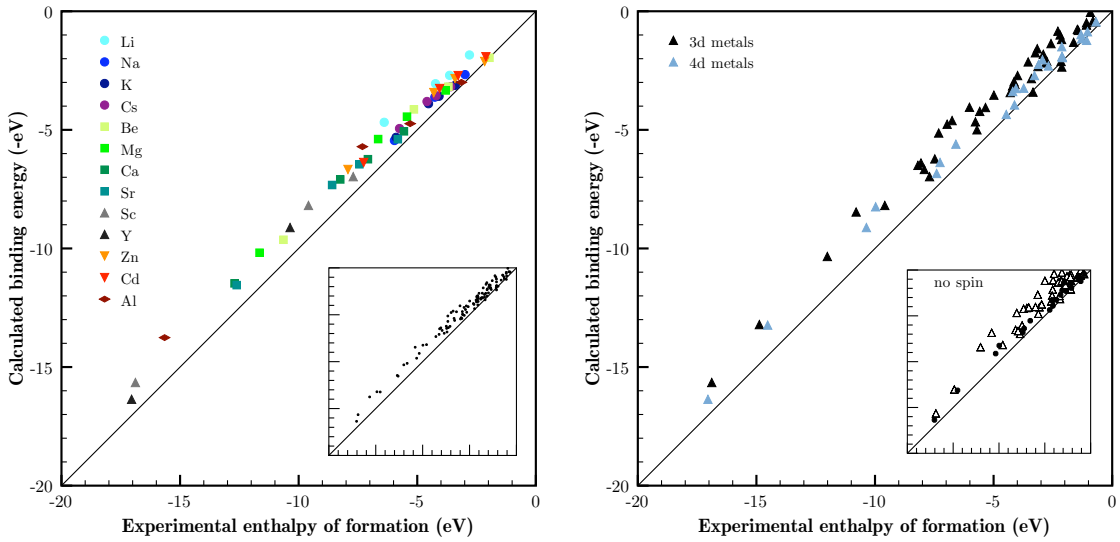

Figure 3.14: Calculated binding energy vs experimental standard enthalpy of formation for metal halides. Left: non magnetic metals; Left inset: includes the spin-polarized calculations. Right: spin-polarized 3*d* and 4*d* metals; Right inset: same metals without from non-spin-polarized calculations.

The calculations reproduce the trends in experimental formation enthalpies of metal halides systems in the range of almost 20eV, where a clear linear relationship can be seen. In general the calculated binding energies are too low, the deviation increasing with the binding energy and essentially gone for the systems with lowest binding energy. If the deviation was caused by the heat capacity, one might expect a correlation of the deviation with the ionic masses, which is not the case here. Nor is it likely that the heat capacity alone could amount to a difference of around 2eV when going to the highest binding energies. It is more likely that something is missing in the electronic energy, and we know we are ignoring the van der Waals interaction. Initial calculations on trying to include the van der Waals interaction in the calculation of these systems by implementing the scheme in [32], indicate that this increases the stability of both the metal halide systems and the metal ammine systems treated later. However, additional testing of the convergence with respect to unit cell sizes and density cutoffs need to be performed before conclusions can be made.

The lithium halides systems seem to fall above the rest, i.e. the calculated stabilities are too low for the lithium systems. This could have a connection to the under-coordination also found in

these systems. For the 3*d*-metals the correlation is significantly improved when the calculations are done spin-polarized, but even then some of the points fall around 1eV above the rest. A deviation of this size could mean that more stable structures exist for these systems.

Regression analysis has been performed for different subsets of the data in Section A.2 and summarized in Table 3.1. From this it is seen, that the correlations are generally good, and that slightly different slopes are achieved for the different anions.

Subset	R^2	σ^2	calc/exp
All, spin-polarized	0.981353	0.212507	0.914955
no 3*d*, no Li	0.992534	0.0897507	0.910638
no 3*d*, no Li, only F	0.992911	0.142524	0.928259
no 3*d*, no Li, only Cl	0.98345	0.0933664	0.894237
no 3*d*, no Li, only Br	0.988693	0.0326968	0.8814
no 3*d*, no Li, only I	0.991204	0.019183	0.916061

Table 3.1: Linear regression parameters for different subsets of the metal halides systems when comparing experimental formation enthalpies to calculated binding energies.

3.3 Analysis

3.3.1 Trends in structures and stabilities

Some trends can be seen directly from Figures 3.5–3.11. For Cl, Br and I the relative energies of different structures are almost conserved. When moving to F the footprint changes somewhat, perhaps indicating size effects; the smaller fluorine ions make new structures possible. When filling the *d*-band, the energy gained by forming a crystal generally increases until the band is half filled, and then decrease again. For the MA_3 the picture is more disturbed.

As an example of more detailed analysis, we consider the relative energies of the MA_2-o$MgBr_2$ and MA_2-o$CaCl_2$ structures. For most flouride systems the MA_2-o$CaCl_2$ is most stable, but as the size of the anion increases the MA_2-o$MgBr_2$ becomes more and more stable. An explanation for this could be that in the layered MA_2-o$MgBr_2$ structure, electron density from the anion is pushed into the interlayer space (see charge density difference calculations in included Paper I) making the effective ionic radius of the anion smaller. This means that the anion can come closer to the metal before ligand repulsion take over, which is favorable if the metal–anion distance is otherwise larger than the optimum. In the internal relaxation of the MA_2-o$MgBr_2$ structures, the individual layers were contracted and for the large majority of MA_2 systems, the metal–anion distance were smaller in the MA_2-o$MgBr_2$ than in the MA_2-o$CaCl_2$ structures; on average the difference was 0.04Å.

An alternative explanation could be that the F atoms has a high preference for a planar trigonal coordination, which they achieve in the MA_2-o$CaCl_2$ structure. In comparison, for the MA_2-o$MgBr_2$ structure the metal to anion coordination is an incomplete tetrahedral.

3.3.2 Stability and electronegativity

Later we will see how the Pauling electronegativity can be used as a descriptor for the stability of metal tetrahydorates, and here we will also try to link the calculated stabilities to electronegativities.

We wanted to rule out structural effects and simply try to calculate the bond-strength between the metal and halide atoms. As a measure of this, we use the binding energy of the molecule, and for some of the systems calculated there is a clear correlation with the electronegativity as seen in Figure 3.15. We have used the square of the electronegativity difference multiplied with the number of anions to a metal, which according to the definition of Pauling electronegativity[33, 34], should give a linear relationship.

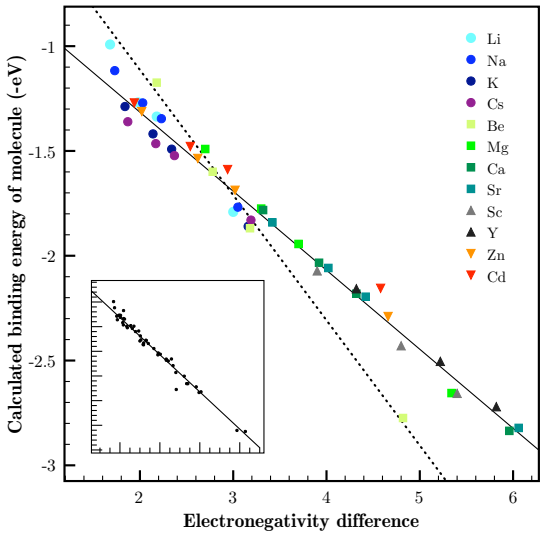

Figure 3.15: Metal–halide bond strength measured as the binding energy of the molecule vs the square of the electronegativity difference of the metal and halide.

It seems that the strength of the metal–halide bond for the systems included, can be calculated using an ionic model, except for beryllium. The beryllium points fall on a line with a much steeper slope, as indicated, and this could be an indication that the binding in beryllium halides systems are mainly covalent[35]. Worth to note is it, that the lithium points tend to go in that direction too.

3.3.3 The under-coordination in lithium halides

The surprising discrepancy for the lithium halides visible in Figure 3.5, where for instance the LiF-tetra is as much as 0.55eV lower in energy than the experimental rock-salt structure of LiF, was investigated further. Of the monovalent systems, lithium was not the only metal showing this behavior; also copper and silver systems with anions larger than fluoride, also preferred tetrahedral or lower coordination.

However, phases of LiI and LiBr do exist where lithium has a tetrahedral coordination[36]. In those structures the spacegroup is $P6_3mc$ (analoguous to the high-temperature structure of $LiBH_4$ studied later) and the structure is very similar to the tetrahedral prototype structure used. (Calculation give energy differences within 0.02eV.) It is not unlikely that similar phases exist at low temperatures for LiCl, LiF and the copper and silver halides.

Perhaps it is actually surprising that the lithium halides have the octahedral NaCl structure. Most other second row elements are often found to have tetrahedral coordinations. And lithium itself has a tetrahedral coordination in lithium tetrahydroborate as we will see later.

The possibility remains that this is a problem in the method, for instance with the pseudopotential used for lithium. However, both the experimental evidence of tetrahedral LiI and LiBr structures, and the similar behavior of copper an silver systems points in the other direction.

In the investigation of lithium halides systems an interesting result appeared. In Dacapo, the lattice optimization of LiF in its experimental rock-salt structure showed two minima (Figure 3.16). This can either witness some interesting physics or the flaws of the calculations. A possible explanation could have something to do with a minimum for covalent interaction and another for ionic; or it could be that the preferred Li–F distance is different for Li and F, and one minimum corresponds to where the Li has its preferred distance, and the other where F has its preferred distance. Unfortunately, the different exchange correlation functionals do not agree on which minimum that is the global, and the RPBE functional used here (and the revPBE[1] functional) actually predicts the wrong minimum when compared to the experimental volume of 16Å^3[37]. However, LiF is the

only system found that show this behavior and for all other systems tested the different functionals agree, and for LiF the functionals also agree that the tetrahedral structure is the most stable.

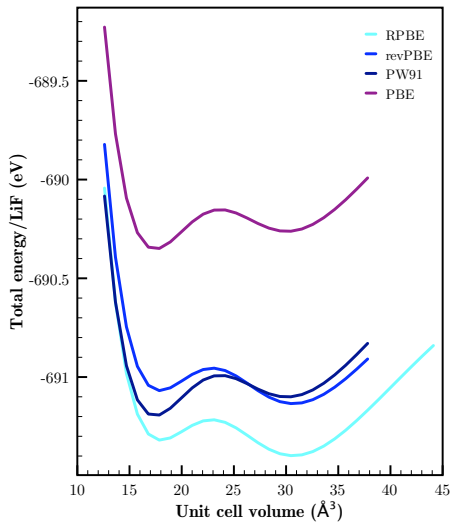

Figure 3.16: Total energy vs unit cell volume of LiF in its experimental rock-salt structure, for different exchange-correlation functionals[1, 2, 3]. The experimental volume is close to 16Å^3.

It is difficult to say whether or not one should trust these artifacts of the lithium systems, and it would be valuable to get input from calculations at a higher level of theory. As we shall see in the next section, the under-coordination might be a more general problem.

3.3.4 Preferred coordination

In a model where the ions are treated as hard spheres we can estimate when the anion–anion repulsion begin to make a certain coordinations unfavorable. If we assume that the surfaces of the metal and the anion spheres are always tangent, the ratio between the radii of the metal and the larger anions below, which the anion spheres begin to overlap was calculated for the different coordinations and shown in the table.

Coordination	Anions overlap when:
Box	$r_+/r_- < \sqrt{3} - 1 \approx 0.73$
Octahedral	$r_+/r_- < \sqrt{2} - 1 \approx 0.41$
Tetrahedral	$r_+/r_- < \sqrt{3/2} - 1 \approx 0.22$

Table 3.2: Critical ratio of metal vs anion radius for different ligand coordinations.

To calculate the ratio for each system we needed the ionic radii. Each cation radius was calculated from the cation–anion distance by subtracting the anion radius that was kept constant for all systems. The four anion radii was calculated from the Cs–anion distance in the rock-salt structure by fixing the Cs radius to 1.88 Å, and the values are shown in Table 3.3 that also include the Pauling ionic radii. It can be seen that the calculated distance with the RPBE functional are 3-5% larger than the Pauling radii. Table 3.2.

Since cesium is the most electropositive of the elements included here, this should set upper bounds on the anionic radii. When the anions form bonds with more electronegative metals, the metals will draw more electron density towards them than cesium does. As a consequence, the cations become larger, the anions become smaller and the ratio of the two radii increases.

Anion	r_-	r_- (Pauling)	r_{Cs}/r_-	r_{Cs}/r_- (Pauling)
F	1.42	1.36	1.32	1.24
Cl	1.90	1.81	0.99	0.93
Br	2.05	1.95	0.92	0.87
I	2.29	2.16	0.82	0.78

Table 3.3: Anion radii calibrated to a Cs radius of 1.88Å compared to Pauling ionic radii.

Moreover, since the charge on the anions decrease they become less repulsive and a larger overlap of the anions can be accepted. Both effects serve to relax the demands listed in Table 3.2.

The ratio between the cation radius and the anion radius was calulated for the systems that were found in either the database of experimental structures, or the database of experimental standard enthalpies of formation, and plotted in Figure 3.17 together with the three limits from Table 3.2.

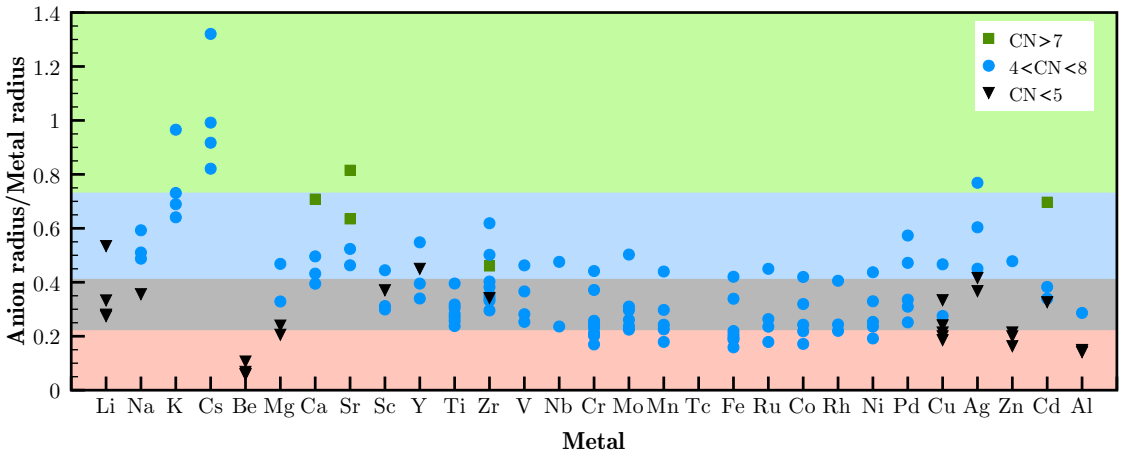

Figure 3.17: The calculated r_+/r_- ratio and their most stable coordinations for observed metal halides. Green area: no anion overlap; blue area: anion overlap for box coordination; grey area; anion overlap for box and octahedral coordinations; red area: anion overlap for box, octahedral and tetrahedral coordinations.

A general consideration is noted before discussing Figure 3.17; if there was no such thing as a preferred coordination, then ligand–ligand repulsions would always make the lowest available coordination number the most stable. Or put another way, if the observed coordination is octahedral then we know that the preferred coordination is not tetrahedral or lower; it must be octahedral or higher, since if the ligand repulsion allows an octahedral coordination, then it would certainly also allow a tetrahedral where the ligand repulsion is smaller.

There are some modifications to this truth. The preferred metal–ligand distance of the tetrahedral coordination could be smaller than the preferred octahedral distance. If this difference is large enough then the ligand repulsion could become larger for the tetrahedral coordination than for the octahedral. We must also not forget the anion coordination, which could force the metal to have an octahedral coordination to satisfy its own preferred coordination, even though the metal prefers a tetrahedral coordination. In principle it is maybe impossible to conclude anything from plots like the one in Figure 3.17, but we will try anyways.

We begin with Cs, which points are up in the green area so a box configuration could be possible for all the cesium halides. However, the calculations predict the octahedral to be most stable and this must consequently be the preferred coordination. For Li we can understand why LiCl, LiBr and LiI choose a tetrahedral coordination since the points are down in the grey area, and if it

was not for LiF, we could not say what the preferred coordination of Li was. But since the ratio of the radii in LiF is large enough to sustain an octahedral coordination, and LiF still chooses a tetrahedral coordination then it seems that the preferred coordination of Li is tetrahedral. If we assume that Na, K prefers the octahedral as Cs, then it makes sence that NaI is tetrahedral simply because of the ligand repulsion, and KF is octahedral even though a box coordination is allowed.

For the alkaline earth metal halides, the first thing we note is that the covalent binding in the Be halides again is apparent; the Be points are way down in the red area in company with other covalent bonded halides like Al. If the bonding in Be was ionic the anion–anion repulsion would be too large to be down in this area. Again, we guess that the preferred coordination of Mg, Ca and Sr is the box coordination, and we can see that Mg is never able to get its preferred coordination because it is too small; only CaF_2, SrF_2 and $ScCl_2$ have large enough ratios. From $ScCl_2$ it seems that the preference for a box coordination is rather strong since it can compete with some amount of ligand repulsion, since the box point is down in the blue area.

For $MgBr_2$ and MgI_2 it should be noted that these tetrahedral structures were not included in the original screening from Figure 3.5. Since the original octahedral points for Mg was down in the grey area, it was decided to screen additional tetrahedral structures for the Mg halides. All the tetrahedral structures in Figure 3.4a-e were screened and $MgBr_2$ gained 0.02eV by choosing the $ZnCl_2$-a type structure, while MgI_2 gained 0.12eV when going from the octahedral to the tetrahedral BeI_2 type structure.

The Figure 3.17 is not discussed further except that is should be added, that recent results (not included here) from spin-polarized screening of Mn, Fe, Co and Ni halides in the tetrahedral structures in Figure 3.4a-e also turn out in favor for the tetrahedral structures. As for $MgBr_2$ and MgI_2 this is in disagreement with the experiment where one observes octahedral structures for all the systems, and a systematic picture is beginning to appear.

For halides of Li, Cs, Mg, Mn, Fe, Co, Ni the calculations predict a lower coordination number than observed. But for LiBr, LiI and the Cs halides some experiments actually observe these structures with lower coordination. It is possible that this could be a general trend: at lower temperatures structures with lower coordination is preferred. It would be interesting to do experiments and calculation to investigate this further to see if it can be explained by the entropy. This could of course be an error in the calculations, and for instance including van der Waals might reduce the ligand–ligand repulsion. A pointer in the direction that ligand–ligand repulsion might be overestimated in the calculations is given by the fact that the $MgCl_2$ layers are slightly repulsive. The energy difference between bulk $MgCl_2$ and $MgCl_2$ layers in vacuum is 0.02eV per formula unit.

3.4 Summary

Although, there are some structural issues that need to be investigated further regarding the undercoordination of certain systems, in general the method succeeded in predicting both structures and relative stabilities. As mentioned in Section 2.1.3 the relative energies or trends are practically all we need to be able to design functional materials, and an important result from the study of the metal halides is that using very simple model structures, the trends were reproduced for a large set of data in a wide range of stabilities. This result provides hope that the same will hold for the tetrahydroborates when the halide anions are exchanged with BH_4^{-1} ions, and for the ammines when ammonia is absorbed in the metal halides.

4

Tetrahydroborates

The complex engineering challenges of the full macroscopic storage system have directed research towards complex materials with extreme hydrogen storage capacity, and the metal tetrahydroborates $M(BH_4)_x$ represents a class of complex hydrides with the highest densities, both volumetric and gravimetric[38]. Unfortunately, many of the known binary tetrahydroborates have problems concerning stability, kinetics or reversibility. The alkali tetrahydroborate, *e.g.* $LiBH_4$,[39, 40] are too thermodynamically stable, the alkaline earth compounds are kinetically too slow and practically irreversible[41], and the transition metal borohydrides are either unstable or irreversible[42]. These problems might be solved for a ternary or a quartenary tetrahydroborate and mixed systems are searched (e.g. [43],[42],[44]), but even the binary tetrahydroborates are in general difficult to synthesize.

In order to improve synthesization of known tetrahydroborate, aid the synthesization of unknown tetrahydroborates, and in the hope of being able to improve reversibility and kinetics, one seeks insight into the atomic structures of the tetrahydroborates. However, due to the small cross-section for hydrogen in X-ray diffraction and the high absorption of neutrons by boron in neutron diffraction, it is difficult to characterize the structures of tetrahydroborates experimentally. This is made even harder by the fact that the tetrahydroborates are very polymorphic, so different structures are found at different temperatures. A good overview of some detected structures are given in [45]. Computer simulations can therefore be an aid in the structural search (e.g. [46, 47, 48]).

In this chapter the tetrahydroborates are investigated computationally by comparing their energies in different prototype structures. The prototype structures are based on the assumption that the BH_4^{-1} ions are stable, which might not be the case when the electronegativity of the metal becomes to high. Some of the experimental and theoretical proposed structures will be reviewed and compared, and new structures will be added. The chapter ends with a screening study of ternary tetrahydroborates and some examples of advanced design.

As for the metal halides studied in the previous chapter the model structures are simple containing up to four f.u. per unit cell in a few cases but in most cases only one or two f.u. per unit cell. The validity of modeling complex structures by simple structures was investigated for the extreme case of $Mg(BH_4)_2$, for which a full free energy comparison between the huge experimental structures and a number of simple model structures was performed, and the important result from this was that since energy differences were small, the simple model structures can be used to approximate the stability of the material, as long as the local coordination is right. This result helps to justify the use of simple model structures in the screening study.

The aim of the screening study is to destabilize the alkali tetrahydroborates by substituting part of the alkali metal atoms with other metals. In this case the screened systems were limited to ternary tetrahydroborates with a one-to-one mixture of the alkali and the other metal, that were calculated in a number of prototype structures. Besides the promising candidate materials predicted by this study, the knowedge gained can be used for future studies of e.g. ternary tetrahydroborates with non-stoichiometric mixtures, or even quarternary or higher tetrahydroborates.

Also on the anion side one can try tuning the stability of a tetrahydroborate. In this chapter we will see how the fractional substitution of BH_4^{-1} with iodine affects the relative stabilities of the low- and high-temperature phases of $LiBH_4$, which has a completely different use as a possible solid state electrolyte for ion-conduction in batteries.

4.1 Polymorphism of tetrahydroborates

The halide ion has been substituted by a tetrahydroborate complex ion which adds more structural complexity. Besides the preferred cation and anion coordinations the coordination of the hydrogen in the first coordination shell is important. There are more competing elements in determining the stability, and this gives a larger set of structures close in energy. In addition rotation of the BH_4^{-1} ions gives larger entropic contribution which means that different polymorphs are stable at different temperatures.

4.2 Alkali metals

4.2.1 The octahedral structures

The $NaBH_4$, KBH_4 and $CsBH_4$ systems are all observed in the NaCl type structure, in which both the metal and the BH_4^{-1} ion has an octahedral coordination[49]. Each BH_4^{-1} group points its six edges towards a metal and a bidentate connection occurs. Rotation of the BH_4^{-1} ions leads to disorder; for high pressure or low temperature, a transition to an ordered phase is observed for $NaBH_4$[49]. The ordered phase is used for the calculations here and is shown in Figure 4.1a. For $NaBH_4$ another phase has been observed[50] (see Figure 4.1b). In this structure, with spacegroup *Pnma*, two orientations of the coordination octahedra are apparent. The octahedra themselves are somewhat distorted.

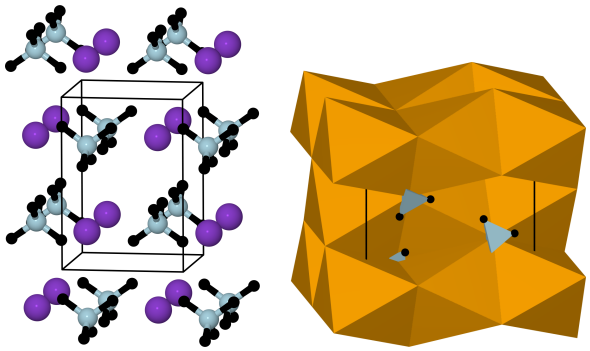

Figure 4.1: Left: Ordered octahedral rock-salt structure of Na, K and Cs tetrahydroborate. Right: Distorted high-pressure octahedral *Pnma* structure of $NaBH_4$.

In Section 4.2.4 we compare the energies of these structures, but first lithium tetrahydroborate and its structures with tetrahedral coordination are reviewed.

4.2.2 From octahedral to tetrahedral structures

Experiments report a high-temperature and a low-temperature phase for $LiBH_4$, that both include the BH_4^{-1} ions in a tetrahedral coordination to the Li atoms[51]. In the calculations reported here, the low-temperature structure also give the lowest energy when calculated for $NaBH_4$, as we shall see later.

In order to provide some structural insight, on how the systems can go from one phase to the next, it helps to look at the tetrahedral structures as simple transformations from the octahedral NaCl-type structure (Figure 4.2). For simplicity the hydrogen is excluded, and we consider instead the LiCl system. A set of calculations were originally performed to investigate why calculations of the lithium halides resulted in structures with tetrahedral coordination having a lower energy than the experimental NaCl structure; all the transitions in Figure 4.2 happened without a barrier for LiCl, lowering the energy when moving from the octahedral to tetrahedral structures.

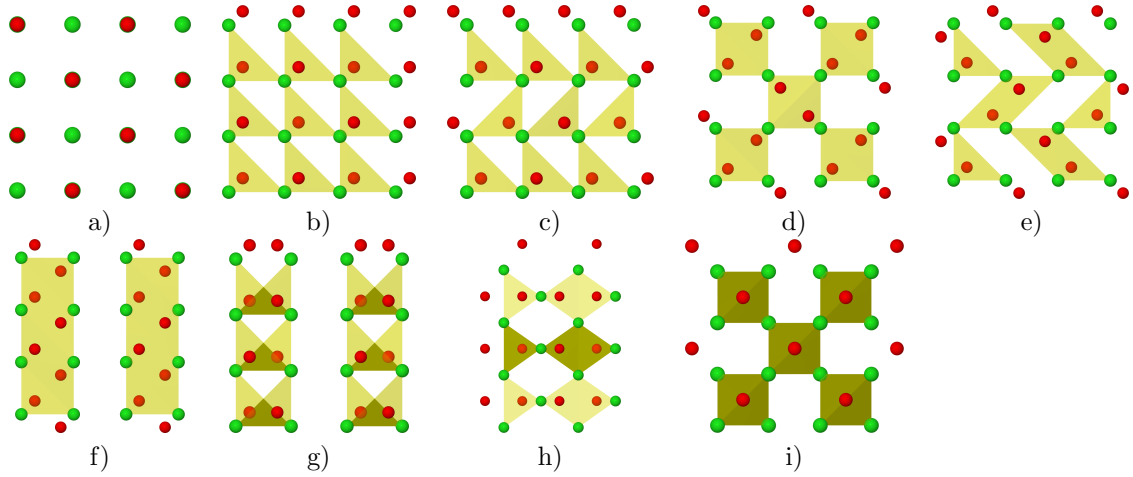

Figure 4.2: Tetrahedral structures of LiCl obtained by moving Li in the rock-salt structure.

When a lithium atom moves towards an edge of the octahedron of Cl atoms that surrounds it in the NaCl structure, its coordination number decreases from 6 to 4. If the Cl atoms are kept fixed, it moves into an asymmetric tetrahedron, but these can easily be made symmetric by contracting and skewing the unit cell. To help the eye, the Cl atoms are kept in fixed in Figure 4.2. The unit cell, that was used as a basis for all the transitions, consisted of a cube of four Li and four Cl atoms, corresponding to for instance the lower left quarter of the end-view in Figure 4.2a.

Different structures appear as a result of moving the Li atoms in different combinations of directions. In Figure 4.2b, all lithium atoms are moved towards the upper right edge, leading to the most simple tetrahedral structure; later we refer to this as "simple tetrahedral". When half the Li are moved to the upper left instead (Figure 4.2c), the analogue to the high-temperature $P6_3mc$ structure of $LiBH_4$ appears. The analogue to the low-temperature $Pnma$ structure (Figure 4.2e) is reached by moving all four Li in different directions. When transitions between the low-temperature and the high-temperature structure were investigated, the structure in Figure 4.2d came up as a possible intermediate. This can also be reached from the NaCl structure by moving all Li in different directions.

Many other structures are possible, as can be seen in Figure 4.2, and the number of different structures naturally increases, as the unit cell used as basis for the transformations is enlarged. The original coordination octahedra in the NaCl structure are edge-sharing, and a different set of transformations consists of keeping the Cl atoms fixed and moving the Li through the face of the octahedron, and into the tetrahedral interstice. These tetrahedra are already regular, and the unit cell only needs to be scaled proportionally to relax the metal anion distances. Two such structures are shown in Figure 4.2h-i; the latter corresponds to a high-pressure polymorph of $LiBH_4$ detected by Filinchuk et al. [52](see also Figure 4.3d).

4.2.3 Lithium

The LiCl analogues to the low-temperature and the high-temperature phases of $LiBH_4$ have already been introduced, and substituting Cl^- with BH_4^{-1} and relaxing the unit cell and atomic positions leads to the lithium tetrahydroborate structures in Figure 4.3.

The high-temperature phase has been connected with some controversy between theoretical and experimental work[45]. In the experimental reported structure, the BH_4^{-1} groups all point their faces toward the lithium atoms (see Figure 4.4a). However, the Li–boron distances are not the same for all BH_4^{-1} ions which is somewhat surprising. Three metal–boron distances are 3.11Å and the final is 2.50Å. We have calculated $LiBH_4$ in this structure and in another version with same spacegroup, in which one BH_4^{-1} ion points one hydrogen and three BH_4^{-1} point two hydrogens towards Li (Figure 4.4b).

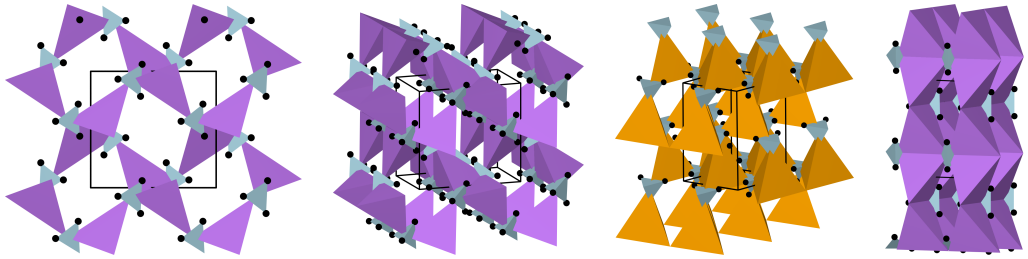

a) *Pnma* end-view b) *Pnma* c) $P6_3mc$ d) Ama_2

Figure 4.3: Optimized structures of $LiBH_4$: a)-b) low-temperature structure; c) high-temperature structure; d) high-pressure polymorph.

In the calculation of the experimental structure all Li–boron distances are the same in the optimized structure in Figure 4.4a in disagreement with the experimental result. For the other version, which gives a lower energy (0.25eV per Li!) the distances agree with the experiment, when it is taken into acount that distances in the calculations in general are 7.6% larger. The experimental Li–boron distances scaled with 107.6% give 3.35Å and 2.69Å in almost perfect agreement with the calculated values of 3.37Å and 2.69Å. As we will see in the next section there is a general trend connecting the preferred hydrogen coordination number with the size of the alkali metal ion, that explains why the calculated version in Figure 4.4b should be the preferred for Li.

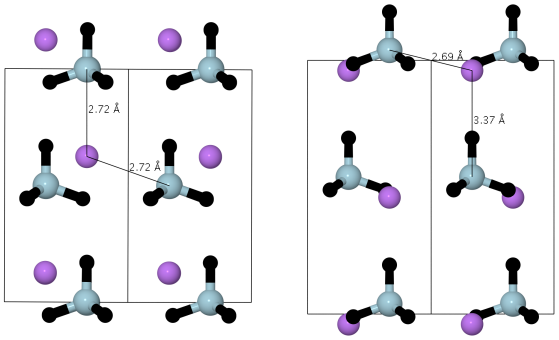

a) 0 eV b) -0.25eV per Li

Figure 4.4: Experimental a) and theoretical b) position of the Li atoms in the $P6_3mc$ structure of $LiBH_4$.

In Section 3.3.4 when studying the metal halides systems, it was mentioned that the calculations could overestimate the ligand repulsion leading to too low coordination numbers predicted by the calculations. This might also be the explanation of the discrepancy between the experimental structure in Figure 4.4a and the calculated in Figure 4.4b. However, the two different experimental Li–boron distances that scaled with 107.6% agree with the calculated distances in Figure 4.4b is quite convincing, while it is surprising that the experimental structure in Figure 4.4a should have different distances. If the high-temperature structure of $LiBH_4$ is truly the version in Figure 4.4b, then the overestimation of the ligand repulsion by the calculation perhaps just serve to explain the 7.6% larger metal ligand distances.

4.2.4 Relative energies

All the alkali tetrahydroborates were calculated in a set of structures including: the two octahedral from Figure 4.1, the low-temperature Figure 4.3a-b and both versions of the high-temperature $LiBH_4$ structures in Figure 4.4, the high-pressure polymorph Figure 4.3d and the simple tetrahedral structure Figure 4.11a. Energies are compared in Figure 4.5.

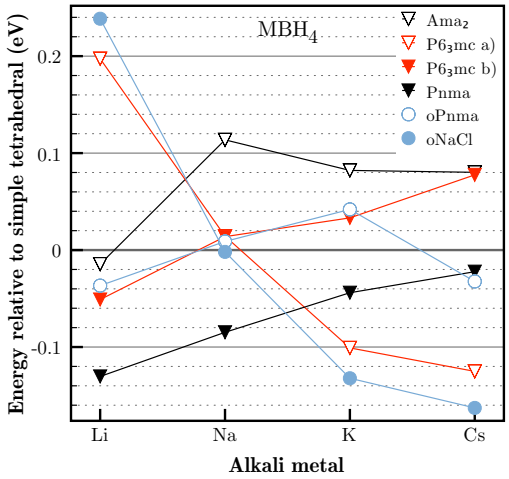

Figure 4.5: Relative energies of alkali tetrahydroborates in different structures.

For $LiBH_4$, KBH_4 and $CsBH_4$ the most stable structures in the calculations are also the ones observed experimentally. In the case of $NaBH_4$, we see yet another example of the calculations giving a 0K structure with a lower coordination of the one observed, hence the low-temperature $LiBH_4$-*Pnma* structure is also the most stable for $NaBH_4$. Here we should note that the octahedral *Pnma* structure (Figure 4.1b) is transformed into the tetrahedral *Pnma* (Figure 4.3a-b) structure during the relaxation of both $LiBH_4$ and $NaBH_4$; the two points are not falling as low as the tetrahedral *Pnma* points due to differences in lattice parameters.

The two versions of the high-temperature $LiBH_4$-$P6_3mc$ structure (the red series in Figure 4.5) show interestingly a strong dependence on cation size; the experimental version first becoming the most stable for K and Cs. For $LiBH_4$, the energy difference is as much as 0.25eV, which could explain why theoreticians have had difficulty accepting the original $P6_3mc$ structure (labeled $P6_3mc$ a) in the plot). As mentioned, the difference between the two versions is the denticity of the BH_4^{-1} ligands: in $P6_3mc$ a) there are 4 tridentate, in $P6_3mc$ b) 3 bidentate and 1 monodentate. It makes sence that a larger cation size make space for a higher denticity, which is why the $P6_3mc$ a) only has a lower energy for K and Cs. This trend is confirmed by the simple tetrahedral structure, which is represented in the plot by the zero line. In this structure the denticities of the BH_4^{-1} ions are 3 bidentate and 1 tridentate, which you could say are between the denticities in the two $P6_3mc$ structures and correspondingly its stability (the zero line) lies between the two $P6_3mc$ series.

4.2.5 Iodine doped lithium tetrahydroborate for ion conduction

In the search of a solid state electrolyte for ion conduction in Li ion batteries, the high-temperature (HT) phase of $LiBH_4$ has proved to be a good candidate[53]. Recent work by Orimo's group aims at stabilizing the HT phase by doping the material with different cations and anions (see included Paper IV). They have found that partly substituting the BH_4^{-1} ions with I^- ions makes the HT phase stable at lower temperatures than for the pure system. For a fractional iodine content below 50% they also observe an intermediate phase.

To supplement their work we performed a series of calculations, where BH_4^{-1} was substituted with I^- at different sites, for different fractions in the HT and the low-temperature (LT) structures. We also proposed a structure for the intermediate state, which is based on the structure in Figure 4.2d, that as mentioned originally was found when phase transitions between the LiCl analogues to the LT and HT structures were investigated, but which also appeared as a simple transformation of the NaCl structure as indicated in Figure 4.2d.

Some examples of the iodine doped structures after relaxation is given in Figure 4.6 together with the relative energies for different fractional substitution of BH_4^{-1} with I^-.

As seen from Figure 4.6e the calculated stability of the HT phase increases with iodine content,

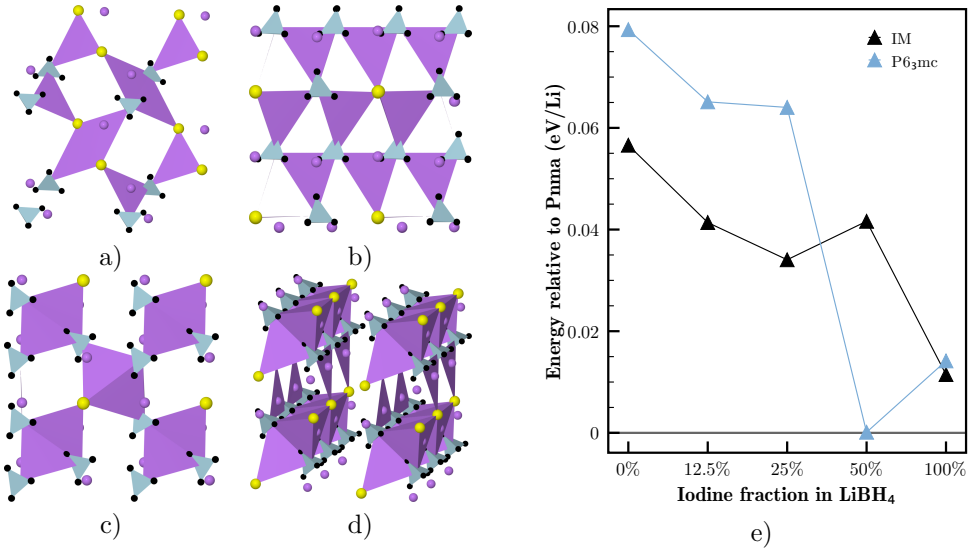

Figure 4.6: Iodine doping in $LiBH_4$ in low-temperature (LT), high-temperature (HT) and intermediate (IM) phase. a) LT *Pnma* structure for 50% I; b) HT $P6_3mc$ structure for 25% I; c) IM structure for 25% I. d) IM structure for 50% I. e) relative energies of the three phases vs fractional iodine content.

reaching a maximum for 50% substitution where the energy becomes almost identical to the LT energy, and falling slightly when moving to pure LiI. The energy of the intermediate state (IM) lies between the two for fractions below 50% including the case of pure $LiBH_4$, while for 50% the HT energy has dropped below the IM energy and for pure LiI the two are almost equal. This seems to agree with the IM phase only being observed for fractions below 50% in the experiments.

4.3 Alkaline earth metals

4.3.1 Experimental structures

Our main effort in modeling alkaline earth tetrahydroborates was in dealing with $Mg(BH_4)_2$, and the focus here is therefore on that system. For $Be(BH_4)_2$ we just note that a polymeric structure has been observed[54], whereas for $Ca(BH_4)_2$ different structures have been detected[55].

Two structures have been reported experimentally for $Mg(BH_4)_2$, a low-temperature with a $P6_1$ spacegroup and a high-temperature with a *Fddd* spacegroup[56, 57, 41]. Both represent complicated 3D networks of corner-sharing coordination tetrahedra, with 330 atoms in the unit cell for $P6_1$ and 704 for *Fddd*. Here we just show the low-temperature structure (Figure 4.7).

As indicated by the coloring in Figure 4.7 the $P6_1$ structure can be viewed as three identical networks that are folded into each other and some places connected via shared BH_4^{-1} groups. (i.e. the vertices of the tetrahedra). Each network contains 5 and 8 membered rings of coordination tetrahedra.

4.3.2 Model structures

Experience gained from the metal ammine systems was used to do a one week manual search of model structures for $Mg(BH_4)_2$. During this search, around 150 different structures were build, optimized and energetically compared, and the one that initially gave the lowest energy is shown in Figure 4.8a, in which Mg has a square planar coordination of BH_4^{-1} ligands. However, distorting the structure a little and relaxing atomic coordinates showed that this structure represented a saddle point in the potential energy, and a long relaxation took the structure from the planar coordination

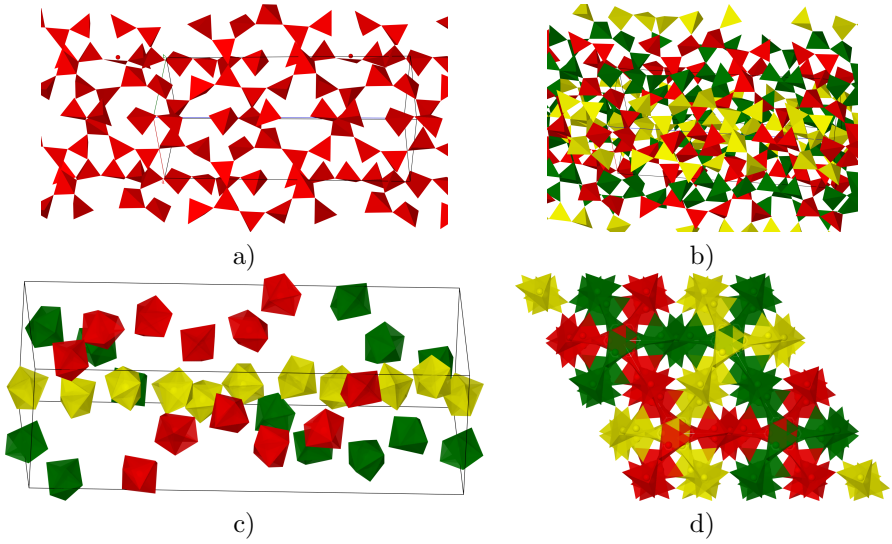

Figure 4.7: Experimental low-temperature $P6_1$ structure of $Mg(BH_4)_2$: a) a single network; b) the three networks folded together, and connected via shared BH_4^{-1} ions at the vertices of the coordination tetrahedra shown; c) hydrogen coordination polyhedra around Mg; d) end-view of the three networks.

to a tetrahedral coordination, which after optimizing the unit cell parameters resulted in the final structure shown in Figure 4.8b 0.2eV below the planar. This structure is an open low-density 3D network of corner-sharing tetrahedra with spacegroup $I\bar{4}m_2$, different from all structures reported at that time, that were all layered, polymeric or even had an octahedral coordination[48].

At almost the time, experimentalists reported the two structures described in the previous section, that were very similar in the sense that these also were 3D networks of corner-sharing tetrahedra, albeit much more complicated. The theoretical $I\bar{4}m_2$ structure was published for the first time a year later in a paper by Ozolins et al. [46] who found it by completely different means, using an wonderful algorithm to optimize the electrostatic interaction. That the structure was found independently by so different means might improve its chances for being the true energy minimum.

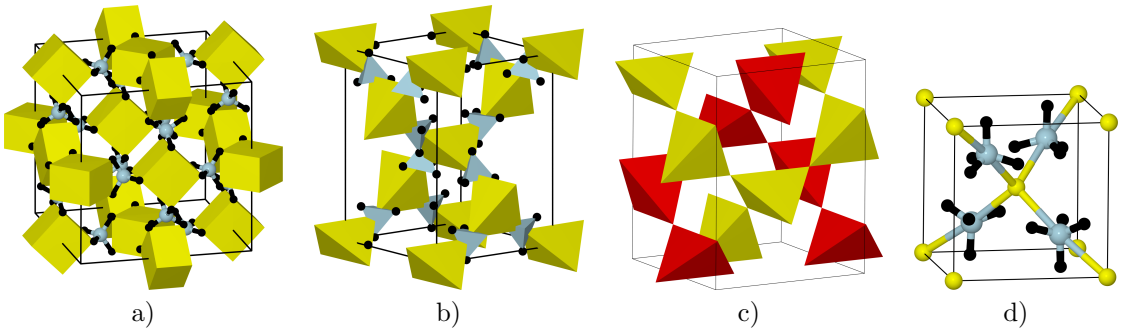

Figure 4.8: Model structures of $Mg(BH_4)_2$: d) the planar coordination, that after relaxation transformed into b) theoretical low-temperature $I\bar{4}m_2$ structure; c) two $I\bar{4}m_2$ networks folded to a $I4_1/amd$ structure; c) a symmetric $P\bar{4}2m$ version of the $I4_1/amd$ structure.

There is an important difference between the complicated experimental structures and the simple theoretical one, namely the density, which is much lower in the theoretical structure ($0.56\,g/cm^3$). However, as can be seen in Figure 4.8c two $I\bar{4}m_2$ structures can be folded into each other resulting in a structure with spacegroup $I4_1/amd$ and almost the double density $1.01\,g/cm^3$,

which is higher than the densities of the $P6_1$ ($0.82\,g/cm^3$)and the $Fddd$ ($0.90\,g/cm^3$), but in agreement with an experimental result[58] of $0.99\,g/cm^3$ of an uncharacterized tetragonal structure. (The $I4_1/amd$ structure is tetragonal as well.) A cubic version of the folded structure, in which the tetrahedra are regular, has the spacegroup $P\bar{4}2m$ and is shown in Figure 4.8d.

Higher densities can also be achieved within a single network without going to the complexity of the $P6_1$and the $Fddd$ networks. The quartz structure for SiO_2 was used as a template to create a model structure for $Mg(BH_4)_2$ with three formula units in the unit cell shown in Figure 4.9b, and this structure has a density of $0.66\,g/cm^3$.

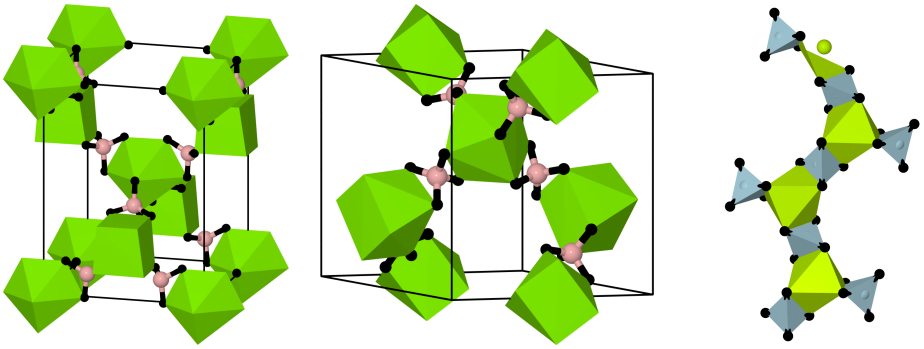

a) b) c)

Figure 4.9: Hydrogen coordination in $Mg(BH_4)_2$ and a Be structure: a) two different polyhedra for the $I\bar{4}m_2$ structure, one is the same as in the experimental $P6_1$ (Figure 4.7c) and one is box; b) box coordination in the quartz structure; c) polymeric $Be(BH_4)_2$;

In Figure 4.9 the coordination of the hydrogen atoms to Mg is shown, and we see that for the quartz structure (Figure 4.9b) the hydrogen coordination polyhedra is close to a box in shape. In the case of the $I\bar{4}m_2$ (and the folded versions $I4_1/amd$ and $P\bar{4}2m$) half the Mg has the box coordination and the rest has coordination polyhedra similar to the one of $P6_1$as can be seen by comparing Figure 4.9a to Figure 4.7c. We have not yet found any structure more simple than the $P6_1$ in which all the Mg atoms have the same hydrogen coordination as in the $P6_1$, and one could speculate that the hydrogen coordination is part of the reason why these huge superstructures are preferred.

4.3.3 Relative energies

All alkali tetrahydroborates were relaxed in the following structures: $I\bar{4}m_2$ referred to as simple tetrahedral (Figure 4.8b), $P\bar{4}2m$ referred to as folded (Figure 4.8b), quartz (Figure 4.9b), planar (Figure 4.8a), octahedral (Figure 4.11h) and the polymeric referred to as chain (Figure 4.9c) and their energies are compared in Figure 4.10.

From Figure 4.10 it seems that size effects are dominating; the repulsion between the BH_4^{-1} ions makes it impossible for some of the systems to keep an octahedral coordination, and according to the calculations the tetrahedral structures are the most stable even for Ca. Only for Sr does the octahedral structure get lower in energy. The folded tetrahedral structure also suffers from ligand–ligand repulsion, but in this case between the BH_4^{-1} ions of the two networks. Except for Be the metals do prefer the tetrahedral for the square and trigonal planar coordinations; for $Be(BH_4)_2$, the polymeric structure is the only real candidate.

It seems from the small differences in the energies of the $I\bar{4}m_2$ and the quartz structure that, either the hydrogen coordination does not play an important role for these systems, or it does, and the two different hydrogen coordination polyhedra of $I\bar{4}m_2$ are equally favorable.

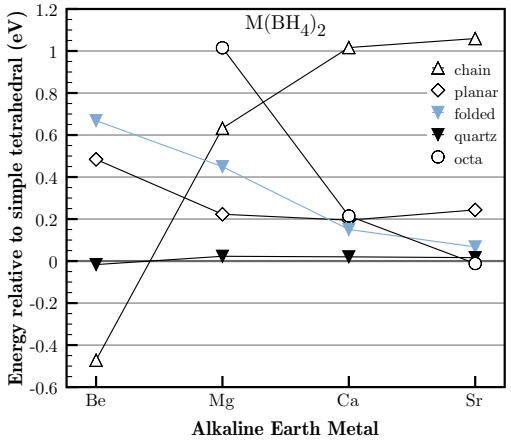

Figure 4.10: Relative energies of alkaline earth tetrahydroborates in different structures.

4.3.4 Free energy comparison

In [15] (included Paper II) we used a symmetry constraining algorithm to optimize the huge experimental structures of $Mg(BH_4)_2$, and phonon density of states calculations were performed to compare the free energies of the experimental with the $I\bar{4}m_2$, $I4_1/amd$ and some other theoretical structures. This showed that the $I\bar{4}m_2$ was the most stable, and that in general the energy differences were within 10kJ/mol H_2. Apparently, the system does not gain a lot when going to the large super structures. This is an important result, since this means that we can use simple model structures to calculate the thermodynamic properties of $Mg(BH_4)_2$ and hopefully similar systems as well, as long as we get the local coordination right. In the next section, we shall see how this result was used to perform a so-called local coordination screening of mixed tetrahydroborate systems.

4.4 Screening alkali-X mixtures

Based on the assumption that one can use simple model structures to asses the stability of metal tetrahydroborate systems, which was supported by the studies of the $Mg(BH_4)_2$ system, we prepared a screening study of mixed tetrahydroborate systems that was performed by the students attending the CAMD summer school in 2008. The project and the results are described in the included Paper III, and for convenience the systems, model structures used and the main result are summarized here.

Out of 757 investigated $M_1M_2(BH_4)_{2-5}$ (M_1 = alkali metal and M_2 = alkali, alkaline earth or 3d/4d transition metal) compositions and structures, a total of 22 were found to form stable alloys with promising decomposition energies. The systems were calculated in a set of prototype structures to probe different coordinations of BH_4^{-1} ions to the two metals. Different oxidation states of the transition metal were also screened. The template structures used are illustrated in Figure 4.11.

To be able to calculate the stability of a mixed tetrahydroborate towards phase separation into the binary tetrahydroborates of the involved species, we needed some reference energies of all the binary tetrahydroborates. For consistency, the reference energies were calculated by using the most stable structure that could be obtained by relaxing the each binary tetrahydroborate in the same template structures (or slight modifications hereof) used for the mixed systems. This for instance meant that the reference structure for $LiBH_4$ was the simple tetragonal in a slightly distorted unit cell. Exceptions to this were $Sc(BH_4)_3$, $Y(BH_4)_3$, $Al(BH_4)_3$, $Ti(BH_4)_4$ and $Zr(BH_4)_4$. Of the remaining transition metals Ni, Pd, Cu and Ag preferred a monovalent state and the structure also used for $LiBH_4$. The largest part Mg, Ca, V, Nb, Cr, Mo, Mn, Fe, Co, Zn and Cd (including

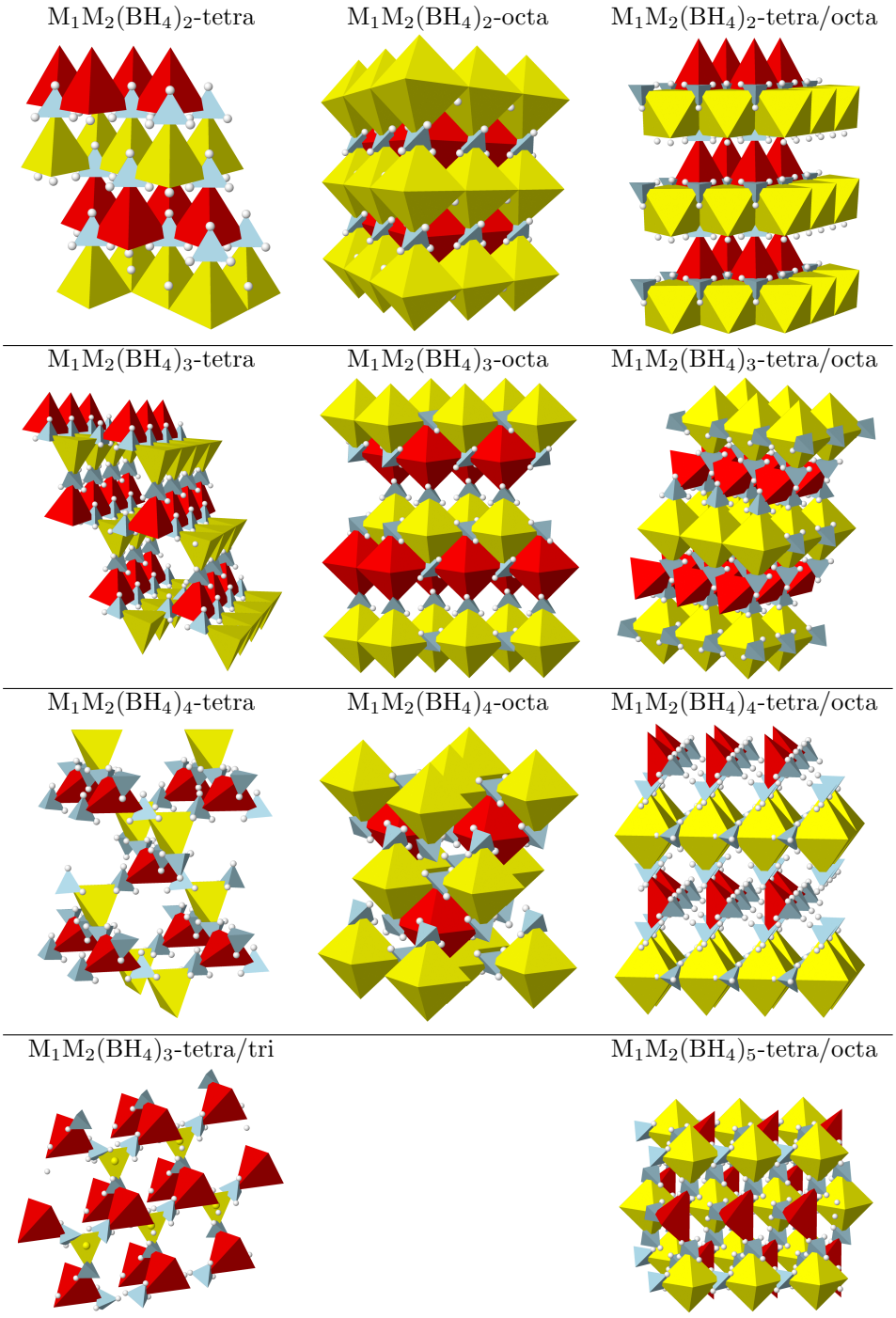

Figure 4.11: The template structures of $M_1M_2(BH_4)_{2-5}$. Red and yellow polyhedra show the coordination of the B atoms around the M_1 and M_2 atoms, respectively; blue tetrahedra represent the BH_4^- groups. The octa/tetra structures are obtained by switching M_1 and M_2 in the tetra/octa structures.

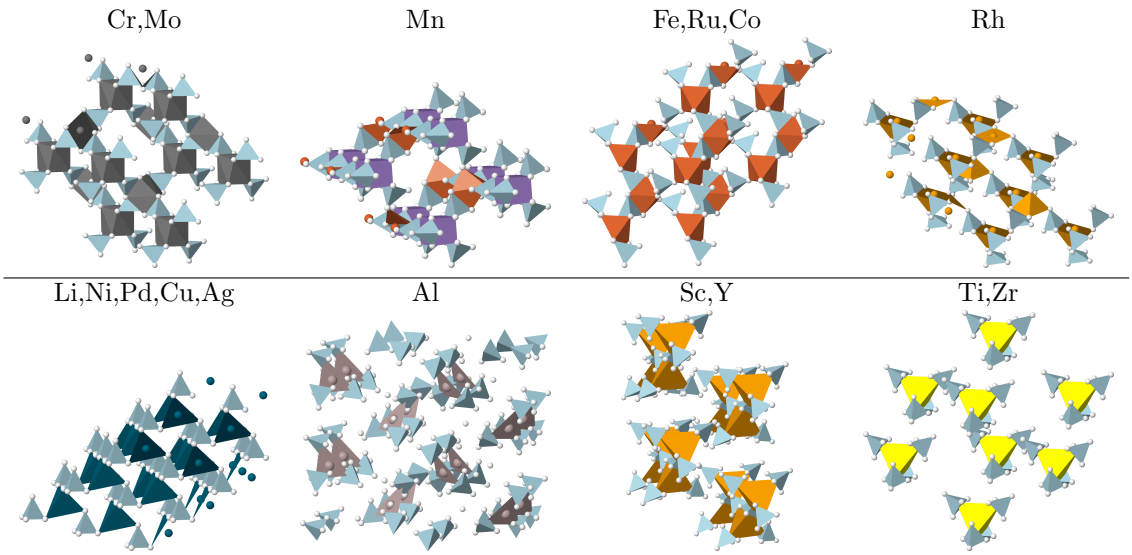

Figure 4.12: The structures used for calculating the binary reference energies. For Cr, Mo, Fe, Ru, Co, Rh, Li, Ni, Pd, Cu and Ag, the polyhedra show the coordination of the H atoms; the coordination of the $(BH_4)^-$ are tetrahedral in these structures. Besides the structures shown in the figure, the following templates were used: $M_1M_2(BH_4)_2$-octa for Na and K; and $M_1M_2(BH_4)_4$-tetra for Mg, Ca, V, Nb, Zn and Cd.

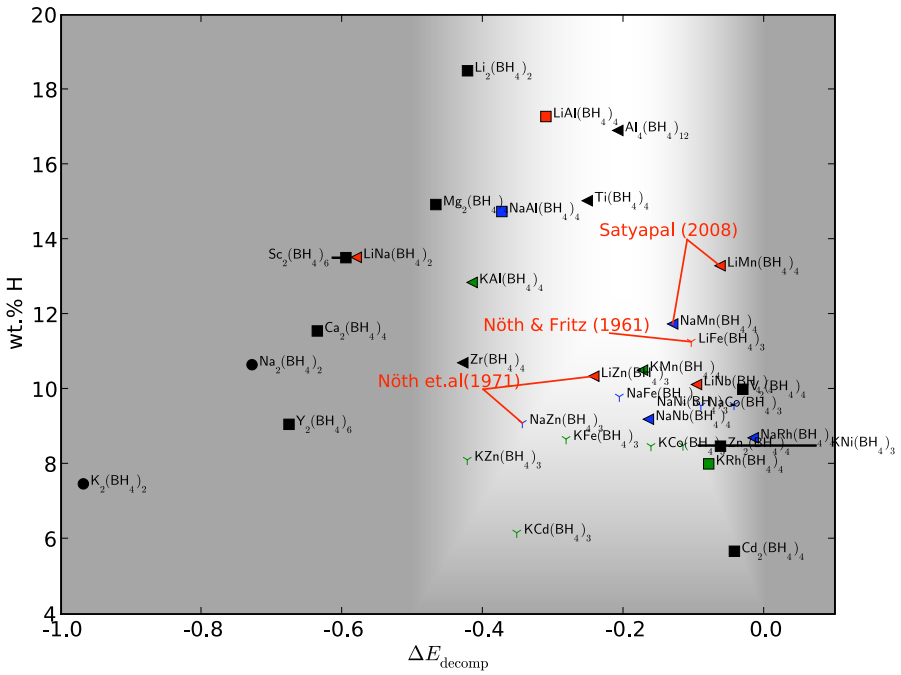

Figure 4.13: Stable ternary tetrahydroborates proposed from the screening study. The white area indicate the opti'mal window for the stability. Experimentally detected systems are indicated [4, 5, 6].

the alkaline earth metals) preferred the $I\bar{4}m_2$ structure, or slight variations of it. The reference structures when different from structures already shown are presented in Figure 4.12.

The goal of the screening study was to provide some candidates for mixed metal tetrahydroborate systems along with their estimated stabilities. In Figure 4.13 a plot show the systems predicted to be stable

Besides the candidate structures, the screening study provided valuable information about for instance binding in these systems and structural trends, and this information is still being processed. In the remaining part of this chapter, we shall see an example of how this can be used to do more advanced design of mixed systems.

4.5 Energy contributions

In order to be able to design stable mixed tetrahydroborate systems, we now consider the different energy contributions that determine the stability of a metal tetrahydroborate structure.

4.5.1 Metal–tetrahydroborate coordination

Probably the most important structural parameter that affects the stability is the coordination of BH_4^{-1} ligands to the metal. In the investigation of alkali and alkaline earth tetrahydroborates, we saw size effects play an important role. When moving to the smaller transition metals, the ligand repulsion becomes even more dominant, and all the systems are forced into a tetrahedral coordination or lower. On the other hand, for the metals large enough to obtain an octahedral coordination (K,Cs,Sr), the energy cost of going to a lower coordination is not that expensive (see Figures 4.5–4.10).

4.5.2 Tetrahydroborate–metal coordination

We have not performed a systematic investigation on the preferred coordination of metals around a BH_4^{-1} ions, but from all the structures calculated and found in literature, it seems that bridging tetrahydroborate ions prefer to connect bidentate to the metal, or correspondingly, via the edges of its hydrogen tetrahedron. Moreover, structures with a linear coordination seem to be preferred.

4.5.3 Metal–hydrogen coordination

Where the hydrogen coordination to the alkali and alkaline earth metals did not show any particular preferences (except for Li), beyond the simple electrostatic demand of maximizing H–H distances of different BH_4^{-1} ions, a trend is apparent for the mono- and divalent transition metals in Figure 4.12. The coordination number decreases when filling the *d*-band going from 8 for V, Nb, Cr, Mo through 7 for Mn, 6 for Fe, Ru, Co and 5 for Rh and 4 for Ni, Pd, Cu, Ag.

To investigate this further, metal hydride systems of the form MH_{1-3} have been calculated for M∈{Li,Na,K,Cs,Be,Mg,Ca,Sr,3d-metals,4d-metals} in structures with different hydrogen coordination of the metal. Most of the structures were also used for the halide systems, and they are all presented and their optimized energies are compared in Figure 4.14

For the monovalent Li, Ni, Pd, Cu, Ag we see from Figure 4.14b that a tetrahedral hydrogen coordination is either optimal or close to optimal, among the structures included in Figure 4.14a. This corresponds to the relaxed hydrogen coordination in the tetrahydroborate structures in Figure 4.12. The same holds for the divalent 3d transition metals, where the box coordination has the lowest energy until around Mn and Fe (Figure 4.14d), which is also here the shift happened for the tetrahydroborates. For the 4d metals the shift in the hydrides happens later than in the tetrahydroborates.

Interestingly, Cu and Ag seem to prefer a square planar coordination, and Cd and Zn a tetrahedral. A closer look at the $ZnBH_4$ structure Figure 4.15a, and at $CuBH_4$ in the quartz structure Figure 4.15b (where it has a lower energy), reveals that the metals also here seem to be have the same preferences.

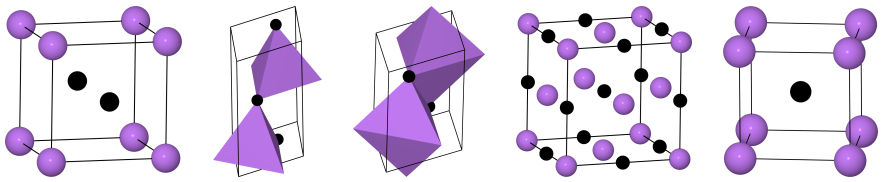

a) Structures for MH type metal hydrides.

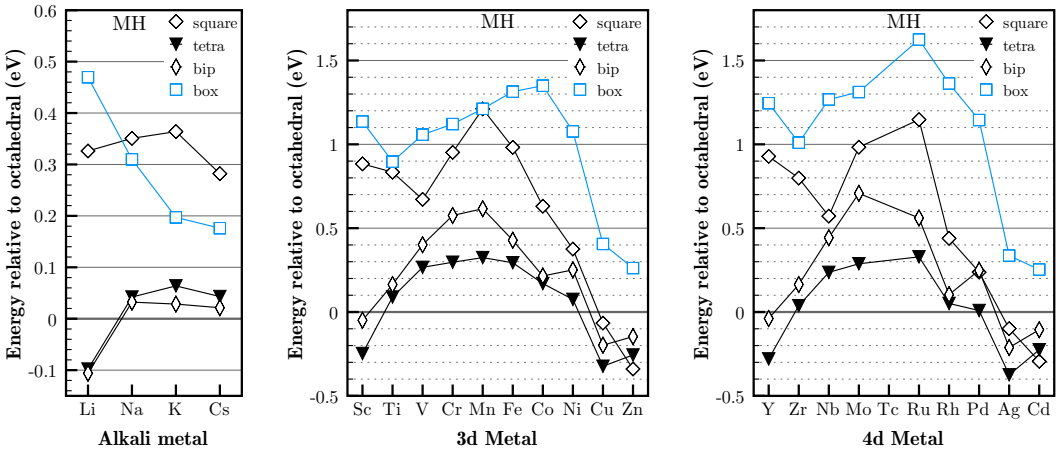

b) Relative energies of MH type metal hydrides.

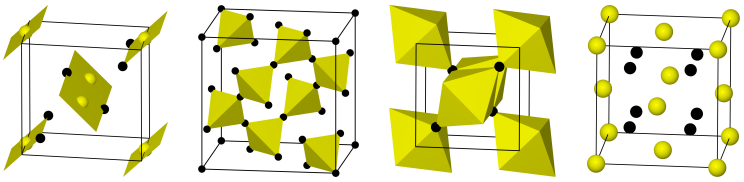

c) Structures for MH_2 type metal hydrides.

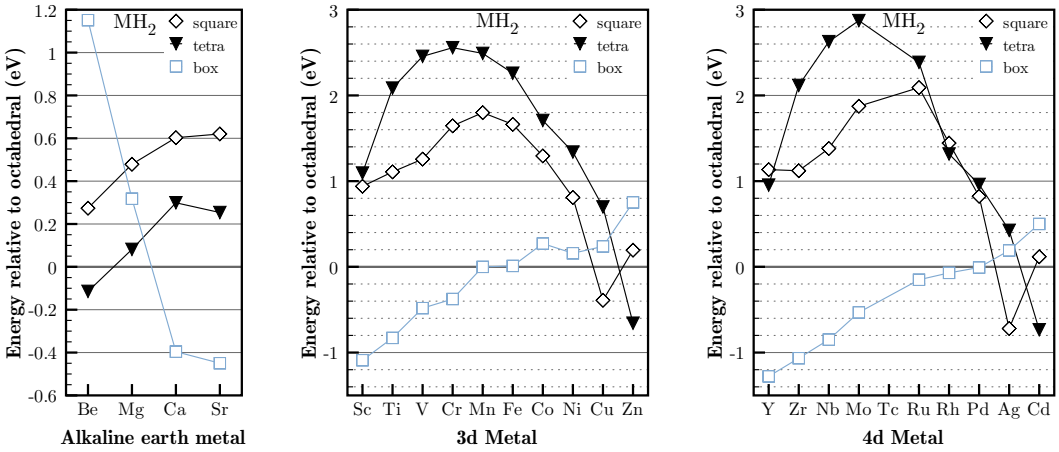

d) Relative energies of MH_2 type metal hydrides.

Figure 4.14: Structures and relative energies of metal hydrides.

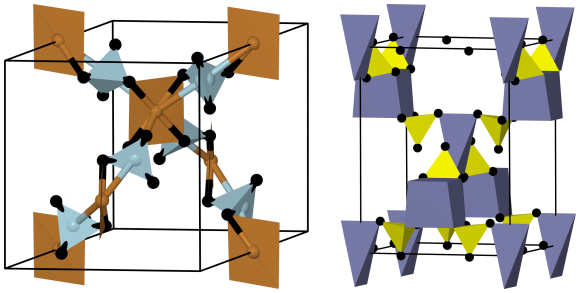

Figure 4.15: Hydrogen coordination for Cu and Zn tetrahydroborate: a) $Cu(BH_4)_2$ in the quartz structure obtain a square planar coordination; b) $Zn(BH_4)_2$ in the $I\bar{4}m_2$ structure forces a distorted tetrahedral H coordination for half the Zn atoms.

4.6 Advanced design

4.6.1 Polymeric tetrahydroborates

The insight gained was tested on a few systems to see if structures could be designed that had a lower energy than the previously used. Specifically, two polymeric structures and one layered structure was calculated for MBH_4;M∈{Li,Ni,Pd,Cu,Ag}. The structures are presented in Figure 4.16 together with an energy comparison that also includes the low- and high-temperature phase of $LiBH_4$, the simple tetrahedral and a tetrahedral where the hydrogen coordination is also tetrahedral (similar to the structure in Figure 4.11e).

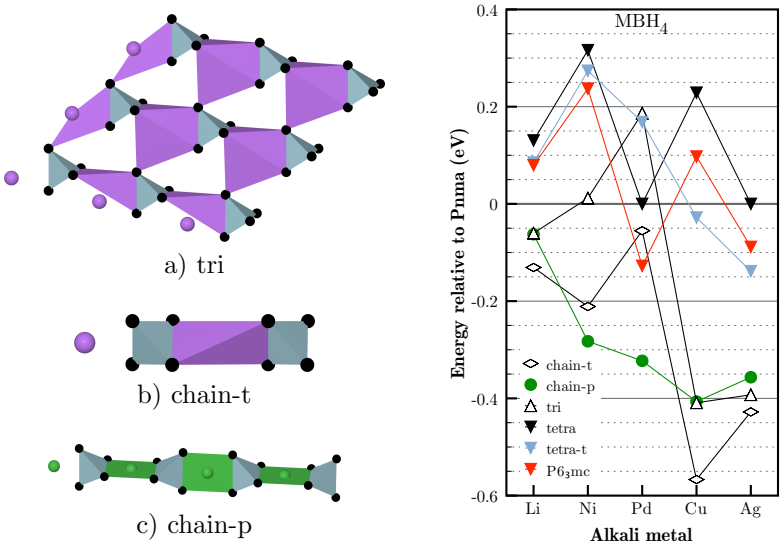

Figure 4.16: Low dimensional structures of Li, Ni, Pd, Cu, Ag mono tetrahydroborates designed to optimize H coordination. a) Trigonal structure with distorted trigonal bipyramidial H coordination; b) polymeric or chain structure with tetrahedral H coordination; c) chain with planar rectangular H coordination.

In the layered structure the metal has a trigonal planar coordination of the BH_4^{-1} ions, and a distorted bipyramidal coordination of hydrogen. In the two polymeric structures the BH_4^{-1} ions (and therefore also the metals) have a linear coordination of metals to which it connects

bidentately, giving the metal a tetrahedral hydrogen coordination in Figure 4.16b and rectangular planar hydrogen coordination in Figure 4.16b.

From the relative energies, that are plotted relative to the low-temperature *Pnma* structure of $LiBH_4$ we see that, with a few exceptions, all the designed structures have lower energies than the other. The polymer with tetrahedral hydrogen coordination gives the lowest energy for Cu and Ag, while for Ni and Pd the planar version is preferred. The Ni, Pd, Cu and Ag tetrahydroborates are still unstable, but the interest in these metals (especially Cu and Ni) relies on the ability to mix them with something lighter, and for that purpose it is important to know which structure they prefer.

Perhaps, most interestingly, the tetrahedral polymeric structure of $LiBH_4$ is about 0.15eV more stable than the experimental *Pnma* structure. Whether there actually exists a polymeric phase for $LiBH_4$ is left to answer. It could also mean that a bulk phase that is even more stable exists, or that we are missing something important here, like van der Waals interactions.

4.6.2 Building mixed systems

In this final section we present some examples on how the new insight can be used to design structures for mixed tetrahydroborates. All the structures presented have lower energies than the same systems in the structures used in the screening study described earlier, but are still in the borderline of being stable.

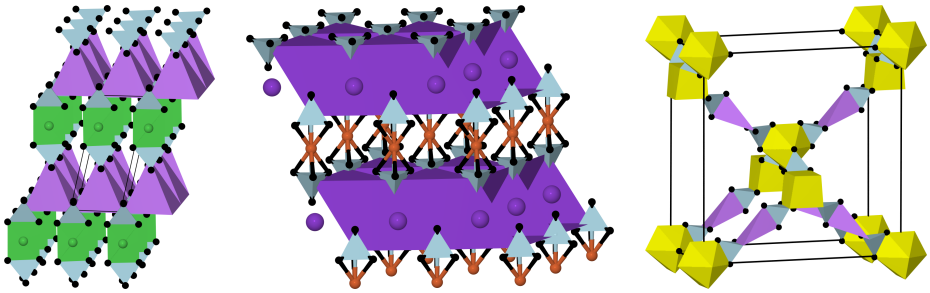

a) $LiNi(BH_4)_2$ b) $KFe(BH_4)_2$ c) $LiMg(BH_4)_3$

Figure 4.17: Mixed structures with linear coordination. a)-b) pillared layered structures of mixed monovalent tetrahydroborates; c) Li inserted in linear coordination in $I\bar{4}m_2$ structured $Mg(BH_4)_2$.

In Figure 4.17 we see the optimized structures of mixed systems, where the half the metals have a linear coordination. These are either functioning as pillars in pillared layers of monovalent coordination polyhedra (Figure 4.17a-b), or inserted in between half the corner-sharing tetrahedra in the $I\bar{4}m_2$ structure(Figure 4.17c). Besides optimizing the local coordination of in this case Ni, Fe and Li, the metal–boron distances can be relaxed independently for the two metals in the mix, which was shown in the screening study to be a critical demand to the mixed systems. For the pillared layer type structures (e.g. Figure 4.17a-b) one might suspect that they could show interesting features in terms of the ion-conduction. In a version where Li ions function as the pillars one could imagine that the Li ions could move rather freely between the layers.

As an example of a three component (metals) mixture, an optimized structure for $Li_4MgCr(BH_4)_8$ is presented in Figure 4.18. This structure is made by introducing a Li (and a BH_4^{-1}) in between all the shared corners of the tetrahedra in the $I\bar{4}m_2$ structure, and populating half the tetrahedra with Cr and the other half with Mg. In this way, each Cr has its preferred (or what we assume it prefers) box coordination of hydrogen, while each Mg atom has the hydrogen coordination similar to the one in the experimental low-temperature structure.

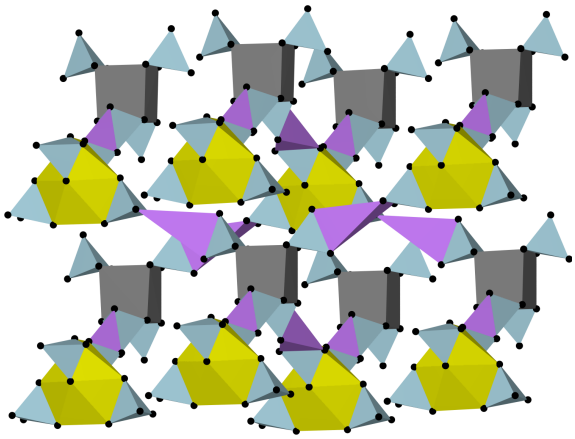

Figure 4.18: A stable ternary tetrahydroborate structure for $Li_2MgCr(BH_4)_8$ with preferred H coordinations for all metals. The structure is a folded version of the $I\bar{4}m_2$ structure of $Mg(BH_4)_2$ with half the Mg substituted by Cr and Li introduced between all tetrahedra.

5 Ammines

The metal ammine salts $M(NH_3)_xA_2$ were proposed as a promising solid form of hydrogen storage in 2005 [59], exemplified by $Mg(NH_3)_6Cl_2$ that store 9.1 wt.% hydrogen. As NH_3 is released the hydrogen storage is indirect and the storage needs to be combined with an ammonia decomposition catalyst, and since cracking the ammonia costs energy this lowers the onboard energy efficiency. Alternatively, the ammonia can be used directly in a solid oxide fuel cell[60]. The first use of the metal ammines that will be implemented in cars will also use the ammonia directly though not for energy storage but for cleaning the exhaust of diesel engines by the means of Selective Catalytic Reduction(see [61] and www.amminex.net).

The metal ammines have some favorable properties, the storage is completely reversible, the material can be compacted to obtain more than 95% of its theoretical volumetric densities, kinetics are fast, and macroscopic NH_3 transport is facilitated by the nanopores that evolve as the ammonia desorbes[62, 63]. Desorption of NH_3 happens in steps and for $Mg(NH_3)_6Cl_2$ the first step release 4 NH_3 molecules and then at elevated temperatures 1 NH_3 and finally the last NH_3 at a even higher temperature. The transition metal ammines of Mn, Fe, Co, Ni also follow this decomposition path, while Ca for instance store 8 NH_3 and go through a 8,4,2,1 sequence. The decomposition temperatures vary from metal to metal. (see for instance [64, 65]).

At the atomic scale ammonia is absorbed in a metal halide by a ligand substitution process. Bonds between the metal and the halide atoms are broken and substituted by bonds between the metal and ammonia molecules. In the different phases the metal atoms can be coordinated to both halide atoms and ammonia molecules or to ammonia alone. During absorption the crystal structure of a metal ammine is cut along certain directions, in some case taking it from a bulk structure to a layered structure, from a layered structure to a chain-like structure, or from a chain-like structure to isolated complexes. These layers, chains or complexes are kept together by hydrogen bonds between the positively charged hydrogen atoms of the ammonia molecules and the negatively charged halide ions.

In this chapter the calculations on the metal ammines systems are presented. The structures, stabilities and kinetics were investigated for the magnesium and calcium ammines, and the magnesium structures were used to calculate stabilities of ammines of Mn, Fe, Co, Ni and Ca, that were compared to experimental results. The ability of the model structures to reproduce experimental trends in stabilities for the known systems is used to search for improved materials.

Relative to an ideal storage system, the first desorption temperatures of $Ca(NH_3)_8Cl_2$ are too low while the last of $Mg(NH_3)_6Cl_2$ are too high, and mixed system were investigated to see if a compromise could be obtained. Ideally, one would prefer that all the ammonia desorb at once when the desired temperature is reached, as is the case for $Ba(NH_3)_8Cl_2$ (with 7 wt.%) and almost for $Sr(NH_3)_8Cl_2$ (with 8 wt.%, that goes through an 8,1 sequence), both systems desorb the ammonia at quite low temperatures however. This study do not include those systems, but future studies are planned that seek insight into why Sr and Ba have fewer desorption steps and to see if this behavior can be adopted by mixed systems

The slow absorption of ammonia in Ca ammines is seeked improved by fractional substitution of the anion.

Details of the magnesium system concerning desorption mechanisms, hydrogen positions and desorption via ligand exchange with water, are also included in this chapter.

5.1 Ammines of magnesium chloride

5.1.1 Experimentally observed structures

The stable phases observed when ammonia is introduced in magnesium chloride are $Mg(NH_3)_{1,2,6}Cl_2$. This can for instance be seen by measuring the ammonia released while gradually heating samples of the fully loaded salt, which show three peaks in a TPD spectrum (see included Paper I).

Experimentally observed structures have been reported for $Mg(NH_3)_{2,6}Cl_2$[66, 67], while the $Mg(NH_3)Cl_2$ structure is still unknown, however, the observed structure of the nickel analogue $Ni(NH_3)Cl_2$[68] is a good candidate, since $Mg(NH_3)_xCl_2$ and $Ni(NH_3)_xCl_2$ are isostructural for $x \in \{0, 2, 6\}$[66]. If we assume that the two are also isostructural for $x = 1$ the absorption can be explained as follows (Figure 5.1): the $MgCl_2$ layers, in which the Mg atoms are octahedrally coordinated to six Cl atoms, are cut into edge-sharing double octahedral chains of $Mg(NH_3)Cl_2$, in which each Mg is coordinated to five Cl atoms and one NH_3 molecule; in the next step the $Mg(NH_3)Cl_2$ chains are cut into edge-sharing octahedral chains of $Mg(NH_3)_2Cl_2$, where the coordination octahedra are formed by four Cl atoms and two NH_3 molecules; in the final transition the $Mg(NH_3)_2Cl_2$ chains are stretched to the extent that the Cl atoms loose their coordination to the Mg atoms, that then become coordinated to six ammonia molecules. Strictly speaking the chain structure has disappeared in the fully loaded salt and the structure can be viewed as $(Mg(NH_3)_6)^{2+}$ complexes situated in the body centered position of every second cell of a cubic lattice of Cl atoms (see [69];a sideview can be seen in Figure 5.13); however, it can be useful to retain the chain picture when considering the transition between the di- and hexaammine phases.

5.1.2 Model structures

We have based our model of the $Mg(NH_3)_xCl_2$ system on the experimental structures of $Mg(NH_3)_{0,2,6}Cl_2$ and $Ni(NH_3)Cl_2$. For $Mg(NH_3)_{0,2,6}Cl_2$ the model structures are identical to the experimental ones; for $Mg(NH_3)Cl_2$ we have used a simpler arrangement of the double octahedral chains, which we found gave no significant energy difference. The positions of the hydrogen will be dealt with later in this chapter. An end view and a 3D view of the model structures for the full cycle is shown in Figure 5.1. The structure shown for $MgCl_2$ is actually the $MgBr_2$, which has a simpler stacking of the layers. In some calculations the $MgBr_2$ were used for practical reasons (to obtain a orthorhombic unit cell) but the energy difference of the different stacking is not significant, except for $NiCl_2$ in a spin-polarized calculation, where the $MgCl_2$ gave a lower energy and therefore was used. All calculations involving Mn, Fe, Co, or Ni were done spin-polarized.

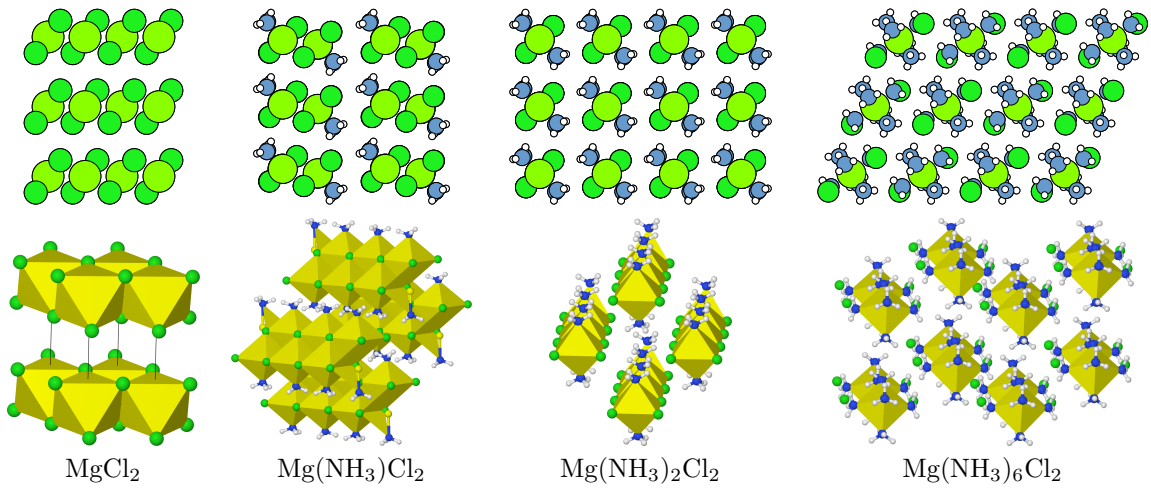

Figure 5.1: End-view and 3D of $Mg(NH_3)_xCl_2$ structures.

5.2 Ammines of calcium chloride

5.2.1 Experimentally observed structures

The $CaCl_2$ salt can store op to eight mole ammonia and stable phases are observed for $Ca(NH_3)_{1,2,4,8}Cl_2$[65, 64]. We have only found one article reporting experimental structures of calcium ammines, and they were only able to characterize the structures for $Ca(NH_3)_{2,8}Cl_2$[70]. They report a layered structure for $Ca(NH_3)_2Cl_2$, and the final $Ca(NH_3)_8Cl_2$, six NH_3 molecules surround a Ca atom in a trigonal prismatic coordination, and two NH_3 molecules are kept in between the complexes. We turn to the model structure to complete the cycle.

5.2.2 Model structures

We have calculated $Ca(NH_3)_{2,8}Cl_2$ in the experimental reported structures. For the monoammine, we considered the transition from $Ca(NH_3)_{2-0}Cl_2$ and applied the principles known from the $Mg(NH_3)_xCl_2$ cycle, and came up with a realistic guess of what the monoammine structure might be, by removing half of the ammonia and connecting the layers. The $CaCl_2$ structure is then directly obtained by applying the same principle and removing the ammonia from the monoammine layers and connecting the layeres.

The $Ca(NH_3)_4Cl_2$ structure is harder to predict since the transition from $Ca(NH_3)_{8-2}Cl_2$ is not obvious. A large number of candidate structures for $Ca(NH_3)_4Cl_2$ was calculated, the best turned out to be structure with isolated complexes (see Figure 5.2).

In summary the cycle we propose is (see Figure 5.2): The bulk structure of $CaCl_2$, is cut into layers of $Ca(NH_3)Cl_2$, that are cut once more into layers of $Ca(NH_3)_2Cl_2$. As for the magnesium analogue each Ca atom go from being octahedrally coordinated to six Cl atoms, through five Cl and one NH_3 to four Cl and two NH_3 molecules. The diammine layers are cut into to complexes of $Ca(NH_3)_4Cl_2$ containing four NH_3 and two Cl in a octahedron, that are expanded to give room for two NH_3 around the Ca in a trigonl prismatic coordination an two NH_3 between the complexes.

The experimental structure for $Ca(NH_3)_8Cl_2$ contains four f.u. or 130 atoms and calculations get very heavy. We have therefore created some simpler model structures containing only one f.u. that mimic the local coordination of the experimental one. Energy differences are 0.11eV and 0.06eV (see Figure 5.3).

Finally, the calcium systems in $Mg(NH_3)_xCl_2$ structures were calculated, and the energies was compared to the ones of the Ca structures. And it turns out that the two dangling NH_3 are only bound by 0.03eV per NH_3. The too low binding is supposedly due to the fact that we ignore van der Waals forces.

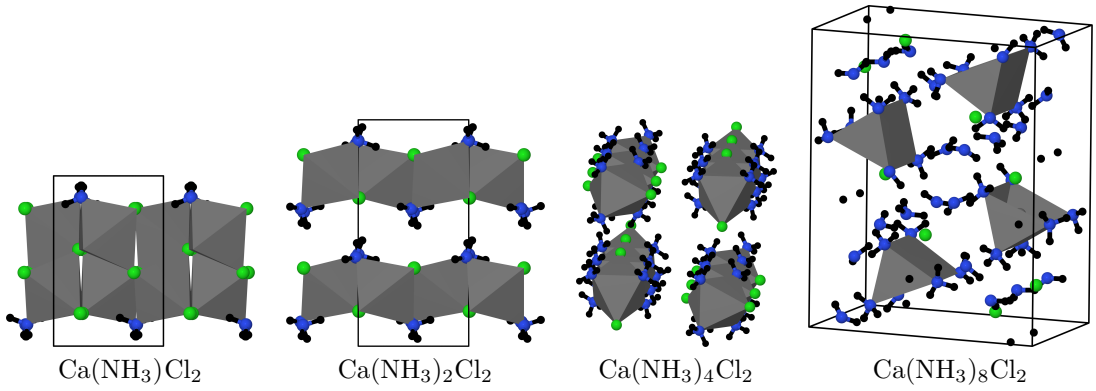

Figure 5.2: Structures for $Ca(NH_3)_xCl_2$. Only di- and octaammine are reported in experiments.

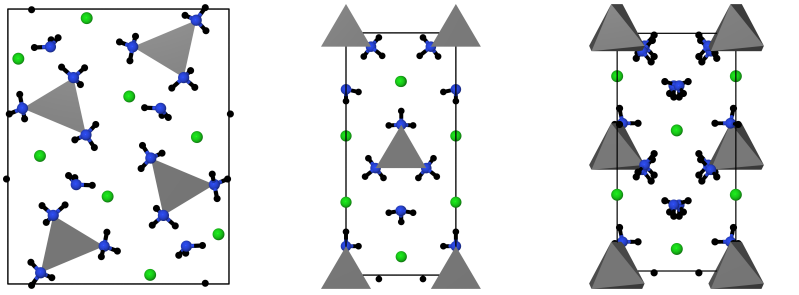

Figure 5.3: End-view of experimental and two model structures of $Ca(NH_3)_8Cl_2$

5.3 Modeling desorption enthalpies of metal ammines

5.3.1 Setup

Metal ammines of the form $M(NH_3)_{0,1,2,6}Cl_2$;M∈{Mg,Ca,Mn,Fe,Co,Ni} were modeled using the structures for $Mg(NH_3)_xCl_2$ presented in Section 5.1.2, and the $Ca(NH_3)_{0,2,4,8}Cl_2$ structures from Section 5.2.2 for calcium as well. For each system an initial guess was constructed by replacing Mg with the metal at hand and scaling distances according to ionic radii obtained from previous studies. The structure was relaxed by a initial relaxation of the internal degrees of freedom, followed by a proportional scaling of the unit cell, and a final relaxation of the internal degrees of freedom. Electronic energies were calculated with a kinetic energy cutoff of 350eV, a density cutoff of 700eV and a Brioullin zone sampling of approximately 15 k-points per $Å^{-1}$ in each direction. Molecular NH_3 was modeled by a Γ-point calculation of a single molecule in a 10Å×10Å×10Å vacuum box.

5.3.2 Results

The structures did not change much during the relaxation. To estimate the desorption enthalpies one measures in a TPD experiment, we calculated the binding energy per NH_3 when going from one phase to the next, as the energy differences between the two phases including the required number gas-phase NH_3 for the one with lower ammonia content. The binding energies are compared to experimental desorption enthalpies in Figure 5.4.

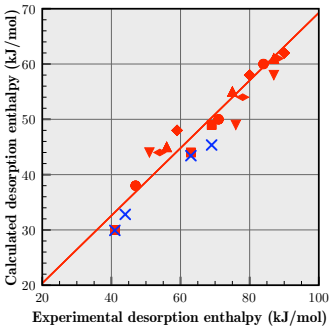

Figure 5.4: Calculated binding energies of NH_3 vs experimental desorption enthalpies for Mg, Ca, Mn, Fe, Co, Ni in the $Mg(NH_3)_xCl_2$ structures. Blue points are the Ca energies as calculated in its own structures.

Apparently, the calculations are able to describe the trends in the desorption enthalpies for this range of materials. As in the case of the binding energies of the halides systems treated earlier, the slope of the line is too low, and the deviation from the experimental value increases with the

binding energy. Also here, we have done some attempts at including van der Waals interaction[32], and this seems to give quantitive agreement with experiments; however, a lot more testing is needed before we can say if these results can be trusted.

In Figure 5.4 the calculation of the binding energies in the calcium ammines using the experimental structures are included as blue points, and except for the last step they do not add anything new. The 8→4 energy is captured by the 6→2 energy in the Mg type structures, the 2→1 energies are also close while the energy for the 1→0 transition is somewhat larger in the Mg model but closer to the best fit. It seems that using the Mg type structures to calculate binding energies in Ca based ammines, is a reasonable approximation.

5.4 Screening of mixed metal ammines

5.4.1 Setup

Metal ammines of the form $M_1M_2(NH_3)_{0,2,4,12}Cl_4$;$M_1 \in$\{Mg,Ca\};$M_2 \in$\{Mg,Ca,Mn,Fe,Co,Ni\} and of the form $M_2(NH_3)_{0,2,4,12}Cl_xA_{4-x}$;M$\in$\{Mg,Ca\};A$\in$\{F,Br,I\};$x \in$\{0,2,3\} were modeled using the structures for $Mg(NH_3)_xCl_2$ presented in Section 5.1.2. For each system, an initial guess was constructed by replacing Mg or Cl with the metals or halide atom at hand and scaling distances according to ionic radii obtained from previous studies. To minimize the stress in the mixed structures we using the mixing schemes illustrated in Figures 5.5 and 5.6. Each structure was relaxed by a proportional scaling of the unit cell, followed by a final relaxation of the internal degrees of freedom. Electronic energies were calculated with a kinetic energy cutoff of 350eV, a density cutoff of 700eV and a Brioullin zone sampling of approximately 15 k-points per $Å^{-1}$ in each direction. Molecular NH_3 was modeled by a Γ-point calculation of a single molecule in a 10Å×10Å×10Å vacuum box.

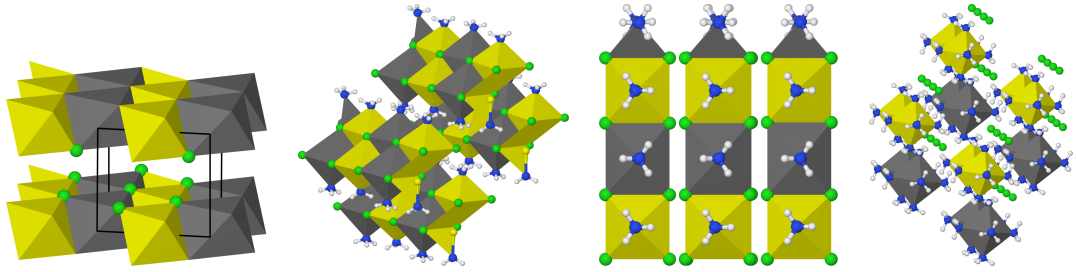

Figure 5.5: Structures of metal mixed ammines.

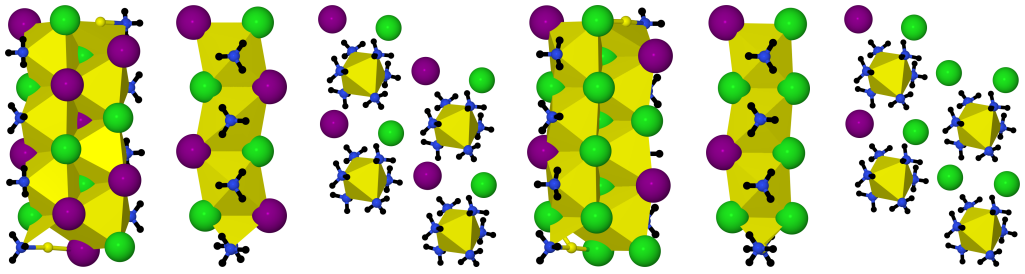

Figure 5.6: Structures of anion mixed ammines. The metal halide mix can be deduced from the monoammine chains by removing the ammonia and connecting multiple chains.

5.4.2 Results

We have calculated the energy gain or loss by mixing the metals and anions in the ammine systems. This mixing energy per f.u. is plotted in Figure 5.7.

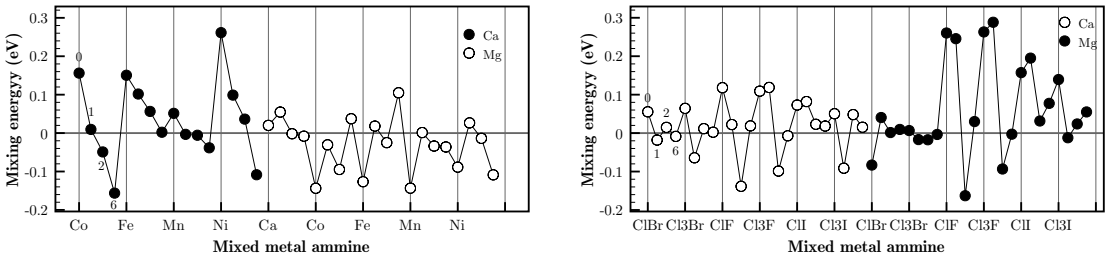

Figure 5.7: Mixing energies of mixed ammines

The mixing energies in Figure 5.7 show large variations which could mean that more optimal structures exists for some of the mixtures. Most of the hexammine systems (i.e. the last points before a vertical line) and the diammine systems (the next-to-last points before a vertical line) are following each other in terms of the mixing energy, and so calculating the first desorption energy might give precise values. Many of the CaM mixtures are unstable, but for these systems the real structures the system would choose might be very different owing to the different structures of the pure Ca ammines. The Mg type structures could however still give reasonable values for the binding energies.

To get an estimate of the experimental desorption enthalpies we use the fit from the pure systems in Figure 5.4. Estimates of the desorption enthalpies for all three steps of each mixed system are presented in Figures 5.8 and 5.9 together with the experimental desorption enthalpies of the pure systems.

The shaded areas represent quality criteria, and the points should preferably fall in the central white area. If the points move into the blue area, the material needs to be cooled down to keep the ammonia from desorbing, and if the points move into the red area excess heat is needed to release the ammonia. Of the values chosen here, the low limit corresponds roughly to a release temperature of 10°C and the high limit to 230°C. In real life, the real values one will choose for these limits will depend on the situation. If the priority is high safety a higher value for the lower limit is chosen, and if the priority is energy efficiency (or economy) a lower value for the higher limit is chosen. Ideally, one wants to lower the high limit without affecting the lower limit, but as can be seen from Figures 5.8 and 5.9, this might not be so easy. A few mixed systems look interesting though, MgMn,MgFe,MgCo,CaFe$(NH_3)_{12}Cl_4$ and perhaps $Ca(NH_3)_6Br_2$, $Mg_2(NH_3)_{12}Cl_3F$.

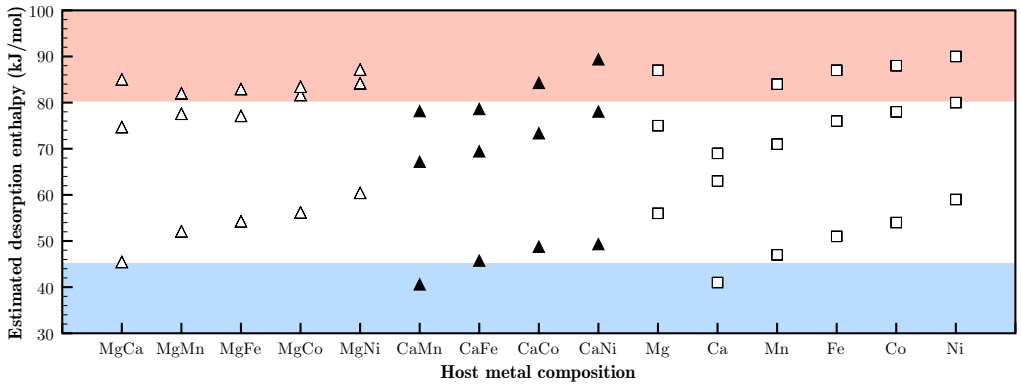

Figure 5.8: Estimated desorption enthalpies of metal mixed ammines.

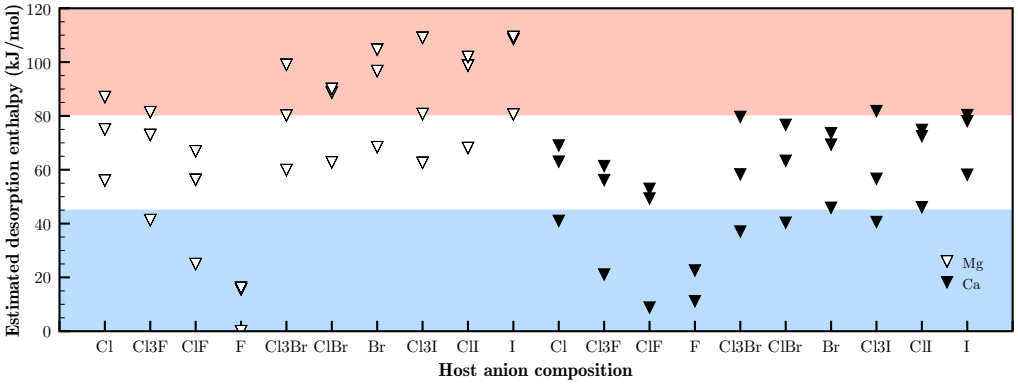

Figure 5.9: Estimated desorption enthalpies of anion mixed ammines.

Comparing the enthalpies of the mixed metal systems with the pure systems in Figure 5.8, it seems that the mixed enthalpies to some extend are averages of the enthalpies of the two pure systems they are a mix of. The same seems to be the case for when mixing the anions in Figure 5.9. This relation is investigated further in the next section.

5.5 Stability trends

5.5.1 Electronegativity

To understand the binding energy we shall try to separate and asses the different contributions. We assume that the binding energy of a NH_3 in a metal ammine can be described as

$$E_{bind} = E_{M-NH_3} + E_{H-A} - E_{A-M}. \tag{5.1}$$

The binding terms are the binding between ammonia and the metal and the hydrogen bonds between the NH_3 and the anions. When an ammonia molecule desorbs, an anion takes its place in the coordination to the metal atoms thereby stabilizes the final state. This consequently lowers the binding energy with E_{A-M}. We saw earlier (Figure 3.15) that the strength of the metal–anion bond increases with the electronegativity difference, so the binding energy of NH_3 could be expected to decrease with the electronegativity difference. This is confirmed in Figure 5.10 where the desorption enthalpy of the first and the last steps are plotted against the squared electronegativity difference.

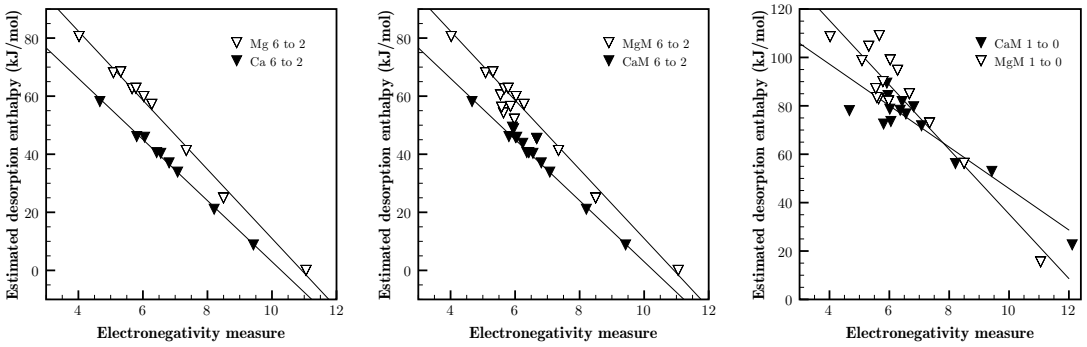

Figure 5.10: Estimated desorption enthalpy vs the squared electronegativity difference of metal and anion for the mixed metal ammines. Left: 6 to 2 transition for anion mixtures; Center: as left but including metal mixtures; Right: As center but for 1 to 0 transition.

The Mg and Ca systems (Figure 5.10a) show clear linear relations between E_{bind} and the electronegativity measure. The lines are not the same due to the remaining terms in Equation 5.1, and when mixing with other metals (Figure 5.10b) these points fall on different lines between the two (not drawn).

Of the remaining terms the energy of the hydrogen bonds between the NH_3 and the anions has been calculated by comparing the energy of a bulk structure of an ammine with the energy of a single chain of the ammine in vacuum. For ammines where the anion was chlorine, this calculation was done for all the pure systems, and the binding between the chains per NH_3 showed very small variations (0.03eV) around an average value of 0.236eV or roughly 0.1eV per hydrogen bond (each ammonia is making two hydrogen bonds in the ammine structures). The binding between chains of ammines with F, Br and I was only calculated for Ca and Mg ammines, and the result was 0.08eV per hydrogen bond for F and I, and for 0.1eV per hydrogen bond for Br. In conclusion, the hydrogen bond is roughly 0.1eV in all the ammines and the E_{H-A} term in (5.1) is constant.

The last contribution to the binding energy is the bondstrength of the metal–ammonia bond. While this can be estimated by removing an ammonia from the ammine and calculating the energy, we will instead assume that it is constant for the hexaammines with the same metal. A difference in bondstrength between Mg–ammonia and Ca–ammonia will shift one of the lines with respect to the other, which is what we observe in Figure 5.10a. The slight difference in slopes of the lines is also present in Figure 3.15, in which the lighter elements of a group have a steeper slope.

5.6 Kinetics and desorption mechanism

5.6.1 Desorption principles

As a starting point in trying to understand why some metal ammine salts show very fast ab- and desorption kinetics and others do not, we discuss different possibilities on what mechanisms that could take place at the atomic scale. We focus on the desorption and the magnesium ammine as a prototype system.

From the end-view of the $MgCl_2$ layers and the $Mg(NH_3)_{1,2,6}Cl_2$ chains in Figure 5.1, it seems that going from one phase to the next can happen in a very continuos way. In each decomposition step, ammonia molecules are removed, Mg–Cl bonds are formed and no major restructuring is needed. A demand for this picture to be valid, is that only the ammonia of one side of a chain is removed. Calculations where half the NH_3 molecules was removed from a $Mg(NH_3)_2Cl_2$ chain in vacuum, both from the same side and from opposite sides of the chain, showed that it is preferred to remove the ammonia from one side of the chain. Another demand is that the ammonia can be transported out of the crystal. For now, we assume that diffusion of ammonia along the chains can happen readily, i.e. a NH_3 molecule can jump from one Mg atom to the next with no significant barrier.

An important question arises – what happens with the under-coordinated Mg atoms left behind? If we consider for instance the $Mg(NH_3)_{2\rightarrow1}Cl_2$ transition, we know that eventually the Cl^- ions from a neighboring chain will take the place of the ammonia that was removed, and complete the octahedral coordination of the Mg atom, but in this picture, that first happen when all the NH_3 molecules have been removed from both chains. The energy cost of creating an ammonia vacancy is significant, (around 0.8eV in the diammine) and any intermediate state involving many under-coordinated Mg atoms is unlikely. Either the chains are very short or something else happens. In the case of long chains, the under-coordination of Mg must be dealt with along the way, so that the energy cost of creating the intermediate state, does not build up and scale with the length of the chain.

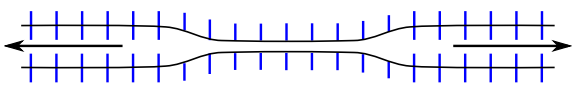

Figure 5.11: Principle of diammine chain combination in the center of the material as NH_3 molecules (blue lines) between the two chains diffuses out in both directions.

One solution could be that the chains combine when a critical number of NH_3 molecules are removed. If this is happening while conserving the bulk structure, the chains need to combine inside the crystal, since the ammonia is emptied from the inside by bulk diffusion. One could imagine the combination of two diammine chains took place like illustrated in Figure 5.11. A conceptual problem with this picture, is perhaps, that the desorption of a NH_3 molecule happens at the surface, while the combination of the vacancies (i.e. the under-coordinated Mg atoms) happens in the center of the material; the vacancies need somehow to be "synchronized". In the next section we will see a similar suggestion for a desorption mechanism, but in that case the combination of chains happens at the surface, simultaneous with the desorption of the NH_3 molecules.

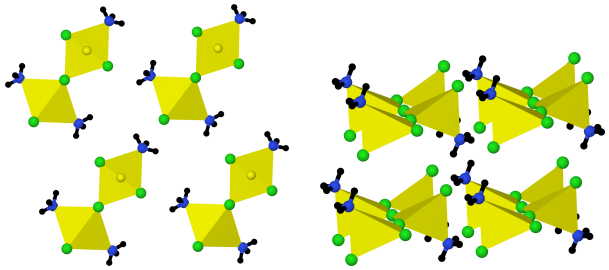

Figure 5.12: Possible intermediates of the $Mg(NH_3)_{2\rightarrow1}Cl_2$ transition: a) A half-empty chain completes its octahedra by combining with the edge of full chain. When the other chain desorbs half of its ammonia, the two chain combine into the final monoammine chain by rotation along the shared-Cl axis; b) the chains transform into a tetrahedral coordination.

Completely different mechanisms could be possible. An intermediate state, in which two chains combine as the ammonia is removed from one chain and forme metastable $Mg(NH_3)_3Cl_2$ chains (Figure 5.12a), or a restructuring of a single chain that transform the incomplete coordination octahedra into complete tetrahedra (Figure 5.12b). All the considered mechanisms rely on bulk diffusion of ammonia to happen at the temperatures considered. We now look into this subject in more details.

5.6.2 Bulk diffusion or surface reaction

In previous work, barriers for diffusion of NH_3 along the chains of $Mg(NH_3)_{1,2,6}Cl_2$ were calculated. An example of diffusion in $Mg(NH_3)_6Cl_2$ is given in Figure 5.13. While the diffusion barrier in $Mg(NH_3)_xCl_2$ was close to the experimental desorption enthalpy, barriers in $Mg(NH_3)_{1,2}Cl_2$ initially turned out too high in the calculations.

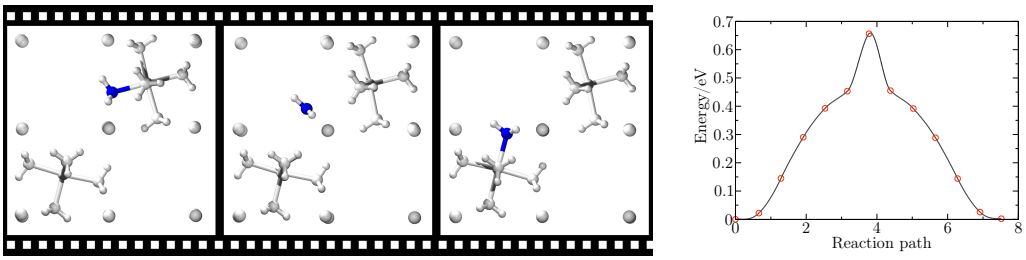

Figure 5.13: Ammonia diffusion in $Mg(NH_3)_6Cl_2$, showing initial, transition and final state. The barrier at the right also contain the intermediate images.

An alternative mechanism for desorption and absorption, that did not rely on bulk diffusion of NH_3 was sought. To that end, the binding between the $Mg(NH_3)_nCl_2$ chains was considered. The chains are kept together by hydrogen bonds between the hydrogen of NH_3 and the Cl^- ions,

each NH_3 molecule binding with two if its hydrogen. Since the energy of the hydrogen bonds are close to 0.1eV, per NH_3 this gives 0.2eV, which is significantly smaller than the diffusion barriers ranging from 0.6-1.2eV.

In [65] (included Paper I) the proposed mechanism for desorption was a surface reaction, where chains of the material give up their hydrogen bonds and are released from the surface. Ammonia can be released directly from a chain into the atmosphere, and two chains can freely combine, while the ammonia is being released. The intermediate state is a free chain of the final ammine, or rather free chains, that subsequently connects through hydrogen bonds into clusters and eventually the bulk structure of the final ammine. A similar mechanism could happen during absorption and the full cycle is illustrated in Figure 5.14.

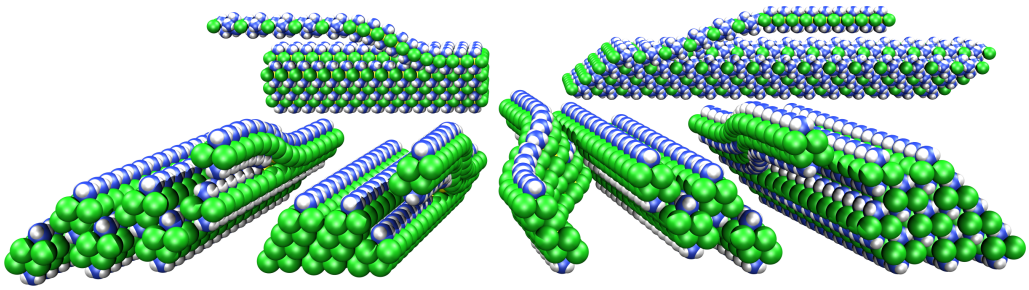

Figure 5.14: Proposed alternative mechanism for NH_3 absorption to the left, and desorption to the right in $Mg(NH_3)_xCl_2$ type ammines.

We did not ruled out bulk diffusion in these systems yet, and more detailed investigations were performed searching for lower diffusion barriers. There are different possibilities to search; for the $Mg(NH_3)_{1,2}Cl_2$ systems, a slight expansion of the crystal making the distance between the chains larger making and more room for the diffusing ammonia could decrease the barriers. Also, we have mentioned the van der Waals interaction some times now, and including it here might stabilize the transition state in the diffusion event, where the NH_3 has completely given up its bond to the Mg and is only bound by hydrogen bonds to the Cl^- ions. It is not unlikely that the electrostatic nature of the van der Waals forces could have a relatively large effect on the hydrogen bonds, and therefore stabilize the transition state, and ultimately lower the diffusion barrier.

In the included Paper V we found that for $Mg(NH_3)_1Cl_2$ and $Mg(NH_3)_2Cl_2$ distortion of the unit cells not only lowered the energy but significantly lowered the barriers for diffusion, to the point where they become comparable to the binding energies of ammonia, as was the case for $Mg(NH_3)_6Cl_2$. This meant that ammonia transport in and out of the systems could be dominated by bulk diffusion after all. However, as explained in Section 5.6.1 low diffusion barriers is a necessary but not sufficient condition for a bulk diffusion mechanism, but combined with intermediate states like e.g. shown in Figures 5.11 and 5.12 this could be realistic.

5.6.3 Desorption enthalpies revisited

In [65] the chain model from Figure 5.14 was also used to calculate hypothetic non-equilibrium desorption enthalpies, where the desorption reaction was treated as going from the bulk initial phase (for instance bulk $Mg(NH_3)_6Cl_2$) to the final phase as free chains (correspondingly the free $Mg(NH_3)_2Cl_2$ chains). Instead of calculating binding energies as the difference in stabilities of the bulk initial and final phases, we calculated the stability difference between the initial bulk phase and the final phase as a single chain in vacuum. Since the final phase essentially had been destabilized this gave higher calculated desorption enthalpies as shown in Figure 5.15.

Whether this is a realistic way to calculate desorption enthalpies, is doubtful. The experiments indicate that during desorption the initial and final phases are actually in equilibrium. More likely, this is related to the van der Waals interaction as mentioned earlier. Excluding the hydrogen bonds in the final state corresponds to counting them twice when determining the binding energy of ammonia. Effectively the strength of the hydrogen bonds are increased which is what you also might expect if the van der Waals interaction was included instead.

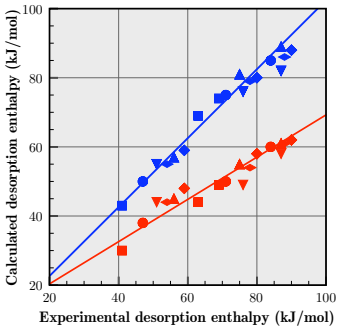

Figure 5.15: Calculated binding energies of NH_3 vs experimental desorption enthalpies for Mg, Ca, Mn, Fe, Co, Ni in the $Mg(NH_3)_xCl_2$ structures. Red: initial and final structure: bulk; Blue: inital structure: bulk, final state: chain in vacuum

5.6.4 Slow calcium, layers and chains

Absorption of ammonia in $CaCl_2$ is very slow, while the Mg,Mn,Fe,Co and Ni ammines show fast absorption kinetics, and the reason might be very simple considering their structures. The $CaCl_2$ structure is bulky compared to the layered structure of $MgCl_2$ and, whether or not, the surface reaction in Figure 5.14 is realistic for the layered metal chlorides, we know that eventually the layers need to be cut into chains.

For $CaCl_2$, the bulk structure has to be cut into layers of the monoammine, that then need to be cut once more into layers of diammine, and it is first when going to the $Ca(NH_3)_4Cl_2$ that the layers are cut into chains (see Figure 5.2). It seems logical that cutting a bulk structure (or a layer) into layers is kinetically slower than cutting a layer into chains. Both can happen by a zipper-like process, so to speak, but in the former case this a two dimensional zipper and in the latter a one dimensional zipper.

If the slow absorption kinetics in calcium ammines truly is caused by this structural difference, one might improve the kinetics by adding dopants that can make the layered structure preferred for the empty salt. As can be seen from Figure 3.5 the energy difference between the oCaCl2 and the layered oMgBr2 is very small for $CaCl_2$ in favor for the $CaCl_2$ structure in agreement with the observed. For CaI_2 it is the opposite way around (actually also for $CaBr_2$, but this is in disagreement with the experiments) and we therefore chose iodide as a dopant.

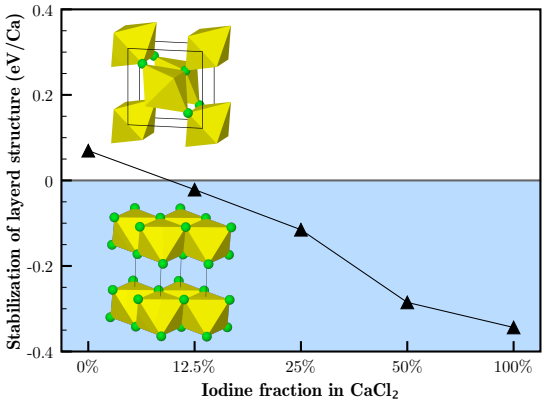

Figure 5.16: Stabilization of layered structure by doping $CaCl_2$ with iodide.

In Figure 5.16 the energy of the layered structure is plotted relative to the energy of the bulky $CaCl_2$ structure, for different fractional substitution of Cl with I. According to the calculations

around 10% iodide is enough to make the shift, which only reduces the gravimetric density from 9.8% to 9.1%.

5.7 Hydrogen positions

5.7.1 Rotation of ammonia and order/disorder transitions

In all the $Mg(NH_3)_{1,2,6}Cl_2$ structures, each NH_3 molecule points the N towards the Mg and the three H atoms towards a rectangle of Cl atoms. As mentioned, the H are positively charged and are attracted to the negatively charged Cl^- ions, and hydrogen bonds are formed, but there is a mismatch between the three H and the four Cl, so each NH_3 can only form hydrogen bonds with two of its H at a time connecting them to an edge of the Cl rectangle. The mismatch leads to disorder in the hydrogen positions, and at ambient temperatures, the NH_3 are rotating around the non-directional Mg–N bond, jumping from edge to edge of the Cl rectangles. At low temperatures one generally observe a transition to an ordered phase[71, 72, 73].

In the ordered phase of $Mg(NH_3)_2Cl_2$ the ammonia molecules are oriented as shown in Figure 5.17a[73]. Besides minimizing the repulsion between the H of neighboring NH_3 on the same side of a chain, energy is gained by making the Cl rectangles around half the Mg shorter along the direction of the chain. The Cl edges that are shortened are the ones towards which only one H are pointing, and the shorter H–Cl distances creates two new hydrogen bonds. (or two half in terms of energy). We have calculated the energy difference between the ordered and the disordered phase of $Mg(NH_3)_2Cl_2$ and it was 0.01eV per NH_3, which is the same as the energy of a hydrogen bond.

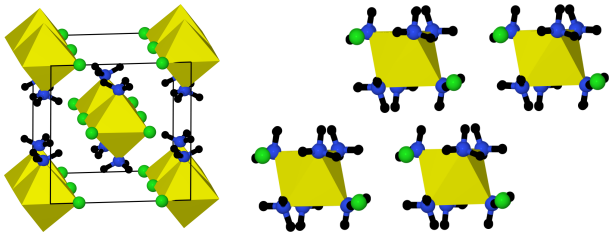

Figure 5.17: Ordered low-temperature structures of $Mg(NH_3)_2Cl_2$ and $Mg(NH_3)_6Cl_2$.

For $Mg(NH_3)_6Cl_2$ the transition to an ordered phase involves more restructuring and the space-group changes to a hexagonal type. Since this is all the experimental information that is available, we have searched for a low temperature structure. One can expect an energy gain of 0.06eV per f.u. corresponding to a hydrogen bond per NH_3 in $Mg(NH_3)_6Cl_2$. We did find a structure where all H were making hydrogen bond with Cl atoms, and the energy difference was correspondingly 0.06eV per f.u.. The ordered structure is shown in Figure 5.17b; more details can be found in the included Paper V.

While these small energy differences is not that important for the calculated desorption enthalpies, the structural differences can impact calculated diffusion barriers as we show in the included Paper V.

5.7.2 Vibrational spectra

In unpublished work the vibrational spectra of the $Mg(NH_3)_{6,2,1}Cl_2$ systems was recorded during the decomposition of $Mg(NH_3)_6Cl_2$. It turned out that the vibrational spectra were all very much alike, which is perhaps not surprising since the local environment of the NH_3 molecules are similar in the three phases. We calculated vibrational spectra for all the phases and they were all similar to the experimental spectra, except that the experimental ones had an extra peak around $1400cm^{-1}$ not found in the calculations.

From the calculated spectrum for $Mg(NH_3)_6Cl_2$ in Figure 5.18, we see that the mode at $1200cm^{-1}$ is connected to the wobbling mode of the NH_3 molecules. In the gas-phase the nitrogen

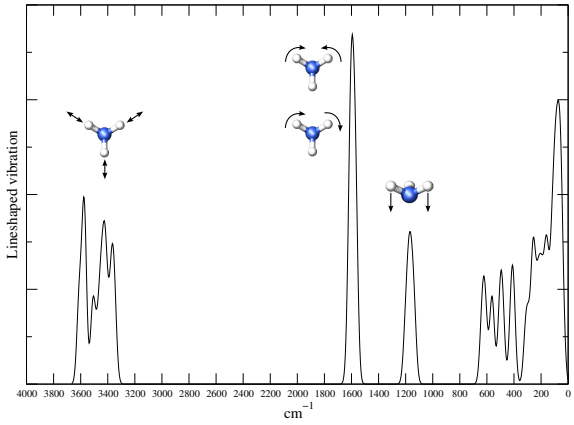

Figure 5.18: Vibrational spectrum of $Mg(NH_3)_6Cl_2$.

in ammonia is known to tunnel through the three hydrogen atoms (see for instance [74, 75, 76]), flipping the NH_3 molecule as it does in the diffusion process in Figure 5.13; this is known as the ammonia inversion. The ammonia inversion splits the peak of the wobbling mode in two in the vibrational spectrum of gas-phase NH_3. It is possible that a similar effect could happen in the metal ammines explaining the extra peak in the vibrational spectrum. However, there is an important difference between NH_3 in the gas-phase and NH_3 in a metal ammine. In the latter the nitrogen binds to the central metal and flipping the nitrogen through the hydrogen triangle will break this bond. Since the energy loss is around 0.5eV this seems unlikely.It could also be due to impurities like water. The infrared spectrum reported for $Mg(NH_3)_6Cl_2$ in [77] does not have the peak at 1400cm$^-$ in agreement in the calculations performed here.

5.8 Desorption by water ligand exchange

We close this chapter on the metal ammines by considering a theoretically appealing idea of using a ligand exchange mechanism to drive the desorption of ammonia without the use of heat. It is based on the fact that the systems that form ammines often also form hydrates in which water acts as the ligand instead of ammonia, and these tend to be more stable. The idea is to introduce water (which is available from the exhaust of the fuel cell) into the metal ammine. The H_2O molecules take the place of the NH_3 molecules in the coordination complex and thereby forcing them out. In principle, we just use chemical energy instead of heat to desorb the ammonia.

A set of calculation were performed to investigate this idea at the atomic scale. The NH_3 ligands in $Mg(NH_3)_6Cl_2$ were exchanged with H_2O one at a time and the system was optimized by relaxing atomic positions and scaling the unit cell proportionally. From these calculations it turned out that four of the six NH_3 can be substituted exothermically. For the last two the ligand exchange is not favorable, but including restructuring would probably change this.

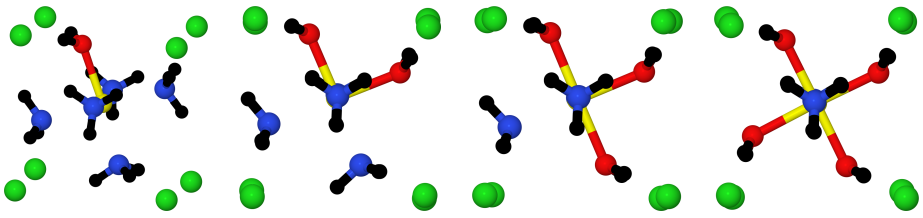

Figure 5.19: Ligand exchange $Mg(NH_3)_{5-2}(H_2O)_{1-4}Cl_2$. Exchanging the last two costs 0.08eV and 0.15eV.

For these particular systems the interest might only be theoretical since you give up some of the favorable features of the material, regarding reversibility and macroscopic kinetics. With water in the salt, you cannot simply recharge it by running ammonia through the systems; the water needs to be removed first. As mentioned, the macroscopic transport of ammonia in and out of the storage materials is enhanced by the pores that evolve as the crystallites shrink during desorption. However, substituting the ammonia with water will not reduce the size of the crystal as much and the porosity is diminished. Nevertheless, if these problems somehow can be solved the ligand exchange mechanism offers an interesting onboard energy economy.

6 Summary and outlook

6.1 Summary

Two classes of high capacity hydrogen storage materials, the metal tetrahydroborates and the metal ammines, were investigated at the atomic scale using density functional theory simulations. By using simple model structures to calculate the ground state electronic energy without zero point correction and Van der Waals interactions, the following results were achieved:

- Trends in stabilities were reproduced for metal halides, tetrahydroborates and ammines. The correlations with experimental observed stabilities was used to estimate the stabilities of ternary tetrahydroborates and ternary ammines, and a few such materials were suggested for further investigation. A trend connecting the stability of metal ammines to the electronegativity difference between the metals and anions involved was found, and the opposite trend known for binary tetrahydroborates was shown to hold for ternary borohydrides as well.

- The fast kinetics observed for the ab-/desorption of ammonia in $Mg(NH_3)_nCl_2$ type systems and the correspondingly slow kinetics in $Ca(NH_3)_nCl_2$ systems were investigated in details. It was shown that the fast bulk diffusion of NH_3 in $Mg(NH_3)_6Cl_2$ is likely to be dependent on the disordered phase preferred at ambient conditions, and that higher diffusion barriers in $Mg(NH_3)_{1,2}Cl_2$ could favor an alternative decomposition mechanism where chains of the material is released at the surface to aid the ab-/desorption. It was argued that the slow absorption kinetics of calcium ammines is related to the structure of $CaCl_2$ not being layered, and the calculations showed that exchanging 10% or more of the chloride ions with iodide ions could make a layered structure preferred and thereby improving absorption kinetics.

- The effect of using simple model structures was investigated for $Mg(BH_4)_2$, for which the experimentally observed structures are very complex, in a free energy comparison and the conclusion was that, since energy differences were small, the simple model structures could be expected to capture the thermodynamics of even complex systems.

- Experimental observations of a stabilization of the high-temperature phase of $LiBH_4$, by fractional substitution of BH_4^{-1} with I^-, was confirmed by the calculations, and a candidate structure for an observed but unresolved intermediate phase was proposed. The stabilization of the high-temperature phase is essential to Li-ion batteries based on $LiBH_4$ since only the high-temperature phase has a high Li^+-ion-conduction.

- Finally, insight gained from the systematic calculations and comparison of the systems (that also included metal hydrides) in different prototype structures, was used to find structures with lower electronic energy (at the applied level of theory) than the experimental structures. This included an hitherto unknown polymeric version of $LiBH_4$. These findings were used to design new structures of a few ternary and one quaternary tetrahydroborate, with a lower energy than the initially screened structures.

6.2 Outlook

The general trend we observe when tetrahydroborates or ammines are mixed is that the stability of the mix is the weighted average of the stabilities of the separated systems. In other words, the alloying or mixing energy is close to zero. From this it follows that any trend that holds for the pure systems, for instance the electronegativity trend, will also hold for the mixed systems.

However, many of the mixed systems are unstable, and while we can think of many reasons for this, like the mismatch of lattice constants, it is relevant to ask, what factors could make a mixed structure stable? In case of the tetrahydroborates, we saw in Section 4.6.2, how Li was mixed with metals with a higher valence in a bulk structure, that allowed the Li atoms to obtain a linear coordination of BH_4^{-1} ions and a tetrahedral coordination of H atoms, which according to the calculations seems to be preferred. Thinking of this in more general terms, when two metals with different valence are mixed, a whole new spectrum of structures become available. These tetrahydroborate structures could very well be more optimal for the two metals, than the structures that were available to them when they were separated.

As an example, consider the $Al(BH_4)_3$ structure in Figure 4.12 and the low-temperature *Pnma* structure of $LiBH_4$ in Figure 4.3a. Alone Al has to keep three BH_4^{-1} ions per metal atom, and if it the preferred coordination of Al is tetrahedral, it has to choose among structures like the Sc,Y structure in Figure 4.12, where some BH_4^{-1} ions are at isolated vertices of the coordination tetrahedra. Li, on the other hand, has the opposite problem where the coordination tetrahedra have to be edge-sharing to obtain a certain coordination of the hydrogen atoms. When the two systems are mixed the average valence is 2 and a new set of structures becomes available, for instance the $Mg(BH_4)_2$ structure in Figure 4.8b, which gives very low energies for the divalent metals, and it turned out, for the LiAl mixture as well.

For the metal ammine systems only metals with the same valence have been mixed in this study, and here other factors might make the mixed phase preferred. This could be related to the spin state of the electrons, or the coordinations of metals to the anions.

In short, trends like the electronegativity trend can guide us in choosing the components for a designed material, by providing us with a quick estimate of the final stability; to find out if a mixture is stable towards separation and to confirm the predicted stability, we need the structure. To find the most stable structure of a new system, we should use the knowledge about preferred coordinations and distances of the involved species.

All the prototype structures presented in this work was made by hand. While this approach can be used, ideally all the information about preferred coordinations etc. should be kept in a database, and a computer could use this information to automatically produce a number of candidate structures for an arbitrary input system. The systematic calculations of e.g. the halide systems presented in Chapter 3 is actually the first step of a plan to build such a database. In the future, more systematic calculations will be added to decipher preferred coordinations etc. and to quantify the energy cost or gain when going from one coordination to another for each element (or molecule). If the assumption, that the stability of these class of systems (and others) can be reverse engineered into different energy contributions, is correct, then a database of these energy contributions could be used to give estimates of relative energies of different structures, that might be good enough to make the DFT calculations unnecessary for the initial screening. And combined with the right algorithms it could even be used to construct optimal structures.

While this may be some years away, I close my thesis by referring to Section A.1 where an example of using Mathematica to do a constrained optimization of structure is given. The example is fairly simple, the ligand–ligand repulsion of a structure of corner-sharing tetrahedra with two tetrahedra in the unit cell is minimized by maximizing the unit cell volume, and it is seen that the analogue of the $Mg(BH_4)_2$ structure in Figure 4.8b results. The approach is quite general and other constraints and the hydrogen atoms can be added. It is likely that future algorithms for this job will be very different, but for now it is just relieving to see that the $Mg(BH_4)_2$ structure, that it took me one week to find, is found by Mathematica in 1 second.

A Appendix

A.1 Using Mathematica for structure building

In[1]:=
```
rotx = RotationMatrix[#, {1, 0, 0}] &;
roty = RotationMatrix[#, {0, 1, 0}] &;
rotz = RotationMatrix[#, {0, 0, 1}] &;
p[4] = PolyhedronData["Tetrahedron", "VertexCoordinates"];
c = {x[#1], y[#1], z[#1]} &;
cell = {{ax, ay, az}, {bx, by, bz}, {cx, cy, cz}};
b = c[#1] +
    d[#1] Transpose[rotz[θ[#1]].roty[ϕ[#1]].rotx[ψ[#1]].Transpose@p[cn[#1]]][[#2]] &;
varsxyz := Table[Table[b[i, j], {j, 1, cn[i]}], {i, 1, np}];
vars := {d[#], c[#], θ[#], ϕ[#], ψ[#]} & /@ Range[np] // Flatten;
dcons := Flatten[Table[d[i] == dn[i], {i, 1, np}]]
np := Length@polyhedra;
cn = polyhedra[[#]][[1]] &;
dn = polyhedra[[#]][[2]] &;
polyhedra = {{4, 2.45}, {4, 2.45}};
pcons := {
  b[1, 1] == b[2, 1],
  b[1, 2] + cell[[1]] == b[2, 2],
  b[1, 3] + cell[[2]] == b[2, 4],
  b[1, 4] + cell[[3]] == b[2, 3]
 }
cons := {Det[cell]^2, dcons, pcons, c[1] == {0, 0, 0}}
```

In[17]:=
```
Timing[sol = FindMaximum[cons, Join[vars, Flatten@cell]]][[1]]
Graphics3D[
 Polygon[Join[varsxyz, (cell[[1]] + #) & /@ # & /@ varsxyz, (cell[[2]] + #) & /@ # & /@ varsxyz,
    (cell[[3]] + #) & /@ # & /@ varsxyz, (cell[[3]] + cell[[2]] + #) & /@ # & /@ varsxyz,
    (cell[[1]] + cell[[2]] + #) & /@ # & /@ varsxyz, (cell[[1]] + cell[[3]] +
          #) & /@ # & /@ varsxyz ] /. sol[[2]]] ]
```

Out[17]= `1.08496`

Out[18]=

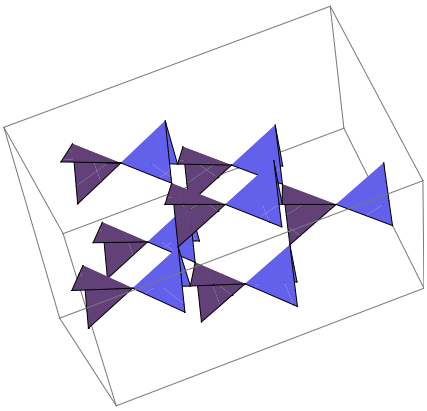

A.2 Linear regression for metal halides

Data	Regression	Plot
All	ParameterTable → 1: 0.439913, 0.0781783, 5.62705, 1.50872×10^{-7}; x: 0.91495, 0.01225, 74.6901, 0. RSquared → 0.981353, AdjustedRSquared → 0.981177, EstimatedVariance → 0.212507, ANOVATable → Model 1 1185.5 1185.5 5578.6 0.; Error 106 22.5258 0.212507; Total 107 1208.02	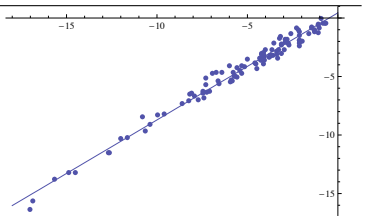
4d other no Li	ParameterTable → 1: 0.186979, 0.0719104, 2.60017, 0.0119423; x: 0.910638, 0.0106499, 85.5071, 0. RSquared → 0.992534, AdjustedRSquared → 0.992398, EstimatedVariance → 0.0897507, ANOVATable → Model 1 656.208 656.208 7311.46 0.; Error 55 4.93629 0.0897507; Total 56 661.144	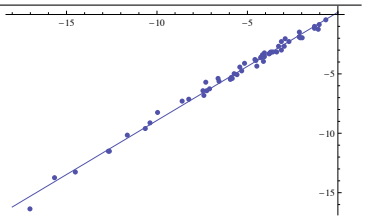
4d other no Li F	ParameterTable → 1: 0.294714, 0.241263, 1.22155, 0.245334; x: 0.928259, 0.0226413, 40.9985, 2.88658×10^{-14} RSquared → 0.992911, AdjustedRSquared → 0.992321, EstimatedVariance → 0.142524, ANOVATable → Model 1 239.565 239.565 1680.87 2.87548×10^{-14}; Error 12 1.71029 0.142524; Total 13 241.275	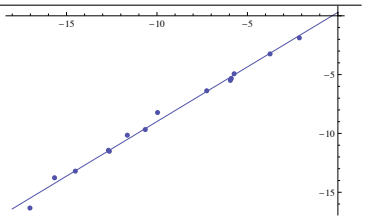
4d other no Li Cl	ParameterTable → 1: 0.279316, 0.193043, 1.44691, 0.171603; x: 0.894237, 0.0321737, 27.7941, 5.77982×10^{-13} RSquared → 0.98345, AdjustedRSquared → 0.982177, EstimatedVariance → 0.0933664, ANOVATable → Model 1 72.1265 72.1265 772.511 5.77982×10^{-13}; Error 13 1.21376 0.0933664; Total 14 73.3403	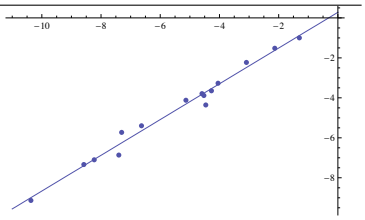
4d other no Li Br	ParameterTable → 1: 0.135223, 0.128229, 1.05454, 0.312407; x: 0.8814, 0.0272103, 32.3921, 4.73843×10^{-13} RSquared → 0.988693, AdjustedRSquared → 0.98775, EstimatedVariance → 0.0326968, ANOVATable → Model 1 34.307 34.307 1049.25 4.73843×10^{-13}; Error 12 0.392362 0.0326968; Total 13 34.6994	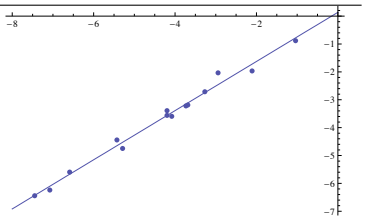
4d other no Li I	ParameterTable → 1: −0.00487819, 0.0837401, −0.0582539, 0.954505; x: 0.916061, 0.0249108, 36.7736, 1.04805×10^{-13} RSquared → 0.991204, AdjustedRSquared → 0.990471, EstimatedVariance → 0.019183, ANOVATable → Model 1 25.9412 25.9412 1352.3 1.04805×10^{-13}; Error 12 0.230196 0.019183; Total 13 26.1714	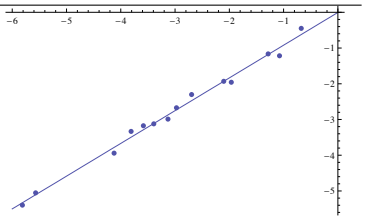

Bibliography

[1] Zhang, Y. and Yang, W. *Physical Review Letters* **80**(4), 890–890 (1998).

[2] Hammer, B., Hansen, L., and Norskov, J. *Physical Review B (Condensed Matter)* **59**(11), 7413–7421 (1999).

[3] Perdew, J. and Wang, Y. *Phys. Rev. B* **45**(23), 13244–13249 (1992).

[4] Noth, H. and Fritz, P. *Angewandte Chemie* **73**(11) (1961).

[5] Noth, H., Wiberg, E., and Winter, L. *Zeitschrift fur anorganische und allgemeine Chemie* **386**(1) (1971).

[6] Satyapal, S., Ordaz, G., Read, C., Stetson, N., Adams, J., Alkire, J., Bakke, P., and Thomas, G. In *2007 DoE Hydrogen Program Merit Review and Peer Evaluation Meeting*, (2007).

[7] Hubbert, M. *Nuclear energy and the fossil fuels*. Shell Development Co., Exploration and Production Research Division, (1956).

[8] Rhodes, C. J. *Sci Prog* **91**(Pt 4), 317–375 (2008).

[9] Bentley, R. *Energy Policy* **30**(3), 189–205 (2002).

[10] Kavalov, B. and Peteves, S. *Institute for Energy* (2007).

[11] Zerta, M., Schmidt, P., Stiller, C., and Landinger, H. *International Journal of Hydrogen Energy* **33**(12), 3021–3025 (2008).

[12] Chan, C., Peng, H., Liu, G., McIlwrath, K., Zhang, X., Huggins, R., and Cui, Y. *Nature Nanotechnology* (2007).

[13] Satyapal, S., Petrovic, J., Read, C., Thomas, G., and Ordaz, G. *Catalysis Today* **120**(3-4), 246–256 (2007).

[14] Krishnan, A., Lu, X., Pal, U., and McClaine, A. In *Materials Research Society Symposium Proceedings*, volume 837, 143. Warrendale, Pa.; Materials Research Society; 1999, (2005).

[15] Voss, J., Hummelshøj, J., Łodziana, Z., and Vegge, T. *Journal of Physics: Condensed Matter* **21**, 012203 (2009).

[16] Born, M. and Oppenheimer, R. *Phys* **84**, 457 (1927).

[17] Schrödinger, E. *Physical Review* **28**(6), 1049–1070 (1926).

[18] Hohenberg, P. and Kohn, W. *Physical Review* **136**(3B) (1964).

[19] Kohn, W. and Sham, L. *Physical Review* **140**(4A) (1965).

[20] Pauli, W. *Zeitschrift für Physik* **31**(1), 765–783 (1925).

[21] Hamilton, I., Mosna, R., and Site, L. *Theoretical Chemistry Accounts: Theory, Computation, and Modeling (Theoretica Chimica Acta)* **118**(2), 407–415 (2007).

[22] Bahn, S. and Jacobsen, K. *Computing in Science and Engineering* **4**(3), 56–66 (2002).

[23] Vanderbilt, D. *Physical Review B (Condensed Matter)* **41**(11), 7892–7895 (1990).

[24] Pulay, P. *Chem. Phys. Lett* **73**, 393–399 (1980).

[25] Mermin, N. *Phys. Rev* **137**(5A), A1441–A1443 (1965).

[26] Gillan, M. *J. Phys.: Condens. Matter* **1**, 689–711 (1989).

[27] Shannon, R. *Crystal Physics, Diffraction, Theoretical and General Crystallography* **32**(5), 7394 (1976).

[28] Fluck, E. *Journal of research-national institute of standards and technology* **101**, 217–220 (1996).

[29] Afeefy, H., Liebman, J., and Stein, S. *PJ Linstrom and WG Mallard, National Institute of Standards and Technology, Gaithersburg MD* **20899** (2001).

[30] Weast, R. and Company., C. R. (1988).

[31] Blackman, M. and Khan, I. *Proceedings of the Physical Society* **77**, 471–475 (1961).

[32] Dion, M., Rydberg, H., Schroder, E., Langreth, D., and Lundqvist, B. *PHYSICAL REVIEW LETTERS.* **92**(24), 246401–246401 (2004).

[33] Pauling, L. *J. Am. Chem. Soc* **54**(9), 3570–3582 (1932).

[34] Gordy, W. and Thomas, W. *The Journal of Chemical Physics* **24**, 439 (1956).

[35] Bell, N. *Advances in Inorganic Chemistry and Radiochemistry* , 255 (1972).

[36] Fischer, D., Muller, A., and Jansen, M. *Zeitschrift fur anorganische und allgemeine Chemie* **630**(15) (2004).

[37] Debye, P. and Scherrer, P. *Physikalische Zeitschrift* **19**, 474 (1918).

[38] Zuttel, A., Borgschulte, A., and Orimo, S. I. *Scripta Materialia* **56**(10), 823–828 May (2007).

[39] Zuttel, A. *Materials Today* **6**(9), 24–33 (2003).

[40] Lodziana, Z. *Physical Review Letters* **97**(11), 119602 (2006).

[41] Chłopek, K., Frommen, C., Léon, A., Zabara, O., and Fichtner, M. *Journal of Materials Chemistry* **17**(33), 3496–3503 (2007).

[42] Hagemann, H., Longhini, M., Kaminski, J. W., Wesolowski, T. A., Cerny, R., Penin, N., Sorby, M. H., Hauback, B. C., Severa, G., and Jensen, C. M. *J Phys Chem A* **112**(33), 7551–7555 Aug (2008).

[43] Nickels, E. A., Jones, M. O., David, W. I. F., Johnson, S. R., Lowton, R. L., Sommariva, M., and Edwards, P. P. *Angew. Chem.* **120**, 2859 (2008).

[44] Yang, J., Sudik, A., and Wolverton, C. (2007).

[45] Filinchuk, Y., Chernyshov, D., and Dmitriev, V. *Zeitschrift fur Kristallographie* **223**(10), 649–659 (2008).

[46] Ozolins, V., Majzoub, E., and Wolverton, C. *Physical Review Letters* **100**(13), 135501 (2008).

[47] Vajeeston, P., Ravindran, P., Kjekshus, A., and Fjellvåg, H. *Journal of Alloys and Compounds* **387**(1-2), 97–104 (2005).

[48] Vajeeston, P., Ravindran, P., Kjekshus, A., and Fjellvåg, H. *Appl. Phys. Lett.* **89**(7), 071906 (2006).

[49] Abrahams, S. and Kalnajs, J. *J. chem. Phys* **22**, 434 (1954).

[50] Kim, E., Kumar, R., Weck, P., Cornelius, A., Nicol, M., Vogel, S., Zhang, J., Hartl, M., Stowe, A., and Daemen, L. *Journal of Physical Chemistry B* **111**(50), 13873 (2007).

[51] Soulie, J., Renaudin, G., Cerny, R., and Yvon, K. *Journal of Alloys and Compounds* **346**, 200–205 (2002).

[52] Filinchuk, Y., Chernyshov, D., Nevidomskyy, A., and Dmitriev, V. *ChemInform* **39**(17) (2008).

[53] Matsuo, M., Nakamori, Y., Orimo, S., Maekawa, H., and Takamura, H. *Applied Physics Letters* **91**, 224103 (2007).

[54] Marynick, D. and Lipscomb, W. *Inorg. Chem* **11**(4), 820–823 (1972).

[55] Riktor, M., Sørby, M., Chłopek, K., Fichtner, M., Buchter, F., Züttel, A., and Hauback, B. *Journal of Materials Chemistry* **17**(47), 4939–4942 (2007).

[56] Her, J.-H., Stephens, P. W., Gao, Y., Soloveichik, G. L., Rijssenbeek, J., Andrus, M., and Zhao, J.-C. *Acta Crystallogr., Sect. B: Struct. Crystallogr. Cryst. Chem.* **63**, 561 (2007).

[57] Cerny, R., Filinchuk, Y., Hagemann, H., and Yvon, K. *Angew Chem Int Ed Engl* **46**(30), 5765–5767 (2007).

[58] Konoplev, V. and Bakulina, V. *Russian Chemical Bulletin* **20**(1), 136–138 (1971).

[59] Christensen, C. H., Soerensen, R. Z., Johannessen, T., Quaade, U. J., Honkala, K., Elmoee, T. D., Koehler, R., and Noerskov, J. K. *J. Mater. Chem.* **15**(38), 4106–4108 (2005).

[60] Fournier, G., Cumming, I., and Hellgardt, K. *Journal of Power Sources* **162**(1), 198–206 (2006).

[61] Elmøe, T., Sørensen, R., Quaade, U., Christensen, C., Nørskov, J., and Johannessen, T. *Chemical Engineering Science* **61**(8), 2618–2625 (2006).

[62] Hummelshoj, J. S., Sorensen, R. Z., Kustova, M. Y., Johannessen, T., Norskov, J. K., and Christensen, C. H. *J Am Chem Soc* **128**(1), 16–17 (2006).

[63] Jacobsen, H. S., Hansen, H. A., Andreasen, J. W., Shi, Q., Andreasen, A., Feidenhans'l, R., Nielsen, M. M., Ståhl, K., and Vegge, T. *Chemical Physics Letters* **441**, 255–260 (2007).

[64] Lepinasse, E. and Spinner, B. *International Journal of Refrigeration* **17**(5), 309–322 (1994).

[65] Sorensen, R. Z., Hummelshoj, J. S., Klerke, A., Reves, J. B., Vegge, T., Norskov, J. K., and Christensen, C. H. *J Am Chem Soc* **130**(27), 8660–8668 Jul (2008).

[66] Olovsson, I. *Acta Crystallographica* **18**, 889–893 (1965).

[67] Leineweber, A., Friedriszik, M. W., and Jacobs, H. *J Solid State Chem* **147**(1), 229–234 (1999).

[68] Leineweber, A., Jacobs, H., and Ehrenberg, H. *Z Anorg Allg Chem* **626**(10), 2146–2152 (2000).

[69] Vegge, T., Sørensen, R., Klerke, A., Hummelshøj, J., Johannessen, T., Nørskov, J., and Christensen, C. *Solid State Hydrogen Storage: Materials and Chemistry, ed. G. Walker, Woodhead Publishing, Cambridge, UK* (2008).

[70] Westman, S., Werner, P., Schuler, T., and Raldow, W. *Acta Chem. Scand. A* **35**, 467–472 (1981).

[71] Figgis, B., Sobolev, A., and Reynolds, P. *Acta Crystallographica, Section B (Structural Science)* **B54**, 613–625 (1998).

[72] Mockenhaupt, C., Essmann, R., and Lutz, H. *Zeitschrift fuer Naturforschung B (Chemical Sciences)* **54B**(7), 843–848 (1999).

[73] Leineweber, A., Jacobs, H., Fischer, P., and Bottger, G. *J Solid State Chem* **156**(2), 487–499 (2001).

[74] Bleaney, B. and Penronn, R. *Proceedings of the Royal Society of London, Series A (Mathematical and Physical Sciences)* **139**, 358–371 (1947).

[75] McBride, J. and Nicholls, R. *Journal of Physics B (Atomic and Molecular Physics)* **5**(2), 408–417 (1972).

[76] Good, W. *Physical Review* **69**(9-10), 539–539 (1946).

[77] Plus, R. *Journal de Chimie Physique et de Physico-Chimie Biologique* **70**(6), 900–904 (1973).

Paper I

J|A|C|S
ARTICLES

Published on Web 06/13/2008

Indirect, Reversible High-Density Hydrogen Storage in Compact Metal Ammine Salts

Rasmus Z. Sørensen,[†] Jens S. Hummelshøj,[‡,§] Asbjørn Klerke,[†] Jacob Birke Reves,[†] Tejs Vegge,[§] Jens K. Nørskov,[‡] and Claus H. Christensen*[,†]

Center for Sustainable and Green Chemistry, Department of Chemistry, Building 206, Technical University of Denmark, DK-2800 Kgs. Lyngby, Denmark, Center for Atomic-scale Materials Design, Department of Physics, Building 310, Technical University of Denmark, DK-2800 Kgs. Lyngby, Denmark, and Materials Research Department, Risø National Laboratory for Sustainable Energy, NanoDTU, Building 228, Technical University of Denmark, DK-4000 Roskilde, Denmark

Received September 14, 2007; E-mail: chc@kemi.dtu.dk

Ⓦ **This paper contains enhanced objects available on the Internet at http://pubs.acs.org/jacs.**

Abstract: The indirect hydrogen storage capabilities of $Mg(NH_3)_6Cl_2$, $Ca(NH_3)_8Cl_2$, $Mn(NH_3)_6Cl_2$, and $Ni(NH_3)_6Cl_2$ are investigated. All four metal ammine chlorides can be compacted to solid tablets with densities of at least 95% of the crystal density. This gives very high indirect hydrogen densities both gravimetrically and volumetrically. Upon heating, NH_3 is released from the salts, and by employing an appropriate catalyst, H_2 can be released corresponding to up to 9.78 wt % H and 0.116 kg H/L for the $Ca(NH_3)_8Cl_2$ salt. The NH_3 release from all four salts is investigated using temperature-programmed desorption employing different heating rates. The desorption is found mainly to be limited by heat transfer, indicating that the desorption kinetics are extremely fast for all steps. During desorption from solid tablets of $Mg(NH_3)_6Cl_2$, $Mn(NH_3)_6Cl_2$, and $Ni(NH_3)_6Cl_2$, nanoporous structures develop, which facilitates desorption from the interior of large, compact tablets. Density functional theory calculations reproduce trends in desorption enthalpies for the systems studied, and a mechanism in which individual chains of the ammines are released from the surface of the crystal is proposed to explain the fast absorption/desorption processes.

Introduction

The rising concern over dwindling resources and the environmental impact of burning fossil fuels has generated interest in using hydrogen as an alternative energy carrier. Significant challenges remain in the development of economically viable solutions for production, storage, and use of hydrogen as an energy carrier.[1–6]

Widespread use of hydrogen as a fuel is limited by the lack of safe and efficient systems for its storage.[7] The large deviation from ideality observed upon compression of hydrogen to high pressures, combined with the low condensing point and low density even in the liquid state, has limited the use of conventional storage systems, and a plethora of strategies for direct storage of hydrogen have been proposed.[8–14] Clearly, direct hydrogen storage methods will involve the lowest possible number of chemical transformations, and thereby minimize the inherent losses associated with multistep chemical reactions, but in practice there are still a large number of challenges to be dealt with before such large-scale direct hydrogen storage is technically and economically feasible. This has led to increased interest in indirect storage of hydrogen, e.g., in the form of methanol, ethanol, ammonia, urea, or guanidine.[15–18]

[†] Center for Sustainable and Green Chemistry, Department of Chemistry.
[‡] Center for Atomic-scale Materials Design, Department of Physics.
[§] Materials Research Department, Risø National Laboratory for Sustainable Energy.

(1) Dresselhaus, M.; Crabtree, G.; Buchanan, M. Basic Research Needs for the Hydrogen Economy; U.S. Department of Energy: Washington, DC, 2003. (available online at http://www.sc.doe.gov/bes/hydrogen.pdf).
(2) Crabtree, G.; Dresselhaus, M.; Buchanan, M. *Phys. Today* **2004**, *57, 12*, 39–44.
(3) Kennedy, D. *Science* **2004**, *305*, 917.
(4) Turner, J. A. *Science* **2004**, *305*, 972–974.
(5) Wu, W.; Kawamoto, K.; Kuramochi, H. *J. Mater. Cycles Waste Manag.* **2006**, *8*, 70–77.
(6) Avci, A. K.; Önsan, Z. I.; Trimm, D. L. *Top. Catal.* **2003**, *22*, 359–367.
(7) Takimoto, M.; Hou, Z. *Nature* **2006**, *443*, 400–401.
(8) Zütel, A. *Naturwissenschaften* **2004**, *91*, 157–172.
(9) Cheng, P.; Xiong, Z.; Lou, J.; Lin, J.; Tan, K. L. *Nature* **2002**, *420*, 302–304.
(10) Bououdina, M.; Grant, D.; Walker, G. *Int. J. Hydrogen Energy* **2006**, *31*, 177–182.
(11) Stephens, F. H.; Baker, R. T.; Matus, M. H.; Grant, D. J.; Dixon, D. A. *Angew. Chem., Int. Ed.* **2006**, *46*, 746–749.
(12) Bogdanoviæ, B.; Felderhoff, M.; Pommerin, A.; Schüthe, F.; Spielkamp, N. *Adv. Mater.* **2006**, *18*, 1198–1201.
(13) Latroche, M.; Surblé, S.; Serre, C.; Mellot-Draznieks, C.; Llewellyn, P. L.; Lee, J.-H.; Chang, J.-S.; Jhung, S. H.; Férey, G. *Angew. Chem., Int. Ed.* **2006**, *45*, 8227–8231.
(14) Welch, G. C.; Juan, R. R. S.; Masuda, J. D.; Stephan, D. W. *Science* **2006**, *314*, 1124–1126.
(15) Metkemeijer, R.; Achard, P. *Int. J. Hydrogen Energy* **1994**, *19*, 535–542.
(16) Thomas, G.; Parks, G. Potential Roles of Ammonia in a Hydrogen Economy; U.S. Department of Energy: Washington, DC, 2006. (available online at http://hydrogen.energy.gov/pdfs/nh3_paper.pdf).
(17) Christensen, C. H.; Johannessen, T.; Sørensen, R. Z.; Nørskov, J. K. *Catal. Today* **2006**, *111*, 140–144.

10.1021/ja076762c CCC: $40.75

Table 1. Mass and Volume of 10 kg of Hydrogen Stored Reversibly by Six Different Methods[a]

$Mg(NH_3)_6Cl_2$	H_2 (liquid)	Mg_2NiH_4	$LaNi_5H_6$	$NaAlH_4$	H_2 (g, 200 bar)
91.4 L	141.2 L	252.6 L	276.9 L	380.9 L	714.2 L
109 kg	10 kg	392 kg	730 kg	286 kg	10 kg

[a] All data are based on the best-obtained reversible densities reported in the literature without considering the space occupied by the container.[26–32]

Molecular ammonia contains 17.8 wt % hydrogen and can be used directly as a fuel in internal combustion engines[19] or in solid oxide fuel cells,[20] but it can also be catalytically converted to hydrogen and nitrogen at temperatures below 650 K[21–23] in high yields. The production of ammonia from hydrogen and nitrogen using natural gas as the feedstock has been optimized in the Haber−Bosch process,[24] which is among the largest catalytic processes currently in industrial operation.[25] Commercially, ammonia is transported as a liquid at a pressure around 16 bar, achieved by addition of nitrogen, but for distribution to consumers the safety of this solution is a concern.[26]

In Table 1, the practically obtainable hydrogen storage density of a selection of the more promising direct hydrogen storage approaches is compared to the results of a recently published method of hydrogen storage in the ammine complex $Mg(NH_3)_6Cl_2$. From Table 1, it is evident that reversible storage of 10 kg of H in a compact and convenient way is not a trivial task. Since the comparison indicates that the hexaammine magnesium salt is a promising candidate for hydrogen storage, it is interesting to explore the hydrogen storage potential for a broader range of metal ammine salts. Recently, metal ammines have also been proposed for ammonia storage in connection with vehicular $DeNO_x$ systems,[33] giving an extra incentive for studying these materials in more detail.

Here, $Ca(NH_3)_8Cl_2$, $Mn(NH_3)_6Cl_2$, and $Ni(NH_3)_6Cl_2$ are investigated and compared with $Mg(NH_3)_6Cl_2$ as hydrogen/ammonia storage materials to demonstrate that the family of metal ammine salts, in fact, represents a large number of compounds that can potentially be used for reversible, indirect hydrogen storage. Furthermore, the investigated metal ammine complexes are found to exhibit facile ammonia release kinetics.

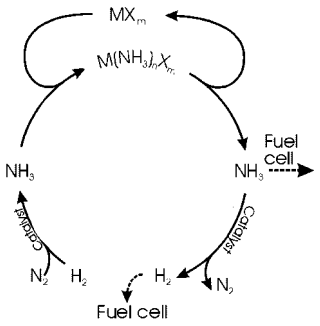

Figure 1. Principle of hydrogen storage in metal ammine salts of the general formula $M(NH_3)_nX_m$.

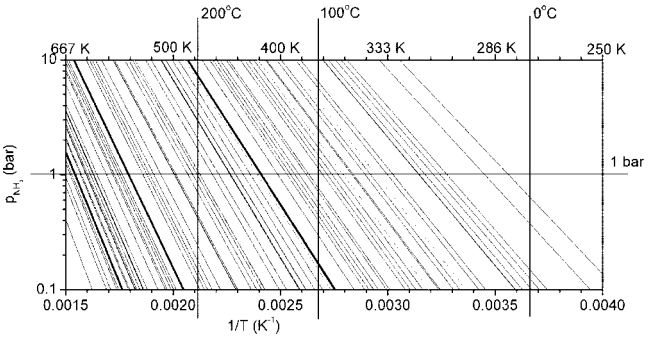

Figure 2. Van't Hoff plot showing the equilibrium pressure of ammonia over 90 metal ammine halides of the general formula $M(NH_3)_nX_2$.[34] The complete list of complexes is given as Supporting Information.

The general principle of storing hydrogen in metal ammine complexes is shown in Figure 1. The absorption of ammonia is exothermic (negative absorption enthalpy) for all salts. Thus, the release is necessarily endothermic and must require the same amount of energy as is released during the absorption. The equilibrium vapor pressures can be determined by the van't Hoff relationship given as eq 1, from which it is seen that the safer the storage material (low vapor pressure at ambient temperature), the more energy required for releasing NH_3 at a given pressure.

$$\ln(p) = -\frac{\Delta H_{\mathrm{des}}}{RT} + \frac{\Delta S_{\mathrm{des}}}{R} \qquad (1)$$

The possibility for choosing a metal ammine salt with the desired thermodynamic properties is illustrated in Figure 2.

Compared to hydrides and alanates with comparable storage pressures, the pressure change with temperature is larger for metal ammines. This is because the ammine salts generally have higher entropies of desorption than those of metal hydrides. Thus, it is evident from the van't Hoff relationship that metal complexes also have higher enthalpies of desorption than hydrides with similar vapor pressures at a given temperature.

The formation of metal ammine complexes and the thermodynamics of ammonia desorption from these have been thoroughly described in the early chemical literature. From these literature data, it is possible to find general trends for the NH_3

(18) Van Vechten, J. A. Presented at the 2007 APS March Meeting, Denver, CO;; American Physical Society: College Park, MD, 2007; Abstract S39.00010.
(20) Fournier, G. G. M.; Cumming, I. W.; Hellgardt, K. *J. Power Sources* **2006**, *162*, 198–206.
(19) Steele, R. B. *Chemtech* **1999**, (August), 28.
(21) Raróg-Pilecka, W.; Szmigiel, D.; Kowalczyk, Z.; Jodzis, S.; Zielinski, J. *J. Catal.* **2003**, *218*, 465–469.
(22) Li, X.-K.; Ji, W.-J.; Zhao, J.; Wang, S.-J.; Au, C.-T. *J. Catal.* **2005**, *236*, 181–189.
(23) Boisen, A.; Dahl, S.; Nørskov, J. K.; Christensen, C. H. *J. Catal.* **2005**, *230*, 309–312.
(24) Schlögl, R. *Angew. Chem., Int. Ed.* **2003**, *42*, 2004–2008.
(25) Eggmann, T. *Kirk-Othmer Encyclopedia of Chemical Technology: Ammonia*; John Wiley & Sons, Inc.: New York, 2001.
(26) Appl, M. *Ullmann's Encyclopedia of Industrial Chemistry: Ammonia*; Wiley-VCH Verlag GmbH & Co. KGaA: Weinheim, 2007.
(27) Mosher, D.; Tang, X.; Arsenault, S. High Density Hydrogen Storage System Demonstration Using $NaAlH_4$ Based Complex Hydrides. FY 2006 Annual Progress Report, DOE Hydrogen Program; U.S. Department of Energy: Washington, DC, 2006; pp 281−284. (available online at http://www.hydrogen.energy.gov/pdfs/progress06/iv_a_1_mosher.pdf).
(28) Liu, X.; Zhu, Y.; Li, L. *Int. J. Hydrogen Energy* **2007**, *32*, 2455–2460.
(29) Nomura, K.; Fujiwara, S.; Hayakawa, H.; Akiba, E.; Ishido, Y.; Ono, S. *Journal of the Less-Common Metals* **1991**, *169*, 9–17.
(30) Suissa, E.; Jacob, I.; Hadari, Z. *J. Less-Common Metals* **1984**, *104*, 287–295.
(31) El-Osairy, M. A.; el-Osery, I. A.; Metwally, A. M.; Hassan, M. A. *Int. J. Hydrogen Energy* **1993**, *18*, 517–524.
(32) Laidler, K. J.; Meiser, J. H. *Physical Chemistry*, 3rd ed.; Houghton Mifflin Co.: New York, 1999.
(33) Elmøe, T. D.; Sørensen, R. Z.; Quaade, U.; Christensen, C. H.; Nørskov, J. K.; Johannessen, T. *Chem. Eng. Sci.* **2006**, *61*, 2618–2625.
(34) Biltz, W.; Messerknecht, C. *Z. Anorg. Allg. Chem.* **1923**, *129*, 161–175.

desorption properties of metal ammine halides.[35–37] The most general trend in these original data is that the desorption enthalpy of ammonia increases from chloride through bromide to iodide. The data available for fluorides indicate that fluoride does indeed follow the same trend, but, in fact, only a few metal ammine fluorides have been investigated in detail.[35,37–39] The effect of the metal cation is not as clear, but some trends can be seen. For the alkali and alkaline earth metals, the enthalpy of desorption decreases down through the groups,[37,38] and for the transition metals, the enthalpy of desorption increases slightly when moving from left to right in the Periodic Table, i.e., from manganese to nickel in oxidation state 2+.[37]

For a metal ammine complex to be considered useful as an indirect hydrogen storage material, it needs to desorb ammonia in a relatively narrow temperature range around or above ambient temperature. For the storage to be safe, the ammonia vapor pressure should preferably be below 1 bar at ambient temperature. Possibly, somewhat higher pressures could be handled appropriately in practical systems. However, with such materials, leaks would represent a significant hazard. At the same time, 1 bar of ammonia pressure should preferably be reached below 650 K for all desorption steps to avoid desorption of ammonia becoming too energy intensive. This is so because the ammonia decomposition reaction is best conducted above 650 K, where a sufficiently high rate can be achieved and simultaneously a sufficiently low equilibrium ammonia concentration is reached. Moreover, the gravimetric and volumetric hydrogen density of the chosen metal ammine salt(s) should clearly be as high as possible. This criterion obviously favors light cations and anions such as alkali metals and fluorides. These are, however, impractical because the alkali metals do not bind ammonia sufficiently well at ambient temperature according to the above criteria, and the fluorides are usually toxic and can form hydrofluoric acid when they are heated to desorb the ammonia.[39]

So far, the only metal ammine complex which has been investigated in any detail as an indirect hydrogen storage material is $Mg(NH_3)_6Cl_2$.[40] $Mg(NH_3)_6Cl_2$ was chosen initially because it has a vapor pressure of only 2.2 mbar at 300 K, and additionally $MgCl_2$ is both widely available and nontoxic. However, other salts can similarly bind ammonia to form interesting indirect hydrogen storage materials. For one, $CaCl_2$ binds eight ammonia molecules to form $Ca(NH_3)_8Cl_2$ at 300 K and 1 bar of NH_3. This gives an even higher indirect hydrogen storage density than that achieved in $Mg(NH_3)_6Cl_2$ on both a mass and volume basis, but it also results in an equilibrium ammonia pressure of 0.77 bar at 300 K. In $Ca(NH_3)_8Cl_2$, only six of the NH_3 molecules are coordinated directly to calcium. The last two are more freely bound in the crystalline structure.[41] $MnCl_2$ and $NiCl_2$ coordinate ammonia to form $Mn(NH_3)_6Cl_2$ and $Ni(NH_3)_6Cl_2$, respectively. Both of these have higher molar masses than $Mg(NH_3)_6Cl_2$, but as their crystal densities are also higher,[42] the volumetric hydrogen contents are essentially the same as in $Mg(NH)_6Cl_2$. The temperatures at which the equilibrium vapor pressure is 1 bar for the first desorption step in the four different complexes are 305 ($Ca(NH_3)_8Cl_2$), 358 ($Mn(NH_3)_6Cl_2$), 413 ($Mg(NH_3)_6Cl_2$), and 449 K ($Ni(NH_3)_6Cl_2$).[43] The theoretical storage capacities of the metal ammine complexes are given in Table 2, and desorption enthalpies for the individual desorption steps are reported separately in Table 3.

Table 2. Indirect Hydrogen Storage Capacity of Four Metal Ammine Salts

	ρ,[a] g/cm^3	gravimetric H, wt % H	volumetric H, kg H/L
$Mg(NH_3)_6Cl_2$	1.25	9.19	0.115
$Ca(NH_3)_8Cl_2$	1.19	9.78	0.116
$Mn(NH_3)_6Cl_2$	1.41	7.96	0.112
$Ni(NH_3)_6Cl_2$	1.53	7.83	0.119

[a] Crystal densities.[42]

Table 3. Ammonia Desorption Enthalpies for Each Desorption Step for Four Different Metal Ammine Complexes[43]

$Mg(NH_3)_nCl_2$		$Ca(NH_3)_nCl_2$		$Mn(NH_3)_nCl_2$		$Ni(NH_3)_nCl_2$	
n	ΔH_{des}, kJ/mol	n	ΔH_{des}, kJ/mol	n	ΔH_{des}, kJ/mol	n	ΔH_{des}, kJ/mol
6→2	55.7	8→4	41.0	6→2	47.4	6→2	59.2
2→1	74.9	4→2	42.3	2→1	71.0	2→1	79.5
1→0	87.0	2→1	63.2	1→0	84.2	1→0	89.8
		1→0	69.1				

In utilizing the present approach for indirect hydrogen storage above the gram scale, it is important that the complexes can be compacted into tablets or other shaped bodies with as little void space as possible. This was previously reported to be possible for $Mg(NH_3)_6Cl_2$, and it was found that, during desorption of ammonia from tablets of this salt, a sponge-like structure maintaining the shape of the original tablet was formed featuring a nanopore system, which facilitates desorption of ammonia from the interior of the compact material.[44,45]

The compactability, the ability to form of nanopores, and the kinetics of ammonia desorption are investigated in this study for $Ca(NH_3)_8Cl_2$, $Mn(NH_3)_6Cl_2$, and $Ni(NH_3)_6Cl_2$, and the results are reported in the following sections.

Experimental Methods

Commercial anhydrous salts ($CaCl_2$, Alfa Aesar, 97%; $NiCl_2$, Aldrich, 98%; $MnCl_2$, Aldrich, 98%) were transferred to the reaction vessel in a glovebox containing dry air (6−8 ppm H_2O) and dried at 400−500 °C in a stream of N_2 before use. The vessel was purged with NH_3 gas (Hede Nielsen, N45) and left overnight under a pressure of NH_3 slightly above 4 bar. NH_3 uptakes were determined gravimetrically. Each metal ammine halide was pressed into tablets to determine the maximal bulk density of the storage material. Tablets of the material were also subjected to measurements of pore size distributions. These were performed using nitrogen absorption and desorption measurements on a Micrometrics ASAP 2020N, with pretreatment of the samples at temperatures and pressures chosen to give the desired levels of NH_3 desorption.

(35) Ephraim, F. *Chem. Ber.* **1912**, *45*, 1322–1331.
(36) Biltz, W.; Hüttig, G. F. *Z. Anorg. Allg. Chem.* **1919**, *109*, 88–110.
(37) Biltz, W. *Z. Anorg. Allg. Chem.* **1923**, *130*, 93–139.
(38) Biltz, W.; Hansen, W. *Z. Anorg. Allg. Chem.* **1923**, *127*, 1–33.
(39) Patil, K. C.; Secco, E. A. *Can. J. Chem.* **1972**, *50*, 567–573.
(40) Christensen, C. H.; Sørensen, R. Z.; Johannessen, T.; Quaade, U.; Honkala, K.; Elmøe, T. D.; Køhler, R.; Nørskov, J. K. *J. Mater. Chem.* **2005**, *15*, 4106–4108.
(41) Westman, S.; Werner, P.-E.; Schuler, T.; Raldow, W. *Acta Chem. Scand.* **1981**, *35*, 467–472.
(42) Gmelin Data: 2000−2006, Gesellschaft Deutscher Chemiker licensed to MDL Information Systems GmbH; 1988−1999, Gmelin Institut für Anorganische Chemie und Grenzgebiete der Max-Planck-Gesellschaft zur Foerderung der Wissenschaften.
(43) Lepinasse, E.; Spinner, B. *Rev. Int. Froid.* **1994**, *17*, 309–321.
(44) Hummelshøj, J. S.; Sørensen, R. Z.; Kustova, M. Y.; Johannesen, T.; Nørskov, J. K.; Christensen, C. H. *J. Am. Chem. Soc.* **2006**, *128*, 16–17.
(45) Jacobsen, H. S.; Hansen, H. A.; Andreasen, J. W.; Shi, Q.; Andreasen, A.; Feidenhans'l, R.; Nielsen, M. M.; Ståhl, K.; Vegge, T. *Chem. Phys. Lett.* **2007**, *441*, 255–260.

Table 4. Tablet Densities

	ρ_{tablet}, g/cm^3	$\rho_{crystal}$, %	volumetric H, kg H/L
$Mg(NH_3)_6Cl_2$[33]	1.19	95	0.11
$Ca(NH_3)_8Cl_2$	1.18	99	0.12
$Mn(NH_3)_6Cl_2$	1.34	95	0.11
$Ni(NH_3)_6Cl_2$	1.41	95	0.11

Desorption characteristics were determined by temperature-programmed desorption (TPD). Samples of 0.5 g were transferred to a closed test tube under an NH_3 atmosphere and heated following a desired temperature ramp. NH_3 was released into a carrier stream of Ar through a T-joint with a thin connection tube to maintain the NH_3 atmosphere over the sample. This procedure gave an NH_3 pressure slightly above atmospheric pressure over the ammine sample. For TPDs of $Mg(NH_3)_6Cl_2$, a sample obtained from Amminex A/S was used as received. The ammonia content in the carrier stream was determined using a Fischer-Rosemount NGA 2000 equipped with an MLT analyzer calibrated to NH_3 concentrations from 0.03 to 30%. Desorption rates were calculated from the ammonia content in the carrier stream and the flow of Ar, which was kept constant at 213 mL of N/min using a calibrated Brooks 5850 TR mass flow controller. For all four metal ammine salts, TPDs were obtained with heating rates of both 1 and 5 K/min.

Results and Discussion

The behavior of the four different metal ammine chlorides during TPD is shown in Figure 3. In accordance with literature data, the trend in temperature for the first desorption peak is Ca < Mn < Mg < Ni. During TPD, $Ca(NH_3)_nCl_2$ has stable compositions with $n = 8$, 4, 2, and 1, and essentially all ammonia desorbs in the temperature range of 300−550 K. $Mn(NH_3)_nCl_2$ has stable compositions with $n = 6$, 2, and 1 and two compositions with $n < 1$. Stable structures with less than one ammonia molecule per metal atom are well known for a range of transition metal ammine salts and are therefore not unlikely, even though they have not been previously reported for $MnCl_2$. For this compound, essentially all ammonia desorbs in the temperature range of 350−675 K. TPDs of $Mg(NH_3)_nCl_2$ were reported previously, and there are stable compositions with $n = 6$, 2, and 1. Here, essentially all ammonia desorbs in the temperature range of 410−700 K. During TPD, $Ni(NH_3)_nCl_2$ shows stable compositions with $n = 6$, 2, and 1, and all ammonia desorbs in the temperature range of 440−700 K. Independently of the temperature ramp, all the TPD peaks start within a few degrees of the temperature for 1 bar equilibrium pressure calculated from literature data.[43] This and the nearly exponential rise in desorption rate with temperature indicate that desorption is equilibrium-limited, even at high desorption rates. During fast desorption, the endothermic reaction causes the sample to cool, which is evident as a small deviation from the predefined temperature ramp when the desorption peaks (data not shown). This cooling will, in effect, decrease the equilibrium vapor pressure and thereby alter the desorption rate. Hence, for large samples, heat transport to the reaction zone seems to be the main limitation on the desorption rate for all four metal ammine salts studied. This is also supported experimentally, as the shape of TPD peaks depends on the sample size (data not shown). When the sample is large, the peak is broadened and the slopes (both increasing and decreasing) are less steep. This corresponds to a larger temperature distribution inside the sample. In an earlier work, computational modeling showed heat transport to be the main limiting factor for desorption from $Mg(NH_3)_6Cl_2$.[33] The present results indicate that it is a general feature for metal ammine salts that desorption is not limited by diffusion kinetics or large activation energies, but only by thermodynamic equilibrium, and hence by heat transport to the reaction zone.

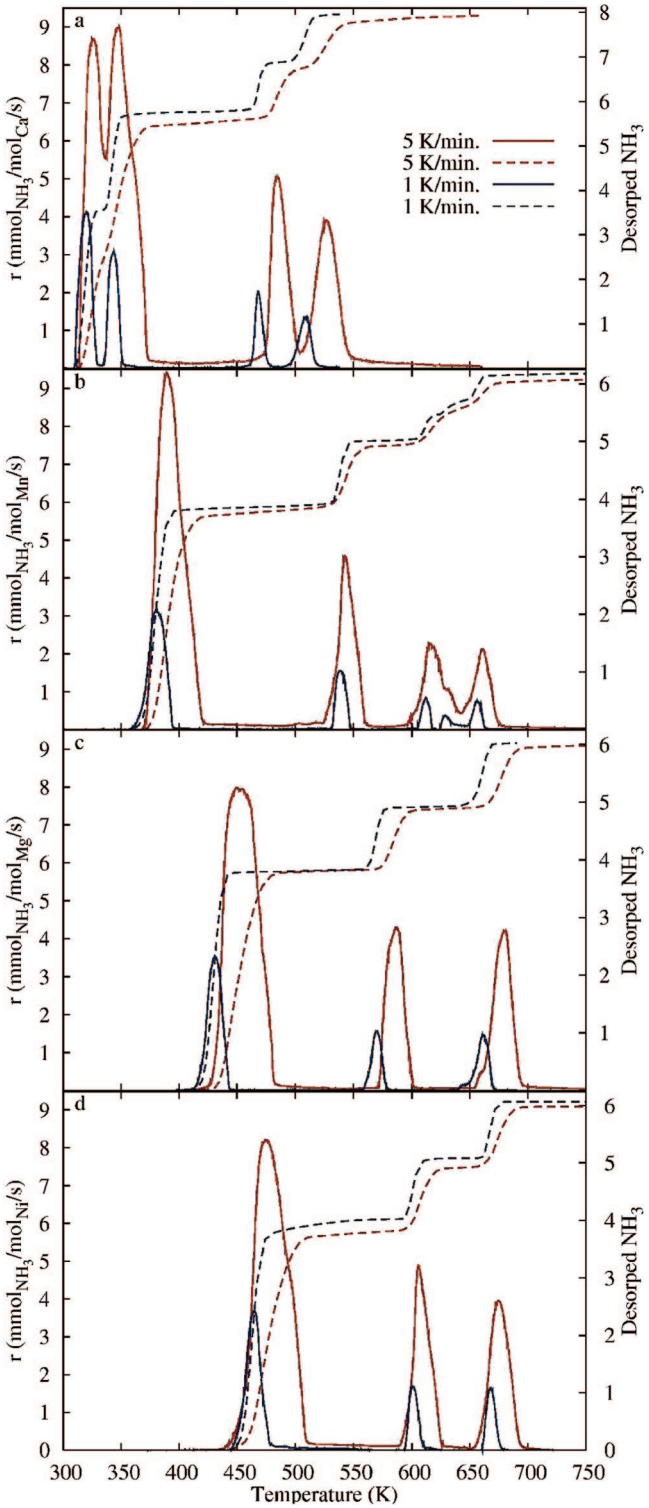

Figure 3. TPDs of (a) $Ca(NH_3)_8Cl_2$, (b) $Mn(NH_3)_6Cl_2$, (c) $Mg(NH_3)_6Cl_2$, and (d) $Ni(NH_3)_6Cl_2$, with a temperature ramp of 5 K/min (red) and 1 K/min (blue). The solid lines show the desorption rate, and the dashed lines show the total amount of desorbed ammonia.

The desorption of ammonia from $Ni(NH_3)_6Cl_2$ was also examined by thermogravimetric analysis coupled with a mass spectrometer. This confirmed that the sample was maintained

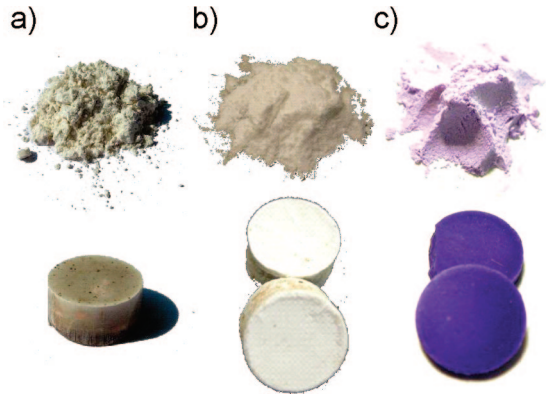

Figure 4. Photos of (a) $Mn(NH_3)_6Cl_2$, (b) $Ca(NH_3)_8Cl_2$, and (c) $Ni(NH_3)_6Cl_2$ as powder and tablets.

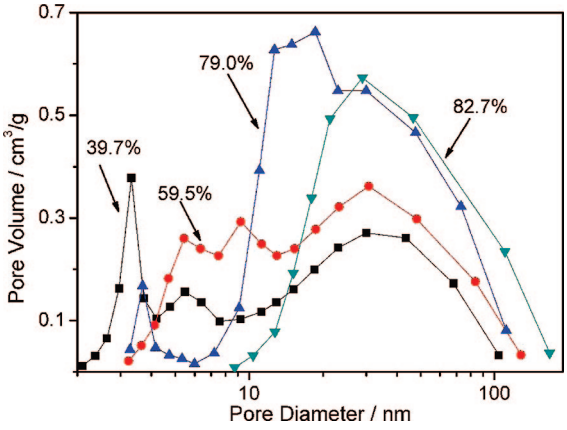

Figure 5. Pore structures developed after different levels of ammonia desorption from a $Mn(NH_3)_6Cl_2$ tablet.

at complete ammonia saturation during handling and that the only gas which desorbed from the sample was ammonia.

The densities of the metal ammine chloride tablets are reported and compared to the crystal densities in Table 4. In all cases, the metal ammine halides exhibit tablet densities of at least 95% of their crystal densities. Photos of powders and tablets are given in Figure 4.

For desorption of ammonia to be facile from dense bodies of metal ammine complexes such as the present tablets, it is important that a pore structure develops through which ammonia can leave the tablet without a long diffusion path in the solid state. The development of nanopores during ammonia desorption has previously been demonstrated experimentally for $Mg(NH_3)_6Cl_2$.[44,45] Here, pore size distributions for both $Mn(NH_3)_6Cl_2$ and $Ni(NH_3)_6Cl_2$ were measured after desorption of part of the ammonia from dense tablets of these materials. Before the measurements, the samples must be evacuated at ambient temperature or higher. Therefore, some NH_3 necessarily desorbs before the first measurement. For $Ni(NH_3)_6Cl_2$, this loss is negligible since the vapor pressure at room temperature is very low. Hence, the porosity in the initial tablet could be characterized carefully. For $Mn(NH_3)_6Cl_2$, the initial porosity can be calculated from the tablet density in Table 4 and the crystal density in Table 2 to be 0.07 cm^3/g. In Figure 5, it is seen that, in the first part of desorption of NH_3 from $Mn(NH_3)_6Cl_2$, pores of 2−3 nm are formed along with some pores around 30−50 nm. As more and more NH_3 is desorbed, the smaller pores disappear while the number of larger pores increases. From 79.0% desorbed to 82.7% desorbed, something

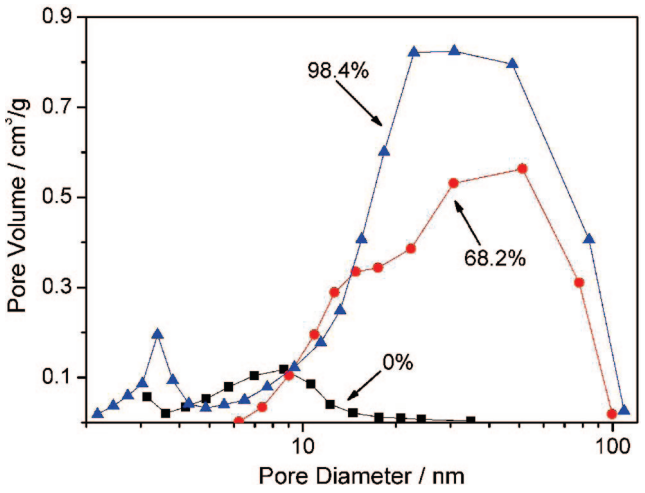

Figure 6. Pore structures developed after different levels of ammonia desorption from a $Ni(NH_3)_6Cl_2$ tablet.

Table 5. Pore Characteristics for $Mn(NH_3)_6Cl_2$

NH_3 desorbed, %	BET area, m^2/g	average pore size, nm	total pore volume, cm^3/g
0.0			0.07
39.7	89.6	10.9	0.308
59.5	84.0	15.6	0.421
79	91.7	20.3	0.560
82.7	43.3	35.7	0.507

Table 6. Pore Characteristics for $Ni(NH_3)_6Cl_2$

NH_3 desorbed, %	BET area, m^2/g	average pore size, nm	total pore volume, cm^3/g
0.0	12.0	6.8	0.051
68.2	53.9	25.5	0.432
98.4	120.5	21.1	0.687

different happens. The pores of 20−30 nm diameter disappear without the number of pores in the size range 30−50 nm increasing. For $Ni(NH_3)_6Cl_2$, the data are not as detailed, but it is evident from Figure 6 that, from a relatively small pore volume with pore sizes distributed from 3 to 20 nm in the initial tablet, a larger volume of pores in the size range 10−100 nm develops as NH_3 desorbs. As a consequence of this development in pore structure, the average pore sizes and total pore volumes in both salts generally increase during the desorption. Table 5 lists the Brunauer−Emmett−Teller (BET) areas measured at various stages during the desorption of NH_3 from $Mn(NH_3)_6Cl_2$. They are almost constant until the last measurement, where a decrease is seen. For $Ni(NH_3)_6Cl_2$, however, the BET area continues to increase during the desorption process (see Table 6). As the increase in surface area makes more surface available for desorption of ammonia, this facilitates desorption of ammonia from the interior of dense bodies of the material.

Modeling of Ammonia Desorption. A series of periodic density functional theory (DFT) calculations, using the Dacapo planewave pseudopotential implementation,[46–48] were performed to determine this method's ability to accurately calculate ammonia desorption enthalpies for metal ammine salts, specifically $Mg(NH_3)_6Cl_2$, $Ca(NH_3)_8Cl_2$, $Mn(NH_3)_6Cl_2$, and $Ni(NH_3)_6Cl_2$. The calculations were also used to provide additional understanding of

(46) Kresse, J. *Comput. Mater. Sci.* **1996**, *6*, 15–50.
(47) Vanderbilt, D. *Phys. Rev. B* **1990**, *41*, 7892–7895.
(48) Hammer, B.; Hansen, L. B.; Norskov, J. K. *Phys. Rev. B* **1999**, *59*, 7413–7421.

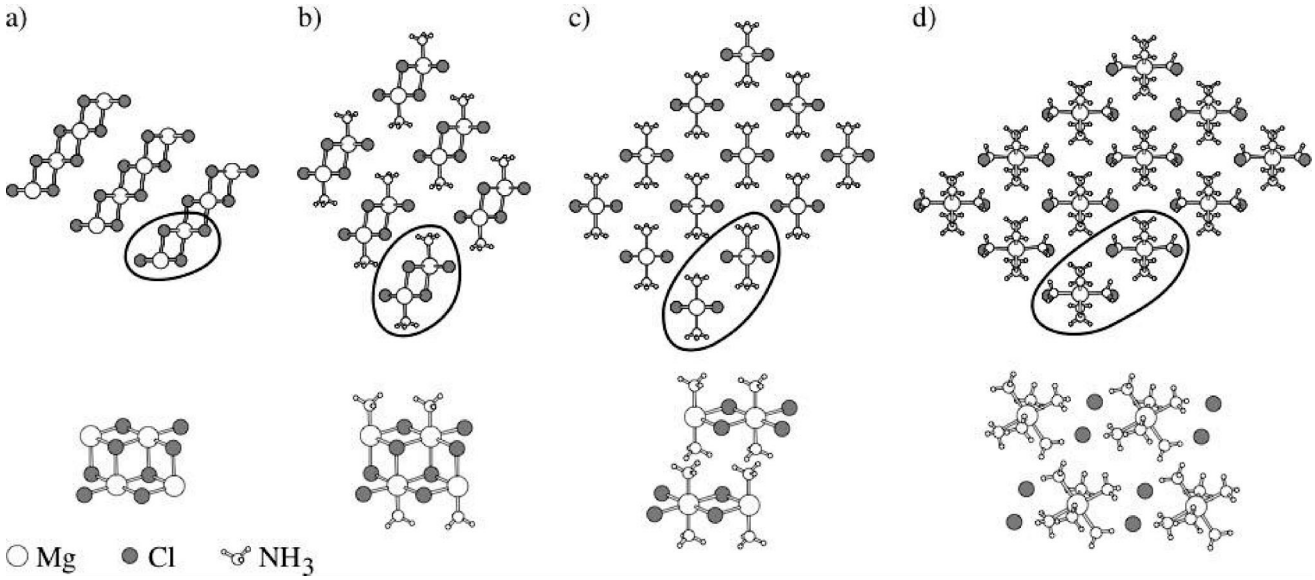

Figure 7. Optimized structures found using DFT for (a) $MgCl_2$, (b) $Mg(NH_3)Cl_2$, (c) $Mg(NH_3)_2Cl_2$, and (d) $Mg(NH_3)_6Cl_2$, viewed along the chains that continue infinitely in and out of the picture. Four formula units are shown from the side, corresponding to the highlighted fragments in the end view.

the mechanistic details underlying the fast ab/desorption processes observed for these materials as described above, and finally also to predict potential electronic trends, which can be utilized in the design of novel metal ammines with optimized properties in hydrogen/ammonia storage.

Calculation of Desorption Enthalpies. We determine the desorption enthalpy of going from one phase to another as the difference in total energy between the most stable structures found for the two phases plus the gas-phase energy of the released ammonia molecules. The energy of an ammonia molecule in the gas phase is calculated by placing one molecule in a vacuum cube of side length 10 Å; zero-point energies are not included.

Structures of $Mg(NH_3)_nCl_2$. To determine the most stable structures for the different ammine phases, a rigorous search was first performed on the $Mg(NH_3)_nCl_2$ ($n = 6, 2, 1, 0$) systems based on the experimentally reported structures.[49–52] In all the structures, a central magnesium atom is coordinated octahedrally to six ligands, i.e., either chlorine atoms for $n = 0$, ammonia molecules for $n = 6$, or a combination of the two for $n = 2$ or 1, as shown in Figure 7.

For $n = 6$, the structure is of the K_2PtCl_6 type[49] and is traditionally described as octahedral $Mg(NH_3)_6$ complexes contained in a cubic lattice of chlorine atoms, with Mg body-centered and NH_3 face-centered in every second cube of chlorine atoms, but the structure can also be described as chains of $Mg(NH_3)_6Cl_2$, as seen in Figure 7d, running along the face diagonals of the cubes. In the optimized DFT structure, the experimentally observed K_2PtCl_6 structure is slightly distorted.

For $n = 2$, each chlorine atom is shared by two neighboring magnesium atoms in edge-sharing octahedral chains. The space group is *Cmmm*, with cell parameters $a = 8.73$ Å, $b = 8.82$ Å, and $c = 4.17$ Å somewhat larger than the experimental ones of $a = 8.18$ Å, $b = 8.21$ Å, and $c = 3.76$ Å.[50]

For $n = 1$, a chlorine atom is shared by three magnesium atoms in edge-sharing double octahedral chains. In the experimental structure found for $Ni(NH_3)Cl_2$,[51] which is believed to be isostructural with the $Mg(NH_3)Cl_2$ equivalent, the double octahedral chains have two orientations in the $I2/m$ space group. This structure was reproduced in our calculations; however, a structure very similar to this one with respect to coordination of the H atoms, but with only one orientation of the chains, was found to have the same energy. For practical computational reasons, the simple structure as shown in Figure 7b was chosen for further calculations.

For $n = 0$, the octahedra of chlorine atoms with central magnesium atoms share half of their edges, resulting in layers of $MgCl_2$ of the $CdCl_2$ type. The space group is $R\bar{3}m$, with $a = 3.78$ Å and $c = 18.52$ Å, compared to $a = 3.64$ Å and $c = 17.67$ Å in the experiment.[52] As found in experiments,[52] the octahedra that are occupied by Mg are flattened, and the empty octahedra between the layers are elongated. The ratio of the short and the long edges of the occupied octahedra are $r = 0.92$, close to the value of $r = 0.934$ from the experiment.[52] In general, the lattice is a little expanded in the calculations due to the RPBE[48] functional used. The RPBE functional is known to overestimate lattice constants slightly. For a weakly bonded system like the one treated here, we expect to see this problem even more clearly—this is a general feature of GGA-type exchange correlation functionals. We will show in the following that this does not affect the ability of the RPBE functional to describe trends in stability of the ammines.

The interaction between individual $Mg(NH_3)_nCl_2$ chains in the respective structures can be examined quantitatively by comparing the total energy of a $Mg(NH_3)_nCl_2$ structure with the total energy of a $Mg(NH_3)_nCl_2$ chain in vacuum. This shows that the energy per Mg atom needed to move a chain of $Mg(NH_3)_nCl_2$ from the bulk to vacuum is 26, 48, and 76 kJ/mol for $n = 1$, 2, and 6, respectively. For $n = 0$, the corresponding value is 15 kJ/mol, calculated as the binding between fragments (highlighted in Figure 7a) of the $MgCl_2$ layers. The layers of $MgCl_2$ are actually slightly repulsive in this description.

To understand the nature of the interaction between the chains and layers of $Mg(NH_3)_nCl_2$, we use density difference plots, where the ground-state electron density of a given structure is subtracted from that of the individual atomic species comprising

(49) Olovsson, I. *Acta Crystallogr.* **1965**, *18*, 889–893.
(50) Leineweber, A.; Friedriszik, M. W.; Jacobs, H. *J. Solid State Chem.* **1999**, *147*, 229–234.
(51) Leineweber, A.; Jacobs, H.; Ehrenberg, H. *Z. Anorg. Allg. Chem.* **2000**, *626*, 2146–2152.
(52) Partin, M. *J. Solid State Chem.* **1991**, *95*, 176–183.

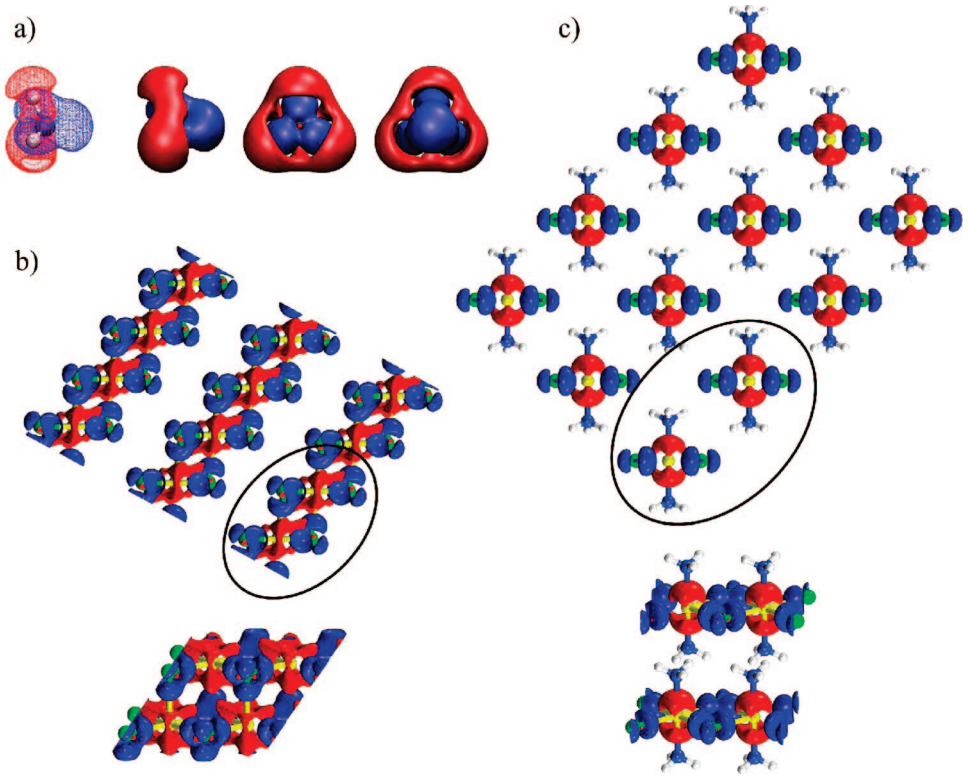

Figure 8. Density difference plots of (a) a NH_3 molecule, (b) $MgCl_2$, and (c) Mg and Cl in $Mg(NH_3)_2Cl_2$ (yellow, Mg; green, Cl; blue, N; and white, H). Blue areas correspond to an excess of electrons or negative charge, and red indicates depletion of electrons or positive charge. In (b) and (c), four formula units are shown from the side, corresponding to the highlighted fragments in the end view.

the structure treated alone and in the same positions. This effectively shows how the electron density is redistributed, and by plotting isosurfaces of density increments and decrements, negatively and positively charged areas become visible.

Some density difference plots are shown in Figure 8, where one can see (i) the lone pair of ammonia and the positively charged hydrogen atoms (Figure 8a); (ii) how the electrons concentrate around the chlorine atoms in a $MgCl_2$ layer (Figure 8b), with the negatively charged areas protruding the layer, rendering them slightly repulsive; and (iii) the charge redistribution caused by Mg and Cl alone in the $Mg(NH_3)_2Cl_2$ structure (Figure 8c), showing how the ammonia molecules fit nicely. In general, the lone pair of ammonia connects to the positively charged areas surrounding the magnesium atoms, and the positively charged hydrogen atoms connect to the negatively charged areas near the chlorine atoms.

Thus, the chains for $n = 6$, 2, and 1 are interconnected by the electrostatic attraction between the positively charged H atoms of an ammonia molecule and the negatively charged Cl atoms (Figure 8a,c). For $n = 0$, the layers are slightly repulsive, and the real structure is therefore mainly held together by van der Waals forces, which are not accurately described in these DFT calculations.

Structures of the Ca, Mn, and Ni Salts. The structures found for the Mg salt were also used for the three other salts (Ca, Mn, Ni) by simply exchanging the metal atoms and letting the structures relax while scaling the unit cell size linearly until a minimum in total energy was reached.

For $Mn(NH_3)_nCl_2$ and $Ni(NH_3)_nCl_2$, this approximation is expected to be rather precise, since these salts are known to be isostructural with the magnesium analogue for $n = 6$ and 0 and for nickel with $n = 2$ as well.[49,53,54] The $Ca(NH_3)_nCl_2$ structures, on the other hand, are different and, moreover, go through $n = 8$, 4, 2, 1, and 0. However, since the experimental enthalpies for the 8→4 and 4→2 transitions are very close in energy (41 and 42 kJ/mol, respectively; see Table 3), we rely on the 6→2 reaction enthalpy of the model to provide a reasonable approximation for both of these; here, an enthalpy of 41 kJ/mol was chosen for comparison with the 6→2 reaction enthalpy of the model.

Results I: Desorption Enthalpies from a Stable Structure Comparison. The calculated desorption enthalpies are compared with experimental values (see Figure 9), and it is seen that the DFT model is able to quite accurately describe the trends in desorption enthalpies of the metal ammine salts studied here.

A straight line is obtained in Figure 9, but the slope is less than 1; i.e., the calculated enthalpies of desorption are too low by a certain factor. The inclusion of zero-point energies or the use of other exchange-correlation functionals only amounts to a shift of the line and cannot account for the slope being less than 1. Although the absolute numbers are not accurate, the trend is very clear, and the precision of Figure 9 is usually considered more than acceptable in a DFT study like this.[48]

Fast Ab/Desorption Processes. To understand the fast ab/desorption of ammonia in the metal ammine salts, we considered the structures again, but this time from the perspective of how ammonia can get in and out of these materials. We restrict the discussion to involve only the isostructural Mg, Mn, and Ni salts and focus on the magnesium salt as a representative.

As mentioned previously, clean $MgCl_2$ has a layered structure, while the structures of $Mg(NH_3)_nCl_2$ for $n = 1$, 2, and 6 consist

(53) Ferrari, A.; Bigliard, G.; Braibant, A. *Acta Crystallogr.* **1963**, *16*, 846–847.
(54) Leineweber, H. *J. Solid State Chem.* **2000**, *152*, 381–387.

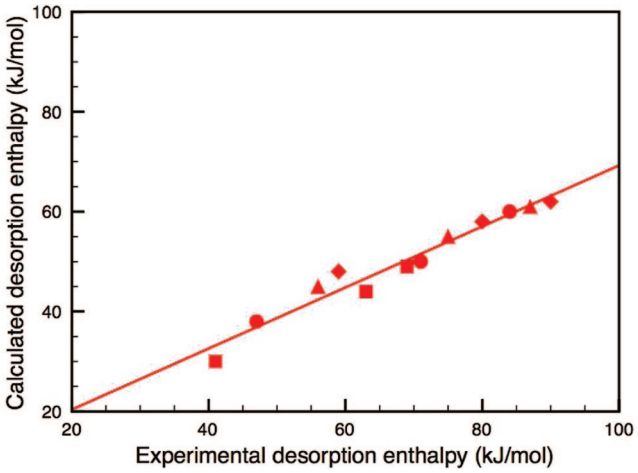

Figure 9. Calculated versus experimental desorption enthalpies for the different desorption steps, 6→2, 2→1, and 1→0, of $Mg(NH_3)_6Cl_2$ (triangles), $Ca(NH_3)_8Cl_2$ (squares), $Mn(NH_3)_6Cl_2$ (circles), and $Ni(NH_3)_6Cl_2$ (diamonds) and in a comparison of stable structures. The calcium salt is approximated by model hexaammine salt $Ca(NH_3)_6Cl_2$, which follows the same desorption route as the three other salts. In this approximation, the first desorption step is representative of the first two desorption steps of the real octaammine salt, $Ca(NH_3)_8Cl_2$.

of chains (see Figure 7). Going from one phase to another, the chains/layers of the initial structure are either cleaved to absorb ammonia or recombined to desorb ammonia. For the 6→2/2→6 reactions, the chains are merely stretched/compressed (see Figure 7). In all cases, the resulting chains or layers are rearranged to produce the final structure.

The details of this cleavage and recombination and the detailed mechanism for transport of ammonia into and out of the materials are unknown, but both desorption and absorption are known from experiments to be facile.[40] We shall first consider the situation where bulk diffusion of ammonia is the dominant transport process.

Bulk Diffusion in Metal Ammines. The transport of ammonia out of the systems during desorption could be dominated by bulk diffusion of ammonia. Indeed, from Figure 7, it seems likely that, if ammonia desorbs by diffusing along the chains of $Mg(NH_3)_nCl_2$, the system can transform from one bulk phase directly to another in a continuous way. However, the barriers for diffusion need to be sufficiently small that no competing mechanisms become dominant.

The barriers for diffusion along the chains of $Mg(NH_3)_nCl_2$ have been calculated to be 58, 135, and 121 kJ/mol for $n = 6$, 2, and 1, respectively; this is clearly too high for $n = 2$ and 1 when compared with the experimental desorption enthalpy. If bulk diffusion of ammonia were indeed rate-limiting, one would expect the last two peaks in a TPD experiment to be broader than the first peak, which is not the case, as seen in Figure 3.

Although the bulk diffusion picture cannot be ruled out, at least for the $n = 6$ case, an alternative mechanism would be desirable. In the following, such a mechanism, which explains the fast kinetics for both the absorption and desorption processes, is proposed.

Restructuring at the Surface. We now consider the rather weak binding between the individual chains in $Mg(NH_3)_nCl_2$ (15, 26, 48, and 76 kJ/mol for $n = 0$, 1, 2, and 6, respectively), which allows for an alternative desorption process in which the individual chains are released from the surface to facilitate desorption or absorption of ammonia from or to the chains (see Figure 10), as investigated in the following.

Three principles underlie the proposed mechanism for understanding the dynamics of ammonia absorption and desorption: (a) it is energetically preferred for Mg to retain a six-fold coordination to the ligands (either Cl or NH_3), (b) chains are released from the surface to facilitate desorption or absorption, and (c) reactions involving a minimal number of chains are expected to be faster.

When a chain is released from the hexammine (Figure 10a), it releases four of its six NH_3 molecules per Mg and transforms into a diammine chain, thus maintaining the energetically preferred six-fold coordination of the Mg atoms (four Cl's substitute the released NH_3). If the hexammine chain were to release more than four NH_3 molecules directly, it would require the expectedly slower combination of two or more chains to keep the Mg atoms fully coordinated. The formed diammine chains will subsequently arrange into the bulk structure of $Mg(NH_3)_2Cl_2$.

As the temperature is further increased, chains break off from the diammine structure (Figure 10b). For this desorption reaction, a minimum of two chains must combine to release (half their) NH_3 molecules, in order to maintain the six-fold Mg coordination. The resulting monoammine chains later rearrange into the bulk structure of $Mg(NH_3)Cl_2$.

Similarly, for the monoammine structure (Figure 10c), chains combine in pairs to give $Mg(NH_3)_{0.5}Cl_2$ chains. This combination of chains to release NH_3 and form chains of lower ammonia content can, in principle, continue until all the ammonia is desorbed and the layered structure of $MgCl_2$ is formed. The intermediate $n < 1$ chains are, in general, not expected not to be stable, and therefore not detected in the experiments, except for $Mn(NH_3)_nCl_2$, which finds a stable arrangement of the $Mn(NH_3)_{0.5}Cl_2$ chains (see Figure 3b).

For absorption the picture is reversed, and the chains/layers are cleaved instead of combined (Figure 10d−f).

Results II: A New Scheme for Calculating Desorption Enthalpies. We have presented a model for the detailed mechanism behind desorption and absorption processes in metal amine salts, and we now return to the modeling of desorption enthalpies. In the alternative mechanism, the system does not transform directly from one stable structure to the next during desorption. Instead, it goes through an intermediate state where chains of the final phase are free and uncoordinated. These free chains could combine sufficiently fast into the final structure to make it reasonable to compare the energies of the stable structures, as done in Figure 8. However, it is also interesting to model the desorption enthalpies under the assumption that the free chains are sufficiently long-lived to be detected experimentally. In that case, the relevant energy to calculate is the difference between the initial ammine in its stable bulk form and the final ammine as a chain in vacuum. For the 1→0 transition, the relevant free chains are the $Mg(NH_3)_{0.5}Cl_2$ chains, as shown in Figure 10c.

This can easily be done in the DFT calculations, and the results of this scheme applied to all four salts are again compared with apparent experimental desorption enthalpies and shown in Figure 11.

Although the straight line in Figure 11 has a slope of 1, it does not confirm the mechanism presented in Figure 10, nor does it prove that desorption in the TPD experiments is not equilibrated. The slope of less than 1 in Figure 9 could very well be due to limitations in the calculations. However, it does provide a valid way to predict desorption enthalpies using DFT, which appears to be more precise than comparing the energies of the stable structures. More importantly, the mechanism which, as mentioned, is also compatible with the equilibrium situation

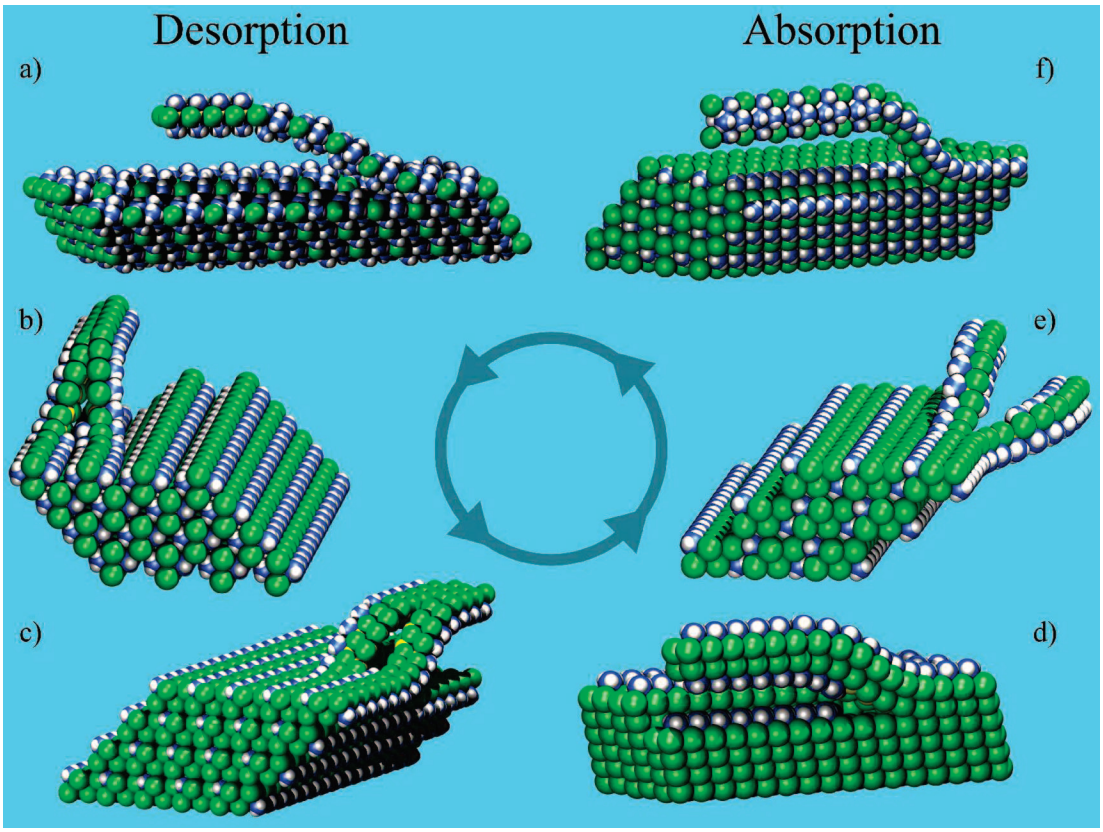

Figure 10. Proposed mechanism for desorption and absorption of ammonia in $Mg(NH_3)_nCl_2$, $Mn(NH_3)_nCl_2$, and $Ni(NH_3)_nCl_2$.

Ⓦ Animations illustrating front and side views of the desorption of ammonia from modeling studies are available.

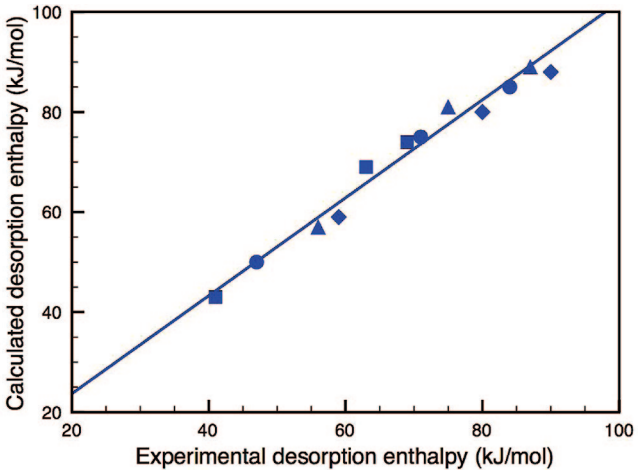

Figure 11. Calculated versus apparent experimental desorption enthalpies for the different desorption steps of $Mg(NH_3)_6Cl_2$ (triangles), $Ca(NH_3)_8Cl_2$ (squares), $Mn(NH_3)_6Cl_2$ (circles), and $Ni(NH_3)_6Cl_2$ (diamonds) for the proposed mechanism in Figure 10.

explains why desorption and absorption can happen fast in all the steps of the ab/desorption processes.

Conclusion

It is demonstrated that metal ammine complexes can be utilized as reversible, indirect hydrogen storage materials. The desorption of ammonia from $Ca(NH_3)_8Cl_2$, $Mn(NH_3)_6Cl_2$, and $Ni(NH_3)_6Cl_2$ is shown to be controlled mainly by thermodynamic equilibrium and heat transfer, as previously shown for $Mg(NH_3)_6Cl_2$. It is shown that the metal ammine complexes can be compacted to tablets with densities very close to the crystal densities and still maintain the same desorption properties. This is due to the development of nanopores in the tablets during desorption of ammonia. The nanopores facilitate diffusion of ammonia through the dense tablets.

DFT calculations are shown to reproduce accurately the trends in desorption enthalpies for all the systems studied. On the basis of extensive DFT calculations, we propose a mechanism for absorption and desorption of ammonia from metal ammine salts in which chains of the ammines are released from the surface of the crystal to explain the fast ab/desorption processes observed experimentally.

Acknowledgment. The authors thank Marina Y. Kustova and Mo Hongling Sønnichsen for experimental assistance and Amminex A/S for providing $Mg(NH_3)_6Cl_2$. The Danish National Research Foundation sponsors the Center for Sustainable and Green Chemistry. Lundbeck Foundation sponsors the Center for Atomic-scale Materials Design. The project is also supported by The Danish Council for Strategic Research (project no. 2104-05-0016) and the European Commission DG Research (contracts SES6-2006-51827/NESSHy and MRTN-CT-2006-032474/HYDROGEN).

Supporting Information Available: Table of thermodynamic properties of 90 metal ammine complexes. This information is available free of charge via the Internet at http://pubs.acs.org.

JA076762C

Paper II

IOP FTC
IOP PUBLISHING JOURNAL OF PHYSICS: CONDENSED MATTER
J. Phys.: Condens. Matter **21** (2009) 012203 (7pp) doi:10.1088/0953-8984/21/1/012203

FAST TRACK COMMUNICATION

Structural stability and decomposition of $Mg(BH_4)_2$ isomorphs—an *ab initio* free energy study

J Voss[1,2], J S Hummelshøj[1,2], Z Łodziana[3] and T Vegge[1]

[1] Materials Research Division, Risø National Laboratory for Sustainable Energy, Technical University of Denmark, Roskilde, Denmark
[2] Center for Atomic-scale Materials Design, Department of Physics, Technical University of Denmark, Kongens Lyngby, Denmark
[3] Department of Mobility, Environment, and Energy, EMPA Materials Sciences and Technology, Dübendorf, Switzerland

E-mail: tejs.vegge@risoe.dk

Received 16 October 2008, in final form 30 October 2008
Published 1 December 2008
Online at stacks.iop.org/JPhysCM/21/012203

Abstract

We present the first comprehensive comparison between free energies, based on a phonon dispersion calculation within density functional theory, of theoretically predicted structures and the experimentally proposed α ($P6_1$) and β ($Fddd$) phases of the promising hydrogen storage material $Mg(BH_4)_2$.

The recently proposed low-density $I\bar{4}m2$ ground state is found to be thermodynamically unstable, with soft acoustic phonon modes at the Brillouin zone boundary. We show that such acoustic instabilities can be detected by a macroscopic distortion of the unit cell. Following the atomic displacements of the unstable modes, we have obtained a new $F222$ structure, which has a lower energy than all previously experimentally and theoretically proposed phases of $Mg(BH_4)_2$ and is free of imaginary eigenmodes. A new meta-stable high-density $I4_1/amd$ structure is also derived from the $I\bar{4}m2$ phase.

Temperatures for the decomposition are found to be in the range of 400–470 K and largely independent of the structural complexity, as long as the primary cation coordination polyhedra are properly represented. This opens a possibility of using simple model structures for screening and prediction of finite temperature stability and decomposition temperatures of novel borohydride systems.

S Supplementary data are available from stacks.iop.org/JPhysCM/21/012203

1. Introduction

The search for novel hydrogen storage materials which combine high hydrogen content with the potential for reversible storage under near ambient conditions has directed the focus from alanates to borohydride systems. The binary alkali borohydrides, e.g. $LiBH_4$ [1, 2], are found to be too thermodynamically stable, whereas the divalent $Ca(BH_4)_2$ and in particular $Mg(BH_4)_2$ have extracted interest, since empirical [3] and density functional theory (DFT) calculations on model structures [4] have indicated highly favorable thermodynamical properties.

Although originally synthesized in 1950 [5], a specific crystal structure was not proposed for $Mg(BH_4)_2$ until 2007, when Černý *et al* [6] and Her *et al* [7], independently, proposed a hexagonal 'low-temperature' (α) $P6_1$ phase consisting of 330 atoms in the unit cell and a density of $\rho = 0.78$ g cm^{-3}. Her *et al* [7] furthermore proposed an anti-phase boundary modification of an orthorhombic $Fddd$ super structure (704 atoms) as a 'high-temperature' (β) phase ($\rho = 0.76$ g cm^{-3}), and observed at least one additional modification. Chłopek *et al* [8] have presented XRD and DSC data, which indicates that even the $P6_1$ (α) phase could be meta-stable. Neither

of these structures can, however, account for the tetragonal, high-density ($\rho = 0.99$ g cm^{-3}) phase originally obtained by Konoplev and Bukulina in 1971 [9], using a different synthesis procedure.

Prior to the characterization of the α-phase, a number of simpler structures had been proposed on the basis of density functional theory (DFT) calculations: a hexagonal structure in space group $P\bar{3}m1$ [4] and a orthogonal structure in space group $Pmc2_1$ [10]; recently, the ground state energies of the α and β phases were calculated independently by Ozolins *et al* [11] and Dai *et al* [12]. Van Setten *et al* [13] later estimated free energies from the Γ-point frequencies, excluding unstable modes with larger wavevectors, that lead to larger structures with lower energies.

The phase stability can only be determined from the free energy, and we present the first direct comparison of free energies based on the calculation of the phonon dispersion of the most stable theoretically predicted structures and the experimentally proposed α and β super-structures, yielding surprisingly small differences between ground state energies and free energies of these structures.

Based on a vibrational analysis of the recently proposed low-density $I\bar{4}m2$ phase [11], which indicates thermodynamic instability of this phase, we obtain a new $F222$ structure of $Mg(BH_4)_2$. We find the $F222$ phase to have a lower free energy than any other proposed experimental or theoretical structure. We also identify the existence of a new metastable high-density ($\rho = 1.01$ g cm^{-3}) tetragonal $I4_1/amd$ structure without instabilities, which may account for the experimentally observed and uncharacterized tetragonal high-density structure ($\rho = 0.99$ g cm^{-3}) [9]. This phase can be interpreted as a folded form of the low-density $I\bar{4}m2$ structure ($\rho = 0.56$ g cm^{-3}).

We believe that the specific conditions of the current chemical synthesis procedure [8] combined with kinetically limited phase transitions between the large super-structures could account for the lack of (recent) experimental observations of $F222$ or $I4_1/amd$, and we anticipate future experimental verification of a highly complex phase diagram, similar to that of $Ca(BH_4)_2$ [14], e.g., by use of high pressure experiments.

The calculations also show that the thermodynamic properties of even highly complex borohydride super-structures can be well estimated by DFT using even simple model structures, if the primary coordination polyhedra are correctly accounted for. A purely thermodynamic estimate, i.e. not considering the inherently slow kinetics of borohydride systems [8], of the decomposition temperature yields values of 400–470 K for the idealized decomposition, $Mg(BH_4)_2 \rightarrow MgH_2 + 2B + 3H_2$, for the complex and the simple unit cell structures.

These findings enable faster screening studies of thermodynamic stability and decomposition temperatures for, e.g., ternary and quaternary borohydride systems; not only in terms of reduced computational effort due to smaller system sizes, but also with the advantage that the exact space group need not be known *a priori*.

2. Computational details

Total energies and gradients were calculated within density functional theory [15] (DFT) using the Vienna *ab initio* Simulation Package (VASP) [16]. The Kohn–Sham wavefunctions [17] were expanded in plane-wave basis sets with energy cut-offs of up to 500 eV. Brillouin zone sampling was performed on meshes with a k-point spacing of $\leqslant 0.03$ Å^{-1} (for the larger $P6_1$ and $Fddd$ structures, the spacing was $\leqslant 0.06$ Å^{-1}). The Perdew-Wang-91 exchange–correlation functional [18, 19] was used in combination with the projector-augmented wave method [20], using parametrizations due to Kresse and Joubert [21].

Phonon dispersions and phonon densities of states were calculated by the direct method in the harmonic approximation with the software package Phonon [22], using the Hellmann–Feynman forces from minimal sets of atomic displacements. To resolve inter-atomic couplings, super-cells containing no less than eight formula units of $Mg(BH_4)_2$ were used.

Due to the large system sizes, the $P6_1$ and $Fddd$ structures were treated separately and only the contributions of the dispersion folded to the Γ-point in super-cells containing 330 and 704 atoms, respectively, were considered; this is generally a good approximation due to the very large super-cells. The corresponding densities of states have been obtained by differentiating a spline interpolation of the integrated phonon density of states at the super-cell Γ-point. The integrated density $G(\omega)$ is given by

$$G(\omega) = \sum_{i=1}^{3N} \Theta(\omega - \omega_i), \tag{1}$$

with the Heaviside function $\Theta(\omega)$ and the phonon frequencies ω_i.

For perfect crystalline solids, the vibrational contribution to the free energy is most important, and can be calculated in the harmonic approximation from the normalized phonon density of states $g(\omega)$ as

$$F_{\mathrm{vib}}(T) = r\, k_{\mathrm{B}} T \int_0^\infty \mathrm{d}\omega\, g(\omega) \ln\left[2 \sinh\left(\frac{\hbar\omega}{2k_{\mathrm{B}}T}\right)\right], \tag{2}$$

where r is the number of degrees of freedom in the unit cell and k_{B} is Boltzmann's constant.

3. Analysis

The experimentally [6, 7, 9] and theoretically [4, 10, 11] proposed phases of $Mg(BH_4)_2$ vary significantly in density, coordination and complexity. In order to evaluate the stability of the proposed structures, we present the first comparison of the stability of the different $Mg(BH_4)_2$ phases based on DFT lattice free energy calculations. We have calculated the ground state energies and phonon density of states for the experimentally proposed $P6_1$ [6] and $Fddd$ [7] structures, and theoretically proposed $Pmc2_1$ [10], $P\bar{3}m1$ [4], and $I\bar{4}m2$ [11] phases. We furthermore present results for three other structures, a monoclinic Pm (figure 2; coordinates and

Table 1. Calculated lattice parameters and Wyckoff coordinates of $I4_1/amd$-$Mg(BH_4)_2$.

$I4_1/amd$	$a = 8.252$ Å	$c = 10.474$ Å
Mg	(4*a*) (0, 0.75, 0.125)	
	(4*b*) (0, 0.25, 0.375)	
B	(16*h*) (0, 0.4846, 0.2305)	
H	(16*h*) (0, 0.6135, 0.2880)	
	(16*h*) (0, 0.4970, 0.1142)	
	(32*i*) (0.8368, 0.3745, 0.4902)	

Table 2. Calculated lattice parameters and Wyckoff coordinates of $F222$-$Mg(BH_4)_2$.

$F222$	$a = 9.928$ Å	$b = 11.183$ Å	$c = 11.891$ Å
Mg	(4*a*) (0, 0, 0); (4*c*) (1/4, 1/4, 1/4)		
B	(16*k*) (0.09904, 0.1383, 0.1316)		
H	(16*k*) (0.1314, 0.1030, 0.2252)		
	(16*k*) (0.1651, 0.08003, 0.06345)		
	(16*k*) (0.1223, 0.2438, 0.1127)		
	(16*k*) (0.9769, 0.8735, 0.8747)		

unit cell parameters in the supplementary material available at stacks.iop.org/JPhysCM/21/012203) phase, a tetragonal $I4_1/amd$ (figure 3(b); coordinates and lattice constants in table 1), and the orthorhombic $F222$ structure (figure 4; coordinates and unit cell parameters in table 2), which all capture the ideal local coordination and display interesting characteristics.

3.1. Structural coordination

In order to understand why $Mg(BH_4)_2$, in contrast to most metal borohydrides, apparently forms large superstructures, and to understand the significance of the structural contributions to the total energy, we first analyze the coordination of the proposed structures.

Based on this analysis, we propose a $I4_1/amd$ (figure 3(b)) structure, which has the same topology as the experimental structures and the high-density phase observed in [9].

All the $Mg(BH_4)_2$ structures compared here show a tetrahedral arrangement of BH_4^- ions around the Mg ion, except for $P\bar{3}m1$ proposed by Nakamori *et al* [4], which consists of identical layers of edge-sharing octahedra. For all the tetrahedral structures, the tetrahedra are corner sharing, but the connection of the coordination polyhedra is much more complex for the α- and β-phases than for the theoretically proposed phases [7].

The octahedral $P\bar{3}m1$ phase can be interpreted as consisting of an ABAB$\cdots$ stacking of boron planes with magnesium in half of the octahedral interstices (figure 1(a)), and it is the most dense of the structures, with a density of 1.04 g cm^{-3}. This structure is in essence close packed, and therefore provides an upper bound of the mass density that can be achieved. The dense $Pmc2_1$, Pm, and $I4_1/amd$ structures follow an ABCABC$\cdots$ stacking (figures 1(b)–(d)). The Pm phase is the smallest structure (11 atoms per unit cell) which captures the optimal primary coordination.

The new $I4_1/amd$ corresponds to two identical $I\bar{4}m2$ sub-lattices of corner-sharing tetrahedra folded into each other

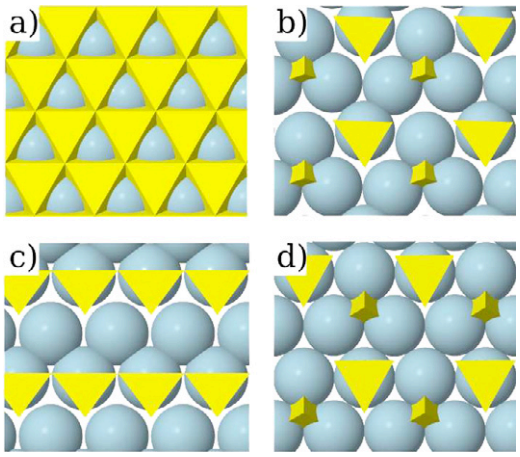

Figure 1. The (a) $P\bar{3}m1$ ($\rho = 1.04$ g cm^{-3}) and (b) $Pmc2_1$ ($\rho = 0.88$ g cm^{-3}) and the proposed (c) Pm ($\rho = 0.91$ g cm^{-3}) and (d) $I4_1/amd$ ($\rho = 1.01$ g cm^{-3}) structures of $Mg(BH_4)_2$. The blue spheres represent the Mg atoms and the yellow tetrahedra the BH_4^- groups. Note the small difference between the $Pmc2_1$ and the $I4_1/amd$ phases.

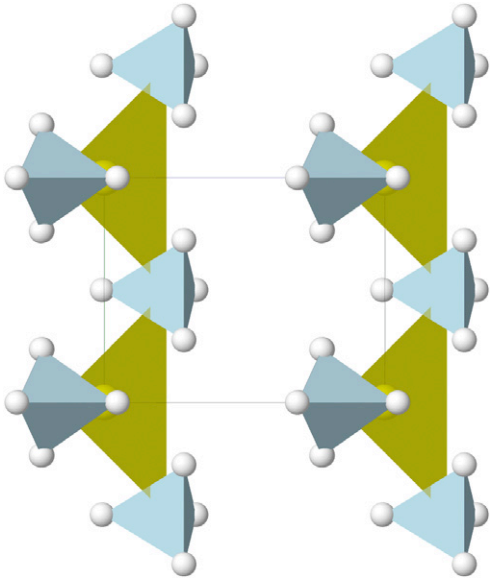

Figure 2. The structure of Pm. Yellow tetrahedra represent the Mg–B coordination and blue tetrahedra the BH_4^- groups.

and thereby forming a close-packed structure (figure 3(b)). The main difference between the $I\bar{4}m2$, $I4_1/amd$, and $F222$ structures and the previously proposed theoretical ones lies in the arrangement of the polyhedra; the latter being layered and the first forming 3D networks, as observed for the experimental structures. Where the experimental structures have huge unit cells with five, eight, and ten membered rings of tetrahedra in $P6_1$ and four and eight membered rings in $Fddd$, the $I\bar{4}m2$ unit is much simpler and has only one kind of six membered rings. In $P6_1$ the rings penetrate each other, while for $I4_1/amd$ the rings belonging to each of the two $I\bar{4}m2$ sub-lattices penetrate the other (figure 5).

In the following, the influence of the differences in coordination on the structural stability is studied energetically,

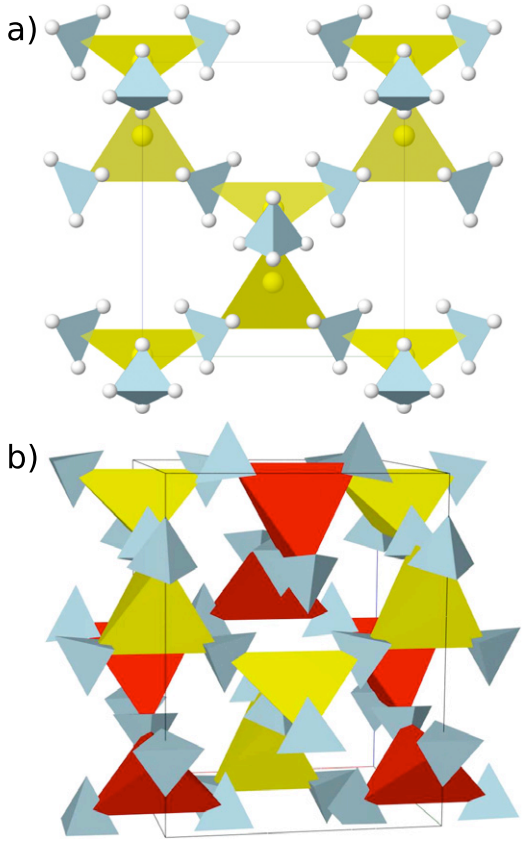

Figure 3. The (a) $I\bar{4}m2$ and (b) $I4_1/amd$ structures of $Mg(BH_4)_2$. Note the similarity of the $I4_1/amd$ phase to a double-folded $I\bar{4}m2$ structure. The yellow and red tetrahedra show the coordination of the B atoms around the Mg atoms. Blue tetrahedra represent the BH_4^- groups.

Table 3. Comparison of densities and ground state and lattice free energies per formula unit (ΔE_{gs} (relative to ground state energy of $P6_1$) and F_{vib}, respectively) of the considered $Mg(BH_4)_2$ phases.

	ρ (g cm^{-3})	ΔE_{gs} (eV)	F_{vib} (eV) (300 K)
$F222$	0.54	−0.10	2.02
$I\bar{4}m2$	0.56	−0.09	2.06
$I4_1/amd$	1.01	0.14	2.04
$P6_1$	0.82	0.00	2.12
$Fddd$	0.90	0.10	2.09
$Pmc2_1$	0.88	0.14	2.02
Pm	0.91	0.23	2.00
$P\bar{3}m1$	1.04	0.35	2.07

taking into account both the ground state energy of the electron–ion system and the lattice free energy.

3.2. Electronic density of states (DOS)

To study the influence of changing the coordination on the electronic structure, the electronic densities of states have been calculated.

A comparison of the electronic density of states (DOS) for the proposed structures (see figure 6) shows only small differences between the shapes of the DOS. All phases are insulators with calculated band gaps of around 6 eV.

The electrostatic ion–ion and ion–electron interaction energy is significantly higher for the low-density $I\bar{4}m2$ and

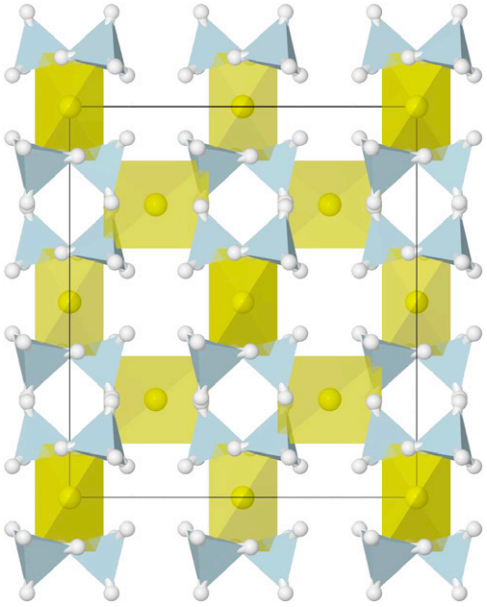

Figure 4. The structure of $Mg(BH_4)_2$ in space group $F222$ (blue tetrahedra, coordination of the B atoms; yellow tetrahedra, coordination of Mg with B atoms).

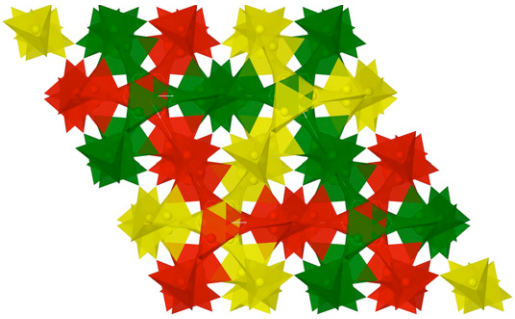

Figure 5. The structure of $P6_1$ $Mg(BH_4)_2$. Shown are the Mg–B tetrahedra. Different colors are used to distinguish different coordination rings.

$F222$ phases than for the other phases. This energy difference is slightly overcompensated by lower electronic energies, resulting in a lower total energy for the $F222$ phase (see table 3) than all other previously proposed structures (the electronic densities of states in figure 6 are plotted against the Fermi levels; the Fermi level is e.g. 1.54 eV lower per formula unit for the $F222$ than for, e.g., the $P6_1$ phase).

3.3. Phonon DOS

To investigate the stability and the influence of the structural differences on the vibrational free energies and the decomposition temperatures, we have calculated the phonon densities of states (PDOS) for the different phases.

Figure 7 shows the calculated PDOS for the analyzed structures. All spectra share general characteristics consisting of three separate bands (except for $P\bar{3}m1$, which shows further splitting). The low frequency regime at 0–20 THz is due to acoustic modes and optical modes in the magnesium/boron

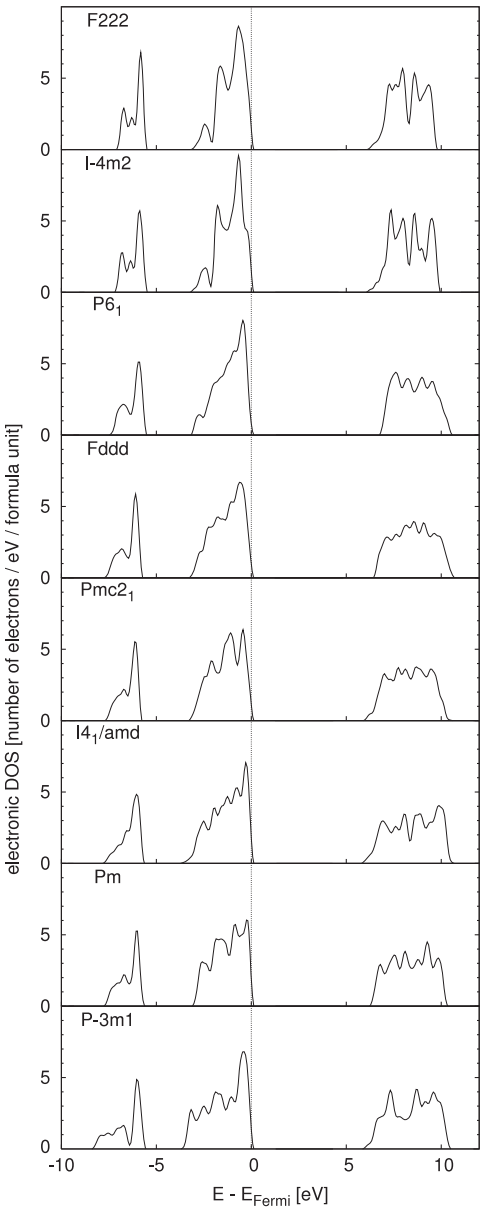

Figure 6. Electronic densities of states for different phases of $Mg(BH_4)_2$ plotted relative to the respective Fermi energies.

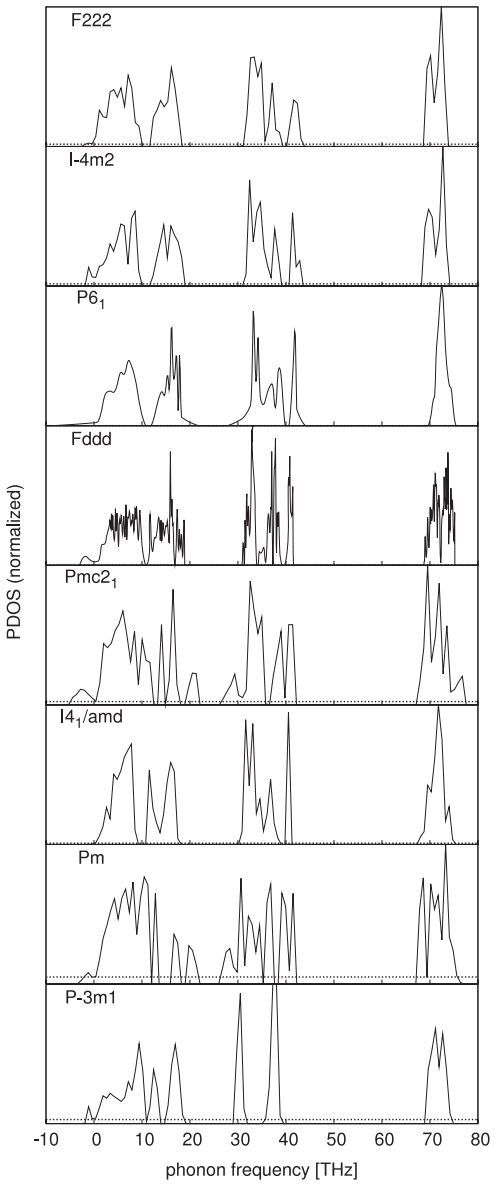

Figure 7. Normalized phonon densities of states for different phases of $Mg(BH_4)_2$. Imaginary frequencies are represented by negative real values. The dashed lines indicate the error of 0.1 THz^{-1} per mode in the PDOS associated with the modes, due to the numerically unresolved translational symmetry.

framework, the medium range (30–40 THz) corresponds to libration modes, and the narrow high frequency regime at ∼70 THz to B–H stretching vibrations.

The PDOSs of the structures are very similar, in particular for the most stable $F222$, $I\bar{4}m2$, $I4_1/amd$ and $P6_1$ phases (the $Pmc2_1$ phase was recently shown to be unstable by Ozolins *et al* [11]), all displaying optical modes in the low frequency domain and a very narrow B–H stretching band. In contrast to the other phases, the librational band of the $P\bar{3}m1$ phase is split into two peaks, caused by the differences in primary structure.

The existence of imaginary modes not resulting from numerically unresolved symmetries (see figure 7) is an indication of phase instabilities; the corresponding atomic displacements can, however, be followed in order to determine the stable phase. The uncertainty in PDOS per mode due to the numerically unresolved translational invariance is about 0.1 THz^{-1} in the systems considered, as indicated by dashed lines in figure 7.

We have analyzed the phonon dispersion of the most promising previously proposed $I\bar{4}m2$ structure in detail. At the Γ-point, all frequencies are real within the range of numerical accuracy. At the N-point of the Brillouin zone (the center of the zone facet) two acoustic modes become unstable. This is an indication of instability due to long wavelength acoustic vibrations. Instability of the low frequency acoustic phonons can be detected via macroscopic deformation of the unit cell. Indeed, an $\epsilon_{x,y}$ shear deformation combined with a relaxation of the internal degrees of freedom and the volume of the unit cell leads to a lowering of the total energy by 6 meV/f.u.

In order to identify the corresponding ground state structure, we have simultaneously imposed atomic coordinate displacements corresponding to the above mentioned unstable modes of the $I\bar{4}m2$ phase. Following the atomic displacements of these modes, we find that the conventional $I\bar{4}m2$ cell is distorted (in agreement with the shear instability mentioned above) to the primitive cell of a structure in space group $C222_1$ and further to $F222$ symmetry (containing 22 atoms per primitive cell). The ground state energy of the $F222$ phase is lower by 10 meV/f.u. compared to the $I\bar{4}m2$ phase. The phonon dispersion of the $F222$ phase shows, within the numerical accuracy, no imaginary frequencies, and we do not find any instabilities with respect to lattice strains, supporting the thermodynamic stability. Also for the proposed $I4_1/amd$ phase, the numerically calculated PDOS is free of imaginary modes, which supports a meta-stability and possible high-pressure existence of this high-density structure.

A zone boundary instability of acoustic modes in the $I\bar{4}m2$ structure points out that a normal mode analysis at the Γ-point may fail in predicting meta-stability of the structure. Therefore, calculations of the stability of the structure with respect to a macroscopic deformation of the unit cell should be applied as an additional measure. For stable structures, deformation of the unit cell leads to an increase in energy according to the elastic properties of the compound ($E_{\mathrm{tot}} \sim C\epsilon^2$, where E_{tot} is the total energy of the system, C is the elastic constant, and ϵ is the deformation tensor of the unit cell). A deviation from harmonic behavior, especially a decrease of the total energy for strained structures, indicates a negative value of C, and therefore that the given structure is thermodynamically unstable with respect to macroscopic deformations.

3.4. Free energies

The free energies of the structures determine the relative stability of the different phases. In order to predict at which temperatures phase transitions would occur, we have calculated the lattice free energies from the PDOS above using equation (2). In order to show that the decomposition temperature of $Mg(BH_4)_2$ can be estimated, even if a stable ground state structure is not known, we have also calculated free energies in the presence of unstable modes by omitting the corresponding imaginary part (~1% integrated PDOS for the unstable structures) of the PDOS from the integration in equation (2).

Plotting the change in free energy as a function of temperature relative to the low-temperature $P6_1$ phase (figure 8), we find the free energy differences for the $Mg(BH_4)_2$ phases to be relatively small owing to the similar PDOSs. The calculated ground state energies (see table 3) are also quite similar, differing by less than 0.1 eV per H_2 (typically <0.05 eV), even though a comparison of the mass densities shows a large variation for the different phases. The simple tetragonal $I\bar{4}m2$ and orthorhombic $F222$ phases are unique, having the lowest ground state energies and a significantly lower density than the other phases. The stable $F222$ structure has the lowest energy of all investigated $Mg(BH_4)_2$ phases.

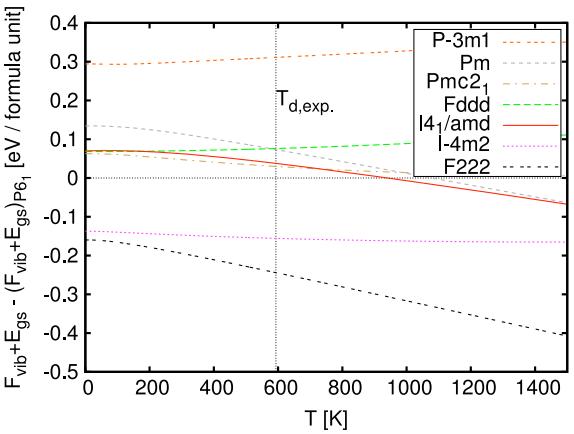

Figure 8. Comparison of free energies with respect to the $P6_1$ low-temperature phase. $T_{\mathrm{d,exp.}} = 320\,^{\circ}\mathrm{C}$ is the experimentally determined temperature for the first decomposition step of $Mg(BH_4)_2$ [8].

The phase with third lowest energy is the $P6_1$ phase. According to our calculations, none of the free energies of the higher energy phases cross that of the $P6_1$ phase below the experimentally determined initial decomposition temperature [8] of 320 °C (figure 8). The $P\bar{3}m1$ (erroneous coordination), and surprisingly also the $Fddd$ phase, show no intersection with the free energy of the $P6_1$ phase at all in the temperature range considered here. We note that the $Fddd$ phase is reported to be composed of disordered layers parallel to the b, c-plane [7], which gives rise to entropic contributions not considered here; both ground state configuration and free energy might therefore be different for the experimentally observed phase. Other non-phononic degrees of freedom, like rotations, will furthermore be of relevance at elevated temperatures [23].

To assess or predict at which temperatures the corresponding most stable phases would decompose to release hydrogen, the free energies of the decomposition products also have to be determined.

3.5. Desorption temperatures

The decomposition of $Mg(BH_4)_2$ was recently proposed to proceed in several steps including the formation of dodecaboranate species [8, 24], but to assess the stability of $Mg(BH_4)_2$ we consider only the following idealized decomposition step:

$$\mathrm{Mg\,(BH_4)_2 \rightarrow MgH_2 + 2B + 3H_2}. \qquad (3)$$

We estimate the desorption temperature by comparing the free energies of the $Mg(BH_4)_2$ phases to the Gibbs free energy of the right hand side of reaction (3) (we neglect pV terms for the solid phases). The lattice free energies of MgH_2 (space group $P4_2/mnm$) and B (space group $R\bar{3}m$) have been calculated using the software package Phonon [22], and values for the Gibbs free energy of H_2 have been interpolated from data in [25].

The temperature dependence of the free energies is shown in figure 9. The desorption temperature for reaction (3) can be

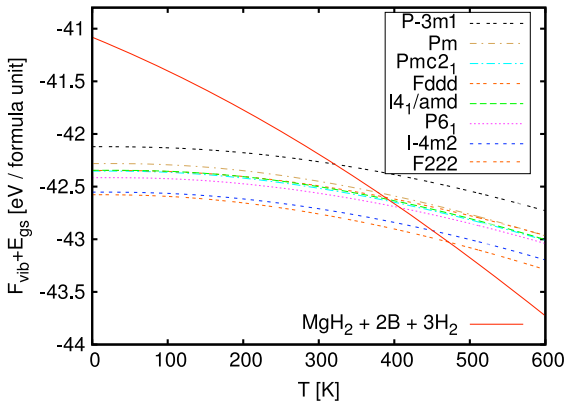

Figure 9. The sum of ground state energy E_{gs} and lattice free energy F_{vib} per formula unit for the different phases of $Mg(BH_4)_2$ and the decomposition products $MgH_2 + 2B + 3H_2$.

estimated to be 400–470 K for all phases with correct primary coordination. Especially if we disregard the high energy of the configurationally different $P\bar{3}m1$ structure, the estimated desorption temperatures differ only a little compared to the accuracy of the DFT-based estimate.

Due to similar PDOSs, the proposed structures would all start to decompose at 400–470 K. This is ∼150 K below the experimentally observed decomposition temperature [8]. This high decomposition temperature is thought to be due to kinetic barriers (in a more complex reaction than (3) [24]) rather than thermodynamic equilibrium properties [8], which have been considered in the calculations presented here.

4. Conclusions

We have analyzed the structural stability of different candidate structures for the promising hydrogen storage material $Mg(BH_4)_2$.

The electronic and phonon density of states are very similar for the investigated phases, resulting in only very small differences in free energies for phases which obey the primary coordination of Mg. By analysis of the instability of the previously proposed $I\bar{4}m2$ phase with respect to a macroscopic transformation of the unit cell characterized by acoustic mode zone boundary instabilities, we have obtained a new structure with $F222$ symmetry. This phase is free of instabilities and has a lower free energy than all other previously proposed structures.

Decomposition temperatures of 400–470 K have been obtained. Since the calculated free energies for the different phases of $Mg(BH_4)_2$ are quite similar from simple systems to very large unit cells, thermodynamic screening studies in, e.g., ternary and quaternary borohydride systems are possible by considering only simple model unit cells for an estimate of the structural stability of these compounds, as long as the expected primary coordination is obeyed.

This means that simple model structures can be used to investigate structural stability of complex structures, even if the crystal symmetries are not known *a priori*. In alloyed systems, e.g. mixed Mg and Ca borohydride, a simple structure should thus allow for tetrahedral and octahedral coordination of Mg and Ca with B atoms, respectively.

We have shown that acoustic instability can be easily detected by macroscopic deformation of the unit cell, constituting a simple method to determine corresponding structural stabilities beyond a vibrational analysis.

Acknowledgments

The authors acknowledge financial support by the NABIIT program funded by the Danish Research Councils for Strategic Research, the European Commission DG Research (contract SES6-2006-51827/NESSHy), and the Danish Center for Scientific Computing (DCSC) for computer time. The Center for Atomic-Scale Materials Design is supported by the Lundbeck Foundation.

References

[1] Ohba N, Miwa K, Aoki M, Noritake T, Towata S I, Nakamori Y, Orimo S I and Züttel A 2006 *Phys. Rev.* B **74** 075110
[2] Łodziana Z and Vegge T 2004 *Phys. Rev. Lett.* **93** 145501
[3] Sarner S F 1966 *Propellant Chemistry* 1st edn (New York: Reinhold)
[4] Nakamori Y, Miwa K, Ninomiya A, Li H, Ohba N, Towata S, Züttel A and Orimo S 2006 *Phys. Rev.* B **74** 045126
[5] Wiberg E and Bauer R 1950 *Z. Naturf.* b **5** 397
[6] Černý R, Filinchuk Y, Hagemann H and Yvon K 2007 *Angew. Chem.* **119** 5867
[7] Her J H, Stephens P W, Gao Y, Soloveichik G L, Rijssenbeek J, Andrus M and Zhao J C 2007 *Acta Crystallogr.* B **63** 561
[8] Chłopek K, Frommen C, Leon A, Zabara O and Fichtner M 2007 *J. Mater. Chem.* **17** 3496
[9] Konoplev V N and Bakulina V M 1971 *Bull. Acad. Sci. USSR Div. Chem. Sci.* **20** 136 (Engl. Transl.)
[10] Vajeeston P, Ravindran P, Kjekshus A and Fjellvåg H 2006 *Appl. Phys. Lett.* **89** 071906
[11] Ozolins V, Majzoub E H and Wolverton C 2008 *Phys. Rev. Lett.* **100** 135501
[12] Dai B, Sholl D S and Johnson J K 2008 *J. Phys. Chem.* C **112** 4391
[13] Setten M J v, Wijs G A d, Fichtner M and Brocks G 2008 *Chem. Mater.* **20** 4952
[14] Riktor M D, Sørby M H, Chłopek K, Fichtner M, Buchter F, Züttel A and Hauback B C 2007 *J. Mater. Chem.* **17** 4939
[15] Hohenberg P and Kohn W 1964 *Phys. Rev.* **136** B864
[16] Kresse G and Furthmüller J 1996 *Phys. Rev.* B **54** 11169
[17] Kohn W and Sham L J 1965 *Phys. Rev.* **140** A1133
[18] Perdew J P, Chevary J A, Vosko S H, Jackson K A, Pederson M R, Singh D J and Fiolhais C 1992 *Phys. Rev.* B **46** 6671
[19] Perdew J P, Chevary J A, Vosko S H, Jackson K A, Pederson M R, Singh D J and Fiolhais C 1993 *Phys. Rev.* B **48** 4978
[20] Blöchl P E 1994 *Phys. Rev.* B **50** 17953
[21] Kresse G and Joubert D 1999 *Phys. Rev.* B **59** 1758
[22] Parlinski K, Li Z-Q and Kawazoe Y 1997 *Phys. Rev. Lett.* **78** 4063
Parlinski K 2005 *Software Phonon* Cracow
[23] Łodziana Z and Vegge T 2006 *Phys. Rev. Lett.* **97** 119602
[24] Hwang S J, Bowman R, Reiter J, Rijssenbeek J, Soloveichik G, Zhao J C, Kabbour H and Ahn C 2008 *J. Phys. Chem.* C **112** 3164
[25] Ke X and Tanaka I 2005 *Phys. Rev.* B **71** 024117

Paper III

DFT based screening of ternary alkali-transition metal borohydrides - a computational materials design project

J. S. Hummelshøj, D. D. Landis, J. Voss, T. Jiang, A. Tekin, N. Bork, M. Dułak, J. J. Mortensen, L. Adamska, J. Andersin, J. Baran, G. D. Barmparis, F. Bell, A. L. Bezanilla, J. Bjork, M. E. Björketun, F. Bleken, F. Buchter, M. Bürkle, P. D. Burton, B. B. Buus, A. Calborean, F. Calle-Vallejo, S. Casolo, B. Chandler, D. H. Chi, I. Czekaj, S. Datta, A. Datye, A. DeLaRiva, V. Despoja, S. Dobrin, M. Engelund, L. Ferrighi, P. Frondelius, Q. Fu, A. Fuentes, J. Fürst, A. García-Fuente, J. Gavnholt, R. Goeke, S. Gudmundsdottir, K. D. Hammond, H. A. Hansen, D. Hibbitts, J. G. Howalt, S. L. Hruby, A. Huth, L. Isaeva, J. Jelic, I. J. T. Jensen, E. H. Junior, K. Kacprzak, A. Kelkkanen, D. Kelsey, D. S. Kesanakurthi, J. Kleis, P. J. Klüpfel, I. Konstantinov, R. Korytar, P. Koskinen, C. Krishna, E. Kunkes, A. H. Larsen, J. M. G. Lastra, H. Lin, O. Lopez-Acevedo, M. Mantega, J. I. Martínez, I. N. Mesa, D. J. Mowbray, J. S. G. Mýrdal, Y. Natanzon, A. Nistor, T. Olsen, H. Park, L. S. Pedroza, V. Petzold, C. Plaisance, J. A. Rasmussen, H. Ren, M. Rizzi, A. S. Ronco, C. Rostgaard, S. Saadi, L. A. Salguero, E. J. G. Santos, A. L. Schoenhalz, J. Shen, M. Smedemand, O. J. Stausholm-Møller, M. Stibius, M. Strange, H. Su, B. Temel, A. Toftelund, V. Tripkovic, M. Vanin, V. Viswanathan, A. Vojvodic, S. Wang, J. Wellendorff, K. S. Thygesen, J. Rossmeisl, T. Bligaard, K. W. Jacobsen, J. K. Nørskov and T. Vegge[1,*]

[1] *The 2008 CAMD Summer School in Electronic Structure Theory and Materials Design, Center for Atomic-scale Materials Design, Department of Physics, Technical University of Denmark, DK-2800 Kongens Lyngby, Denmark*[†]

(Dated: March 13, 2009)

Abstract

We present a computational screening study of ternary metal borohydrides for reversible hydrogen storage based on density functional theory. We investigate the stability and decomposition of alloys containing 1 alkali metal atom, Li, Na or K (M_1); and 1 alkali, alkaline earth or 3d/4d transition metal atom (M_2) plus 2–5 $(BH_4)^-$ groups, *i.e.* $M_1M_2(BH_4)_{2-5}$, using a number of model structures with trigonal, tetrahedral, octahedral and free coordination of the metal-borohydride complexes. Of the over 700 investigated structures, about ∼20 were predicted to form potentially stable alloys with promising decomposition energies. The $M_1(Al/Mn/Fe)(BH_4)_4$, $(Li/Na)Zn(BH_4)_3$ and $(Na/K)(Ni/Co)(BH_4)_3$ alloys are found to be the most promising, followed by selected $M_1(Nb/Rh)(BH_4)_4$ alloys.

PACS numbers: 63.20.-e, 64.60.-i, 65.40.-b

Keywords: hydrogen storage, metal borohydrides, computational materials design, thermodynamic stability, ab initio, first principles, electronic structure

I. INTRODUCTION

The development of sustainable energy solutions for the future requires new and improved materials. Specifically designed materials properties are needed to solve the grand challenges in energy production, storage and conversion. Within energy storage, hydrogen has been investigated extensively over the last decade[1] as one of the few promising energy carriers which can provide a high energy density without resulting in CO_2 emission by the end user. Finding materials for efficient, reversible hydrogen storage, however, remains challenging. Here, the specific requirements of the rapidly growing transportation sector coupled with complex engineering challenges[2] have directed research towards complex materials with extreme hydrogen storage capacity[3] such as metal borohydrides[4] and metal ammines[5]. Finding materials with high reversible hydrogen content and optimal thermodynamic stability is essential if hydrogen is going to be used as a commercial fuel in the transport sector. The binary metal borohydrides have been studied extensively: the alkali based compounds, *e.g.* $LiBH_4$,[6–8] are too thermodynamically stable, the alkaline earth compounds are kinetically too slow and practically irreversible,[9] and the transition metal borohydrides are either unstable or irreversible[10]. This leaves hope that mixed metal ("alloyed") systems might provide new opportunities.

The use of computational screening techniques has proved a valuable tool in narrowing the phase space of potential candidate materials for hydrogen storage[11,12]. Recent density functional theory (DFT) calculations have shown that the thermodynamic properties of even highly complex borohydride superstructures can be estimated by DFT using simple model structures, if the primary coordination polyhedra are correctly accounted for[13]. These findings enable faster screening studies of thermodynamic stability and decomposition temperatures for, *e.g.* ternary and quaternary borohydride systems; not only in terms of reduced computational effort due to smaller system sizes, but also with the advantage that the exact space group does not need to be known *a priori*.

In the present paper, we apply a "Local Coordination Screening" (LCS) approach to search for novel metal borohydrides. The vast majority of the calculations were performed

as part of the 2008 CAMD summer school in electronic structure theory and materials design, where more than 100 scientists combined DFT calculations, database methods, and screening techniques to investigate the structure and stability of promising ternary borohydrides. A few additional calculations were subsequently performed based on the insight gained from the initial screening.

Out of 757 investigated $M_1M_2(BH_4)_{2-5}$ (M_1 = alkali metal and M_2 = alkali, alkaline earth or 3d/4d transition metal) compositions and structures, a total of 22 were found to form potentially stable alloys with promising decomposition energies, which should subsequently be subjected to more detailed theoretical and experimental verification.

II. COMPUTATIONAL SETUP

Groups of alloy compositions and structures were divided among different groups of scientists, each of which was responsible for its own subset of the alloy configuration space. A number of predefined structural templates and optimization procedures had been prepared to assist the groups in setting up structures and calculations for the initial optimization (see Section II B). This was done to ensure a sufficient accuracy in all calculations (*i.e.* convergence with respect to planewave cut-off, k-point sampling, etc.).

To ensure reliability of the generated results, an automated checking procedure was enforced before a result could be included in the database (see Section III) to ensure the presence of the required output (total energies, lattice constants, etc.).

A. Computational parameters

The total energies and gradients were calculated within density functional theory[14] implemented by the software package Dacapo[15]. A planewave basis sets with cut-off energies of 350 eV (density grid cut-off of 700 eV) and the RPBE exchange-correlation functional[15] were used for all calculations. Dacapo uses ultrasoft pseudopotentials[16] for a description of the ionic cores. The coordinate optimization was implemented and performed within the Atomic Simulation Environment[17]. The electronic Brillouin zones were sampled with

$(4 \times 4 \times 4)$ k-points (spacings of $\sim$0.05 Å^{-1}). A quasi-Newton method[18] was used for all relaxations.

B. Configuration space and template structures

The alloys which were initially screened have the general formula $M_1M_2(BH_4)_x$, where $M_1 \in$ {Li,Na,K} and x=2–4. The x=2 alloys were investigated for $M_2 \in$ {Li,Na,K}, and x=3,4 for $M_2 \in$ {Li,Na,K,Mg,Al,Ca,Sc–Zn,Y–Mo,Ru–Cd}.

In order to limit the total number of calculations, only template structures with tetrahedral and octahedral coordination of the $(BH_4)^-$ groups to the metal atoms were used. Most metals prefer an octahedral coordination of their ligands, but for the metal borohydrides the ligand-ligand repulsion between the relatively large $(BH_4)^-$ ions often forces a lower coordination number. The primary structures observed and reported in literature for the alkali and alkaline earth borohydrides are either tetrahedral (for the smallest Li and Mg) or octahedral (for the larger Na, K and Ca), while a trigonal planar ligand arrangement is observed for $Al(BH_4)_3$. However, Al can also have a tetrahedral coordination as is the case of the stable $LiAl(BH_4)_4$ alloy obtained here (see Section V), and since the radii of the considered ions lie between the radius for K and the radius for Al, the tetrahedral and octahedral primary structures are expected to be representative.

For each alloy composition, four different template structures were used to sample the tetrahedral and octahedral primary structures in the combinations: tetrahedral/tetrahedral, octahedral/octahedral, tetrahedral/octahedral and octahedral/tetrahedral, referring to the coordination of the $(BH_4)^-$ groups to the M_1 and M_2 atoms, respectively. The coordination polyhedra were either corner-sharing, edge-sharing or a combination to yield the required stoichiometric ratio of $(BH_4)^-$ groups (see Figure 1). All structures were designed to have a unit cell containing only one formula unit (see Section II D). It has previously been shown that these simple template structures can be within $\sim$0.1 eV (10 kJ/mol H_2) of the true ground state energy, if the local coordination is correctly accounted for; e.g. $M_1M_2(BH_4)_2$-tetra for $LiBH_4$,[7] $M_1M_2(BH_4)_4$-octa for $Ca(BH_4)_2$,[19] and even $M_1M_2(BH_4)_4$-tetra for the

free energy of $Mg(BH_4)_2$ super structures.[13]

The initial optimization of the structures only relaxed the hydrogen positions and the unit cell volume while keeping the metal–boron coordination polyhedra fixed. For a given set of (M_1,M_2), the most stable structure was then used as the starting point for a calculation in which all atomic positions and the unit cell were relaxed. Even though many of the structures did not change significantly during the final relaxation, it added, in principle, an additional structure to the phase space for each set of (M_1,M_2). These are included as "other" structures in the results (Figures 3 to 12) to distinguish them from the structures with fixed metal–boron coordination polyhedra, even though in many of them the original coordination polyhedra are only slightly distorted.

A number of structures were subsequently added based on the knowledge gained from the initial screening and the reference binary borohydride structures (see sections IV and VI). In some of these structures, the metal ions had the same valence as in the reference structures, which meant that the four x=2 templates were also applied to $M_2 \in$ {Ni,Pd,Cu,Ag}, while a new template for x=5 was investigated for $M_2 \in$ {Ti,Zr} in the two combinations tetrahedral/octahedral and octahedral/tetrahedral. An alternative x=3 tetragonal/trigonal template was applied to $M_2 \in$ {Mg,Al,Ca,Sc–Zn,Y–Mo,Ru–Cd} to investigate possible size effects. In this structure, the M_1 ion has a tetrahedral coordination while the M_2 atom is surrounded by three $(BH_4)^-$ groups in a trigonal planar arrangement (see Figure 2). This enabled the metal–boron distances for the two metals to be optimized independently, which was not possible in the original x=3 templates, but found to be required to obtain the preferred local coordination of certain alloys.

In total, 757 structures have been simulated and are reported herein.

C. Group calculations

The 69 sets of M_1/M_2 combinations investigated in this study were divided among 32 groups of scientists for the initial screening. Each group followed step I of the calculational procedure outlined below for each alloy containing M_1 and M_2 and step II for the most

stable resulting structure.

D. Calculational procedure

a. Step I An initial structure was set up by calling a function that populates one of the four template structures with two supplied metal ions, *e.g.* Li and Sc. The function utilizes the ionic radii obtained from the calculations of binary reference borohydrides, $i.e.$ individual metal-atom borohydrides, to calculate metal–boron distances, where the ionic radius used for a $(BH_4)^-$ group depends on whether a face, edge or corner of the H-tetrahedron points towards the metal atom. In general, this ensured that the effective lattice constant and the c/a ratio were close to the optimum. The initial structure was used as the initial guess for the first iteration of the following procedure.

All hydrogen positions were relaxed until the maximum force on the atoms reached 0.05 eV/Å or, alternatively, a maximum of 50 quasi-Newton steps had been performed. The resulting structure was then contracted and expanded to 90%, 95%, 105% and 110% of the unit cell volume by a proportional scaling of the unit cell, while keeping the B–H distances in each $(BH_4)^-$ group fixed; a single total energy calculation was performed for each volume. A Murnaghan equation-of-state was fitted to the calculated five points to estimate the optimal unit cell volume, to which the unit cell was then scaled (again while conserving B–H distances), followed by a relaxation of the hydrogen positions to a force convergence of 0.05 eV/Å.

After each iteration, an energy vs. unit cell volume plot was inspected visually to decide whether the minimum had been sufficiently sampled or an additional iteration of the procedure should be performed; in the latter case, a structure resulting from the first iteration was used as the starting guess for the next iteration.

b. Step II When all the template structures for each of the (M_1,M_2) alloys had been optimized in step I, the most stable structure was relaxed without constraints by repeating the procedure that first relaxes all atomic positions for a fixed cell and then the unit cell for fixed internal positions. To limit the computational time used by this algorithm, the

number of iterations was limited to 5, and the number of steps per iteration was limited to 12 for the internal relaxation and 5 for the unit cell relaxation.

c. Procedure for the additional structures For the structures calculated later, the x=2 structures (monovalent transition metals) followed the same procedure mentioned above, whereas only a single free optimization was performed on the extra x=3 and x=5 structures, in which all atoms were allowed to relax.

III. DATA COLLECTION AND STORAGE

Every group executed the calculation procedures for steps I and II. After each step, the validity of the results was checked by the group and the results were checked in (stored in a global location for indexing) to the common database.

1. Front-end

A Python[20] script took care of checking in all relevant files that were needed for subsequent checking. This included the calculation script, and the output files containing the atoms, energies and the calculational parameters. A Subversion (svn) version control system[21] assisted to manage groups and users, store results and assuring transaction consistency.

2. Back-end

A second Python script was used to extract the relevant parameters, *i.e.* the total energy, unit cell volume, chemical symbols, structure and the calculational parameters such as k-points, number of bands, density wave cutoff, and to select the best structure; (at any given time) for every borohydride to create/update the intermediate result plots, which were accessible to all participants. Python, in combination with Matplotlib[22], was used to ensure a flexible user interface and to generate the plots. A special Python class managed the resulting data, consisting of approximately 5500 calculations. This class provided basic database operations like selecting, sorting and filtering of data and facilitated the creation

of the plots considerably.

The overall construction of the database and data retrieval procedures will also facilitate screening for possible correlations between combinations of a number of different values in future projects.

IV. DATA ANALYSIS

The initial screening procedure presented here is performed to rapidly reduce the number of potential alloys for further investigation, and two simple selection criteria were set up to assess the stability of the investigated alloy structures against phase separation and decomposition. The stabilities were first analyzed against phase separation into the original binary borohydrides as illustrated for $LiSc(BH_4)_4$:

$$\Delta E_{\text{alloy}} = E_{\text{LiSc(BH}_4)_4} - \ (E_{\text{LiBH}_4} + E_{\text{Sc(BH}_4)_3}). \tag{1}$$

Reference energies for the 3 alkali, 2 alkaline earth, $Al(BH_4)_3$ plus 19 transition metal borohydrides were obtained using the most stable structures among the $M_2(BH_4)_{1-4}$ applied model templates (see Table I). Due to computational constraints, the performed calculations are not spin polarized which causes certain reference structures, *e.g.* $Mn(BH_4)_2$, to become unstable. In order not to exclude potentially stable candidates, the assessment in Eq.(1) will be used for all reference structures (see Table I).

For assessing the stability of alloys with a potentially less favorable stoichiometry, like $LiSc(BH_4)_3$, an effective reference value for $E_{\text{Sc(BH}_4)_2}$ was determined from the stable $E_{\text{Sc(BH}_4)_3}$ as $E_{\text{Sc(BH}_4)_2}* = E_{\text{Sc(BH}_4)_3} - 2E_{\text{H}_2} - E_{\text{B}}$.

Using $1/2(B_2H_6 + H_2)$ as a reference only shifts the energy by 0.07 eV/mol H_2 and does not result in new coordination for any of the stable alloys.

The decomposition pathways of binary and ternary metal borohydrides are often highly complex and differ significantly from one system to the next, *e.g.*, $LiBH_4$,[23] $Mg(BH_4)_2$[24] and $LiZn(BH_4)_3$,[25] and the formed products can even depend on the details of the desorption conditions. Certain compounds form transition metal hydrides,[26] others form transition metal borides,[27] di-[10] or dodeca-boranes,[28] and others again, *e.g.*, Cr, Cd, Mn and $Zn(BH_4)_2$

decompose to the elements.[29,30] Given the inclusive nature of this initial screening study and the fact that the true decomposition pathways in most of the investigated alloys are not well known, a simple and generic decomposition pathway was selected, which all interesting mixed borohydrides must be stable against (as a minimum). Here, the alloys decompose into the highly stable alkali- and alkaline earth hydrides, transition metals, boron and H_2:

$$\Delta E_{\text{decomp}} = E_{\text{LiMn(BH}_4)_3} - (E_{\text{LiH}} + E_{\text{Mn}} + 3E_{\text{B}} + 5.5E_{\text{H}_2}). \quad (2)$$

In this definition, ΔE_{decomp} estimates the stability of the alloy against decomposition. Transition metal hydrides, metal borides, higher order boranates and diborane, which may potentially form, are thus not taken into consideration in this first screening.

The analysis is based on the ground state energies only. Although the difference in vibrational entropy between hydrogen in a alkali metal borohydride and in the gas phase is often significantly smaller than in conventional metal hydrides[31], the contributions to the free energy from the vibrational entropy may be significant.

A stability range of $\Delta E_{\text{alloy}} \leq 0.0$ eV/f.u.(formula unit) and $\Delta E_{\text{decomp}} \in \{-0.5; 0.0\}$ eV/H_2 is used to select the most interesting alloys with ΔE_{decomp} = -0.2 eV/H_2 as the target value (see Table II), but given the idealized screening criteria in Eqs. (1) and (2), alloys with only small instabilities, *i.e*, $\Delta E_{\text{alloy}} \leq 0.2$ eV/f.u and $\Delta E_{\text{decomp}} \leq 0.0$ eV/H_2 should not be discarded *a priori* (see Table III).

V. RESULTS

As the first step of the stability screening, we have plotted the alloying energy against the decomposition energy of the 757 investigated alloys (see Figure 3). Most of the alloys are found to be stable against decomposition, but the majority is found to be unstable against separation into their binary components ($\Delta E_{\text{alloy}} > 0.0$ eV/f.u.). Many are still within the 0.2 eV/f.u. boundary regime. The lithium-containing alloys (red) are less stable against decomposition than those containing sodium (blue) and potassium (green). Restricting the plot to only the most stable structure for each M_1M_2 system (see Figure 4) seems to support this observation, and yields a total of 22 stable alloys (see Table II). Figure 4 is dominated by

alloys where (a) both metal atoms are tetrahedrally coordinated to the borohydride groups ($\square$), (b) one is tetrahedral the other trigonal ($\curlyvee$) and (c) so-called "other" ($\triangleleft$), where all constraints have been lifted. Some octa–tetra ($\triangle$) and tetra–octa ($+$) are also observed.

Plotting the hydrogen density of the stable alloys, $\Delta E_{\text{alloy}} \leq 0.0$ eV/f.u. and $\Delta E_{\text{decomp}} \leq 0.0$ eV/H_2, Figure 5 shows that alloys containing potassium (in green) are found to have the lowest density, followed by sodium (in blue) and lithium (in red), as expected. The overall density is found to be around that of liquid hydrogen, which is largely due to the choice of simple template structures; higher densities are expected for real systems as previously observed for $Mg(BH_4)_2$.[9] Alloys containing Al, Mn, Fe and Zn are found to be stable for all alkali metals screened, whereas those based on Co, Ni, Nb and Rh are stable for two out of three alkali metals. The only other stable alloys are $KCd(BH_4)_3$ and $LiNa(BH_4)_2$ (see Table II).

The storage capacity (wt.% hydrogen) of the stable alloys is plotted as a function of the decomposition energy, ΔE_{decomp}, in Figure 6. Here, the data from the binary reference structures has also been included, and it is clearly seen that the stability has been reduced significantly compared to the highly stable binary borohydrides. Most alloys have storage capacities above the DoE 2015 system target of 9 wt.%[3] and several also have favourable stability. A number of these ternary borohydrides have been synthesized either very recently or historically (circled in Figure 6). Of the experimentally observed stable/meta-stable structures, $LiSc(BH_4)_4$,[10] $KNa(BH_4)_2$,[32] and $Li_2Cd(BH_4)_4$[30] show a weak preference for phase separation, but are all found to be potentially stable (see Table III); only $LiK(BH_4)_2$[33]($\Delta E_{\text{alloy}} = 0.202$ eV/f.u. and $\Delta E_{\text{decomp}} = -0.645$ eV/H_2) and $LiNi(BH_4)_3$[30] ($\Delta E_{\text{alloy}} = -0.104$ eV/f.u. and $\Delta E_{\text{decomp}} = 0.069$ eV/H_2) fell marginally outside the selection criteria. Furthermore, $LiMn(BH_4)_3$ and $NaMn(BH_4)_3$ are found experimentally to decompose at $\sim$100 and 110 °C,[34] and $LiZn(BH_4)_3$ and $LiAl(BH_4)_4$ are found to disproportionate at $\sim$130 °C;[25] all structures which are located near the optimal stability in the figure (the non-shaded region).

VI. TRENDS

Given the systematic approach to the screening study it is also possible to extract information from the database about possible trends and correlations, in order to search for predictors and descriptors[35] for the design of future quaternary alloys or alloys with different cation stoichiometry.

A. 3d and 4d transition metals

The stability of the alloys, as produced by the most stable x=3 and 4 initial template structures before the free relaxation, is presented for all 3d transition metals (incl. Mg, Ca and Al) in Figure 7, and for the 4d transition metals in Figure 8. A clear preference for the $M_1M_2(BH_4)_4$-tetra template is observed, which is somewhat surprising, because many of the transition metals have an oxidation state of II in the reference calculations (see Table I). This apparent discrepancy could result from partially non-ionic bonding in these structures, meaning that the coordination of the hydrogen atoms to the metal is the determining factor, not whether the metal has the "correct" valence. For instance, we find no significant energy difference between $Fe_2(BH_4)_3$ and $Fe(BH_4)_2$ as long as the H atoms are octahedrally coordinated to the Fe atom. Size effects also become apparent here since the $M_1M_2(BH_4)_4$-tetra template is the only template structure that allows the coordination polyhedra of M_1 and M_2 to be relaxed independently. This is supported by the larger spacing between most of the Li, Na and K alloy energies produced by the other template structures (see Figures 7 and 8).

To investigate this further, the $M_1M_2(BH_4)_3$-tetra/tri template was applied to all alloys, and in Figures 9 and 10, the final alloy stabilities are presented; these also include the free relaxation and the additional x=2 and x=5 calculations. It is seen that the $M_1M_2(BH_4)_3$-tetra/tri structures now become the most stable for a number of alloys and that the Li, Na and K points lie closer indicating a reduction of the size effects.

There is a general agreement between valencies in the reference calculations and the alloys; divalent metals are found to prefer a $M_1M_2(BH_4)_3$ configuration, whereas trivalent metals

prefer $M_1M_2(BH_4)_4$, tetravalent metals prefer $M_1M_2(BH_4)_5$ and the monovalent Cu and Ag prefer $M_1M_2(BH_4)_2$. Some deviations are found, but given the simple model structures used for both alloys and reference calculations, and given the fact that some of the metals are found by experiments to form ternary borohydrides in different oxidation states, the agreement is good.

The most stable alloys are found for the half-filled d-bands, but interesting alloys are also found for the empty and fully occupied d-bands with the addition of Al, where the $M_1Al(BH_4)_4$ are found to be very promising (see Figures 9 and 10).

Lithium-based alloys (red) are generally found to be the most stable, followed by sodium (blue) and potassium (green), although significant deviations are observed. This follows the observed trend for the storage capacities.

B. Stability vs. electronegativity

A number of recent publications[33,36] have shown an apparent correlation between the decomposition temperature and the average cation Pauling electronegativity. Although this might be expected, given the definition of Pauling's electronegativity, it also indicates that the kinetic barriers - if any - do not appear to be particularly system dependent.

Plotting the calculated alloy stability as a function of the average cation electronegativity for all alloys in their most stable local coordination (see Figure 11) appears to support this observation. The scatter of the data points around the "line" is, however, significant and deviations of $\pm$ 0.1 eV/H_2 can be sufficient to shift a material from interesting to irrelevant for storage applications, or vice versa.

The stable alloys ($\Delta E_{\text{alloy}} \leq 0.0$ eV/f.u.) are seen to cluster around certain average electronegativities of 1.3–1.4 and 1.6 (see Figure 12). The cluster around 1.3–1.4 is highly promising with $\Delta E_{\text{decomp}} \simeq -0.1$ eV/H_2 for Mn and Nb, and particularly for Al, Zn and Fe with $\Delta E_{\text{decomp}} \simeq -0.3$ eV/H_2. The Nb and Rh alloys at electronegativities around 1.6 are found to borderline on decomposition, but experimental work by Nikels *et al.* estimates the decomposition temperature of such compounds to be around 150 °C.[33]

VII. CONCLUSIONS

We have analyzed the thermodynamic properties of possible alkali-transition metal borohydride systems, finding a number of candidates showing favorable properties.

The $M_1(Al/Mn/Fe)(BH_4)_4$, $(Li/Na)Zn(BH_4)_3$ and $(Na/K)(Ni/Co)(BH_4)_3$ alloys are found to be the most promising, followed by selected $M_1(Nb/Rh)(BH_4)_4$ alloys. These findings are in good agreement with experimental observations for $LiFe(BH)_3$,[37] $LiAl(BH_4)_4$,[25] $(Li/Na)Mn(BH)_{3,4}$[38] and $(Li/Na)Zn(BH_4)_3$,[39] whereas the Co, Cd, Nb and Rh and alloys still remain to be synthesized and tested. Although some structures can be observed experimentally in different metal–metal stoichiometries than those used in the screening study, *e.g.* the Li–Zn system[39], the alloy systems were still identified as promising candidates in this screening study. Some of the nearly stable compounds in Table III, *e.g.* $LiSc(BH_4)_4$[10] and $KNa(BH_4)_2$[32] have recently been found to be metastable, while $LiNi(BH_4)_3$[30] was found to be marginally unstable. The Local Coordination Screening approach was found to limit the 757 potential alloys down to 22 promising candidates of which ∼10 are highly promising. These structures can now be pursued further, analyzing their detailed decomposition pathways, both theoretically and experimentally.

Acknowledgments

The authors acknowledge financial support by the European Commission DG Research (contract SES6-2006-51827/NESSHy), the Nordic Energy Research Council (contract 06-HYDRO-C15) and the Danish Center for Scientific Computing (DCSC) for computer time (grant no. HDW-1103-06). The Center for Atomic-Scale Materials Design is funded by the Lundbeck Foundation.

References

---

* Electronic address: tejs.vegge@risoe.dk

† A full list of affiliations can be found as supplementary information

[1] L. Schlapbach and A. Züttel, Nature **414**, 353 (2001).

[2] D. Mosher, X. Tang, and S. Arsenault, FY 2006 Annual Progress Report, DoE Hydrogen Program pp. 281–284 (2006).

[3] URL http://www1.eere.energy.gov/vehiclesandfuels/about/partnerships/freedomcar/fc_goals.html.

[4] S.-I. Orimo, Y. Nakamori, J. R. Eliseo, A. Züttel, and C. M. Jensen, Chem. Rev. **107**, 4111 (2007).

[5] R. Z. Sørensen, J. S. Hummelshøj, A. Klerke, J. B. Reves, T. Vegge, J. K. Nørskov, and C. H. Christensen, J. Am. Chem. Soc. **130**, 8660 (2008).

[6] A. Züttel, S. Rentsch, P. Fischer, P. Wenger, P. Sudan, P. Mauron, and C. Emmenegger, J. Alloys Compd. **356-357**, 515 (2003).

[7] Z. Łodziana and T. Vegge, Phys. Rev. Lett. **93**, 145501 (2004).

[8] Z. Łodziana and T. Vegge, Phys. Rev. Lett. **97**, 119602 (2006).

[9] K. Chłopek, C. Frommen, A. Léon, O. Zabara, and M. Fichtner, J. Mater. Chem. **17**, 3496 (2007).

[10] H. Hagemann, M. Longhini, J. W. Kaminski, T. A. Wesolowski, R. Cerný, N. Penin, M. H. Sørby, B. C. Hauback, G. Severa, and C. M. Jensen, J. Phys. Chem. A **112**, 7551 (2008).

[11] S. V. Alapati, J. K. Johnson, and D. S. Sholl, J. Phys. Chem. C **112**, 5258 (2008).

[12] V. Ozolins, E. H. Majzoub, and C. Wolverton, Phys. Rev. Lett. **100**, 135501 (2008).

[13] J. Voss, J. S. Hummelshøj, Z. Lodziana, T. Vegge, J. Phys.: Condens. Matter, Fast Track Communication **21**, 012203 (2009).

[14] P. Hohenberg and W. Kohn, Physical Review **136**, B864 (1964).

[15] B. Hammer, L. B. Hansen, and J. K. Nørskov, Phys. Rev. B. **59**, 7413 (1999).

[16] D. Vanderbilt, Phys. Rev. B: Condens. Matter Mater. Phys. **41**, 7892 (1990).

[17] S. Bahn and K. Jacobsen, Comput. Sci. Eng. **4**, 56 (2002).

[18] D. F. Shanno, Math. Comput. **24**, 647 (1970).

[19] F. Buchter, Z. Lodziana, A. Remhof, O. Friedrichs, A. Borgschulte, Ph. Mauron, A. Züttel, D. Sheptyakov, G. Barkhordarian, R. Bormann, K. Chłopek, M. Fichtner, M. Sørby, M. Riktor, B.. Hauback and S. Orimo, J. Phys. Chem. B **112**, 8042 (2008).

[20] URL `http://www.python.org`.

[21] URL `http://subversion.tigris.org`.

[22] URL `http://matplotlib.sourceforge.net`.

[23] J. Her, M. Yousufuddin, W. Zhou, S.S. Jalisatgi, J.G. Kulleck, J.A. Zan, S. Hwang, R. Bowman Jr.,and T.J. Udovic, Inorg. Chem. **47**, 9757 (2008).

[24] N. Hanada, K. Chłopek, C. Frommen, W. Lohstroh,and M. Fichtner, J. Mater. Chem. **18**, 2611 (2008).

[25] A. Li, S. Orimo, P. Nakamori, P. Miwa, P. Ohba, P. Towata, and C. Züttel, J. Alloys Compd. **446-447**, 315 (2007).

[26] E. Wiberg, Angew. Chem. **65**, 16 (1953).

[27] X. B. Yu, D. M. Grant, and G. S. Walker, Chem. Commun. **37**, 3906 (2006).

[28] S.-J. Hwang, R. C. Bowman, J. W. Reiter, J. Rijssenbeek, G. L. Soloveichik, J.-C. Zhao, H. Kabbour, and C. C. Ahn, J. Phys. Chem. C **112**, 3164 (2008).

[29] Y. Nakamori, H.-W. Li, M. Matsuo, K. Miwa, S. Towata,and S. Orimo, J. Phys. Chem. Sol. **69**, 2292 (2008).

[30] Y. Nakamori and S. Orimo, in Solid-state hydrogen storage - Materials and chemistry, G. Walker (ed.), Woodhead Publishing Limited, Cambridge, England, 420-449 (2008).

[31] P. Mauron, F. Buchter, O. Friedrichs, A. Remhof, M. Bielmann, C. N. Zwicky, and A. Züttel, J. Phys. Chem. B **112**, 906 (2008).

[32] L. Seballos, J. Z. Zhang, E. Ronnebro, J. L. Herberg, and E. H. Majzoub, J. Alloys Compd. (in press).

[33] E. A. Nickels, M. O. Jones, W. I. F. David, S. R. Johnson, R. L. Lowton, M. Sommariva, and P. P. Edwards, Angew. Chem. Int. Ed. **47**, 2817 (2008).

[34] URL `http://www.docstoc.com/docs/922287/Fundamental-Studies-of-Advanced-High-Capacity-Rev`

[35] F. Studt, F. Abild-Pedersen, T. Bligaard, R. Z. Sørensen, C. H. Christensen, and J. K. Nørskov, Science **320**, 1320 (2008).

[36] Y. Nakamori, K. Miwa, A. Ninomiya, H. Li, N. Ohba, S. I. Towata, A. Zuettel, and S. I. Orimo, Phys. Rev. B **74**, 45126 (2006).

[37] H. Nöth and P. Fritz, Angew. Chem. Int. Ed. **73**, 408 (1961).

[38] URL `http://www.hydrogen.energy.gov/pdfs/review08/st_0_satyapal.pdf`.

[39] H. Nöth, E. Wiberg, and L. Winter, Z. Anorg. Allg. Chem. **386**, 73 (1971).

	wt.% [kg H_2/kg material]	$\Delta E_{\mathrm{decomp}}$ [eV/H_2]
$K(BH_4)$	7.5	-0.968
$Na(BH_4)$	10.7	-0.729
$Li(BH_4)$	18.5	-0.422
$Ag(BH_4)$	3.3	0.278
$Cu(BH_4)$	5.1	0.352
$Pd(BH_4)$	3.3	0.661
$Ni(BH_4)$	5.5	0.680
$Ca(BH_4)_2$	11.6	-0.636
$Mg(BH_4)_2$	14.9	-0.467
$Zn(BH_4)_2$	8.5	-0.063
$Cd(BH_4)_2$	5.7	-0.043
$V(BH_4)_2$	10.0	-0.031
$Nb(BH_4)_2$	6.6	0.066
$Fe(BH_4)_2$	9.4	0.090
$Cr(BH_4)_2$	9.9	0.162
$Mn(BH_4)_2$	9.5	0.174
$Co(BH_4)_2$	9.1	0.264
$Mo(BH_4)_2$	6.4	0.280
$Rh(BH_4)_2$	6.1	0.340
$Ru(BH_4)_2$	6.2	0.351
$Y(BH_4)_3$	9.1	-0.676
$Sc(BH_4)_3$	13.5	-0.595
$Al(BH_4)_3$	16.9	-0.209
$Zr(BH_4)_4$	10.7	-0.429
$Ti(BH_4)_4$	15.0	-0.252

TABLE I: The calculated reference energies for the binary borohydrides in their most stable template structures (see Figure 2).

	wt.% [kg H_2/kg material]	$\Delta E_{\mathrm{alloy}}$ [eV/f.u.]	$\Delta E_{\mathrm{decomp}}$ [eV/H_2]
$LiNa(BH_4)_2$	13.5	-0.020	-0.581
$KZn(BH_4)_3$	8.1	-0.349	-0.423
$KAl(BH_4)_4$	12.9	-0.138	-0.416
$NaAl(BH_4)_4$	14.7	-0.279	-0.373
$KCd(BH_4)_3$	6.2	-0.005	-0.352
$NaZn(BH_4)_3$	9.1	-0.358	-0.344
$LiAl(BH_4)_4$	17.3	-0.391	-0.311
$KFe(BH_4)_3$	8.7	-0.116	-0.282
$LiZn(BH_4)_3$	10.4	-0.362	-0.243
$NaFe(BH_4)_3$	9.8	-0.141	-0.206
$KMn(BH_4)_4$	10.5	-0.148	-0.174
$NaNb(BH_4)_4$	9.2	-0.128	-0.165
$KCo(BH_4)_3$	8.5	-0.089	-0.161
$NaMn(BH_4)_4$	11.7	-0.284	-0.131
$KNi(BH_4)_3$	8.5	-0.120	-0.116
$LiFe(BH_4)_3$	11.3	-0.141	-0.104
$LiNb(BH_4)_4$	10.1	-0.194	-0.097
$NaCo(BH_4)_3$	9.6	-0.143	-0.090
$KRh(BH_4)_4$	8.0	-0.058	-0.079
$LiMn(BH_4)_4$	13.3	-0.358	-0.063
$NaNi(BH_4)_3$	9.6	-0.164	-0.043
$NaRh(BH_4)_4$	8.7	-0.033	-0.016

TABLE II: Structures with alloying energies $\Delta E_{\mathrm{alloy}} < 0.0$ eV/f.u. (formula unit) and decomposition energies $\Delta E_{\mathrm{decomp}} < 0.0$ eV/H_2.

	wt.% [kg H_2/kg material]	$\Delta E_{\mathrm{alloy}}$ [eV/f.u.]	$\Delta E_{\mathrm{decomp}}$ [eV/H_2]
$KNa(BH_4)_2$	8.8	0.095	-0.825
$NaY(BH_4)_4$	9.4	0.115	-0.675
$NaCa(BH_4)_3$	11.2	0.129	-0.645
$LiY(BH_4)_4$	10.4	0.033	-0.609
$LiCa(BH_4)_3$	13.2	0.052	-0.556
$LiSc(BH_4)_4$	14.5	0.143	-0.534
$NaCd(BH_4)_3$	6.7	0.003	-0.271
$KNb(BH_4)_4$	8.4	0.016	-0.207
$NaV(BH_4)_4$	12.1	0.076	-0.188
$NaAg(BH_4)_2$	5.0	0.193	-0.177
$LiCd(BH_4)_3$	7.4	0.102	-0.152
$KCr(BH_4)_4$	10.7	0.199	-0.136
$LiV(BH_4)_4$	13.8	0.061	-0.113
$NaCr(BH_4)_4$	12.0	0.050	-0.095
$KPd(BH_4)_3$	6.4	0.047	-0.095
$KMo(BH_4)_4$	8.3	0.185	-0.079
$KRu(BH_4)_3$	6.5	0.168	-0.061
$NaMo(BH_4)_4$	9.0	0.056	-0.035
$LiCr(BH_4)_4$	13.6	0.029	-0.021
$NaPd(BH_4)_3$	7.0	0.052	-0.014

TABLE III: Structures with alloying energies $0 < \Delta E_{\mathrm{alloy}} < 0.2$ eV/f.u. (formula unit) with decomposition energies $\Delta E_{\mathrm{decomp}} < 0.0$ eV/H_2.

List of Figures

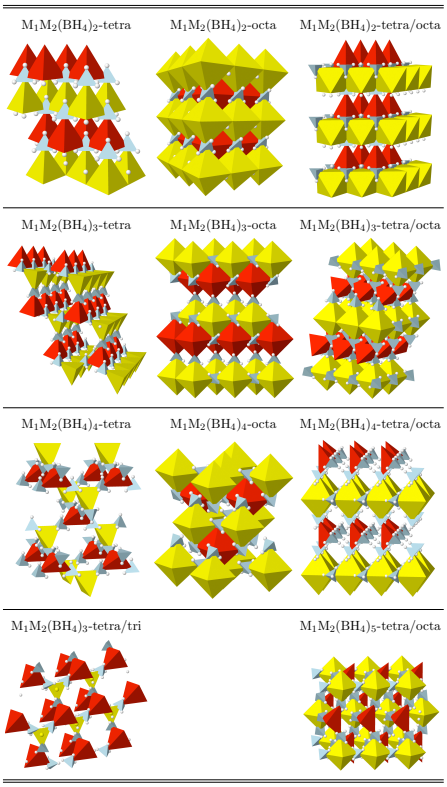

FIG. 1

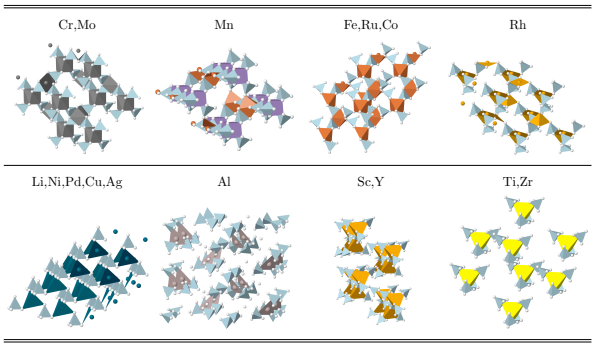

FIG. 2

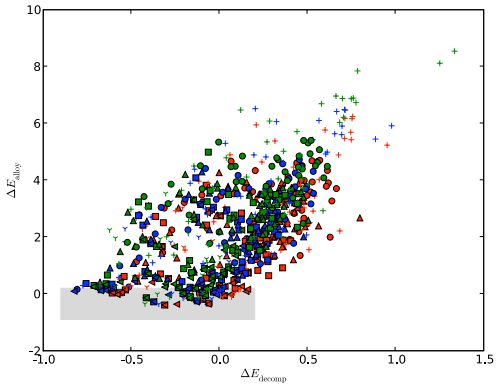

FIG. 3

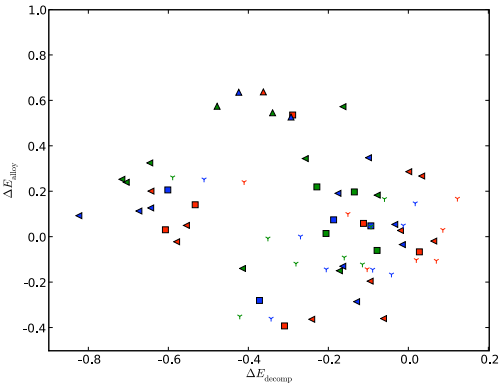

FIG. 4

25

26

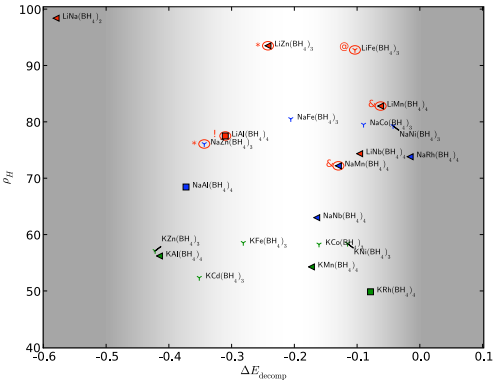

FIG. 5

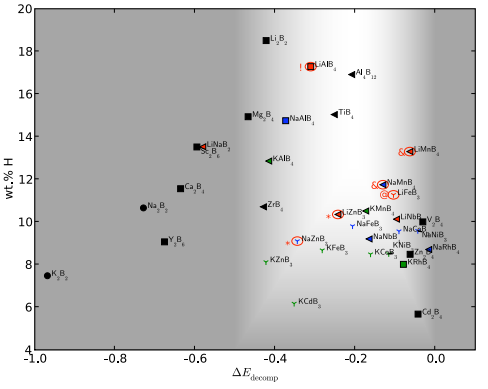

FIG. 6

27

28

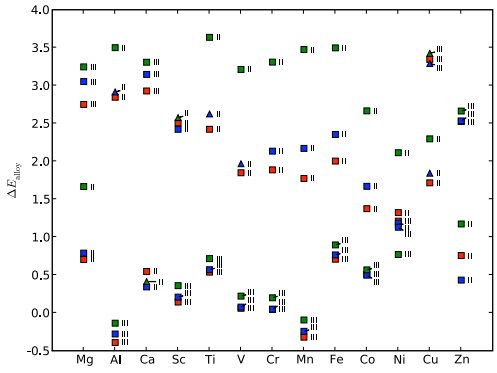

FIG. 7

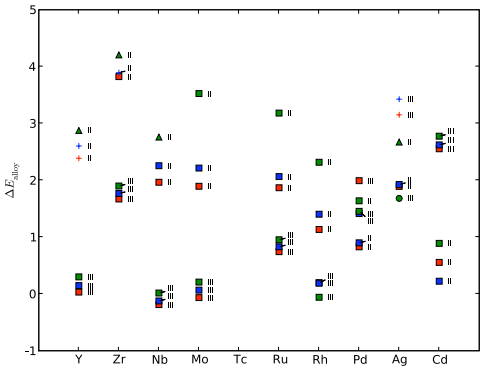

FIG. 8

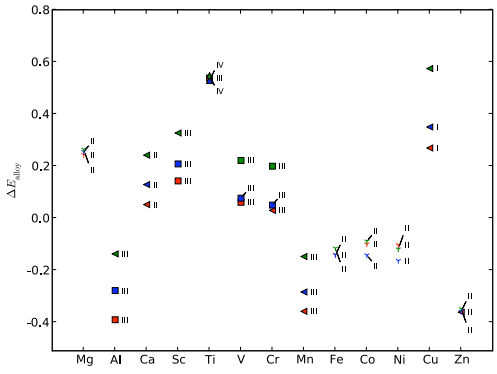

FIG. 9

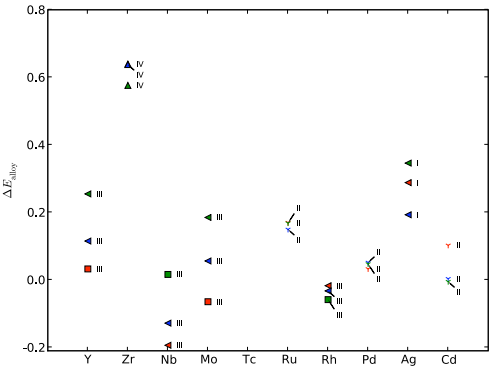

FIG. 10

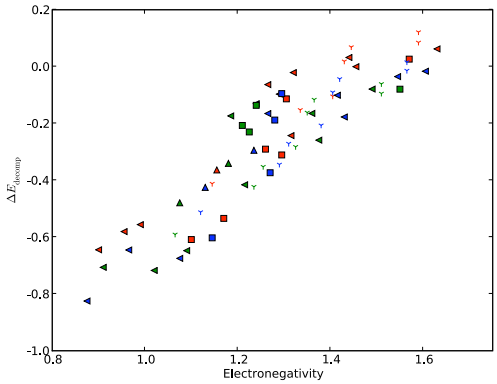
0.2
0.0
-0.2
-0.4
-0.6
-0.8
-1.0
0.8
1.0
1.2
1.4
1.6
Electronegativity
ΔE_{decomp}

FIG. 11

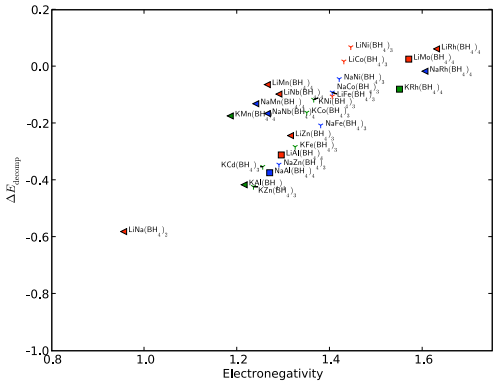
0.2
0.0
-0.2
-0.4
-0.6
-0.8
-1.0
0.8
1.0
1.2
1.4
1.6
Electronegativity
ΔE_{decomp}
$LiNi(BH_4)_3$
$LiRh(BH_4)_4$
$LiCo(BH_4)_3$
$LiMo(BH_4)_4$
$NaRh(BH_4)_4$
$NaNi(BH_4)_3$
$LiMn(BH_4)_3$
$NaCo(BH_4)_3$
$LiNb(BH_4)_4$
$LiFe(BH_4)_3$
$KRh(BH_4)_4$
$NaMn(BH_4)_3$
$KNi(BH_4)_3$
$KMn(BH_4)_3$
$NaNb(BH_4)_4$
$KCo(BH_4)_3$
$NaFe(BH_4)_3$
$LiZn(BH_4)_3$
$KFe(BH_4)_3$
$LiAl(BH_4)_4$
$KCd(BH_4)_3$
$NaZn(BH_4)_3$
$NaAl(BH_4)_4$
$KAl(BH_4)_4$
$KZn(BH_4)_3$
$LiNa(BH_4)_2$

FIG. 12

Paper IV

Appl. Phys. Lett.

Experimental and computational studies on structural transitions in the $LiBH_4$-LiI pseudobinary system

H. Oguchi,[1,2] M. Matsuo,[1] J.S. Hummelshøj,[3,4] T. Vegge,[3] J.K. Nørskov,[4] T. Sato,[1] Y. Miura,[1] H. Takamura,[2] H. Maekawa,[2] and S. Orimo[1,a)]

[1]*Institute for Materials Research, Tohoku University, Sendai 980-8577, Japan*

[2]*Graduate School of Engineering, Tohoku University, Sendai 980-8579, Japan*

[3]*Materials Research Division, Risø National Laboratory for Sustainable Energy, Technical University of Denmark, DK-4000 Roskilde, Denmark*

[4]*Center for Atomic-scale Materials Design, Department of Physics, Technical University of Denmark, DK-2800 Kgs. Lyngby, Denmark*

Abstract

Structural transition properties of the $LiBH_4 + xLiI$ (x = 0 - 1.00) pseudobinary system were examined by powder x-ray diffraction and differential scanning calorimetry combined with periodic density functional theory calculations. We experimentally and computationally confirmed the stabilization of the high-temperature (hexagonal, lithium super(fast-)ionic conduction) phase of $LiBH_4$ with x = 0.33 and 1.00, and the results also imply the existence of intermediate phases with x = 0.07 - 0.20. The studies are of importance for further development of $LiBH_4$ and the derived hydrides as solid-state electrolytes.

PACS numbers: 64.60.Ej, 66.10.Ed, 81.30.Dz

---

a) Electronic mail: orimo@imr.tohoku.ac.jp

Lithium borohydride ($LiBH_4$) exhibits lithium super(fast-)ionic conductivity accompanied by a structural transition from low-temperature (LT, orthorhombic) to high-temperature (HT, hexagonal) phases by heating to approximately 390 K.[1] Since the structural transition is reversible, the HT phase with super(fast-)ionic conductivity transforms into the LT phase with lower conductivity by cooling to around 380 K. It would thus be highly desirable to stabilize the HT phase (or to prohibit the formation of the LT phase by cooling in) of $LiBH_4$ as a potential candidate of solid-state electrolytes at room temperature (RT).

It was recently suggested that, the addition of lithium halides,[2-4] especially LiI,[3] stabilizes the HT phase of $LiBH_4$ below 380 K. For example, judging from the conductivity measurements, the hydride with a nominal composition of $LiBH_4$ + 0.33LiI showed no obvious structural transition from the HT to LT phases by cooling from 420 K down to RT.[3] Accordingly, the value of the conductivity at RT increases from the order of 10^{-8} S/cm for $LiBH_4$ to that of 10^{-5} S/cm for $LiBH_4$ + 0.33LiI. Systematic studies about the structural transition of $LiBH_4$ with and without LiI are highly required for further developments of $LiBH_4$ and the derived hydrides as solid-state electrolytes.

The purpose of the present study is, therefore, to experimentally and computationally examine the LiI-composition dependence of the structural and thermodynamical properties of the $LiBH_4 + x$LiI (x = 0 - 1.00) pseudobinary system.

The samples examined were synthesized from the powders of $LiBH_4$ and LiI (both from Aldrich Co. Ltd.). Approximately 500 mg of the powder mixture with nominal compositions of $LiBH_4 + x$LiI (x = 0, 0.07, 0.14, 0.20, 0.33, and 1.00) were mechanically milled for 5 h under Ar atmosphere. Then the samples were examined by powder x-ray diffraction (XRD, Cu-Kα radiation, at RT) and differential scanning calorimetry (DSC, 5 K/min, under He atmosphere). The samples were always handled in a glove box filled with purified Ar/He.

Periodic density functional theory (DFT) calculations were performed using the Dacapo planewave pseudopotential code[5] and the atomic simulation environment (ASE)

implementation,[6] to investigate the relative ground state stabilities of the LT and HT phases in $LiBH_4$ + *x*LiI. Ultrasoft pseudopotential are used to model the ionic cores and the exchange and correlation effects are described by the revision of the Perdew-Burke-Ernzerhof (RPBE) functional.[5] The Kohn-Sham wavefunctions are expanded in a plane wave basis with a cutoff energy of 350 eV, and the first Brillouin zone is sampled on a *k*-point grid with a spacing of approximately 0.05 $Å^{-1}$ in all directions. Super cells containing 2-8 formula units (Li atoms) are used to describe the systems.

Figure 1 shows the powder XRD profiles of $LiBH_4$ + *x*LiI. The diffraction peak intensities of the LT phase of $LiBH_4$ (x = 0) drastically decrease with x = 0.07. Only the peaks corresponding to the HT phase can be detected with x = 0.33 and 1.00. The tendencies are consistent with the results on the conductivity;[3] the addition of LiI stabilizes the HT phase of $LiBH_4$ at RT. The $LiBH_4$ + *x*LiI pseudobinary system probably forms Li(BH_4-I) solid-solutions, similar to Li(Br-I) in the LiBr + *x*LiI system.[8] The lattice constants of the HT phase[9] (x =0, 0.33, and 1.00) summarized in Table I are found to increase with increasing x; as is well comparable with the previous estimation of the unit-cell volumes.[3]

The thermodynamical properties of $LiBH_4$ + *x*LiI were examined by DSC, and the results of the second heating process are shown in Fig. 2. The endothermic peaks directly indicate the structural transition. (The single peak in each sample might prove its compositional homogeneity). Both the peak temperatures (onset) and enthalpy changes (areas[11]) decrease up to x = 0.20, and the values are summarized in Table I. No endothermic peak was detected over x = 0.33, indicating the HT phase is stabilized at RT. It should be noted that, no change was observed in the DSC profiles for x = 0.33 even after 10 and 20 heating/cooling cycles (heating up to 423 K and cooling down to RT), as shown in Fig. 2; the cyclic property is preferable for solid-state electrolytes.

The structural transition temperatures obtained from Fig. 2 and summarized in Table I were plotted as a function of x (top axis) and of "LiI mol %" (bottom axis), as shown in Fig. 3. We

can confirm the stabilization feature of the HT phase in the $LiBH_4 + xLiI$ pseudobinary system. Near-linear decrease of the structural transition temperatures might be due to increased neighboring $[BH_4]^-$ distance[12] and to induced lattice anharmonicity[9,13,14] by I^- substitution (ionic radius of I^- (0.211 nm) > $[BH_4]^-$ (0.205 nm)).[15]

The enthalpy changes of the structural transition from the LT to HT phases were also determined by periodic DFT calculations and summarized in Table I. Tendencies of both the computational and experimental (from DSC) values show good agreement, that is, a monotonous decrease with increasing x. However, the decrease in the computational values up to $x = 0.33$ is not as pronounced as in the experiments. So far, a number of the crystalline structures of $LiBH_4$ have been proposed and studied.[7,16-23] In the $LiBH_4 + xLiI$ pseudobinary system, possible intermediate (IM) phases are predicted to be stable at low x-values and a crystalline structure of the IM phase with $x = 0.14$ is shown in Fig. 4. The corresponding enthalpy change from the IM to HT phases, 2.3 kJ/mol as in Table I, shows better agreement with the experiment. The powder XRD profiles were indexed (using indexing programs TREOR90[24] and PIRUM[25]) by orthorhombic unit cell for $x = 0$ and by hexagonal one for $x = 0.33$ and 1.00; but both unit cells lead to significant errors for $x = 0.07$ - 0.20.[26] The indexing results imply the existence of the IM phases, as was predicted by the DFT calculations. The details of the structural and thermodynamical properties of the IM phases are under investigation.

In summary, the powder XRD and DSC combined with the periodic DFT calculations revealed the structural and thermodynamical properties of the $LiBH_4 + xLiI$ ($x = 0$ - 1.00) pseudobinary system. The high-temperature (HT, hexagonal, lithium super(fast-)ionic conduction) phase of $LiBH_4$ can be stabilized with $x = 0.33$ and 1.00. Also, no significant change was observed in the DSC profiles for $x = 0.33$ even after 10 and 20 heating/cooling cycles. The experimental and computational results imply the existence of intermediate (IM) phases with $x = 0.07$ - 0.20.

We are grateful to Prof. Hiroki Kuwano for valuable discussion. This work was partially supported by; KAKENHI the Creative Scientific Research Program (No. 18GS0203: Study of nano-energy system creation), the Global-COE Program “Materials Integration (Tohoku University)”, the Integrated Project of ICC-IMR, European Commission DG Research (SES6-2006-51827/NESSHy), Danish Center for Scientific Computing (DCSC), and the Lundbeck Foundation.

References

[1]M. Matsuo, Y. Nakamori, S. Orimo, H. Maekawa, and H. Takamura, Appl. Phys. Lett. **91**, 224103 (2007).

[2]L. Mosegaard, B. Møller, J.E. Jørgensen, Y. Filinchuk, Y. Cerenius, J.C. Hanson, E. Dimasi, F. Besenbacher, and T.R. Jensen, J. Phys. Chem. C **112**, 1299 (2008).

[3]H. Maekawa, M. Matsuo, H. Takamura, M. Ando, Y. Noda, T. Karahashi, and S. Orimo, J. Am. Chem. Soc. **131**, 894 (2009).

[4]M. Matsuo, H. Takamura, H. Maekawa, H.-W. Li, and S. Orimo, Appl. Phys. Lett. **94**, 084103 (2009).

[5]B. Hammer, L.B. Hansen, and J.K. Nørskov, Phys. Rev. B **59**, 7413 (1999).

[6]S.R. Bahn and K.W. Jacobsen, Comput. Sci. Eng. **4**, 56 (2002).

[7]J-Ph. Soulié, G. Renaudin, R. Černý, and K. Yvon, J. Alloys Compd. **346**, 200 (2002).

[8]J. Sangster and A.D. Pelton, J. Phys. Chem. Ref. Data **16**, 509 (1987).

[9]The values of the lattice constants for x = 0 (300 K) are extrapolated ones of the HT (hexagonal) phase of $LiBH_4$ at 381 - 500 K in the reference; Y. Filinchuk, D. Chernyshov, and R. Černý, J. Phys. Chem. C **112**, 10579 (2008).

[10]D. Fischer, A. Müller, and M. Jansen, Z. Anorg. Allg. Chem. **630**, 2697 (2004).

[11]Experimental values of enthalpy change for the structural transition are normalized by the one reported for x = 0 (4.18 kJ/mol); a) A. Züttel, A. Borgschulte, and S. Orimo, Scr. Mater. **56**, 823 (2007); b) S. Orimo, Y. Nakamori, J.R. Eliseo, A. Züttel, and C.M. Jensen, Chem. Rev. **107**, 4111 (2007).

[12]C.C. Stephenson, D.W. Rice, and W.H. Stockmayer, J. Chem. Phys. **23**, 1960 (1955).

[13]F. Buchter, Z. Łodziana, Ph. Mauron, A. Remhof, O. Friedrichs, A. Borgschulte, A. Züttel, D. Sheptyakov, Th. Strässle, and A.J. Ramirez-Cuesta, Phys. Rev. B **78**, 094302 (2008).

[14]A.-M. Racu, J. Schoenes, Z. Łodziana, A. Borgschulte, and A. Züttel, J Phys. Chem. A **112**,

9716 (2008).

[15]CRC Handbook of Chemistry and Physics, 88th ed., edited by D.R. Lide (CRC press, Boca Raton, 2007), pp. 12–27.

[16]Z. Łodziana and T. Vegge, Phys. Rev. Lett. **93**, 145501 (2004).

[17]Z. Łodziana and T. Vegge, Phys. Rev. Lett. **97**, 119602 (2006).

[18]K. Miwa, N. Ohba, S. Towata, Y. Nakamori, and S. Orimo, Phys. Rev. B **69**, 245120 (2004).

[19]T.J. Frankcombe, G.J. Kroes, and A. Züttel, Chem. Phys. Lett. **405**, 73 (2005).

[20]M.R. Hartman, J.J. Rush, T.J. Udovic, R.C. Bowman Jr., and S.-J. Hwang, J. Solid State Chem. **180**, 1298 (2007).

[21]L. Mosegaard, B. Møller, J.E. Jørgensen, U. Bösenberg, M. Dornheim, J.C. Hanson, Y. Cerenius, G. Walker, H.J. Jakobsen, F. Besenbacher, and T.R. Jensen, J. Alloys Compd. **446-447**, 301 (2007).

[22]N.A. Zarkevich and D.D. Johnson, Phys. Rev. Lett. **100**, 040602 (2008).

[23]V. Dmitriev, Y. Filinchuk, D. Chernyshov, A.V. Talyzin, A. Dzwilewski, O. Andersson, and B. Sundqvist, Phys. Rev. B **77**, 174112 (2008).

[24]P.-E. Werner, L. Eriksson, and M. Westdahl, J. Appl. Crystallogr. **18**, 367 (1985).

[25]P.-E. Werner, Ark. Kemi. **31,** 513 (1969).

[26]For example, assuming the hexagonal phase, averaged deviation in 2θ is 0.14 for $x = 0.14$, which is significantly larger than 0.02 for $x = 0$ with orthorhombic one.

Table with caption

TABLE I. Lattice constants, a and c, of the high-temperature (HT, hexagonal, lithium super(fast-)ionic conduction) phase for x = 0, 0.33, and 1.00; structural transition temperature, T_s; and experimental and computational values of enthalpy change, $\Delta H_{exp.}$ and $\Delta H_{theo.}$ (calculated for the transition from the LT to HT phases); for $LiBH_4 + xLiI$. Value of $\Delta H_{theo.}$ in square bracket was calculated for the transition from the IM to HT phases using a possible IM phase of $LiBH_4 + 0.14LiI$ (shown in Fig. 4). Lattice constants for x = 0.07, 0.14, and 0.20 are left blank as none of them are indexed by orthorhombic and hexagonal unit cells. Lattice constants of (hexagonal-)LiI are also added for reference.

x in $LiBH_4 + xLiI$	a (Å)	c (Å)	T_s (K)	$\Delta H_{exp.}$ (kJ/mol)	$\Delta H_{theo.}$ (kJ/mol)
0	4.24±0.02[a]	6.87±0.03[a]	384±3	4.18[c]	7.7
0.07	-	-	354±3	3.5±0.3	-
0.14	-	-	334±3	2.6±0.1	6.3 [2.3]
0.20	-	-	326±3	1.0±0.3	-
0.33	4.354±0.002	7.035±0.005	-	-	6.2
1.00	4.389±0.001	7.073±0.003	-	-	0.0
LiI	4.514±0.001[b]	7.311±0.002[b]	-	-	-

[a]Reference 9
[b]Reference 10
[c]Reference 11

List of figure captions

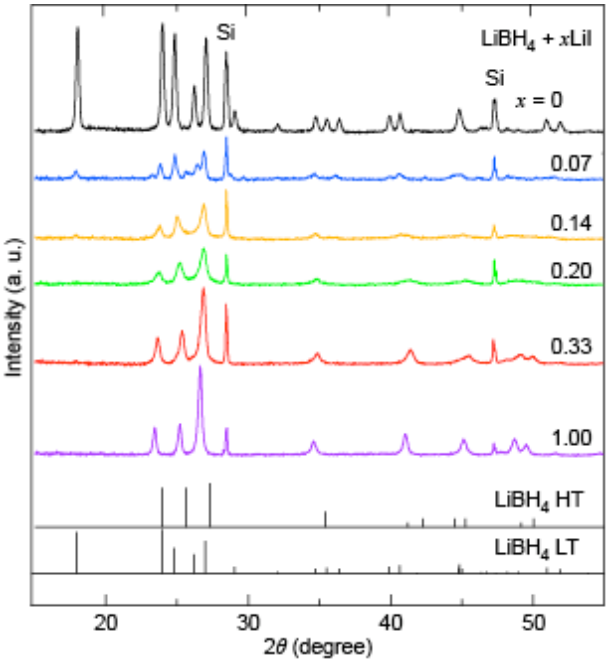

FIG. 1. Powder XRD profiles of $LiBH_4 + xLiI$ (x = 0 - 1.00). The diffraction peaks are calibrated by Si internal standard. The standard diffraction peaks of the low-temperature (LT, orthorhombic) and high-temperature (HT, hexagonal) phases of $LiBH_4$ are shown for references (Ref. 7).

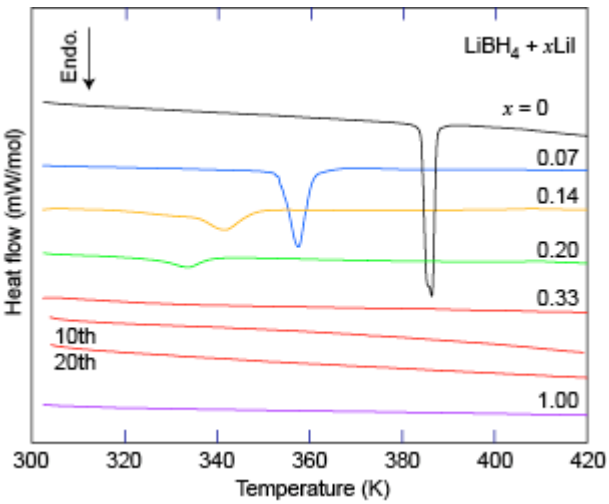

FIG. 2. DSC profiles of $LiBH_4 + xLiI$. The intensities are normalized to show the heat flow per

mole of the formula unit of $LiBH_4$ + xLiI. The area of the endothermic peak of each profile gives the experimental value of the enthalpy change ($\Delta H_{exp.}$), e.g., 4.18 kJ/mol with x = 0.

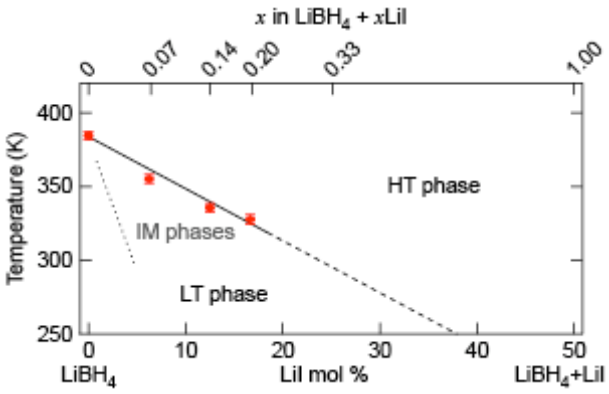

FIG. 3. Structural transition temperatures of $LiBH_4$ + xLiI as a function of value x (top axis) and "LiI mol %" (bottom axis). The IM phases are predicted with x = 0.07 - 0.20.

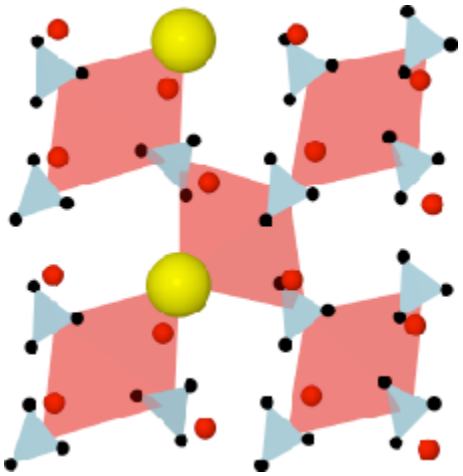

FIG. 4. Crystalline structure of a possible intermediate (IM) phase of $LiBH_4$ + 0.14LiI (in LiI space group $P4_2/mnm$). Red, yellow, and black circles correspond to Li, I, and H sites, respectively. B atoms are embedded in blue $[BH_4]^-$ tetrahedron.

Paper V

Ammonia dynamics in magnesium ammine salts from DFT

Adem Tekin[†,‡], *Jens S. Hummelshøj*[†,‡], *Jens K. Nørskov* [†], *and Tejs Vegge* [*,‡]

[†] Center for Atomic-scale Materials Design (CAMD), Department of Physics, Technical University of Denmark, DK-2800 Lyngby, Denmark
[‡] National Laboratory for Sustainable Energy, Technical University of Denmark, DK-4000 Roskilde, Denmark

teve@risoe.dtu.dk

Energy storage in the form of ammonia stored in metal salts, so-called metal ammines, has many interesting properties. In particular, metal ammines show fast and reversible NH_3 ab- and desorption kinetics. The mechanisms and processes involved in the NH_3 kinetics is investigated by density functional theory (DFT). For this purpose, $Mg(NH_3)_nCl_2$ with n = 6, 2, 1, one the most promising metal ammine with 9.19 wt % H and 0.115 kg H/L, is used in the DFT calculations. First, a crystal structure prediction algorithm based on Simulated Annealing is successfully applied for $Mg(NH_3)_6Cl_2$ by finding three possible low temperature structures with $C2/m$ and $R-3$ symmetries. It is found that rotation of ammonia in hexamine complex requires an activation energy of 0.09 eV in low temperature phase and 0.002 - 0.12 eV in high temperature phase of $Mg(NH_3)_6Cl_2$; effectively having free rotors as observed experimentally. Diffusion rates of 10^5 - 10^6 was found at the desorption temperatures for all n = 6, 2, 1 systems. DFT calculations involving bulk diffusion of NH_3 correctly reproduces the trends observed in the experimental desorption enthalpies. In particular, for n = 6, 2, 1, there is a good agreement between activation barriers and experimental enthalpies. These results indicate that the desorption of NH_3 is likely to be diffusion limited.

1 INTRODUCTION

Hydrogen has a great potential to be used as an energy carrier for the future. Unlike fossil fuels, it only generates water as a by product after usage. Therefore, a hydrogen-based energy infrastructure would be more environmentally friendly by preventing carbon dioxide emission and a reduced dependence on the limited non-renewable energy sources, e.g., petroleum, coal, and natural gas. However, there are still some major challenges waiting to be addressed concerning the production, storage, and the everyday-use of hydrogen.

Since transport requires about one quarter of the world total energy [1], an efficient on-board hydrogen storage technology must be developed to have a hydrogen society. Storing hydrogen as a gas or liquid is possible but not efficient in terms of energy capacity and cost for on-board applications due to the requirement of either high pressures or crygonic temperatures, respectively. Alternatively, hydrogen can also be stored with high capacity in the condensed phase. In particular, metal hydrides [2], carbon nanotubes [2], and recently metal-organic frameworks [2,3] studied extensively for solid hydrogen storage. However, none of these solid mediums are completely promising in terms a of fast, reversible and high-density hydrogen uptake and release.

In addition to these direct hydrogen storage materials, hydrogen can also be stored indirectly e.g., in the form of ammonia in metal salts, so called metal ammines [4–8]. Storing ammonia in metal ammines reduces the ammonia toxicity approximately by three orders of magnitude compared to liquid ammonia [4]. Apart from this safety aspect, metal ammines have better storage properties compared to direct and other indirect hydrogen storage materials. Most importantly, they exhibit a fast and reversible ammonia ab- and desorption kinetics. $Mg(NH_3)_6Cl_2$ could be seen as the prototype of metal ammines with promising 9.19 wt % H and 0.115 kg H/L storage capabilities. Temperature-programmed desorption (TPD) experiments [4] suggested that NH_3 desorbs in three stages in $Mg(NH_3)_6Cl_2$. First, $Mg(NH_3)_6Cl_2$ releases four molecules NH_3 at nearly 440 K by forming $Mg(NH_3)_2Cl_2$. Then, one molecule of NH_3 desorbs from the diammine complex by forming $Mg(NH_3)_1Cl_2$ at around 575 K. Finally, the last remaining NH_3 molecule in the monoamine complex is desorbed at around 675 K. The recent work of Sørensen et al [8] shows surprisingly high barriers for bulk diffusion of NH_3 in n = 2, 1. Following this desorption scheme, we emphasized to study the bulk diffusion of NH_3 in n = 6, 2, 1 complexes to have a better understanding of NH_3 kinetics.

NH_3 dynamics are important for the structural stability and desorption properties, and the correct crystal structures in the computations is important to have a more reliable NH_3 diffusion and rotation kinetics. In $Mg(NH_3)_nCl_2$ with n = 6, 2, 1, all the high temperature structures are experimentally verified, except the low temperature structure (LT1) of n = 6. LT1 is especially required to calculate the NH_3 rotation barrier to account for the order-disorder transitions. In order to find the low temperature structure of n = 6, we applied a global crystal structure prediction method based on Simulated Annealing (SA) [9].

NH_3 diffusion and rotation kinetics can be computationally investigated by employing path techniques such as Nudged Elastic Band (NEB) [10] and Adaptive Nudged Elastic Band (ANEB) [11]. These techniques aim to find a path connecting an initial state to the final one via a transition state. Having an initial and transition state for a process enables us to perform a vibrational analysis to obtain the relevant

eigenfrequencies. By using these frequencies, the rates for the kinetic processes at relevant temperatures can easily be calculated employing harmonic transition state theory (HTST).

In this study, we further investigated the possibility of bulk diffusion NH_3 in n = 2, 1 by considering alternative pathways with a combination of NEB and ANEB methods. For all the considered paths, the transition states were successfully located and subsequently process rates were calculated.

2 CALCULATION DETAILS

2.1 Crystal structure predictions

Since bulk diffusion and rotation barriers are strongly dependent on the starting crystal structure, it is crucial to use the correct structures in the calculations. This point becomes more delicate, if there is no any experimental support on the crystal structure as in the case of low temperature structure of $Mg(NH_3)_6Cl_2$. Therefore, as a first step, we employed a crystal search algorithm based on SA aiming to predict structures of the unknown complexes.

In general, hydrogen bonds between NH_3's hydrogens and chlorine atoms in $Mg(NH_3)_nCl_2$ with n = 6, 2, 1 are important to stabilize the metal complex. This fact is exploited in the SA search method to construct crystal structures by maximizing the number of hydrogen bonds within a ($2 \times 2 \times 2$) cut-through lattice using only several bond length constraints. In the following, the details of this SA search is exemplified for $Mg(NH_3)_6Cl_2$ using a model system illustrated in Fig. 1:

- A fixed coordinate system is used for $Mg(NH_3)_6Cl_2$.
- The coordinates of the chlorine atoms are parameterized.
- Three euler angle parameters (Θ, Φ, Ψ) are used to rotate the Mg-$(NH_3)_6$ complex.
- Each ammonia molecule is rotated by one of the angle parameters (α, β, δ, ϵ, η, λ) around the N-Mg axis.
- The lattice vectors are used as parameters.
- The resulting 24 parameters are globally optimized to maximize the number of hydrogen bonds in $Mg(NH_3)_6Cl_2$.

In addition to the general model above, other models were also investigated in SA optimizations such as instead of using a fixed metal ammine coordinate system, spherical coordinates of all NH_3 molecules are parameterized to be able to search the configurations in which Mg atoms do not prefer an octahedral coordination. However, such crystal structures were found to be higher in energy than the ones where Mg prefers octahedral coordination. Furthermore, in the SA search, the type of crystal system e.g., triclinic, monoclinic, was also used as constraints to be able to reduce the parameter search space.

Since the current SA optimizations only are based on the geometrical features of the studied system (neither empirical potentials nor DFT energies are used), bond length constraints must be carefully introduced into the models discussed above to prevent resulting in an unphysical crystal structure. In particular, if the H - H, Cl - Cl and Cl - Mg distances in the (2 × 2 × 2) cut-through lattice are longer than 2.1 Å, 5.18 Å, and 4.6 Å, respectively, then the crystal structure is accepted in these model systems. The fitness criteria in SA optimizations, the total number of hydrogen bonds in the cut-through lattice, is determined by simply counting the number of H - Cl bonds, if the H - Cl bond is in between 2.4 - 3.5 Å. All these constraints were adjusted with the help of some prelimanary DFT calculations and literature.

The LT1 structure of nickel hexammine salt has been experimentally [12,13] verified to be a monoclinic space group. In a more recent experimental study [14], it has been shown that this monoclinic structure has a *C2/m* symmetry. Since there is no any experimental evidence on the LT1 structure of magnesium hexamine salt, it could be expected that the monoclinic structure adopted by nickel hexamine might be the LT1 structure of magnesium complex. The high temperature structure (LT2) (see Fig. 2 b)) of Mg hexammine complex is based on K_2PtCl_6 type [15], however, this *Fm3m* symmetry was slightly distorted to *I4/m* after the DFT relaxations [8].

For the hexammine case, the SA optimizations yielded three possible low temperature structures with *C2/m* and *R − 3* symmetries. In one of the *C2/m* symmetry structure, the positioning of atoms is almost the same with *R − 3* symmetry structure shown in Fig. 2 a), where each chlorine atoms stabilized by three hydrogen bonds. These four structures were found to be isoenergetic after the further DFT relaxations (all atoms are allowed to be relaxed) (see section 2.2) with energy differences at most 0.01 eV. The *R − 3* symmetry structure obtained from the SA search only differs from Fig. 2 a) by favoring different positions for chlorine atoms. However, the other SA optimized *C2/m* symmetry structure has a distinct structural preference compared to the other three structures. The SA optimizations also yielded an isoenergetic structure with *P − 1* symmetry to the LT2 shown in Fig. 2 b). Moreover, a *C2/m* symmetry structure was also predicted which is geometrically similar to the structure in Fig. 2 b) but lower in energy by 0.03 eV.

This SA strategy was also employed for $Mg(NH_3)_nCl_2$ with n = 2, 1. As shown in Fig. 3, the experimentally verified *C2/m* [16] and *Cmmm* [17] symmetry structures were successfully reproduced for n = 2, 1. The corresponding crystallographic details of structures shown in Figs. 2 and 3 are listed in Table 1. Throughout this study, these structures were used in the NH_3 diffusion and rotation barrier calculations.

2.2 DFT Calculations and system setup

The electronic structure computations are carried out using density functional theory [19] in the DACAPO plane wave basis set implementation [18], with a cutoff energy of 340 eV (for the density grid a cutoff of 500 eV is employed). The exchange-correlation effects are described by the RPBE [18] functional. In DACAPO, the ionic cores are described by ultrasoft pseudopotentials [20]. The electronic Brioullin zones are sampled with (2 × 2 × 2) *k*-points. Structural optimizations are performed until all forces are smaller than 0.01 eV/Å using a

quasi-Newton method [21] within the Atomic Simulation Environment [22]. In the path calculations, the force criterion is raised to 0.05 eV/Å.

In the calculations of NH_3 bulk diffusion, the required NH_3 vacancies were created by removing an NH_3 molecule from the supercell and this was followed by a relaxation of the atomic positions. The NEB method is primarily employed to locate the diffusion pathways of NH_3. Since the NEB technique is too expensive to study the complex NH_3 dynamics, generally 9 intermediate images employed in the reaction path calculations. An initial guess for the positions of the intermediate images was determined by a linear interpolation of the initial and the final images. However, for the paths where an NH_3 flip is required, the linear interpolation does not provide a good set of intermediate images. Therefore, the initial intermediate images are created manually to speed up the NEB calculations.

Since it is not always possible to locate the transition states using NEB, the ANEB method [11] is also used. In ANEB, instead of choosing a large number images to bracket the transition state, the resolution in the neighborhood of the transition state is adaptively increased. In particular, ANEB starts from three intermediate images connecting two local minima and performs a NEB calculation. Then, two images adjacent to the one that has the highest energy in the NEB calculation is chosen as the new starting points for the NEB calculation. Repeating this procedure ultimately allows ANEB to bracket the transition state.

2.3 Harmonic transition state theory

Within a harmonic approximation, the vibrational properties of solids can be expressed in terms of the N normal modes system at the local minimum and the N-1 normal modes at the saddle point. The activation energy, ΔE, is described as the energy difference between the system at the local minimum and at the transition state. ΔE enters into the Arrhenius equation as:

$$\tau^{-1} = \tau_0^{-1} e^{-\Delta E/k_B T} \tag{1}$$

where, τ_0^{-1} is called as the prefactor which can be calculated using the eigenfrequencies of the local minimum and the transition state:

$$\tau^{-1} = \frac{1}{2\pi} \frac{\prod_{i=1}^{N} \omega_i}{\prod_{i=1}^{N-1} \omega_i^{'}} \tag{2}$$

where ω_i and $\omega_i^{'}$ denote the frequencies of the local minimum and the transition state, respectively. These frequencies are calculated within the harmonic approximation by evaluating and diagonalizing the Hessian matrix. All the prefactors, activation energies, and process rates at relevant temperatures are listed in Tables 2 and 3 for the rotation and diffusion barriers, respectively.

3 Results and Discussion

3.1 Ammonia rotation

Ammonia molecules in high temperature phase of metal hexammines $M(NH_3)_6X_2$ with M = Ca, Mn, Fe, Co, Ni, Zn, Cd, and X = Cl, Br, I are generally orientationally disordered [23], in contrast to the low temperature phases. The active role of NH_3 orientations in this phase transitions were shown experimentally [12, 24, 25]. In addition to the hexammine complex, similar order-disorder phase transitions were also experimentally observed in $Mg(ND_3)_2X_2$ with X = Cl, Br [26].

In this study, we considered the NH_3 rotations in hexammine Mg complex both in LT1 and LT2 structures. To calculate the ammonia rotation barriers, NH_3 molecules are rotated by 120° around their N-Mg axis. First, only a single NH_3 rotation barrier was investigated. Since all the six NH_3 molecules are equivalent in LT1, for each NH_3 the same rotation barrier to be 0.09 eV was obtained as shown in Fig. 4. In contrast to LT1, there are three non-equivalent NH_3's in LT2: NH_3 forming two hydrogen bonds (*type I*), NH_3 in which two hydrogens are directed to the chlorines atoms with a longer distance than the usual hyrogen bond (*type II*), and eclipsed NH_3 in which there is no hydrogen bond (*type III*) (see Fig. 5). Amongst these three different NH_3's, the highest rotation barrier was calculated to be 0.12 eV in the *type I* NH_3 as shown in Fig. 4. For the other NH_3 species in LT2, the barriers were obtained to be 0.08 eV and 0.002 eV, respectively. These results indicate that the *type III* NH_3s are effectively free rotors, since the process occurs without a cost by avoiding to break a hydrogen bond.

Figure 6 shows the activation barriers for possible double NH_3 rotations. The activation energies obtained from the NEB calculations are quite similar to the ones obtained from single rotations. For the double rotation, the same activation barriers were obtained when any two molecules of NH_3 are rotated either at the same direction or one is clock-wise and the other one is anti clock-wise in LT1. As clearly seen from the Fig. 6, two NH_3 molecules do not rotate together. More specifically, in LT1, first NH_3 rotates around 60° and then it stops its rotation and immediately the other NH_3 molecule starts to rotate another 60°. A similar rotation pattern was obtained in LT2 (using *type I* and *type II* NH_3). As expected, the highest process rate was found to be in the order of 10^{12} for the *type III* NH_3 in LT2 (see Table 2). The rates were calculated to be in the orders of 10^5 to 10^7 for the other NH_3 moleculess in LT1 and LT2.

3.2 Ammonia diffusion

The desorption of NH_3 from $Mg(NH_3)_nCl_2$ with n = 6, 2, 1 is likely to depend on macroscopic bulk diffusion of NH_3. Therefore, we carried out NEB and ANEB calculations to locate the lowest acvitation barriers of NH_3 transfer in $Mg(NH_3)_nCl_2$ with n = 6, 2, 1. These complexes are known to be stable from the TPD experiments [8].

For the hexammine complex, we performed the barrier calculations using the Fig. 2 a) by creating an NH_3 vacancy in the unitcell. The NH_3 vacancy formation energy in the hexammine complex was calculated to be 0.61 eV. The diffusion barrier for

the high temperature structure shown in Fig. 2 b) was recently reported in Sørensen et al. [8] to be 0.60 eV (jump path). This path requires an additional reorientation (reorient path) of one NH_3 in the host Mg complex to allow a long-range transport pathway. This barrier was found to be 0.17 eV. The corresponding prefactors and rates for these paths including the total process (jump + reorient) were shown in Table 3.

In LT1, there are many possible diffusion pathways with jump lengths (the linear distance in the nitrogen positions in the host and guest Mg complexes) in-between 4.24 -5.11 Å. In all these different paths, the diffusion barriers were calculated to be 0.52 - 0.60 eV. The lowest energy diffusion path was shown in Fig. 7. Here, the NH_3 molecule is rotated around itself and then merged to the vacant position on the guest Mg complex. For this path, the HTST prefactor of $\tau_0^{-1} = 2.3 \times 10^{13}$ Hz obtained from a vibrational analysis of initial and transition states. However, it is not possible to have a long-range transport path as in the case of LT2, if this pathway is considered alone. The additional path can simply be done by creating an NH_3 vacancy on the host Mg complex having the same vacancy position in the guest Mg complex. This arrangement involves an approximately 90° rotation of one NH_3 molecule. The barrier was claculated to be 0.10 eV with a prefactor of 5.6 $\times 10^{12}$ Hz. The requirement for the additional arrangement on the host Mg complex is also valid for the other considered diffusion pathways in hexammine complex. As shown in Table 3, the rate of the overall process in LT1 is approximately 20 times faster than LT2.

Two competing long-range diffusion pathways have been found along and between the chains of the diammine Mg complex. The NH_3 vacancy formation energy was calculated to be 0.79 eV and 0.76 eV in the calculation setups for along the chain and interchain paths, respectively. The "*along the chain*" barrier was obtained to be 0.87 eV using 4 formula unit (f.u.) of Mg complex in the unitcell as shown in Fig. 8 a). This calculated barrier height is in agreement with the experimental desorption enthalpy (0.78 eV) [27]. A prefactor of 6.2 $\times 10^{13}$ Hz was obtained from the vibrational analysis for this path.

The interchain pathway for the diammine complex involves the flipping of NH_3 as shown in Figs. 8 b) and c). In other words, ammonia prefers to be flat in the middle of the diffusion path. Other arrangements that NH_3 could have e.g., rotation of NH_3 around itself are restricted due to the close contacts occuring between hydrogen's of NH_3 and the chlorine atoms in *interchain I* path. In general, making NH_3 planar costs at least 0.21 eV [28]. Therefore, in a path where an NH_3 flips, the diffusion barrier could be expected to be higger than the other conventional paths. However, as shown in Fig. 8 b), the *interchain I* barrier was found to be quite the same with the along the chain path with a prefactor of 3.4 $\times 10^{13}$ Hz. This is likely due to the following observation: one of the chlorine atom bound to the guest Mg replaces almost 1.1 Å in direction to the one of the hydrogen of the flipping NH_3 to form a hydrogen bond in addition to the other hydrogen bond as seen in Fig. 8 b). Furthermore, upon the reallocation of this chlorine atom, the guest Mg atom prefers to form a non-ideal tetrahedral. These rearrangements compensate the cost required by the NH_3 flip.

There is also another interchain path (*Interchain II*) involving NH_3 flip as shown in Fig. 8 c) in the diamine complex. In the *interchain II*, the activation barrier was obtained same as the along the chain and the other interchain pathways with

a prefactor of 3.8 $\times 10^{14}$ Hz. Here, NH_3 might also be rotated around itself with a similar cost instead of flipping. To build a macroscopic transport using the *interchain II*, a reorientation on the host Mg complex is required. However, the barrier for this reorientation was calculated higger by 0.2 eV than the flipping path.

Similar to the diammine case, both interchain and along the chain mechanisms found as possible long-range transport paths for the monoammine complex. The vacancy formation energy was calculated to be 0.66 eV which is smaller than the experimental desorption enthalpy [27] by 0.24 eV. The along the chain NH_3 bulk diffusion barrier was calculated to be 0.9 eV using 4 f.u. unitcell as shown in Fig. 9 a) with a prefactor of 1.6 $\times 10^{14}$ Hz. This calculated barrier height is completely agree with the experimental desorption enthalpy (0.9 eV) [27]. Similar to the along the chain path in diammine complex, there is no a notable change in the positions of chlroine atoms during the motion of NH_3.

Finally, a massive unitcell including 8 f.u. of Mg complex was employed to study the interchain path in monoammine complex. As shown in Fig. 9 b), the barrier was found to be 1.23 eV with a prefactor of 2.8 $\times 10^{14}$ Hz. The similar process rates were obtained to be in the order of 10^5 for both along the chain and interchain paths as listed in Table 3.

In Fig. 10, the calculated desorption enthalpies and the lowest energy diffusion barriers were compared with the experimental desorption enthalpies [27]. It is apparent that, the calculated enthalpies are shifted down by a certain factor. However, the trend observed in the experimental enthalpies are reproduced well with the calculated enthalpies. Moreover, the calculated diffusion barriers for n = 6, 2, 1 agree with the experimental desorption enthalpies.

These results seem to support a desorption mechanism for n = 6, 2, 1, which is diffusion limited. It should, however, be noted that initial calculations with van der Waals (vdW) corrected DFT appears to stabilize the structures and yield better agreement with the experimental desorption enthalpies. Work analyzing possible vdW effects on the rates of the dynamical processes is in progress

4 Conclusions

It is shown that predicting crystal structures employing global optimization techniques such as SA with simple models is possible in situations where there is no experimental evidence on the crystal structure. In this study, this strategy is successfully applied to locate the low temperature structure of hexammine Mg complex and reproduce the experimental structures of the di- and mono ammnine phases.

It is demonstrated that rotation of ammonia in hexamine complex requires an activation energy of 0.09 eV in LT1 and 0.002 - 0.12 eV in LT2; effectively having free rotors as observed experimentally. Diffusion rates of 10^5 - 10^6 was found at the desorption temperatures for all n = 6, 2, 1 systems. Furthermore, a number of different diffusion mechanisms were found to be equaly important in n = 2. DFT calculations involving bulk diffusion of NH_3 correctly reproduces the trends observed in the experimental desorption enthalpies. In particular, for n = 6, 2, 1, there is a good agreement between activation barriers and experimental enthalpies.

As a conclusion, the fast ab- and desorption process observed experimentally could be explained on the basis of a diffusion limited process for n = 6, 2, 1. Calculations which account for vdW forces is in progress.

5 Acknowledgment

The Center for Atomic-scale Materials Design is supported by the Lundbeck Foundation. The authors acknowledge the European Commission DG Research (contract MRTN-CT-2006-032474/Hydrogen and SES6-2006-51827/NESSHy).

References

[1] D. Mori and K. Hirose, *Int. J. Hydrogen Energy* (2008) doi:10.1016/j.ijhydene.2008.07.115.

[2] http://www1.eere.energy.gov/hydrogenandfuelcells/storage/index.html

[3] Y. Liu, H. Kabbour, C. M. Brown, D. A. Neumann, and C. C. Ahn, *Langmuir* 24 (2008) 4772.

[4] C. H. Christensen, R. Z. Sørensen, T. Johannessen, U. J. Quaade, K. Honkala, T. D. Elmøe, R. Køhler, and J. K. Nørskov, *J. Mater. Chem.* 15 (2005) 4106.

[5] J. H. Hummelshøj, R. Z. Sørensen, M. Y. Kustova, T. Johannessen, J. K. Nørskov, and, C. H. Christensen, *J. Am. Chem. Soc.* 128 (2006) 16.

[6] H. S. Jacobsen, H. A. Hansen, J. W. Andreasen, Q. Shi, A. Andreasen, R. Feidenhans'l, M. M. Nielsen, K. Stahl, T. Vegge, *Chem. Phys. Lett.* 441 (2007) 225.

[7] A. Klerke, C. H. Christensen, J. K. Nørskov, and T. Vegge, *J. Mater. Chem.* 18 (2008) 2304.

[8] R. Z. Sørensen, J. S. Hummelshøj, A. Klerke, J. B. Reves, T. Vegge, J. K. Nørskov, and C. H. Christensen, *J. Am. Chem. Soc.* 130 (2008) 8660.

[9] A. Corona, M. Marchesi, C. Martini, and S. Ridella, *ACM T MATH SOFTWARE* 13 (1987) 262.

[10] H. Jónsson, G. Mills, and K. W. Jacobsen, In *Classical and Quantum Dynamics in Condensed Phase Simulations*, Eds: B. J. Berne, G. Ciccoti, and D. F. Coker, Worls Scientific, Singapore, 1998.

[11] P. Maragakis, E. Kaxiras, S. Andreev, Y. Brumer, and D. R. Reichman, *J. Chem. Phys.* 117 (2002) 4651.

[12] A. R. Bates, L. T. H. Ferris, and T. E. Jenkins, *J. Phys.C : Solid State Phys.* 12 (1979) 2945.

[13] A. M. Mikuli, E. Mikuli, and K. Zabinska, *J. Phys.C : Solid State Phys.* 15 (1982) 6565.

[14] http://wwwold.ill.fr/SCO/ExpRep/5-21-771.pdf

[15] I. Olovsson, *Acta Crystallogr.* 18 (1965) 889.

[16] A. Leineweber, H. Jacobs, H. Ehrenberg, *Z. Anorg. Allg. Chem.* 626 (2000) 2146.

[17] A. Leineweber, M. W. Friedriszik, and H. Jacobs, *J. Solid State Chem.* 147 (1999) 229.

[18] B. Hammer, L. B. Hansen, and J. K. Nørskov, *Phys. Rev. B* 59 (1999) 7413.

[19] P. Hohenberg and W. Kohn, *Phys. Rev.* 136 (1964) B864.

[20] D. Vanderbilt, *Phys. Rev. B* 41 (1990) 7892.

[21] D. F. Shanno, *Math. Comput.* 24 (1970) 647.

[22] S. Bahn and K. Jacobsen, *Comput. Sci. Eng.* 4 (2002) 56.

[23] P. Schiebel, A. Hoser, W. Prandl, G. Heger, and P. Schweiss, *J. Phys. I France* 3 (1993) 987.

[24] T. E. Jenkins, L. T. H. Ferris, A. R. Bates, and R. D. Gillard, *J. Phys. C Solid State Phys.* 10 (1977) 521.

[25] T. E. Jenkins, L. T. H. Ferris, A. R. Bates, and R. D. Gillard, *J. Phys. C Solid State Phys.* 11 (1978) 77.

[26] A. Leineweber, H. Jacobs, P. Fischer, and G. Böttger, *J. of Sol. Sta. Chem.* 156 (2001) 487. Sørensen

[27] E. Lepinasse and B. Spinner, *Int. J. Refrig.* 5 (1996) 309.

[28] S. F. A. Kettle, *Symmetry and Structure : Readable Group Theory for Chemists* Published by John Wiley and sons (2007) page 8.

Table 1: Crystallographic details for the structures shown in Figures 2 and 3.

Structure	Z	Space group	a,b,c (Å)	$\alpha,\ \beta,\ \gamma$
Fig. 2 a)	1	*R-3*	8.05, 8.05, 17.08	90, 90, 120
Fig. 2 b)	1	*I4/m*	7.76, 7.76, 10.98	90, 90, 90
Fig. 3 a)	1	*C2/m*	19.26 3.62 6.59	90, 99, 90
Fig. 3 b)	2	*Cmmm*	8.89 8.84 3.75	90, 90, 90

Table 2: List of calculated prefactors, activation energies, and rates at relevant temperatures for all the rotation processes considered in this study.

Structure	Prefactor [Hz]	Activation Energy [eV]	Rate [Hz]	Temperature [K]
LT1	$3.3\ \times 10^{12}$	0.091	$7.1\ \times 10^{6}$	80
LT2 (*type I*)	$1.2\ \times 10^{13}$	0.119	$3.3\ \times 10^{5}$	80
LT2 (*type II*)	$4.2\ \times 10^{12}$	0.082	$3.7\ \times 10^{7}$	80
LT2 (*type III*)	$1.8\ \times 10^{12}$	0.002	$1.3\ \times 10^{12}$	80

Table 3: List of calculated prefactors, activation energies, and rates at relevant temperatures for all the diffusion processes considered in this study.

Structure	Prefactor [Hz]	Activation Energy [eV]	Rate [Hz]	Temperature [K]
		$Mg(NH_3)_6Cl_2$		
LT1 jump	$2.3\ \times 10^{13}$	0.52	$8.3\ \times 10^{7}$	440
LT1 reorient	$5.6\ \times 10^{12}$	0.10	$4.0\ \times 10^{11}$	440
LT1 overall			$8.3\ \times 10^{7}$	440
LT2 jump	$2.3\ \times 10^{13}$ †	0.60 *	$3.7\ \times 10^{6}$	440
LT2 reorient	$5.6\ \times 10^{12}$ †	0.17 *	$6.3\ \times 10^{10}$	440
LT2 overall			$3.7\ \times 10^{6}$	440
		$Mg(NH_3)_2Cl_2$		
Along the chain	$6.2\ \times 10^{13}$	0.87	$5.9\ \times 10^{4}$	575
Interchain I	$3.4\ \times 10^{13}$	1.03	$3.2\ \times 10^{4}$	575
Interchain II	$3.8\ \times 10^{14}$	1.03	$3.6\ \times 10^{5}$	575
		$Mg(NH_3)_1Cl_2$		
Along the chain	$1.6\ \times 10^{14}$	0.90	$3.4\ \times 10^{5}$	675
Interchain	$2.8\ \times 10^{14}$	1.23	$6.0\ \times 10^{5}$	675

† from LT1
* Ref. [5]

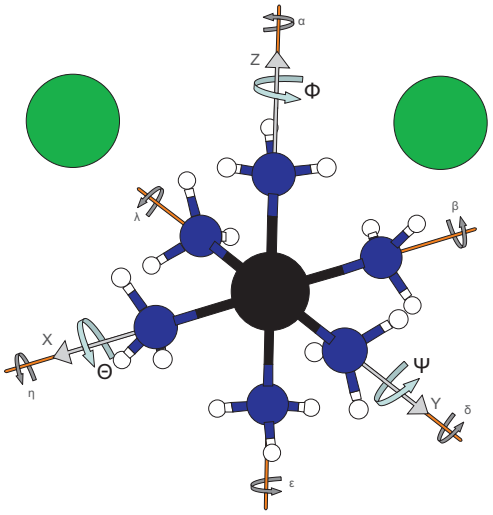

Figure 1: The simplest model system used in SA optimizations. (See details in the text.) Representing colors: chlorine, green; magnesium, black; nitrogen, blue; hydrogen, white.

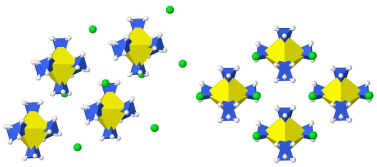

a) 0.00 eV $(R-3)$ b) 0.05 eV $(I4/m)$

Figure 2: a) the low (LT1) and b) high (LT2) temperature structures for hexammine magnesium complex used in NEB and ANEB calculations. Crystallographic details of these structures are given in Table 1. Representing colors: chlorine, green; magnesium, yellow octahedron; nitrogen, blue; hydrogen, white.

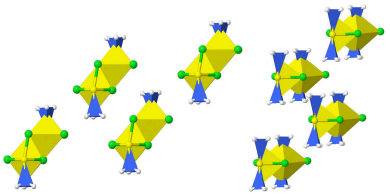

a) $(C2/m)$ b) $(Cmmm)$

Figure 3: Crystal structures of a) monoamine and b) diammine magnesium complex used in NEB and ANEB calculations. Crystallographic details of these structures are given in Table 1.

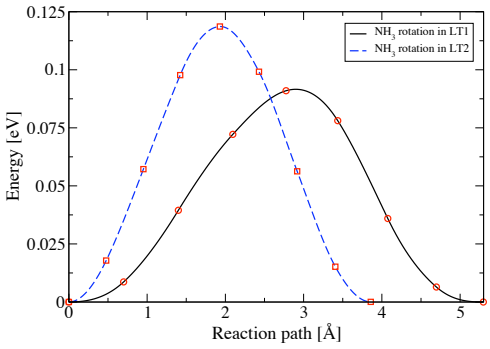

Figure 4: Minimum energy paths for single NH_3 rotations in low and high temperature structures of $Mg(NH_3)_6Cl_2$.

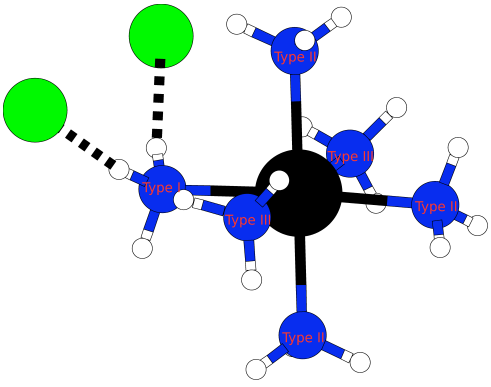

Figure 5: Three types of NH_3 in the high temperature structure of $Mg(NH_3)_6Cl_2$.

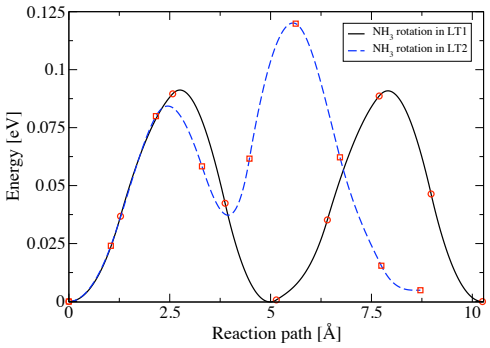

Figure 6: Minimum energy paths for double NH_3 rotations in low and high temperature structures of $Mg(NH_3)_6Cl_2$.

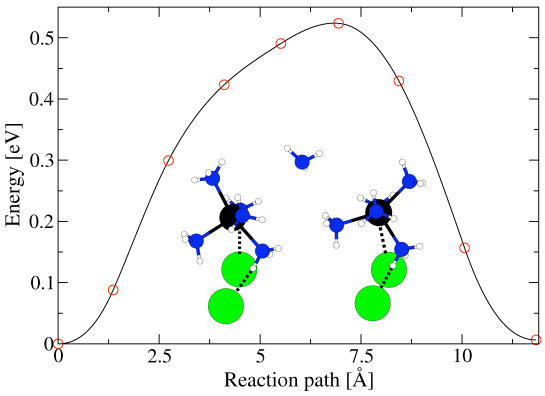

Figure 7: Minimum energy path for NH_3 diffusion in $Mg(NH_3)_6Cl_2$.

a) *along the chain*

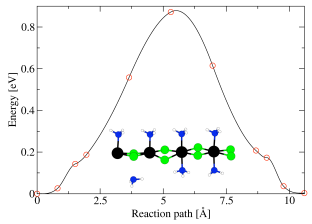

b) *interchain I*

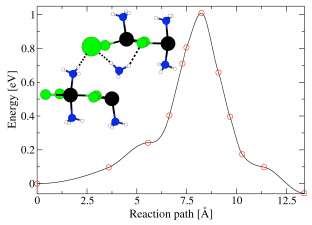

c) *interchain II*

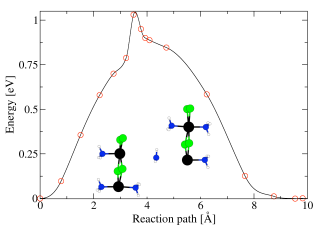

Figure 8: Longe-range NH_3 diffusion paths in $Mg(NH_3)_2Cl_2$ a) *along the chain*, b) *interchain I*, and c) *interchain II*.

a) *along the chain*

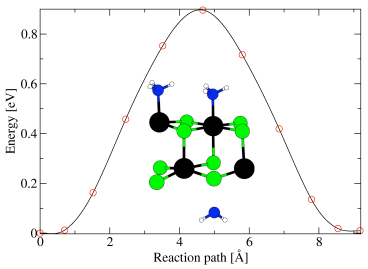

b) *interchain*

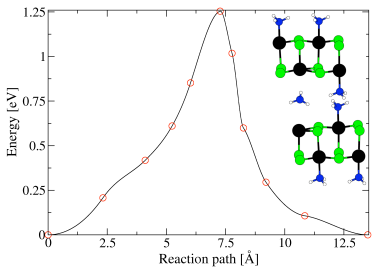

Figure 9: Longe-range NH_3 diffusion paths in $Mg(NH_3)_1Cl_2$ a) *along the chain* and b) *interchain*.

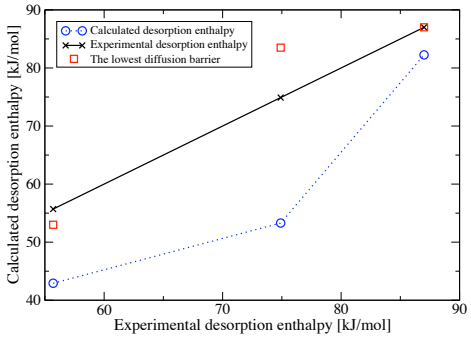

Figure 10: Calculated (dotted line) versus experimental (solid line) desorption enthalpies for the different desorption steps, 6→2, 2→1, and 1→0, of magnesium salt. The lowest activation barriers obtained for NH_3 diffusion are shown in squares.